IMPERIAL COLLEGE LONDON

PhD Thesis

Prediction of Thermoacoustic Instability in Gas Turbine Combustors

by

Yu Xia

A thesis submitted in fulfilment of the requirements
for the degree of Doctor of Philosophy

in the

Department of Mechanical Engineering
Imperial College London
Exhibition Road, London SW7 2AZ, United Kingdom

May 2019

This work is dedicated to Kangrui and Kejun

Declaration of Originality

I, Yu Xia, hereby certify that the work presented in this thesis is the result of my original research, except where acknowledged in the text. Some findings reported throughout this thesis have been presented at conferences or published in scientific journals. This thesis has not been submitted in any other form for another degree or diploma.

Yu Xia,

May 2019

Declaration of Copyright

The copyright of this thesis rests with the author. Unless otherwise indicated, its contents are licensed under a Creative Commons Attribution-Non Commercial 4.0 International Licence (CC BY-NC).

Under this licence, you may copy and redistribute the material in any medium or format. You may also create and distribute modified versions of the work. This is on the condition that: you credit the author and do not use it, or any derivative works, for a commercial purpose.

When reusing or sharing this work, ensure you make the licence terms clear to others by naming the licence and linking to the licence text. Where a work has been adapted, you should indicate that the work has been changed and describe those changes.

Please seek permission from the copyright holder for uses of this work that are not included in this licence or permitted under UK Copyright Law.

Yu Xia,

May 2019

Publications

Some of the work included in this thesis have been published in the form of peer-reviewed journal articles and conference papers during the past 4 years, which are listed below:

Journal Articles:

(*i*) Y. Xia, D. Laera, W. P. Jones, A. S. Morgans. Numerical prediction of the flame describing function and thermoacoustic limit cycle for a pressurized gas turbine combustor. *Combustion Science and Technology*, 2019. https://doi.org/10.1080/00102202.2019.1583221

(*ii*) Y. Xia, I. Duran, A. S. Morgans, X. Han. Dispersion of entropy perturbations transporting through an industrial gas turbine combustor. *Flow, Turbulence and Combustion*, 100(2): 481–502, 2018.

(*iii*) J. Li, Y. Xia, A. S. Morgans, X. Han. Numerical prediction of combustion instability limit cycle oscillations for a combustor with a long flame. *Combustion and Flame*, 185: 28–43, 2017.

Conference Papers:

(*i*) Y. Xia, D. Laera, A. S. Morgans, W. P. Jones, J. W. Rogerson. Thermoacoustic limit cycle predictions of a pressurised longitudinal industrial gas turbine combustor. *Proceedings of ASME Turbo Expo 2018*, Oslo, Norway, 2018. Paper No. GT2018-75146.

(*ii*) Y. Xia, A. S. Morgans, W. P. Jones, J. W. Rogerson, G. Bulat, X. Han. Predicting thermoacoustic instability in an industrial gas turbine combustor: combining a low order network model with flame LES. *Proceedings of ASME Turbo Expo 2017*, Charlotte, NC, USA, 2017. Paper No. GT2017-63247.

(***iii***) Y. Xia, J. Li, A. S. Morgans, X. Han. Computation of local flame describing functions for thermoacoustic oscillations in a combustor with a long flame. *Proceedings of the 8th European Combustion Meeting (ECM8)*, Dubrovnik, Croatia, 2017.

(***iv***) Y. Xia, A. S. Morgans, W. P. Jones, X. Han. Simulating flame response to acoustic excitation for an industrial gas turbine combustor. *Proceedings of the 24th International Congress on Sound & Vibration (ICSV24)*, London, UK, 2017.

(***v***) Y. Xia, I. Duran, A. S. Morgans, X. Han. Dispersion of entropy waves advecting through combustion chambers. *Proceedings of the 23rd International Congress on Sound & Vibration (ICSV23)*, Athens, Greece, 2016.

(***vi***) J. Li, X. Han, Y. Xia, A. S. Morgans. Thermoacoustic analysis of the combustor consisting long flames using low order network model approach. *Proceedings of the International Symposium: Thermoacoustic Instabilities in Gas Turbines and Rocket Engines: Industry Meets Academia*. Munich, Germany, 2016.

Abstract

This thesis numerically predicts thermoacoustic instability in two typical gas turbine combustors. Incompressible large eddy simulation (LES) is used as the main numerical tool to simulate the heat release response of a flame to upstream acoustic perturbations, resulting in linear and nonlinear flame response models. These flame models are then combined with analytical acoustic wave models to predict thermoacoustic instability, and for those unstable operations, the resulting nonlinear limit cycle oscillations. Other features relevant to thermoacoustic instability are also studied, including entropy wave transport within the combustor flow fields, and the axial variation of the heat release response along a long flame length, etc.

This thesis has found that (*i*) the incompressible LES performed by BOFFIN and OpenFOAM can both accurately simulate the reacting flow in realistic gas turbine combustors, and capture the forced flame heat release responses to upstream acoustic perturbations; (*ii*) although different combustion and chemical reaction models lead to different unforced flame behaviour, their influences on the forced flame responses are relatively smaller, suggesting the use of simpler chemistry to reduce computational costs and providing more options for combustion modelling; (*iii*) both the low order network-based and the Helmholtz equation-based thermoacoustic solvers are validated by accurate thermoacoustic predictions; (*iv*) the entropy wave transport within a realistic combustor flow is dominated by the dispersive advection, affected by both mean and unsteady large-scale flow features (with the latter having higher effect). The generated entropy noise is likely to affect the thermoacoustic modes at high flow speed conditions; (*v*) the axial variation of the heat release response along a very long flame needs to be accounted for in the network-based thermoacoustic prediction, which is done by splitting the continuous flame into multiple segments, each treated as an individual flame and represented by a compact flame model. All of the above findings significantly help to gain insight into the prediction of thermoacoustic instability for realistic gas turbine combustors.

Acknowledgements

I would like to firstly thank my PhD supervisors, Professor William P. Jones and Professor Aimee S. Morgans, who have been both very supportive, encouraging and patient during my PhD study at Imperial College London. Prof. Jones is very experienced in combustion and numerical simulations, and Prof. Morgans supervised me on acoustics and mathematics. The combination of their guidance gave me great benefits to my PhD and I truly appreciate their help. Also the humour from them added colour to my everyday research, which I enjoyed a lot and would remember forever.

I am also truly grateful to my collaborators at Imperial College for their generous help and deep discussion on various topics. They are Dr. Xingsi Han, Dr. Jingxuan Li, Dr. Ignacio Durán, Dr. Davide Laera, Dr. Dong Yang and so on. Their rich experience on combustion and acoustics helped me tackle numerous challenges during the early stage and late period of my PhD. Also many thanks to all my colleagues — Dongwon Noh, Daniel Fredrich, Amira (Yu) Gong, Simon Gallot Lavallee, Panayiotis Koniavitis, Juan Inigo Guzman, Francesca Sogaro, Faron Hesse, Xiao Han, Olga Evstafyeva and Laurent Dalla Longa, etc. The brainstorms, drinks, BBQ, Thai food, and all the other experiences we shared together are my lifelong treasure.

Great thanks to Dr. Jim W. Rogerson, Dr. Ghenadie Bulat and Dr. Suresh Sadasivuni from my PhD sponsor — Siemens Industrial Turbomachinery Ltd. All their kind help and guidance kept me on track through the entire PhD journey, and my summer internship there in 2017 allowed me to apply my knowledge to solve real industrial problems. Their permission for the usage of experimental data is also vital for the completion of my PhD. I finally wish to highly appreciate the generous financial support from Siemens, and would never forget.

Sincere thanks to the EPSRC Centre for Doctoral Training (CDT) in Fluid Dynamics Across Scales at Imperial College. I benefited a lot from the MRes year spent there, and the continued

collaboration added fresh ideas to my research. The financial support and platform of various courses built the basis for my PhD and future career.

Finally, I wish to sincerely thank my parents for their unconditional support during the past years, and my wife Kejun Guo for her warm encouragement during all the tough moments and sleepless nights. My PhD would be much less enjoyable without the accompany of my family, and I feel very lucky to celebrate the completion of my PhD with my son, Kangrui (Ray) Xia. Wish all of us a very bright future!

Contents

Abstract vi

Acknowledgements vii

Contents ix

List of Figures xii

List of Tables xviii

Abbreviations xix

Nomenclature xxi

1 Introduction 1
- 1.1 Background . . . 1
- 1.2 Predicting Thermoacoustic Instability: Modelling Theories . . . 5
  - 1.2.1 Acoustic wave modelling . . . 5
  - 1.2.2 Flame response modelling . . . 7
  - 1.2.3 Thermoacoustic solvers . . . 8
- 1.3 Thermoacoustic Instability: Experimental Measurements . . . 9
- 1.4 Thermoacoustic Instability: Numerical Simulations . . . 11
  - 1.4.1 Incompressible large eddy simulation . . . 12
  - 1.4.2 Chemical reaction schemes . . . 13
- 1.5 Entropy Wave Transport . . . 14
- 1.6 Response of a Very Long Flame . . . 16
- 1.7 Motivations and Objectives . . . 17

2 Theoretical Modelling 19
- 2.1 Governing Equations for an Acoustic Wave . . . 19
- 2.2 Acoustic Wave Propagation in a Constant Area Duct . . . 20
  - 2.2.1 Plane wave solutions with zero mean flow . . . 22
  - 2.2.2 Frequency limits for the 1-D wave assumption . . . 23
- 2.3 Flame-Acoustic Interaction in a Constant Area Combustor . . . 24
- 2.4 Thermoacoustic Solvers . . . 28
  - 2.4.1 Wave-based low order network solver: OSCILOS . . . 28

2.4.2 Helmholtz solver via COMSOL . . . 31
2.5 Entropy Wave Transport within a Combustor Flow . . . 32
2.5.1 Entropy wave transport with an entropy source . . . 33
2.5.2 Non-dimensionalisation of entropy transport equation . . . 34
2.6 Segmentation of a Very Long Flame . . . 35
2.7 Summary . . . 37

3 Numerical Methodology 38
3.1 Mathematical Formulation of Incompressible LES . . . 38
3.2 Sub-Grid Scale Turbulence Modelling . . . 40
3.2.1 Constant Smagorinsky model . . . 40
3.2.2 Dynamic Smagorinsky model . . . 41
3.2.3 WALE model . . . 42
3.2.4 One-equation turbulent kinetic energy model . . . 43
3.3 Sub-Grid Scale Combustion Modelling . . . 43
3.3.1 PDF-based Eulerian stochastic field model . . . 44
3.3.2 Partially stirred reactor model . . . 46
3.4 Simulation of Entropy Wave Transport . . . 49
3.5 Summary . . . 49

4 SGT-100 Industrial Combustor: Flow Simulation and Flame Responses 51
4.1 Experimental Set-up . . . 51
4.2 Numerical Framework . . . 54
4.3 Unforced LES Results and Validation . . . 57
4.3.1 Effects of SGS turbulence and combustion modelling . . . 58
4.3.2 Effect of reaction chemistry . . . 64
4.3.3 Effect of mean operating pressure . . . 66
4.3.4 Other factors: wall heat losses and mesh density . . . 72
4.4 Flame Describing Functions . . . 75
4.4.1 Effect of SGS combustion model on FDFs . . . 80
4.4.2 Effect of reaction chemistry on FDFs . . . 81
4.4.3 Effect of operating pressure on FDFs . . . 84
4.4.4 Effect of wall heat losses on FDFs . . . 86
4.5 Summary . . . 87

5 SGT-100 Industrial Combustor: Thermoacoustic Instability 89
5.1 Thermoacoustic Stability Predictions by OSCILOS . . . 89
5.1.1 Acoustic mode predictions with a passive flame . . . 93
5.1.2 Linear thermoacoustic stability predictions . . . 95
5.1.3 Nonlinear thermoacoustic stability and limit cycle predictions . . . 97
5.2 Thermoacoustic Stability Predictions by H-solver . . . 103
5.2.1 Stability analyses . . . 103
5.2.2 Comparison between OSCILOS and H-solver predictions . . . 106
5.3 Summary . . . 107

6 SGT-100 Industrial Combustor: Entropy Wave Transport 109
6.1 Entropy Wave Transport within Combustor Flows . . . 109

6.1.1 Dispersive advection of entropy waves . . . 109
6.1.2 Transport within an unsteady combustor flow . . . 114
6.1.3 Transport within time-averaged combustor flow . . . 116
6.2 Entropy Wave Transport within an Equivalent Pipe Flow . . . 118
6.3 Entropy Noise Effect on Duct Thermoacoustic Modes . . . 122
6.4 Summary . . . 126

7 ORACLES Long Flame Combustor **129**
7.1 Experimental Set-up . . . 129
7.2 Numerical Framework . . . 131
7.3 LES Results and Validation . . . 135
7.4 Flame Describing Functions for the Long Flame . . . 136
7.5 Prediction of Thermoacoustic Limit Cycle . . . 141
7.6 Summary . . . 150

8 Conclusions and Future Work **152**
8.1 Incompressible LES of Reacting Combustor Flows . . . 152
8.2 Forced Flame Responses and Flame Models . . . 154
8.3 Predictions of Thermoacoustic Instability and Limit Cycle . . . 155
8.4 Entropy Wave Transport in Combustor Flows . . . 156
8.5 Future Work Plans . . . 157

Bibliography **160**

List of Figures

1.1 The power of electricity generated by (blue line) combined cycle gas turbines (CCGTs) and (red line) wind energy within one week period in (a) September and (b) December, 2013. Images adapted from [1]. 2
1.2 Thermoacoustic instability schematic: coupling between acoustic wave perturbation and unsteady flame heat release rate response. 3
1.3 Thermoacoustic instability mechanism: a feedback amplifier. 4
1.4 Schematic of development of limit cycle oscillations due to thermoacoustic instability. $\dot{Q} = \iiint_{\mathcal{V}} \dot{q} \mathrm{d}\mathcal{V}$ denotes the total heat release rate. 4
1.5 Damage caused by thermoacoustic instability: (a) fatigue failure of turbine blades [2]; (b) cracks on combustor casing [3]; (c) melted fuel injectors [2]. 5
1.6 Entropy wave transport and the resulting entropy noise. Figure taken from [4]. . 14

2.1 A 3-D constant area duct with upstream and downstream travelling plane acoustic waves. 21
2.2 Motions of upstream and downstream travelling plane acoustic waves. 21
2.3 The first three acoustic wave modes in a constant area duct with both ends open, in the form of axial distributions of (a) pressure p' and (b) velocity u' fluctuations. 23
2.4 A 3-D square duct with constant width and height of a. 23
2.5 Constant area duct with an acoustically compact flame located at $x = 0$. 25
2.6 1-D acoustic waves separated by a 1-D flame sheet in a constant area duct. . . . 25
2.7 The flame heat release rate fluctuation, $\dot{Q}'$, responding to an upstream velocity perturbation, u'_1. 27
2.8 Network representation of a real combustor: connected constant area modules with constant acoustic wave amplitudes in each module. 29
2.9 Sketches of (a) a very long continuous flame and (b) its segmentation as a series of discrete compact flame sheets (figures taken from [5]). The j-th segment ranges between $[x_{j,c}, x_{j+1,c}]$, with its flame sheet located in the centre (i.e. $x = x_j$). . . . 36

4.1 Schematics of (a) DLR high pressure test facility and (b) SGT-100 gas turbine combustor. All dimensions reported in mm, with the x-origin located at the combustion chamber entrance. Images adapted from [6, 7]. 52
4.2 (a) Time-signal of the normalised pressure fluctuation, $p'/\overline{p}$, at 6 bar pressure, measured by DLR at a single location of 231 mm beyond the combustor entrance, at a sampling rate of 10 kHz; (b) Power spectrum of the pressure signal. Experimental data provided by Siemens. 54
4.3 Power spectral densities (PSD) of the pressure time-signal, measured by DLR at 3 bar (solid line) and 6 bar (dash-dotted line) pressure at single location $x =$ 231 mm. Window size: 8192; overlap size: 1024. Experimental data provided by Siemens. 54

4.4 (a) LES computational domain and (b) mesh arrangement for the SGT-100 combustor. 55
4.5 Vertical y-profiles of (a–b) axial, u, and (c–d) vertical, v, flow velocities at $x = 18.7$ mm, for (a, c) mean and (b, d) RMS components. Four SGS turbulence models are used: (*i*) constant Smagorinsky [8] (blue solid line); (*ii*) dynamic Smagorinsky [9] (green dash-dotted line); (*iii*) WALE [10] (red dashed line); (*iv*) one-equation turbulent kinetic energy [11–13] (magenta dotted line). The PIV experimental data [14] are marked by black circles. All simulations based on LES Case I. . . . 59
4.6 Time-averaged contours of (a) axial velocity, $\overline{u}$, (b) temperature, $\overline{T}$, and (c) volumetric heat release rate, $\overline{\dot{q}}$, on symmetry plane $z = 0$, computed at $\overline{p} = 3$ bar by (top-half) Case I with LES-PaSR and (bottom-half) Case II with LES-PDF models. 60
4.7 Central Vortex Core (CVC) along the centreline from chamber exit to mid-chamber, marked by pressure iso-surface of 310,580 Pa. Simulations based on LES Case I. 60
4.8 Vertical y-profiles of mean flow variables at 3 bar pressure for four axial locations: $x = 18.7$, 38.7, 58.7 and 88.7 mm. Blue solid line: Case I with LES-PaSR model; red dotted line: Case II with LES-PDF model; black circle: experimental data [14]. Z is mixture fraction, CH_4, O_2, CO_2 and H_2O are relevant species mass fractions. 62
4.9 Vertical y-profiles of fluctuating (RMS) flow variables at 3 bar pressure, computed by Case I (solid line) and Case II (dotted line). See the caption of Fig. 4.8 for more information. 63
4.10 Laminar burning velocity (S_u) and adiabatic flame temperature (T_a) against equivalence ratio (ϕ_e) at pressure (a) $\overline{p} = 3$ bar and (b) $\overline{p} = 6$ bar, both with ambient temperature $T_m = 650$ K. Cantera with GRI-Mech 3.0 scheme (solid line); Cantera with 4-step scheme ($\triangle$); Cantera with 15-step scheme ($\bigtriangledown$); OpenFOAM with 4-step scheme ($\square$); BOFFIN with 4-step scheme ($\Diamond$); BOFFIN with 15-step scheme ($\bigcirc$). The operating point refers to $\phi_e = 0.6$. 65
4.11 Time-averaged contours of (a) axial velocity, $\overline{u}$, (b) temperature, $\overline{T}$, and (c) volumetric heat release rate, $\overline{\dot{q}}$, computed at $\overline{p} = 3$ bar based on (top-half) Case II with 4-step reaction scheme and (bottom-half) Case III with 15-step reaction scheme. 66
4.12 Vertical y-profiles of mean flow variables at 3 bar pressure for four axial locations: $x = 18.7$, 38.7, 58.7 and 88.7 mm. Blue solid line: Case II with 4-step reaction scheme; red dotted line: Case III with 15-step reaction scheme; black circle: experimental data [14]. 67
4.13 Vertical y-profiles of RMS flow variables at 3 bar pressure, computed by Case II (solid line) and Case III (dotted line). See the caption of Fig. 4.12 for more information. 68
4.14 Time-averaged contours of (a) axial velocity, $\overline{u}$, (b) temperature, $\overline{T}$, and (c) volumetric heat release rate, $\overline{\dot{q}}$, computed at $\overline{p} = 6$ bar based on (top-half) Case IV with 4-step reaction scheme and (bottom-half) Case V with 15-step reaction scheme. 69
4.15 Vertical y-profiles of mean flow variables at 6 bar pressure for four axial locations: $x = 18.7$, 38.7, 58.7 and 88.7 mm. Blue solid line: Case IV with 4-step reaction scheme; red dotted line: Case V with 15-step reaction scheme; black circle: experimental data from DLR. 70

4.16 Vertical y-profiles of RMS flow variables at 6 bar pressure, computed by Case IV (solid line) and Case V (dotted line). See the caption of Fig. 4.15 for more information. 71
4.17 Time-averaged contours of (a) axial velocity, $\overline{u}$, (b) temperature, $\overline{T}$, and (c) volumetric heat release rate, $\overline{\dot{q}}$, all computed by LES Case I. Top-half: adiabatic wall condition; bottom-half: non-adiabatic wall condition with fixed wall temperatures. 72
4.18 Vertical y-profiles of (a–d) mean and (e–h) RMS flow variables at: x =18.7, 38.7, 58.7 and 88.7 mm, all computed by Case I. Blue solid line: adiabatic wall condition; red dotted line: non-adiabatic wall condition with fixed wall temperatures; black circle: experimental data [14]. 73
4.19 A refined unstructured mesh with 14.5 million cells for the LES computational domain of the SGT-100 rig, used by OpenFOAM based on LES case I. 74
4.20 Time-averaged contours of (a) axial velocity, $\overline{u}$, (b) temperature, $\overline{T}$, and (c) volumetric heat release rate, $\overline{\dot{q}}$, computed by LES Case I with (top-half) 7.0-million-cell structured mesh and (bottom-half) 14.5-million-cell unstructured mesh. 75
4.21 Vertical profiles of (a-d) mean and (e-h) RMS flow variables at: x =18.7, 38.7, 58.7 and 88.7 mm, all computed by LES Case I with adiabatic wall condition. Blue solid line: 7 million cell structured mesh; red dotted line: 14.5 million cell unstructured mesh; black circle: experimental data [14]. 76
4.22 Two forced simulations based on Case I with forcing level $A_u = 0.1$ at forcing frequency (left) f_u = 200 Hz and (right) f_u = 1000 Hz. (a) Time-signals of (top) $u_1'/\overline{u}_1$ and (bottom) $\langle\dot{q}\rangle'/\overline{\langle\dot{q}\rangle}$; (b) FFT spectra magnitude of (top) $\widehat{u}_1/\overline{u}_1$ and (bottom) $\widehat{\langle\dot{q}\rangle}/\overline{\langle\dot{q}\rangle}$. The spectra of $\widehat{\langle\dot{q}\rangle}/\overline{\langle\dot{q}\rangle}$ for the unforced Case I are marked by grey dotted lines. 78
4.23 FDFs at forcing level $A_u = 0.1$ (i.e. FTFs), obtained at $\overline{p}$ = 3 bar with 4-step chemistry for Case I with LES-PaSR model (solid line with circles) and Case II with LES-PDF model (dashed line with squares). (Top) gain G; (bottom) phase φ. 81
4.24 FDFs at $\overline{p}$ = 3 bar, obtained for Case III with LES-PDF combustion model using one field (solid line with circles) or 8 stochastic fields (squares). (Top) gain G; (bottom) phase φ. Forcing amplitude: (a) $A_u = 0.1$; (b) $A_u = 0.2$. 81
4.25 FDFs at $\overline{p}$ = 3 bar for Case II with 4-step reaction scheme (solid line with circles) and Case III with 15-step reaction scheme (dashed line with squares), with (top) gain G and (bottom) phase φ. Forcing amplitude: (a) $A_u = 0.1$; (b) $A_u = 0.2$. . 82
4.26 FDFs at $\overline{p}$ = 6 bar for Case IV with 4-step reaction scheme (solid line with circles) and Case V with 15-step reaction scheme (dashed line with squares), with (top) gain G and (bottom) phase φ. Forcing amplitude: (a) $A_u = 0.1$; (b) $A_u = 0.2$. . 82
4.27 Contours of volumetric flame heat release rate, $\dot{q}(x, y, z)$, on a symmetry plane of $z = 0$, all forced by the same perturbation of $A_u = 0.1$, f_u = 300 Hz. (I) $\langle\dot{q}\rangle'/\overline{\langle\dot{q}\rangle}$ = -0.1 (minimum); (II) $\langle\dot{q}\rangle'/\overline{\langle\dot{q}\rangle} = 0$; (III) $\langle\dot{q}\rangle'/\overline{\langle\dot{q}\rangle}$ = 0.1 (maximum). (a) Case II (4-step reaction, $\overline{p}$ = 3 bar); (b) Case III (15-step reaction, $\overline{p}$ = 3 bar); (c) Case V (15-step reaction, $\overline{p}$ = 6 bar). 83
4.28 FDFs obtained for Case III at $\overline{p}$ = 3 bar (solid line with circles) and Case V at $\overline{p}$ = 6 bar (dashed line with squares), both with LES-PDF combustion model and 15-step chemistry. (Top) gain G; (bottom) phase φ. (a) $A_u = 0.1$; (b) $A_u = 0.2$. 84
4.29 FDFs at $\overline{p}$ = 3 bar for forcing amplitude $A_u = 0.1$, obtained for Case I with (solid line with circles) adiabatic wall condition and (squares) non-adiabatic wall condition with fixed wall temperatures. (Top) gain G; (bottom) phase φ. 86

5.1 The simplified network geometry representing the SGT-100 combustor, with the origin $x = 0$ located at the combustion chamber entrance. r: radial coordinate. . 90
5.2 Pressure reflection coefficients at (a) inlet, R_{in}, and (b) outlet, R_{out}, of the network geometry, with $|R|$ the gain and $\angle R$ the phase. Solid line: $\overline{p} = 3$ bar; dash-dotted line: $\overline{p} = 6$ bar. 92
5.3 Axial distributions of time-averaged (a) temperature, $\overline{T}_c(x)$, and (b) axial velocity, $\overline{u}_c(x)$, along the network centreline. $\overline{T}_c(x)$ is reconstructed from experimental data at 3 bar (circles) and 6 bar (squares) pressure; $\overline{u}_c(x)$ is extracted from LES-simulated mean flow field. 93
5.4 Shape of the 2nd acoustic mode predicted by OSCILOS (solid line) and H-solver (dash-dotted line) at $\overline{p} = 6$ bar. $\widehat{p}_{\max}$: maximum pressure fluctuation. 94
5.5 Linear stability maps of the SGT-100 network geometry at (a) $\overline{p} = 3$ bar and (b) $\overline{p} = 6$ bar. The predicted thermoacoustic modes are marked by white stars at the contour minima of the complex $f - \sigma$ plane for $\log_{10}|\delta_e(\omega)|/(\log_{10}|\delta_e(\omega)|)_{\max}$. . 96
5.6 (a) Gain, G, and (b) phase, φ, of the FDF at forcing frequency $f_u = 200$ Hz (solid line) and $f_u = 300$ Hz (dash-dotted line) for forcing amplitudes of $A_u = 0.1 - 0.5$. All forced simulations are performed at $\overline{p} = 6$ bar based on LES Case V. 98
5.7 The variation of the linearly unstable thermoacoustic mode at $\overline{p} = 6$ bar over perturbation amplitude, A_u. (a) $A_u = 0.1$; (b) $A_u = 0.3$; (c) $A_u = 0.4$. 99
5.8 Shape of the linearly unstable mode in the form of normalised pressure fluctuation amplitude axial-profile, $|\widehat{p}/\widehat{p}_{\max}|$. (a) $A_u = 0.1$; (b) $A_u = 0.3$; (c) $A_u = 0.4$. 99
5.9 (a) Evolutions of frequency (f, solid line) and growth rate (σ, dash-dotted line) of the linearly unstable mode at 6 bar with forcing level, A_u. Arrows indicate the frequency, f_{lc}, and growth rate, σ_{lc}, of the limit cycle and the corresponding forcing level, A_u^{lc}. (b) Axial variation of the pressure fluctuation amplitude, $|\widehat{p}|$, when the limit cycle occurs. Red circle: value of $|\widehat{p}|$ at pressure transducer location, $x = 231$ mm. 100
5.10 Computational domain used by the H-solver. 103
5.11 x-z contours of normalised pressure fluctuation amplitude, $|\widehat{p}/\widehat{p}_{\max}|$, corresponding to the thermoacoustic modes at $\overline{p} = 3$ bar, predicted by the H-solver using the FTF for LES Case III at $A_u = 0.1$. 104
5.12 $x-z$ contours of normalised pressure fluctuation amplitude, $|\widehat{p}/\widehat{p}_{\max}|$, corresponding to the thermoacoustic modes at $\overline{p} = 6$ bar, predicted by the H-solver using the FTF for LES Case V at $A_u = 0.1$. 105
5.13 Thermoacoustic modes: frequencies vs. growth rates at (a) $\overline{p} = 3$ bar and (b) $\overline{p} = 6$ bar, predicted by H-solver at $A_u = 0.1$ (◯) and $A_u = 0.2$ (□). The measured modal frequencies are marked by vertical dashed lines. 105
5.14 Thermoacoustic modes at (a) $\overline{p} = 3$ bar and (b) $\overline{p} = 6$ bar, predicted at $A_u = 0.1$ by the H-solver with (◯) or without (□) the perforated plate. The measured modal frequencies are marked by vertical dashed lines. 106
5.15 Shapes of the thermoacoustic modes (in the form of $|\widehat{p}/\widehat{p}_{\max}|$ axial profile) predicted at stable 3 bar condition by OSCILOS (solid line) and H-solver (dashed line), using the same FTF at $A_u = 0.1$ from LES Case III. 107

6.1 Contours of (a) mean volumetric heat release rate, (b) mean axial velocity and (c) instantaneous axial velocity on symmetry plane $z = 0$, all simulated by LES Case I. Black lines: iso-lines of zero axial velocity. 111

6.2 (a) Time-variations of volume-integrated entropy source, $\dot{Q}_{\mathcal{V}}$ (solid line), and entropy fluxes at combustion chamber exit, ϕ_S, after full transport "$A_S+D_S+P_S$" (dashed line), advection and diffusion "$A_S + D_S$" (dash-dotted line), and pure advection "A_S" (dotted line); (b) Zoomed-in plots of (a). 112
6.3 (a) Time-variations of volume-integrated entropy source and entropy fluxes at combustor exit. Superscript "H" denotes the source term dispersion time, $\Delta\tau_1$, is halved and the peak amplitude of the source term doubled; (b) Zoomed-in plots of (a). 113
6.4 Contours of the entropy concentration, S, within an unsteady combustor flow field, plotted on symmetry plane $z = 0$, at four time instants after source injection. 114
6.5 Entropy wave advection within an unsteady combustor flow: (a) time-variations of entropy source, $\dot{Q}_{\mathcal{V}}$ (solid line), exiting entropy flux, ϕ_S (dashed line), and Gaussian-approximation of ϕ_S (dotted line); (b) time-integrals of remaining entropy, S_{vol} (dashed line), exited entropy, $\int_t \phi_S \mathrm{d}t$ (dash-dotted line), and injected entropy, $\int_t \dot{Q}_{\mathcal{V}} \mathrm{d}t$ (solid line). Dotted line: sum of S_{vol} and $\int_t \phi_S \mathrm{d}t$. 115
6.6 Contours of the entropy concentration, S, within time-averaged combustor flow field, plotted on symmetry plane $z = 0$, at four time instants after source injection. 116
6.7 Entropy wave advection within the time-averaged combustor flow field. See the caption of Fig. 6.5 for more information. 117
6.8 (a) Network representation of the SGT-100 combustor chamber, with the height of chamber straight section $H = 0.165$ m, flame-to-straight/contraction interface distance $L_0 = 0.225$ m, and interface-to-exit distance $L_1 = 0.248$ m; (b) equivalent circular pipe for (a), with diameter $D_p = 0.186$ m and length $L_c = 0.349$ m. . . . 119
6.9 (a) Exiting entropy fluxes for the mean (dashed line) and unsteady (dash-dotted line) combustor flows and the equivalent fully-developed pipe flow (solid line); (b) Gaussian approximations of exiting entropy fluxes in (a). 120
6.10 Frequency response (a) amplitudes and (b) phases for entropy wave advection in mean (dashed line) and unsteady (dash-dotted line) combustor flows and in an equivalent pipe flow (solid line). f^*: normalised frequency equal to $fL_c/\overline{u}_d$. . . . 121
6.11 Two circular duct combustors with choked outlet: (a) combustor A, flame-downstream length $L_c = 0.349$ m; (b) combustor B, flame-downstream length $3L_c = 1.047$ m. Both ducts have the same pipe radius of $R_p = 0.093$ m. 123
6.12 Amplitudes of the frequency response functions for entropy wave advection from flame to combustor exit: (a) combustor A; (b) combustor B. 124
6.13 OSCILOS-predicted thermoacoustic modes for the short duct combustor A, located at minima of the f-σ plane for $\log_{10}|\delta_e(\omega)|$ and marked by white stars. . . 125
6.14 OSCILOS-predicted thermoacoustic modes for the longer duct combustor B, located at minima of the complex f-σ plane and marked by white stars. 126

7.1 Schematic of (a) the ORACLES laboratory combustor and (b) its simplified network representation. Figures taken from [5]. 130
7.2 Geometric details of the ORACLES combustion chamber entrance, with all dimensions in mm. Figures adapted from [15]. 130
7.3 (a) LES computational domain, meshed with ∼5.46 million structured cells; mesh grids (b) near domain inlets and (c) within the combustion chamber. (d) Statistics of the normalised wall-normal distance, y^+, for all the cells that are closest to the solid walls. 132

7.4 Contours of the sub-grid activity parameter, s_a, on $x-y$ plane at $z = 0$ m, forced by an upstream velocity perturbation of $A_u = 0.29$ and $f_u = 50$ Hz. Figure adapted from [5]. 135
7.5 Contours of unforced LES-simulated (a) mean axial velocity, $\overline{u}$; (b) Instantaneous axial velocity, u; (c) mean temperature, $\overline{T}$, and (d) mean heat release rate from each cell volume, $\overline{\dot{Q}}_m$. 136
7.6 Vertical y-profiles of normalised (a) mean and (b) RMS axial flow velocities (u) at multiple axial locations, $x/h = 0$, 1, 2 and 3. Markers $\circ$ denote experimental data [15] and continuous lines denote forced LES results at $f_u = 50$ Hz, $A_u = 0.29$. 137
7.7 Vertical y-profiles of normalised (a) mean and (b) RMS vertical flow velocities (v). Refer to the caption of Fig. 7.6 for more information. 137
7.8 Sketches of (a) a long continuous flame and (b) its segmentation as a series of discrete compact flame sheets (replotted from Fig. 2.9). The j-th segment ranges between $[x_{j,c},\, x_{j+1,c}]$, with its flame sheet located in the centre (i.e. $x = x_j$). . . . 138
7.9 (a) Time evolution of heat release rate fluctuation, $\dot{Q}'_j = \dot{Q}_j - \overline{\dot{Q}}_j$ (thin solid line), in the 8th flame segment ($j = 8$, $x \in [0.175, 0.2]$ m), and its filtered signal (thick solid line) and envelope (dashed line). (b) Normalised heat release signal, $\dot{Q}_{j,\mathrm{nml}}$. (c) Normalised velocity perturbation, u'_1/U, at the reference location, x_{ref}. (d) Discrete Fourier transform (DFT) of $\dot{Q}_j$ signal in the 8th segment. The resolution is 5 Hz. $f_u = 50$ Hz, $A_u = 0.4$. Figures adapted from [5]. 139
7.10 Local FDFs for the ORACLES flame, $\mathcal{F}_j$ (with $j = 1, \cdots, N_{\mathrm{seg}}$ and $N_{\mathrm{seg}} = 40$). Top-half: FDF gain $|\mathcal{F}_j|$ ($= G_j$); bottom-half: FDF phase $\angle\mathcal{F}_j/\pi$ ($= \varphi_j/\pi$). Symbols $\circ$: $A_u = 0.1$; $\square$: $A_u = 0.2$; $\triangledown$: $A_u = 0.25$; $*$: $A_u = 0.3$; $+$: $A_u = 0.4$. Solid line: phase lag due to bulk flow convection, φ_c. (a) $f_u = 40$ Hz. (b) $f_u = 50$ Hz. (c) $f_u = 75$ Hz. Figures adapted from [5]. 141
7.11 Axial profiles of cross-sectionally averaged mean flow and thermal properties used in the network, simulated at $f_u = 50$ Hz and $A_u = 0.29$. Figures from [5]. 143
7.12 Discrete local FDFs, $\mathcal{F}_j$, and integrated continuous FDFs, $\mathcal{F}^*_j$, obtained with different total segment numbers, N_{seg}. Top-half: $N_{\mathrm{seg}}\,|\mathcal{F}_j|$ and $N_{\mathrm{seg}}\left|\mathcal{F}^*_j\right|$. Bottom-half: $\angle\mathcal{F}_j/\pi$ and $\angle\mathcal{F}^*_j/\pi$. $f_u = 50$ Hz and $A_u = 0.1$. Figure adapted from [5]. . . 145
7.13 Evolutions of (top-half) frequency, f, and (bottom-half) growth rate, σ, of the dominant thermoacoustic mode over perturbation level, A_u, predicted by OSCILOS ($\triangledown$) and the LEEs method ($\circ$). $+$: limit cycle frequency, f_{lc}; $\times$: corresponding perturbation amplitude, A^{lc}_u. Figure taken from [5]. 145
7.14 Shapes of the dominant thermoacoustic mode predicted by (solid line) OSCILOS and (dashed line) the LEEs method at $A_u = 0.4$, in the form of arbitrary (top-half) pressure and (bottom-half) velocity fluctuation amplitude along x-direction. $\overline{\rho}_1$ and $\overline{c}_1$ are the mean density and speed of sound in the upstream settling chamber. Figure adapted from [5]. 146
7.15 Markers $\circ$: evolutions of limit cycle (bottom-half) frequency, f_{lc}, and (top-half) corresponding forcing level, A^{lc}_u, against $|R_{\mathrm{in}}|$ (bottom axis) with $R_{\mathrm{out}} = -1$. Markers $\times$: evolutions of f_{lc} and A^{lc}_u over $|R_{\mathrm{out}}|$ (bottom axis) with $R_{\mathrm{in}} = 1$. Markers $\triangledown$: evolutions of f_{lc} and A^{lc}_u against the combustion chamber temperature ratio, $\mathcal{T}_{\mathrm{TD}}$ (top axis), with $R_{\mathrm{in}} = 1$ and $R_{\mathrm{out}} = -1$. Figure adapted from [5]. . . . 149

List of Tables

3.1 The simple 4-step chemical reaction scheme for methane [16]. 47
3.2 The systematically reduced 15-step reaction scheme for methane [17]. 47

4.1 Measurement uncertainties for some flow variables, including temperature (T) and species mass fractions in fresh mixture and burnt products [14]. 53
4.2 Prescribed inlet boundary conditions for the computational domain. 55
4.3 Incompressible LES solvers: BOFFIN vs. OpenFOAM. 57
4.4 LES cases used to study the effects of different factors. 58
4.5 Forced flame simulations based on each LES case. f_u: perturbation frequency; A_u: normalised perturbation amplitude. 77

5.1 Variables of the acoustic impedance model for the perforated plate at both operating pressures. 91
5.2 Frequencies of the first 5 acoustic modes predicted by OSCILOS (denoted f_O) and H-solver (denoted f_H) with passive flame and zero mean flow assumptions. . 94
5.3 Dominant thermoacoustic mode (frequency f, growth rate σ) and linear stability of the network at two mean pressures, predicted by an equivalent $n-\tau$ model. . 97
5.4 Limit cycle oscillation frequency (f_{lc}) and amplitude ($|\widehat{p}|$) at pressure transducer location, obtained by prediction and measurement. Error = (predicted value − measured value)/measured value × 100%. 102
5.5 Sensitivities of the predicted limit cycle (f_{lc}, A_u^{lc} and $|\widehat{p}|$) to small changes in the pressure reflection coefficient magnitudes at network inlet ($|R_{\text{in}}|$) and outlet ($|R_{\text{out}}|$).102
5.6 Frequency and growth rate of the unstable thermoacoustic mode predicted by OSCILOS and H-solver, using the same FTF at $A_u = 0.1$ from LES Case V. . . . 107

6.1 Thermal and flow properties in duct combustors A and B. Flame-upstream mean properties (subscript "1") are prescribed, and flame-downstream mean properties (subscript "2") follow from the flow conservation equations [18]. 123
6.2 Effects of entropy noise on the dominant thermoacoustic modes of two simple duct combustors (f: frequency; σ: growth rate). 127

7.1 Frequency (f) and growth rate (σ) of the dominant thermoacoustic mode, the limit cycle frequency, f_{lc}, and the corresponding forcing level, A_u^{lc}, predicted over forcing amplitude (A_u) with different total segment numbers. Data collected from [5]. 148

Abbreviations

ATACAMAC	**A**nalytical **T**ool to **A**nalyse and **C**ontrol **A**zimuthal **M**odes in **A**nnular **C**hambers
BOFFIN	**BO**undary **F**itted **F**low **IN**tegrator
CCGT	**C**ombined **C**ycle **G**as **T**urbine
CFD	**C**omputational **F**luid **D**ynamics
CFL	**C**ourant-**F**riedrich-**L**evy number
CRZ	**C**entral **R**ecirculation **Z**one
CVC	**C**entral **V**ortex **C**ore
DFT	**D**iscrete **F**ourier **T**ransform
DLE	**D**ry **L**ow **E**missions
DLR	**D**eutsches Zentrum für **L**uft-und **R**aumfahrt (The German Aerospace Centre)
DNS	**D**irect **N**umerical **S**imulation
EM2C	Le laboratoire d'**É**nergétique **M**oléculaire et **M**acroscopique, **C**ombustion (The Energy laboratory of Microscopic and Macroscopic Combustion)
FDF	**F**lame **D**escribing **F**unction
FEM	**F**inite **E**lement **M**ethod
FFT	**F**ast **F**ourier **T**ransform
FTF	**F**lame **T**ransfer **F**unction
FVM	**F**inite **V**olume **M**ethod
IRZ	**I**nner **R**ecirculation **Z**one
LEE	**L**inearised **E**uler **E**quation
LES	**L**arge **E**ddy **S**imulation
LHS	**L**eft-**H**and **S**ide of the equal sign
LIC	**L**ine **I**ntegral **C**onvolution
LMSE	**L**inear **M**ean **S**quare **E**stimation
LOMTI	**L**ower **O**rder **M**odelling for **T**hermoacoustic **I**nstability

LOTAN	**L**ower **O**rder **T**hermo-**A**coustic **N**etwork
NTNU	**N**orges **T**eknisk-**N**aturvitenskapelige **U**niversitet (Norwegian University of Science and Technology)
OpenFOAM	**Open** Source **F**ield **O**peration **A**nd **M**anipulation
ORACLES	**O**ne **R**ig for **A**ccurate **C**omparisons with **L**arge **E**ddy **S**imulations
ORZ	**O**uter **R**ecirculation **Z**one
OSCILOS	**O**pen **S**ource **C**ombustion **I**nstability **L**ow **O**rder **S**imulator
PaSR	**Pa**rtially **S**tirred **R**eactor
PBiCG	**P**reconditioned-**BiC**onjugate-**G**radient method
PCG	**P**reconditioned-**C**onjugate-**G**radient method
PDF	**P**robability **D**ensity **F**unction
PIMPLE	Combination of **PI**SO and SI**MPLE** algorithms
PISO	**P**ressure **I**mplicit with **S**plitting of **O**perator
PIV	**P**article **I**mage **V**elocimetry
PLIF	**P**lanar **L**aser **I**nduced **F**luorescence
PSD	**P**ower **S**pectral **D**ensity
RHS	**R**ight-**H**and **S**ide of the equal sign
RMS	**R**oot **M**ean **S**quare
SGS	**S**ub-**G**rid **S**cale
SGT	**S**iemens **G**as **T**urbine
SIMPLE	**S**emi-**I**mplicit **M**ethod for **P**ressure-**L**inked **E**quations
SNR	**S**ignal to **N**oise **R**atio
TVD	**T**otal **V**ariation **D**iminishing
URANS	**U**nsteady **R**eynolds **A**veraged **N**avier-**S**tokes simulation
WALE	**W**all-**A**dapting **L**ocal **E**ddy-viscosity model

Nomenclature

Symbol	Meaning	Unit
A	Amplitude of a downstream-travelling acoustic wave	[Pa]
$\mathcal{A}$	Matrix containing coefficients for the discretised Helmholtz equation	
$\mathbb{A}$	Cross-sectional area or domain surface area	[m^2]
A_i	Amplitude of incident acoustic wave at network end	[Pa]
$\widehat{A}_j^+$ or $\widehat{A}_j^-$	Amplitude of downstream/upstream acoustic wave in network module j	[Pa]
A_L	Linearised entropy advection term	[s^{-1}]
A_{lm}	Downstream wave amplitude for vertical l-th and horizontal m-th modes	[Pa]
$A_{\dot{q}}$	FFT ratio of heat release fluctuation to mean value, $A_{\dot{q}} = \left(\widehat{\langle\dot{q}\rangle}/\overline{\langle\dot{q}\rangle}\right)\vert_{f_u}$	[-]
A_r	Amplitude of reflected acoustic wave at network end	[Pa]
A_S	Volumetric entropy advection term, $A_S = A_L/\mathcal{V}$	[$m^{-3}s^{-1}$]
A_u	Normalised amplitude of velocity perturbation upstream to flame	[-]
A_u^{lc}	Velocity perturbation amplitude corresponding to limit cycle oscillations	[-]
a	Height or width of a 3-D square duct	[m]
B	Amplitude of an upstream-travelling acoustic wave	[Pa]
$\mathcal{B}(\omega)$	Matrix of boundary conditions for the discretised Helmholtz equation	
B_{lm}	Upstream wave amplitude for vertical l-th and horizontal m-th modes	[Pa]
$\mathcal{C}$	Matrix containing coefficients from the discretised Helmholtz equation	
C_d	Constant of the PDF transport equation	[-]
C_k	Constant of the one-equation kinetic energy model	[-]
C_m	Mixing time constant	[-]
C_s	Coefficient of the constant and dynamic Smagorinsky models	[-]
C_s^*	Value of C_s computed at earlier time-steps	[-]
C_ϵ	Constant of the one-equation kinetic energy model	[-]
C_ω	Constant of the WALE model	[-]

C_0^α	Volumetric concentration of the α-th species in a mesh cell	[mol/m^3]
C_1^α	Volumetric concentration of the α-th species exiting a mesh cell	[mol/m^3]
c	Speed of sound	[m/s]
c_p	Specific heat capacity at constant pressure	[J/(kg·K)]
c_v	Specific heat capacity at constant volume	[J/(kg·K)]
c_1	Speed of sound in the upstream settling chamber of the ORACLES rig	[m/s]
D	Mass diffusivity	[m^2/s]
$\mathbf{D}$	Governing matrix of the low order network with a long flame	
$\mathcal{D}(\omega)$	Matrix with source term in Helmholtz equation	
D_L	Linearised entropy diffusion term	[s^{-1}]
D_p	Diameter of the equivalent pipe for the SGT-100 combustor	[m]
D_s	Volumetric entropy diffusion term, $D_s = D_L/\mathcal{V}$	[m^{-3}s^{-1}]
$\mathrm{d}W_i^n$	Increment of a vector Wiener process	[-]
d_h	Hole diameter on the perforated plate in the SGT-100 combustor	[m]
$\widehat{E}_j$	Downstream-travelling entropy wave amplitude in network module j	[Pa]
e	Specific internal energy	[J/kg]
$\mathcal{F}$	Flame transfer or describing function (FTF or FDF)	[-]
$\mathcal{F}_c$	Continuous FDF based on 1-D linearised Euler equations	[-]
$\mathcal{F}_j$	FDF of the j-th flame segment computed in ORACLES rig	[-]
$\mathcal{F}_j^*$	Integrated continuous FDF for the j-th flame segment	[-]
f	Frequency	[Hz]
f	Downstream-travelling acoustic wave amplitude upstream to a flame	[Pa]
f^*	Non-dimensional frequency, $f^* = fL_c/\overline{u}_d$	[Hz]
f_c	Cut-off frequency of the low-pass filter in $n-\tau$ model	[Hz]
f_H	Acoustic mode's frequency predicted by Helmholtz solver	[Hz]
f_{lc}	Frequency of the limit cycle oscillation	[Hz]
f_O	Acoustic mode's frequency predicted by OSCILOS solver	[Hz]
f_u	Frequency of velocity perturbation imposed upstream to a flame	[Hz]
G	Gain of an FTF or FDF	[-]
G_f	LES-filter function	[m^{-3}]
G_{ideal}	Gaussian approximation of entropy flux at equivalent pipe exit	[s^{-1}]
G_j	FDF gain for the j-th flame segment in ORACLES combustor	[-]
G_{out}	Gaussian shape function, approximation for exiting entropy flux, ϕ_s	[s^{-1}]

G_S	Gaussian shape function for the entropy source term, $\dot{Q}_S$	[s^{-1}]
G_0	Gain of an LEEs-based continuous FDF, $\mathcal{F}_c$	[-]
$\mathcal{G}_{1\to N}$	Matrix linking waves from the first to the last network module	
g	Upstream-travelling acoustic wave amplitude upstream to a flame	[Pa]
g_{ij}	Velocity gradient tensor, $g_{ij} = \partial u_j/\partial x_i$	[s^{-1}]
H^1	Height of SGT-100 combustion chamber straight section	[m]
H^2	Height of ORACLES separate rectangular channel cross-section	[m]
h^1	Height of sudden expansion at inlet of ORACLES combustion chamber	[m]
h^2	Specific sensible enthalpy	[J/kg]
h	Downstream-travelling acoustic wave amplitude downstream of a flame	[Pa]
h_e	Specific enthalpy (including the enthalpy of formation)	[J/kg]
h_p	Thickness of the metal plate splitting two separate ORACLES channels	[m]
i	Imaginary unit, $i = \sqrt{-1}$	[-]
J_{h_e}	Sub-grid scale scalar flux for enthalpy	[s^{-3}]
J_α	Sub-grid scale scalar flux for the α-th species	[kg/(m^2·s)]
j	Upstream-travelling acoustic wave amplitude downstream of a flame	[Pa]
k^+ or k^-	Wave number of a downstream or upstream-travelling acoustic wave	[m^{-1}]
k_{lm}	Wave number for the vertical l-th and horizontal m-th acoustic modes	[m^{-1}]
k_p	Wave number of the perforated plate impedance model	[m^{-1}]
k_{sgs}	Sub-grid scale turbulent kinetic energy	[m^2s^{-2}]
k_T	Thermal conductivity	[W/(m·K)]
L	Length of a 3-D duct or characteristic length of a flow field	[m]
L_c	Length of the circular pipe equivalent to SGT-100 combustor	[m]
L_i	Loss of acoustic energy due to dissipation and/or transmission	[Pa·W/m^3]
L_{ij}	Germano identity of the dynamic Smagorinsky model	[Pa]
L_0	Distance from flame to SGT-100 rig straight-contraction interface	[m]
L_1	Distance from straight-contraction interface to SGT-100 rig exit	[m]
Le	Lewis number, Le = Sc/Pr	[-]
l	Integer wave mode number	[-]
l_f	Axial length of a flame segment in ORACLES rig	[m]
l_{011}	Axial length of the settling chamber in ORACLES rig	[m]
l_{012}	Axial length of the contraction duct in ORACLES rig	[m]
l_{02}	Axial length of rectangular channels in ORACLES rig	[m]

l_1	Axial length of settling chamber in ORACLES network	[m]
l_2	Axial length of rectangular channels in ORACLES network	[m]
l_3	Axial length of combustion chamber in ORACLES network	[m]
M	Mach number, $M = U/c$	[-]
M_d	Flame-downstream Mach number	[-]
m	Integer wave mode number	[-]
N	An appropriate integer used to calculate FDF phase φ	[-]
N_f	Total number of Eulerian stochastic fields used in a PDF model	[-]
N_s	Total number of involved scalars for a PDF model, $N_s = N_{sp} + 1$	[-]
N_{seg}	Total number of split flame segments in ORACLES combustor	[-]
N_{sp}	Total number of species	[-]
n_f	Gain of $n - \tau$ flame model	[-]
n_t	Total mode number used to discretise a fluctuating variable	[-]
$\mathbf{P}$	Vector of eigenmodes for Helmholtz equation	
P_L	Linearised entropy production term	[s^{-1}]
P_S	Volumetric entropy production term, $P_S = P_L/\mathcal{V}$	[$\text{m}^{-3}\text{s}^{-1}$]
P_{sgs}	Joint PDF for all the involved scalar variables	[-]
P_α	Probability density function (PDF) of the α-th scalar variable	[-]
Pr	Prandtl number, $\text{Pr} = c_p\mu/k_T$	[-]
p	Pressure	[Pa]
p^*	Filtered pressure including the isotropic stress tensor, $p^* = \bar{p} + \frac{1}{3}\tau_{kk}$	[Pa]
$\widehat{p}_{\text{max}}$	Maximum pressure fluctuation	[Pa]
$\dot{Q}$	Total heat release rate	[W]
$\dot{Q}_{\text{ideal}}$	Entropy source in delta-function form for a circular pipe flow	[s^{-1}]
$\dot{Q}'_j$	Heat release rate fluctuation in the j-th ORACLES flame segment	[W]
$\dot{Q}'_{j,\text{evlp}}$	Envelope of $\dot{Q}'_j$ signal after Hilbert transform	[W]
$\dot{Q}'_{j,\text{flt}}$	Butterworth-filtered $\dot{Q}'_j$ signal	[W]
$\dot{Q}'_{j,\text{nml}}$	Normalised $\dot{Q}'_j$ signal with constant amplitude, $\dot{Q}'_{j,\text{nml}} = \dot{Q}'_{j,\text{flt}}/\dot{Q}'_{j,\text{evlp}}$	[-]
$\dot{Q}_m$	Heat release rate from each mesh cell volume	[W]
$\dot{Q}_S$	Entropy source term	[$\text{m}^{-3}\text{s}^{-1}$]
$\dot{Q}_\mathcal{V}$	Spatially-integrated entropy source term, $\dot{Q}_\mathcal{V} = \iiint_\mathcal{V} \dot{Q}_S \text{d}\mathcal{V}$	[s^{-1}]
$\dot{q}(x, y, z)$	Volumetric heat release rate field	[W/m^3]
$\langle\dot{q}\rangle$	Spatially-integrated volumetric heat release rate, $\langle\dot{q}\rangle = \dot{Q} = \iiint_\mathcal{V} \dot{q} \text{d}\mathcal{V}$	[W]

R	Pressure reflection coefficient at a network end, $R = A_r/A_i$	[-]
R_g	Specific gas constant	[J/(kg·K)]
R_{in} or R_1	Pressure reflection coefficient at network inlet	[-]
R_{out} or R_2	Pressure reflection coefficient at network outlet	[-]
R_p	Radius of a circular pipe	[m]
R_u	Universal (molar) gas constant	[J/(mol·K)]
Re	Reynolds number, $\text{Re} = \rho UL/\mu$	[-]
r	Radial coordinate	[m]
r_o	Radius of network exit plane	[m]
S	Concentration of normalised entropy fluctuation, $S = \breve{s}'/\mathcal{V}$	[m^{-3}]
S_{ij}	Strain rate tensor, $S_{ij} = \frac{1}{2}\left(\frac{\partial u_i}{\partial x_j} + \frac{\partial u_j}{\partial x_i}\right)$	[s^{-1}]
S_{kk}	Isotropic part of the strain tensor, S_{ij}	[s^{-1}]
S_u	Laminar burning velocity	[m/s]
S_{vol}	Total entropy remaining in combustor chamber, $S_{\text{vol}} = \iiint_{\mathcal{V}} S\text{d}\mathcal{V}$	[-]
Sc	Schmidt number, $\text{Sc} = \mu/(\rho D)$	[-]
s	Specific entropy	[J/(kg·K)]
$\breve{s}'$	Normalised entropy fluctuation, $\breve{s}' = s'/c_p$	[-]
s_a	Sub-grid activity parameter	[-]
T^1	Temperature	[K]
T^2	A sufficiently long time period	[s]
$\overline{T}^*$	Mean temperature at $x = 1$ m in the ORACLES combustion chamber	[K]
T_a	Adiabatic flame temperature	[K]
T_b	Bulk flow temperature	[K]
$\overline{T}_c(x)$	Axial-variation of mean temperature along network centreline	[K]
T_d	Flame-downstream temperature	[K]
T_{ij}	Sub-grid scale stress tensor for the test filter's scale	[Pa]
T_m	Ambient temperature	[K]
$\mathcal{T}_{\text{TD}}$	Ratio of inlet to outlet temperature in ORACLES combustor chamber	[-]
T_0	Temperature of the fuel/air pre-mixture in the ORACLES rig	[K]
t	Time	[s]
t_p	Perforated plate thickness	[m]
U	Bulk flow velocity	[m/s]
$U(y)$	Vertical profile of the axial flow velocity	[m/s]

u	Axial flow velocity	[m/s]
$\boldsymbol{u}$	Velocity vector	[m/s]
$\overline{u}_c(x)$	Axial-variation of mean axial velocity along network centreline	[m/s]
u_d	Flame-downstream axial flow velocity	[m/s]
$u_{\max}$	Maximum axial velocity in a circular pipe	[m/s]
u'_{sgs}	Sub-grid scale velocity fluctuation	[m/s]
u_1	Velocity perturbation imposed upstream to a flame	[m/s]
$\mathcal{V}$	Domain volume	[m^3]
v	Vertical flow velocity	[m/s]
W	Cross-sectional width of the ORACLES rig	[m]
W_g	Molar mass of a mixture	[kg/mol]
$\overline{X}$	Matrix containing constants and mean flow properties for a 3-D duct	[-]
x	Axial coordinate	[m]
$\boldsymbol{x}$	Coordinate vector, $\boldsymbol{x} = (x, y, z)$	[m]
x_d	Axial location of a 3-D duct's outlet	[m]
x_f	Axial location of the infinitely thin flame sheet in a network	[m]
x_{ref}	Axial location of upstream velocity perturbation in ORACLES rig	[m]
x_u	Axial location of a 3-D duct's inlet	[m]
$\overline{Y}$	Matrix containing constants and mean flow properties for a 3-D duct	[-]
Y_α	Mass fraction of the α-th species	[%vol]
y	Vertical coordinate	[m]
y^+	Normalised wall-normal distance of the closest mesh nodes	[-]
Z	Mixture fraction	[-]
Z_a	Acoustic impedance of a perforated plate	[-]
z	Horizontal coordinate	[m]

Greek	**Meaning**	**Unit**
α	Parameter of an analytical FDF	[-]
α_E	Effective thermal diffusivity	[m^2/s]
β	Parameter of an analytical FDF	[-]
β_1	Linear coefficient for the gain of an LEEs-based FDF, $\mathcal{F}_c$	[-]
β_2	Linear coefficient for the phase of an LEEs-based FDF, $\mathcal{F}_c$	[-]
γ	Ratio of the specific heat capacities, $\gamma = c_p/c_v$	[-]

Δ	LES filter width, $\Delta = (\Delta_x \Delta_y \Delta_z)^{1/3}$	[m]
Δt	Computational time step	[s]
Δ_x	Mesh cell size in the axial direction	[m]
Δ_y	Mesh cell size in the vertical direction	[m]
Δ_z	Mesh cell size in the horizontal direction	[m]
$\Delta\tau_1$	Dispersion time of Gaussian function for entropy source, G_S	[s]
$\Delta\tau_2$	Dispersion time of Gaussian function for exiting entropy flux, G_{out}	[s]
δe	Error between the estimated and the correct acoustic wave amplitudes	[Pa]
δ_{ij}	Kronecker delta. $\delta_{ij} = 1$ for $i = j$, otherwise zero	[-]
ϵ	Error of consecutive iterations in Helmholtz eqn., $\epsilon = \lvert\Omega_k - \Omega_k^*\rvert$	[rad/s]
ϵ_{sgs}	Sub-grid scale dissipation rate	[m^2/s^3]
ε_t	Turbulent dissipation rate, $\varepsilon_t = -\tau_{ij}\left(\partial\widetilde{u}_i/\partial x_j\right)$	[m^2/s^3]
ε_μ	Molecular dissipation rate, $\varepsilon_\mu = \widetilde{S}_{ij}\left(\partial\widetilde{u}_i/\partial x_j\right)/\text{Re}$	[m^2/s^3]
η	Combustion efficiency	[-]
$\eta_i(t)$	Time-varying fluctuation amplitude of Galerkin method	[-]
η_i^n	A $\{-1, 1\}$ dichotomic random variable	[-]
θ_f	Additional flow resistance of a perforated plate	[-]
κ	Reactive volume fraction of LES-PaSR model	[-]
λ_m	Acoustic wavelength for the m-th mode	[m]
μ	Dynamic viscosity	[Pa·s]
μ_{sgs}	Sub-grid scale eddy viscosity	[Pa·s]
ν	Kinematic viscosity	[m^2/s]
ξ_α^n	Ensemble of N_f stochastic fields used to model P_α $(1 \leq n \leq N_s)$	[-]
ρ	Density	[kg/m^3]
ρ_1	Fluid density in the upstream settling chamber of the ORACLES rig	[kg/m^3]
σ	Growth rate, $\sigma = \mathcal{R}(\omega)$	[rad/s]
σ_h	Hole end correction for a perforated plate	[m]
σ_k	Constant of one-equation kinetic energy model	[-]
σ_m	Prandtl or Schmidt number	[-]
σ_p	Porosity of a perforated plate	[-]
σ_{sgs}	Turbulent Prandtl or Schmidt number	[-]
τ_c	Chemical reaction time	[s]
τ_d	Time delay between downstream and upstream waves after a flame	[s]

τ_f	Time delay between flame response and perturbation in $n-\tau$ model	[s]
τ_{ij}	Sub-grid scale stress tensor	[Pa]
τ_{ij}^E	Effective stress tensor	[Pa]
τ_j^+ or τ_j^-	Time delay of upstream or downstream acoustic wave in module j	[s]
τ_j^s	Time delay of downstream entropy wave in network module j	[s]
τ_K	Kolmogorov time	[s]
τ_{kk}	Isotropic part of the stress tensor, τ_{ij}	[Pa]
τ_m	Turbulent mixing time	[s]
τ_r	Time delay between incident and reflected waves at network outlet	[s]
$\tau_{\text{res}}(r)$	Analytical residence time profile for a 1-D circular pipe flow	[s]
τ_{sgs}	Sub-grid scale mixing time of LES-PDF model	[s]
τ_u	Time delay between downstream and upstream waves prior to a flame	[s]
τ_2	Mean delay time for Gaussian function of exiting entropy flux, G_{out}	[s]
τ_Δ	Sub-grid scale mixing time of LES-PaSR model	[s]
ϕ or ϕ_α	An arbitrary variable	
ϕ_c	Ideal phase lag of bulk flow convection, $\phi_c = -2\pi f x/U$	[rad]
ϕ_e	Fuel-air equivalence ratio	[-]
ϕ_{i0}	Spatial mode shape of Galerkin method	[-]
ϕ_{ideal}	Volumetric flux of entropy concentration at a circular pipe exit	[s^{-1}]
$\phi_{\dot{q}}$	Phase difference between velocity perturbation and flame response	[rad]
ϕ_S	Volumetric flux of entropy concentration at combustor exit	[s^{-1}]
φ	Phase of an FTF or FDF	[rad]
φ_0	Phase of an LEEs-based continuous FDF, $\mathcal{F}_c$	[rad]
ψ_g	Global composition space for all the relevant scalars	[-]
$\psi_i(x)$	Mode function with wave number and mode shape in Galerkin method	[-]
φ_j	FDF phase for the j-th flame segment in ORACLES rig	[rad]
ψ_α	Sample (composition) space for scalar ϕ_α	[-]
Ω	Complex angular frequency, $\Omega = 2\pi f + i\sigma$	[rad/s]
Ω_k^*	Previous iteration result of Ω_k, $\Omega_k^* = \Omega_{k-1}$	[rad/s]
ω	Complex Laplace variable, $\omega = \sigma + i2\pi f$	[rad/s]
$\dot{\omega}$	Chemical reaction rate	[%vol/s]
ω_i	Angular frequency, $\omega_i = \mathcal{I}(\omega) = 2\pi f$	[rad/s]
ω_i^c	Cut-off angular frequency of the low-pass filter in $n-\tau$ model	[rad/s]

ω_{ic}	Upper frequency limit for a valid 1-D wave assumption	[rad/s]
ω_{im}	Angular frequency of the m-th acoustic wave mode	[rad/s]
ω_t	Artificial turbulence fluctuation at ORACLES domain inlet	[-]
$\dot{\omega}_\alpha$	Chemical reaction rate of the α-th species, $\dot{\omega}_\alpha = \dot{\omega}(Y_\alpha)$	[%vol/s]

Operators	**Meaning**
$(\cdot)'$	Fluctuation of variable amplitude in the time domain
$\bar{(\cdot)}$	LES filtering
$\overline{(\cdot)}$	Time-averaging
$\breve{(\cdot)}$	Non-dimensionalisation
$\widetilde{(\cdot)}$	Density-weighted Favre filtering
$\widehat{(\cdot)}^1$	Fluctuation of variable amplitude in the frequency domain
$\widehat{(\cdot)}^2$	LES filtering with a test filter
$\lvert(\cdot)\rvert$	Magnitude of a (complex) variable
$\lvert\lvert(\cdot)\rvert\rvert$	Frobenius form of a variable, $\lvert\lvert(\cdot)\rvert\rvert = \sqrt{2(\cdot)(\cdot)}$
$\langle(\cdot)\rangle^1$	Spatial integration, $\langle(\cdot)\rangle = \iiint_{\mathcal{V}}(\cdot)\mathrm{d}\mathcal{V}$
$\langle(\cdot)\rangle^2$	Spatial averaging over flow domain volume, $\langle(\cdot)\rangle = \left(\iiint_{\mathcal{V}}(\cdot)\mathrm{d}\mathcal{V}\right)/\mathcal{V}$
$\angle$	Angle of a complex variable
∇	Differential operator, $\nabla = \mathbf{i}\frac{\partial}{\partial x} + \mathbf{j}\frac{\partial}{\partial y} + \mathbf{k}\frac{\partial}{\partial z}$, with $\{\mathbf{i}, \mathbf{j}, \mathbf{k}\}$ the unit vectors in $\{x, y, z\}$ coordinates
$\mathrm{D}/\mathrm{D}t$	Material derivative, $\mathrm{D}/\mathrm{D}t = \partial/\partial t + \boldsymbol{u}\cdot\boldsymbol{\nabla}$
$\overline{\mathrm{D}}/\mathrm{D}t$	Material derivative within a mean flow, $\overline{\mathrm{D}}/\mathrm{D}t = \partial/\partial t + \overline{\boldsymbol{u}}\cdot\boldsymbol{\nabla}$
∂	Partial derivative
$\mathcal{I}(\cdot)$	Imaginary part of a complex variable
$\mathcal{R}(\cdot)$	Real part of a complex variable

Superscripts	**Meaning**
a	Anisotropic component of a tensor
d	Traceless symmetric component of a tensor
H	Entropy source with halved dispersion time
N	Non-reacting flow part in a mesh cell for LES-PaSR model
n	Serial number of a stochastic field
R	Reacting flow part in a mesh cell for LES-PaSR model

$+$ or $-$	Downstream or upstream-travelling acoustic wave

Subscripts	**Meaning**
i, j, k	(1) Indices of Einstein notation; (2) a network module
l, m, n	Integer wave mode number
α or β	An arbitrary scalar variable
1 or u	Upstream to a flame
2 or d	Downstream of a flame
in	Network or combustor inlet
max	Maximum value
out	Network or combustor outlet
rms	Root-mean-square
sgs	Sub-grid scale

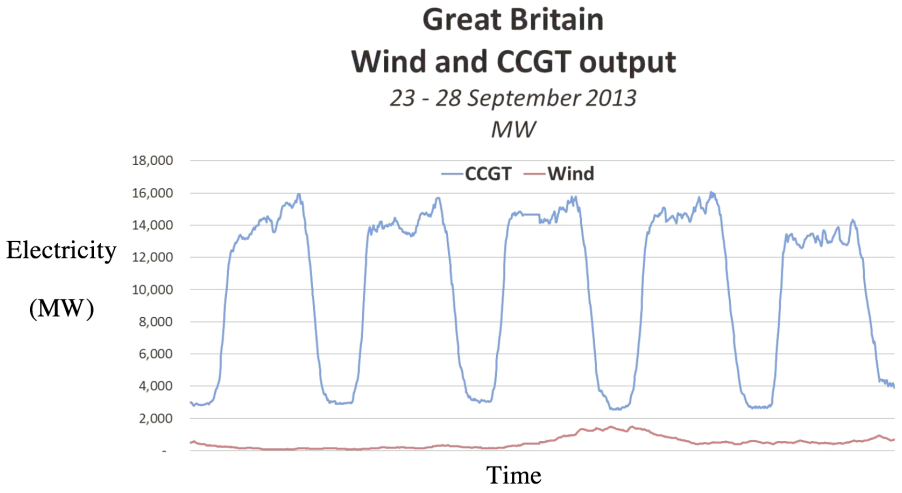
Chapter 1

Introduction

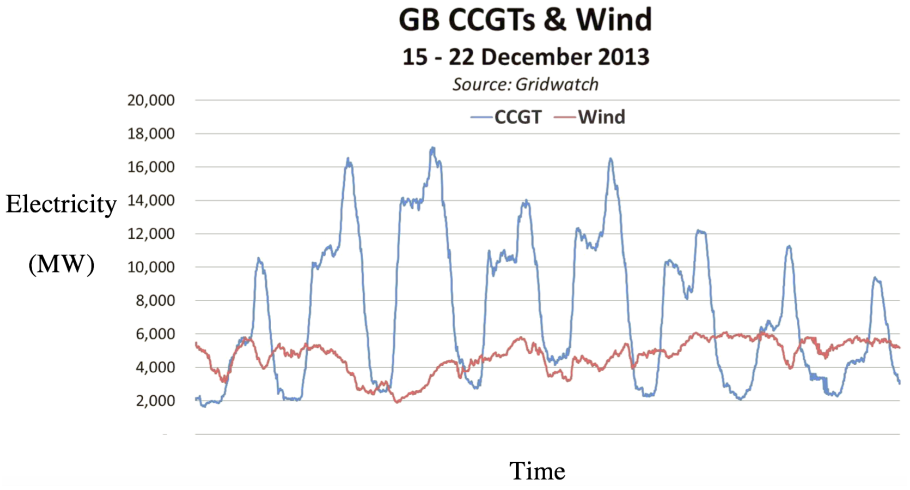
1.1 Background

Gas turbine combustion is predicted to remain popular in the next few decades due to the large demands from civil aviation and power generation industries. Although renewable energy such as wind energy has been used in the recent years, its low output and seasonal intermittency have prevented its wider application. For example, in Britain the electricity generated in 2013 by combined cycle gas turbines (CCGTs) is significantly higher than that produced by wind energy, as compared in Fig. 1.1. This suggests that gas turbine combustion will continue to play an important role in the power industry and may not be completely replaced by other power generation techniques in the foreseeable future.

The combustion of liquid or gaseous fuel in a gas turbine system is often accompanied by the emission of air pollutants such as nitrogen oxides (NO_x), carbon monoxide (CO), and tiny unburnt particles, etc. Due to their negative effects on the environment (e.g., acid rain, eutrophication and haze) and human health, stricter environmental policies are being implemented (e.g., [19]), meaning that these air pollutants must be controlled and reduced to a sufficiently low level. To achieve this goal, the next generation of combustors used by modern aero-engines and stationary gas turbines now apply lean premixed combustion technology, such as the "Dry Low Emissions (DLE)" technique, which allows the fuel to fully or partially premix with an excess of air, resulting in a lean fuel/air pre-mixture before burning. Its main advantage is to lower the temperature of the reaction zone, leading to a considerable decrease of (thermal) NO_x emission [20]. A common side-effect of this technique, however, is a phenomenon called "thermoacoustic instability" [21].



(a) 23 – 28 September 2013



(b) 15 – 22 December 2013

FIGURE 1.1: The power of electricity generated by (blue line) combined cycle gas turbines (CCGTs) and (red line) wind energy within one week period in (a) September and (b) December, 2013. Images adapted from [1].

The thermoacoustic instability is caused by a two-way interaction between acoustic waves and heat release fluctuations within a combustor. These two effects in turn depend on the vorticity waves, mixture inhomogeneities, fuel/air equivalence ratio oscillation and upstream velocity fluctuation, etc. A simplified mechanism is shown in Fig. 1.2: a small perturbation in the flow modifies the flame shape and its surface area, leading to a time-variation in the flame's heat release rate (Fig. 1.2(a)). This heat release rate oscillation (denoted $\dot{q}'$) results in the volume expansion and contraction of the flame region, generating fluctuations in pressure (denoted p'), which propagate as acoustic waves along the duct (Fig. 1.2(b)). At the duct boundaries, some acoustic waves are reflected back and return to the flame with a time delay (Fig. 1.2(c)), which

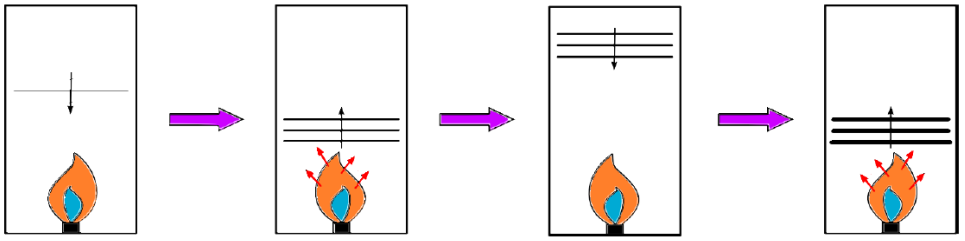


FIGURE 1.2: Thermoacoustic instability schematic: coupling between acoustic wave perturbation and unsteady flame heat release rate response.

may give rise to a stronger perturbation in the heat release rate and lead to the generation of more acoustic waves (Fig. 1.2(d)). Under some conditions a feedback cycle is set up, leading to successively growing amplitudes.

Under these conditions, the total energy generated by the flame-acoustic interaction exceeds the total energy dissipated by radiation, viscosity, boundary acoustic losses, etc. This comparison can be mathematically expressed as:

$$\int_0^T \iiint_{\mathcal{V}} p'(\boldsymbol{x},t)\dot{q}'(\boldsymbol{x},t)\mathrm{d}\mathcal{V}\mathrm{d}t > \int_0^T \iint_{\mathbb{A}} p'(\boldsymbol{x},t)(\boldsymbol{u}'\cdot\boldsymbol{n})\mathrm{d}\mathbb{A}\mathrm{d}t + \int_0^T \iiint_{\mathcal{V}} \sum_i L_i(\boldsymbol{x},t)\mathrm{d}\mathcal{V}\mathrm{d}t, \quad (1.1)$$

where p' denotes pressure fluctuation, $\dot{q}'$ the volumetric heat release rate fluctuation, $\boldsymbol{u}'$ the velocity fluctuation, $\boldsymbol{x} = (x, y, z)$ the coordinate vector, t the time, T a sufficiently long time interval (usually the wave period), $\mathcal{V}$ the domain volume, $\mathbb{A}$ the domain surface area, and $\boldsymbol{n}$ a unit vector normal to the domain surface. This expression is known as the "Rayleigh criterion" [22]: the left hand side (LHS) denotes the total energy generated by the interaction between heat release rate fluctuation and acoustic pressure perturbation. The 1st term on the right hand side (RHS) represents the losses of acoustic energy at domain boundaries, while the 2nd term denotes the acoustic or heat losses caused by all the other dissipation and transmission mechanisms (e.g., friction, radiation) [23]. Equation 1.1 describes the condition for the thermoacoustic instability to happen, and can be represented as a feedback amplifier in the form of a block diagram (see Fig. 1.3).

The most likely dynamics resulting from thermoacoustic instability are "limit cycle oscillations", as shown in Fig. 1.4. The fluctuation amplitudes of pressure (p'), velocity ($\boldsymbol{u}'$) and the induced heat release rate ($\dot{Q}'$) all grow exponentially in time at the beginning, then gradually saturate into a stable oscillation state due to nonlinearity in flame response. This undesirable "limit cycle"

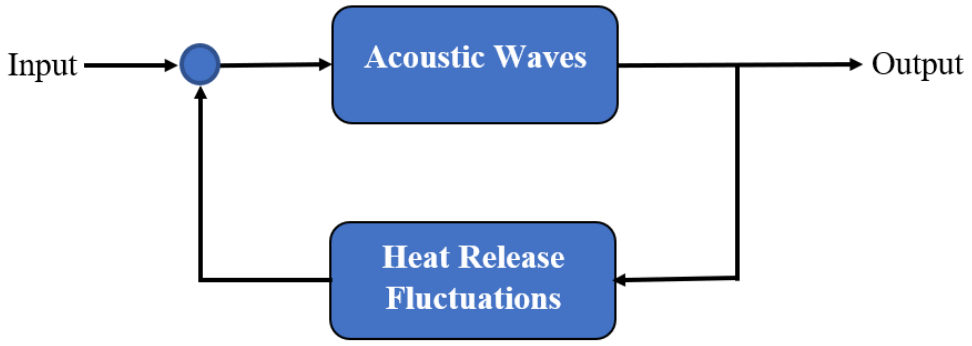


FIGURE 1.3: Thermoacoustic instability mechanism: a feedback amplifier.

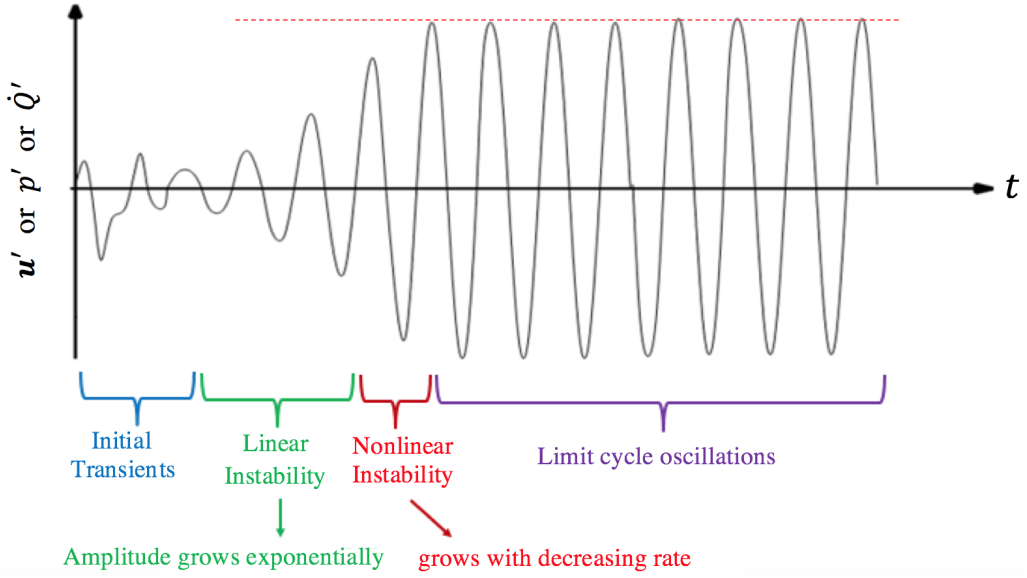


FIGURE 1.4: Schematic of development of limit cycle oscillations due to thermoacoustic instability. $\dot{Q} = \iiint_{\mathcal{V}} \dot{q} \mathrm{d}\mathcal{V}$ denotes the total heat release rate.

usually exhibits large amplitude at approximately fixed frequency, and is an important reason for the fatigue failure of turbine blades [2] or cracks on combustor casings [3], etc., as illustrated in Fig. 1.5(a-b). Furthermore, these large oscillations also lead to overheating and even melting of vital components such as the fuel injectors [2] (see Fig. 1.5(c)). All of the above damage may eventually result in the failure of the entire device, while limit cycle oscillations also contribute to the emission of high-level noise from the combustor.

A popular type of gaseous fuel used by many gas turbine combustors is natural gas, whose main component is methane (CH_4) [24]. Other available gaseous fuels include the renewably-generated hydrogen (H_2) and ammonia (NH_3), etc. It has been seen that the addition of H_2 and NH_3 to the pure methane fuel may both cause significant thermoacoustic instability problems in gas turbine combustors [25–28].



(a) (b) (c)

FIGURE 1.5: Damage caused by thermoacoustic instability: (a) fatigue failure of turbine blades [2]; (b) cracks on combustor casing [3]; (c) melted fuel injectors [2].

1.2 Predicting Thermoacoustic Instability: Modelling Theories

The thermoacoustic interaction involves a large range of different length and time scales, from flame thickness in millimetres and chemical reaction speed in milliseconds, to acoustic wavelengths in metres and pressure oscillation period in seconds, etc. This complexity in length and time scales poses challenges to the prediction of thermoacoustic instability using a single approach. Therefore, the acoustic wave excitation and the flame heat release response are usually modelled separately. Several modelling approaches have been developed for both, and will be briefly introduced in this section.

1.2.1 Acoustic wave modelling

For acoustic waves the associated pressure fluctuation is much smaller than the mean pressure, e.g., $p' < 0.1\%\overline{p}$, thus the wave motion can be assumed linear [29]. This also means that the fluctuations in the flow variables (e.g., velocity u', temperature T') induced by an acoustic wave can be considered small. Based on this, several acoustic modelling methods are available. One example is the "Galerkin method" (e.g., [30–32]), which uses a modal expansion for the fluctuating variables in the time domain. For instance, the pressure fluctuation, p', in a duct can be approximated as a summation of multiple normal modes, $\psi_i(x)$, each with time-varying amplitude of $\eta_i(t)$ [33]:

$$p'(x,t) = \overline{p} \sum_{i=1}^{n_t} \psi_i(x)\eta_i(t), \tag{1.2}$$

with $\overline{(\cdot)}$ the time-averaged quantities, x the axial coordinate, and n_t the total mode number. The mode function, $\psi_i(x)$, only relies on spatial location and can be written as:

$$\psi_i(x) = \sin(k_i x + \phi_{i0}), \tag{1.3}$$

where k_i and ϕ_{i0} are the wave number and spatial mode shape, respectively, both determined by the boundary conditions. Culick et al. [34–36], Benoit et al. [37], Juniper et al. [38, 39] and many others have used this approach to model acoustic waves in simple thermoacoustic systems with non-complex boundary conditions. This approach is based on a continuous spatial approximation [40], which is suitable for combustion systems with largely distributed reaction zones (e.g., the solid rocket engines). For a gas turbine combustor with a compact reaction zone, however, the Galerkin method needs a large amount of modes to accurately capture the velocity discontinuity across the flame.

The second modelling approach is a "wave-based" method (e.g., [41, 42]). For a non-accelerating mean flow within a duct of uniform cross-section, the flow can be modelled as a mean field superimposed with linear acoustic fluctuations, which are controlled by the "convected wave equation" (see Section 2.1 for more details):

$$\frac{1}{\overline{c}^2}\frac{\overline{\mathrm{D}}^2 p'}{\mathrm{D}t^2} - \boldsymbol{\nabla}^2 p' = 0, \tag{1.4}$$

where $\overline{\mathrm{D}}/\mathrm{D}t = \partial/\partial t + \overline{\boldsymbol{u}} \cdot \boldsymbol{\nabla}$, and $\overline{c}$ the mean speed of sound. At low frequencies, the solutions of Eq. 1.4 are plane acoustic waves, one travelling downstream and one upstream, each with separate strengths. Based on this, the pressure fluctuation (p') in the duct can be modelled as:

$$p'(x,t) = \mathrm{f}\left(t - \frac{x}{\overline{c}+\overline{u}}\right) + \mathrm{g}\left(t + \frac{x}{\overline{c}-\overline{u}}\right), \tag{1.5}$$

with f and g the downstream and upstream-travelling acoustic wave strength, respectively, and $\overline{u}$ the mean axial flow velocity. Equation 1.5 can also be expressed in the frequency domain, as explained in Section 2.2. By representing the combustor geometry as a network of connected simple ducts, this approach can be applied to combustion chambers with realistic geometries. By extending the solutions of the convected wave equation to include circumferential waves, it can also be applied to annular geometries. It can account for a wide range of acoustic boundary conditions. Polifke et al. [43], Evesque et al. [44], Dowling et al. [41, 45] and Stow et al. [42, 46], etc., have developed and extensively used this method for thermoacoustic modelling.

The third approach is the "Helmholtz solver" method (e.g., [47]), which models the flow perturbations in the frequency domain and solves the Helmholtz equation based on zero mean flow assumption. Away from the flame, the pressure fluctuation satisfies [48]:

$$\nabla \cdot (\bar{c}^2 \nabla \widehat{p}) + \Omega^2 \widehat{p} = 0, \tag{1.6}$$

where $\widehat{(\cdot)}$ denotes amplitude fluctuation in the frequency domain, and $\Omega = 2\pi f + i\sigma$ is a complex-valued angular frequency, with σ the growth rate and f the frequency. Nicoud et al. [47, 49], Selle et al. [50], Silva et al. [48], Laera et al. [51, 52] and many others have used this solver to capture the thermoacoustic modes in various combustors. More details about this method can be found in Section 2.4.2.

1.2.2 Flame response modelling

Prediction of thermoacoustic instability also requires knowledge of how the flame heat release responds to upstream acoustic perturbations. The nonlinearity which gives rise to saturation in Fig. 1.4 is known to arise due to flame response, at least in gas turbine combustors [53, 54]. As well as being nonlinear, the flame response also involves a variety of physical phenomena. For example, for a turbulent premixed flame, the upstream velocity disturbances (originally induced by acoustic waves) can largely modify the flame kinematics [55] and the fuel/air equivalence ratio [23], etc.

In order to simplify the flame response modelling for use in acoustic models, the fact that the flame thickness (in mm) is much smaller than the dominant acoustic wavelengths (in metres) is often exploited, meaning that the flame can be treated as "acoustically compact" and represented by an infinitely thin flame sheet [56]. In this case, a "flame model" linking the global heat release rate, $\dot{Q}$, to an upstream velocity perturbation, u_1, is established. Initially, the linear limit of such flame models was considered, known as a "flame transfer function (FTF)" (denoted $\mathcal{F}$), defined in the frequency domain as:

$$\mathcal{F}(\omega) = \frac{\widehat{\dot{Q}}/\overline{\dot{Q}}}{\widehat{u}_1/\overline{u}_1} = G(\omega) \exp(i\varphi(\omega)), \tag{1.7}$$

where $\omega = \sigma + i2\pi f$ is another complex angular frequency (also known as the "Laplace variable"). G and φ are the gain and phase of the FTF, both being functions of frequency only. A simple

and well-known FTF is the analytical "$n-\tau$" model [57], i.e. $\mathcal{F} = n_f \exp(i2\pi f\tau_f)$, which has constant gain (n_f) and time delay (τ_f).

The above FTF is considered accurate for small perturbation levels (e.g., $|\widehat{u}_1/\overline{u}_1| \leq 5-10\%$). However, in a realistic combustor, the upstream perturbation amplitude is usually much higher (e.g., $|\widehat{u}_1/\overline{u}_1| > 10\%$), making the flame response nonlinear [58–60]. In this case, a weakly nonlinear "flame describing function (FDF)" has been developed as [53, 54]:

$$\mathcal{F}\left(\omega, |\widehat{u}_1/\overline{u}_1|\right) = \frac{\widehat{\dot{Q}}/\overline{\dot{Q}}}{\widehat{u}_1/\overline{u}_1} = G\left(\omega, |\widehat{u}_1/\overline{u}_1|\right) \exp\left(i\varphi\left(\omega, |\widehat{u}_1/\overline{u}_1|\right)\right). \tag{1.8}$$

Compared to the linear FTF (see Eq. 1.7), both the gain and phase of an FDF are functions of both the frequency, ω, and the normalised perturbation amplitude, $|\widehat{u}_1/\overline{u}_1|$. This allows the FDF to capture the nonlinear thermoacoustic behaviour such as the "limit cycle oscillations" [61], "mode triggering" [60], and "mode switching" [60], etc. Based on the weakly nonlinear theory [62, 63], the flame response to an upstream single-frequency perturbation is now considered nonlinear and occurs over the entire frequency domain, but with its strongest response appearing at the forcing frequency. This means the FDF assumes that the main response frequency still matches the perturbation frequency, but with a gain [53] and phase change [54] depending on both frequency and perturbation amplitude (see Eq. 1.8). Based on this theory, Li et al. [60] developed an analytical FDF model for a duct combustor, by using two parameters, α and β, both of which determine the shape of the nonlinear FDF. This analytical model has been validated by experimental measurements.

1.2.3 Thermoacoustic solvers

The above models for the acoustic wave and flame response can be combined into a "thermoacoustic solver", which is able to predict thermoacoustic instability. There are several solvers available. For example, Stow et al. [42, 46, 64] used wave-based acoustic models to develop a "Low Order Thermo-Acoustic Network (LOTAN)" solver, which solves the unsteady linearised Euler equations and categorises the combustor geometry by finding the transfer function for the response of flow perturbations (e.g., at the fuel injectors) to heat release oscillations. This transfer function is then converted into the time domain through an inverse Fourier transform to obtain the Green's function, which thus relates unsteady flow to heat release at previous times. This solver has been applied to both longitudinal and annular geometries.

Campa et al. [65] then developed the "Low Order Modelling for Thermoacoustic Instability (LOMTI)" solver, along similar lines. The approach builds a time-domain state space system, uniquely represented by the amplitudes of flow variable perturbations and the flame heat release responses. This solver can simplify a combustor geometry into a system of cylinders and annular ducts, with acoustic jump conditions applied at duct interfaces and well-posed boundary conditions at system ends.

Recently, Bauerheim et al. [66] developed an "Analytical Tool to Analyse and Control Azimuthal Modes in Annular Chambers (ATACAMAC)" for predicting purely azimuthal modes in an annular combustor with multiple burners feeding a 1-D annular chamber. It reduces the size of the system by splitting the annular rig into multiple sectors, each sector divided into two parts: an azimuthal propagation in the annular chamber, and an interaction area at the burner/chamber junction. This solver does not apply to rigs open to the atmosphere, but corresponds well to real combustors with a choked exit.

In this work, two thermoacoustic solvers are considered and compared in detail. The first one is called "OSCILOS", standing for the "Open Source Combustion Instability Low Order Simulator", which was developed recently by the group of Morgans [67]. It combines the above wave-based acoustic modelling approach which accounts for the mean flow (see Eq. 1.5) in a simplified network geometry (e.g., [46, 67]). OSCILOS has successfully predicted the longitudinal instability in both linear and nonlinear thermoacoustic regimes [60], and been validated by matching the limit cycle properties measured in a premixed combustor [68]. More details about this solver are explained in Section 2.4.1.

The second solver introduced is called "H-solver" (e.g., [69]), developed based on above Helmholtz acoustic solution (see Eq. 1.6). It retains the original combustor geometry but ignores the mean flow field. More details about this solver can be found in Section 2.4.2. For both of these solvers, the flame heat release is incorporated as a "heat source", whose response to upstream acoustic perturbation can be modelled by the above-mentioned FTF or FDF.

1.3 Thermoacoustic Instability: Experimental Measurements

In order to validate the predictions of thermoacoustic instability as well as to probe the underlying flow physics, experimental measurements are needed. They are especially valuable for

realistic combustors with complex geometries and varying operating conditions. On this front, Paschereit et al. [70, 71] measured the thermoacoustic instability in a gas turbine combustor and developed control methods for it. Lieuwen et al. [72–74] studied the instability of a low NOx combustor across a wide range of operating conditions, and observed the saturation of flame response into a limit cycle oscillation. Sattelmayer [75] evaluated the effect of fuel/air equivalence ratio fluctuation on the thermoacoustic instability by experiments. Recently, Noh et al. [76] performed measurements on the azimuthally-driven, subharmonic thermoacoustic instabilities in a swirl-stabilised combustor. These experiments were usually performed under certain unstable operating conditions.

With recent development of measurement techniques, such as the OH^* chemiluminescence for heat release rate imaging (e.g., [77, 78]), the planar laser induced fluorescence (PLIF) for flame visualisation (e.g., [78]), the 1-D Raman spectroscopy for species concentration field (e.g., [24]), and the particle image velocimetry (PIV) for flow velocity field measurement (e.g., [78]), etc., the measurement of detailed flame characteristics (e.g., structure and forced response) has been made possible. Balachandran et al. [53] were the first ones measuring the non-linear FDF for a turbulent premixed flame, showing that the flame sheet kinematics plays a major role in the saturation mechanism of the lean premixed flame response, and has a large impact on the features of the resulting limit cycle oscillation. The nonlinearity was found to occur when the shear layers rolled up into vortices and parts of the flame stabilised on the inner shear layer close to the recirculation zone collapsed on parts of the flame stabilised on the outer recirculation zone, a phenomenon that was made more prominent with increasing forcing amplitude.

Noiray et al. [54] then measured the FDF for an unconfined laminar flame, and Durox et al. [79] also measured the FDFs for several laminar flames with conical or V-shapes. Palies et al. [80–82] then measured the FDF for a turbulent swirling flame, and correctly captured the limit cycle oscillations. Kim et al. [83, 84] investigated the effect of equivalence ratio (denoted ϕ_e) fluctuation on the responses of partially-premixed and fully-premixed flames, finding this variation in ϕ_e can eventually lead to thermoacoustic instability at some conditions. Later, Ghoneim et al. [85, 86] observed the macrostructures and flow-flame interactions for a turbulent premixed flame, and achieved accurate predictions on the instability features. Recently, Kypraiou et al. [87] measured the responses of both fully-premixed and non-premixed flames to acoustic oscillations, finding that the flame surface area modulation plays an important role for both flames while the equivalence ratio fluctuation only affects the latter.

In order to reduce the experimental costs, many test rigs which feature realistic combustors have been built with only one combustion chamber containing a single flame (e.g., [24, 53]). However, real industrial combustors often consist of multiple burners, and the thermoacoustic oscillation and flame-to-flame interactions in the circumferential direction may play an important role (e.g., [88]). In order to capture these effects, a series of multi-burner facilities have been established recently. For instance, Worth and Dawson [89] built a two-flame rig at Cambridge and measured the interactions between the two bluff-body-stabilised premixed flames, finding that the distance between the two flames significantly affects the gain and phase of the measured FDF. Polifke et al. [90] performed FTF measurements on a fully annular combustor, and used the experimental data to validate a low order network acoustic model. Fanaca et al. [77] also measured the flame behaviour in an annular rig, and found the flame-to-flame interactions have a large impact on the thermoacoustic stability. Bourgouin et al. [91] later measured the nonlinear FDF for an annular combustor. The effects of interactions between neighbouring flames on the limit cycle oscillation amplitude [92] and flame shape [93, 94] have recently been measured by Worth and Dawson for an annular rig at Cambridge [92, 93] and by Durox et al. for the MICCA combustor at EM2C laboratory [94].

It is also notable that many of the above experiments have been performed under atmospheric pressure, while in reality a large number of industrial combustors are operated under elevated pressures. Only a few experiments have been conducted at such elevated pressures, such as Schuermans et al. [95], who measured the FTF for a full-scale combustor at real high engine pressures. Sabatino et al. [96] measured the FDFs for flames with different fuels across a series of pressures from 1 bar to 5 bar. Due to the lack of high pressure facilities, the measurement data of FTF and FDF for a pressurised combustor are still very limited.

1.4 Thermoacoustic Instability: Numerical Simulations

The recent rapid development of computational fluid dynamics (CFD) has made the numerical simulations another promising tool for thermoacoustic instability prediction. Initially the Unsteady Reynolds Averaged Navier-Stokes (URANS) method was used for premixed flame response computation (e.g., [97–100]). More recently, most flame response calculations have been performed using Large Eddy Simulation (LES). Compared to URANS, the LES solves the large-scale turbulence eddies and is thus more accurate for turbulent mixing and unsteady combustion

processes, especially in realistic combustors. For example, Pitsch et al. [101] used LES to compute the features of a turbulent premixed flame. Roux et al. [102] used a compressible LES code to simulate both reacting and non-reacting premixed swirling flames. Bulat et al. [98] defined a hybrid code combining URANS and LES for premixed gaseous flame in a low NOx combustor, and later performed purely LES computations [14, 103, 104] on the same flame. Wolf et al. [105, 106] performed LES computations on an annular combustor, and revealed the impact of self-excited azimuthal unstable modes on the thermoacoustic instability, etc.

Similar to the above experimental measurements, the LES computation of a thermoacoustic interaction has two main focuses: (i) global thermoacoustic stability; (ii) detailed flame response to upstream forced acoustic perturbation. For (i), a fully compressible LES is often used, which computes the acoustic wave motion and the flame response simultaneously. For example, Poinsot et al. [107] applied a high-order finite-volume LES code, AVBP [10, 108], to directly simulate the thermoacoustic instabilities in a single-burner [109] and in an annular configuration [110], respectively. For (ii), compressible LES solvers can also be used to obtain the FTFs or FDFs for a flame, e.g., Palies et al. [111] correctly captured the response of a bluff-body-stabilised swirling flame, but limited their analysis to a very narrow frequency range. Tay-Wo-Chong et al. [112] predicted a complete FTF over a wide frequency range for a premixed swirling flame.

1.4.1 Incompressible large eddy simulation

Although fully compressible LES can capture the nonlinear flame-acoustic interaction, its computational cost is extremely large due to its maximum permitted time step being very small as it is proportional to the inverse of the speed of sound. Recently, the fact that the flame primarily responds to the hydrodynamic disturbances (originally excited by the acoustics) has been exploited [113, 114] using incompressible LES (sometimes termed as "low Mach number LES"): the convective flow speed rather than the speed of sound determines the time step and thus allows much larger values, making incompressible simulations significantly faster than compressible ones. Please note that here "incompressible" does not imply constant density, but rather that the density is independent of pressure variations throughout the flow, i.e. not able to be compressed.

With this approach, Febrer et al. [115] numerically evaluated the impact of acoustic disturbances on the combustion zone. Krediet et al. [116, 117] predicted the FDF for a premixed swirling

flame, and found the nonlinear saturation of the FDF gain with perturbation level for the first time. This has also been accomplished for a bluff-body-stabilised premixed flame recently [118]. Han et al. [119] used an open source incompressible code "Saturne" [120, 121], and accurately computed the FDF for another premixed bluff-body-stabilised flame. They [68] also predicted the complete FDF later for the same flame using OpenFOAM [122], and correctly captured the limit cycle oscillation properties. Xia et al. [5, 123, 124] simulated a nonlinear series of FDFs for a very long flame, and the linear flame response of a stratified flame is predicted by Han et al. [125]. Recently, the effect of sub-grid scale combustion model on an LES-simulated unforced turbulent premixed flame has been investigated by Rochette et al. [126], but such study has not been performed on a forced flame, which may have a varying response to the same upstream perturbation across different combustion models.

1.4.2 Chemical reaction schemes

In most flame LES studies (e.g., [68, 127]), the chemical reaction process is modelled by using a simplified scheme involving only a few reaction steps, such as a one-step methane [127] or propane scheme [128], a two-step methane scheme [129], and a two-step ethylene scheme [127], etc. These simplified schemes have been proved to accurately reproduce low frequency flame dynamics [130], and are usually validated by comparing their computed laminar burning velocity and adiabatic flame temperature against those obtained by more complete mechanisms, e.g., the full 325-step GRI-Mech 3.0 scheme for methane [131] and the UCSD scheme for ethylene [132]. In order to increase the applicability range, the parameters of such simple reaction schemes may sometimes be tuned to match the experimental data across equivalence ratios (e.g., [133]), or to account for the flame-to-wall heat interaction [134] and higher pressure effects (e.g., [135]), etc. Although the impact of reaction chemistry on the LES of an unforced flame was recently investigated [136], ranging from a simple one-step mechanism [129] to a detailed 42-step scheme [137] for methane, to the author's knowledge there is no similar study for a forced flame, where an accurate reproduction of the flame shape is vital to correctly capture the flame responses during a forcing period. This is even more important when the operating pressure is high. Very few LES cases (e.g., [14, 104, 136]) have considered an unforced flame at elevated pressures representative of real combustor operating conditions, and none thus far have realistically accounted for the nonlinear forced flame response at such high pressures. In Refs. [138, 139], the linear FTF in a high pressure rig was computed. Recently, Yang et al. [140] and Scarpato et al. [141]

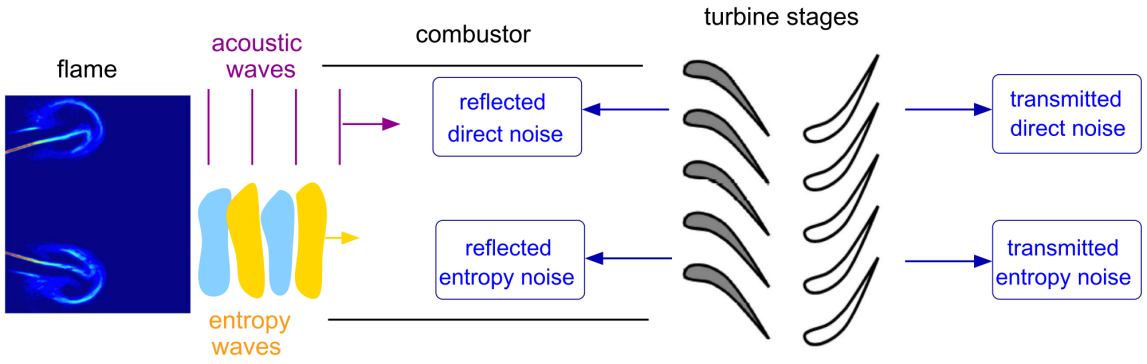


FIGURE 1.6: Entropy wave transport and the resulting entropy noise. Figure taken from [4].

performed linear and nonlinear flame response analyses, respectively, for a reheat combustor, but no complete FDF was computed for such pressurised rig.

1.5 Entropy Wave Transport

Thermoacoustic instability in a gas turbine combustor may also be influenced by the transport of entropy waves and their resulting entropy noise. As shown in Fig. 1.6, entropy waves (or "entropy perturbations") are temperature fluctuations generated by unsteady flame heat release, and are sometimes termed "hot spots". Upon being accelerated, as happens predominantly through the combustion chamber exit and the first turbine stage, but also through subsequent turbine stages, entropy waves generate entropy noise, also known as the "indirect combustion noise". This constitutes both downstream and upstream propagating acoustic waves [142], with the downstream travelling waves eventually appearing at the turbine outlet [143, 144], which for aero-engines contributes to the total exhaust noise level. The upstream travelling waves, generated mainly by the acceleration of entropy waves in the first turbine stator row, mostly propagate back to the flame, which may contribute to further flame heat release rate perturbations [113] and thus affect the propensity to damaging thermoacoustic instabilities [145, 146].

The strengths of both upstream and downstream acoustic waves induced by entropy noise are directly proportional to the amplitude of entropy waves reaching the inlet of the first turbine stage [147], which coincides with the combustion chamber exit plane. Many low order analytical models for entropy noise have been developed, e.g., [142, 148–151]. Analytical, experimental and numerical analyses have suggested that for typical gas turbine accelerations (from low subsonic flow to approximately sonic flow), entropy noise may greatly exceed the "direct combustion noise"

generated by the volume variation of the flame. However, a recent analysis suggested that the direct combustion noise actually dominates [152] and so whether entropy noise is the dominant combustion noise source still remains an open question.

In order to accurately estimate the entropy noise, the existing low order models require knowledge of the entropy wave amplitude at the combustion chamber's exit. Thus far, models generally neglect the effect of entropy wave transport through the combustion chamber, even though numerical simulations suggest that strong entropy waves may reach the first turbine stage [153]. The first models of entropy wave transport were by Sattelmayer [75], with Morgans et al. [154] then using turbulent channel flow simulations to show that advective dispersion causes loss of entropy wave strength, but that significant entropy wave amplitude appears likely to remain at the combustion chamber exit. A recent numerical and experimental investigation into the pipe flow in a smaller-scale rig has been performed by Giusti et al. [155], suggesting that the entropy wave transport can be described by a frequency response function. Mahmoudi et al. [156] studied the entropy dispersion due to a non-uniform mean flow velocity profile using RANS, and improved the low order entropy noise prediction by including the dispersion information.

However, the highly turbulent reacting flow field in a real combustor is very different to a fully developed pipe flow; flow swirl, separation, recirculation zone and vortex cores all act as large-scale hydrodynamic features with the potential to further disperse the entropy wave strength during its transport process. Previous LES [68, 119, 157] and experiments [158] of combustor reacting flow fields have shown that the main large-scale flow features, such as separation and re-circulation zones, are the same whether the flame is fully-premixed [119], partially-premixed [68], or non-premixed [157, 158]. The mean and fluctuating velocity fields are both qualitatively and quantitatively very similar in all cases. It is therefore highly relevant to investigate the effect of these large-scale flow features on the transport of entropy waves within a realistic combustor flow field.

With the shear-dispersed [159] entropy wave amplitude at the combustor exit captured correctly, the effect of the generated entropy noise on the thermoacoustic instability predictions can be evaluated. Previous works (e.g., [146, 154, 160, 161]) on a duct combustor have found that by considering the influence of entropy wave dispersion, the subsequent entropy noise may modify the frequency, growth rate and distribution of the thermoacoustic modes, leading to mode switching, stabilisation or destabilisation [146], etc. It is therefore interesting to see how

the entropy noise affects the thermoacoustic stability of a combustor under realistic operating conditions.

1.6 Response of a Very Long Flame

The above-introduced flame transfer and describing functions (Eqs. 1.7– 1.8) usually consider the flame region to be much shorter than the dominant acoustic wavelengths, known as the "acoustically compact" assumption [162]. This allows the flame-acoustic coupling to be modelled by the acoustic jump conditions across an infinitely thin flame sheet [41, 95, 162], using thermoacoustic solver such as OSCILOS [67]. This assumption can be considered valid for a typical gas turbine combustor (e.g., [24]), where the axial length of its reaction zone (<100 mm) is usually much shorter than the dominant acoustic wavelengths (1 – 4 m).

However, when the flame is very long in the longitudinal direction, the above assumption may become invalid, in which case the flame cannot be considered as a single compact perturbation source or sink [163–165]. The thermoacoustic prediction then needs to account for the spatial variation of the heat release rate response to the upstream perturbation along the flame length. This requires a "local flame model", which continuously varies along the flame's main stretching direction. Recent studies applying such local and continuous flame model are mainly based on analytical assumptions (e.g., [163, 164]). For example, distributed FTFs or FDFs with spatially uniform gains but local time delays determined by a "particle flight time" approach [166] have been incorporated into Helmholtz-equation based thermoacoustic solvers in [69, 167].

A more practical method called "flame segmentation", which splits the continuous flame into a series of equal-sized flame segments, was recently proposed by [115, 168]. It applies a discrete series of FTFs or FDFs at different downstream locations along the flame length. For these local FTFs and FDFs, their simulation or measurement accuracy invokes a trade-off: increasing the number of discrete flame segments may better capture the flame's non-compactness, but it also decreases the signal to noise ratio (SNR) as each flame element contains less heat release rate data. This method has been used for thermoacoustic prediction for the ORACLES combustor via the low order code LOTAN [42], although full details on how the series of sub-flames was treated were not given. Low order network modelling assuming zero-mean-flow was used by [169], which dealt with the distributed heat release field by segmenting the flame into a sequence of

linear $n - \tau$ flame models [57]; the criterion for flame segmentation and the treatment of the mean thermodynamic properties were, however, not detailed.

1.7 Motivations and Objectives

In order to tackle the problems and fill the gaps mentioned in the above introduction, this thesis presents the following tasks:

(*i*) The numerical simulation of turbulent premixed flames in complex-geometry combustors, with affordable computational costs. The effects of sub-grid scale (SGS) turbulence model, SGS combustion model, reaction chemistry, operating pressure, wall heat losses and computational mesh density, etc., on the simulation results need to be evaluated.

(*ii*) The simulation of forced flame heat release responses to upstream acoustic perturbation, with varying perturbation frequency and amplitude applied, leading to the construction of linear FTFs and nonlinear FDFs. The effects of multiple factors mentioned in (i) on the computed flame responses need to be studied.

(*iii*) The prediction of thermoacoustic instability in a realistic gas turbine combustor, using different prediction approaches and under varying operating conditions. For those unstable operations, the resulting nonlinear limit cycle oscillations also need to be predicted.

(*iv*) The simulation of entropy wave transport within real combustor flow fields, and a discussion of the likely influence of the resulting entropy noise on the thermoacoustic modes.

(*v*) The computation of the axially varying response of a very long flame to an upstream perturbation, and the incorporation of the resulting local flame response models for the prediction of thermoacoustic limit cycle.

In order to complete the above tasks, two typical single-burner gas turbine combustors have been investigated. The first is the pressurised SGT-100 industrial combustor [24], simulated by two incompressible LES solvers, OpenFOAM [170] and BOFFIN [171–173], involving two SGS combustion models (LES-PaSR and LES-PDF), two reaction schemes (4-step and 15-step), and two operating pressures (3 bar and 6 bar). The simulated unforced flame is validated by high quality experimental data, then submitted to an upstream velocity perturbation to construct

the FDFs. The effects of combustion model, reaction chemistry, mean pressure and other factors on the simulated flame and its FDF are systematically evaluated. The FDFs are then validated by coupling with both low order network and Helmholtz solvers to predict the thermoacoustic stability and limit cycle properties. The entropy wave transport within the combustor flow field is also simulated, evaluating the effects of different flow features on the dispersive attenuation of entropy wave strength for the first time. Finally, the impact of entropy noise on the simple-duct thermoacoustic modes is predicted using different entropy wave dispersion models.

The second combustor studied is based on a laboratory facility called ORACLES [15], which contains a ∼1.0 m long fully-premixed flame and was measured to be unstable at ∼50 Hz for a normalised upstream perturbation amplitude of ∼0.29 (i.e. 29% of the mean inflow velocity). The axial variation of the flame response along its longitudinal length results in the failure of the acoustical compact assumption. Therefore this long flame has been equally split into multiple segments axially, each has its local heat release response to a perturbation at a fixed upstream location computed, and establishes a series of local FDFs along the flame length. These local FDFs are then combined into a low order network solver, where they appear as discrete compact 1-D flame sheets. The predicted thermoacoustic instability, especially the frequency and amplitude of the resulting limit cycle oscillation, are finally analysed, illustrating the effects of total flame segment number, mean combustor temperature, and the acoustic boundary conditions, etc., on the prediction results.

After completing the above-proposed tasks, a better understanding of the thermoacoustic instability phenomenon and its prediction method may be achieved for realistic gas turbine combustors. The rest of this thesis is organised as follows: the analytical modelling of the acoustic waves and flame response are briefly introduced in Chapter 2. The principle of incompressible LES and the applied sub-grid turbulence, combustion, and chemical reaction models are all explained in Chapter 3. The numerical simulation of the SGT-100 combustor and the computation of its flame responses are presented in Chapter 4, followed by the predictions of thermoacoustic instability (Chapter 5) and entropy wave transport (Chapter 6) in this rig. The axially-varying flame response and the resulting limit cycle oscillation in the long-flame ORACLES combustor are predicted in Chapter 7. The main conclusions and future work plans are finally presented in Chapter 8.

Chapter 2

Theoretical Modelling

In this chapter, the analytical modelling approaches for the motion of acoustic waves in a combustor are firstly introduced, followed by the detailed description of a flame model responding to an upstream perturbation. The acoustic wave and flame models are then combined into different thermoacoustic solvers to predict the combustor's stability. Finally, the theories for the response model of a very long flame and the entropy wave transport within a combustor flow field are both derived and explained. The contents presented in Sections 2.1 – 2.4 are mainly based on the literature and previous researchers' work, while Sections 2.5 and 2.6 are mainly the author's original work.

2.1 Governing Equations for an Acoustic Wave

The general governing equations for the motion of an acoustic wave (without viscous effect and external forcing) are obtained from the compressible Euler equations:

Continuity equation:

$$\frac{\mathrm{D}\rho}{\mathrm{D}t} + \rho\boldsymbol{\nabla}\cdot\boldsymbol{u} = 0, \tag{2.1a}$$

Momentum equation:

$$\rho\frac{\mathrm{D}\boldsymbol{u}}{\mathrm{D}t} + \boldsymbol{\nabla}p = 0, \tag{2.1b}$$

with ρ the density and $\boldsymbol{u}$ the flow velocity vector. $\mathrm{D}/\mathrm{D}t = \partial/\partial t + \boldsymbol{u}\cdot\boldsymbol{\nabla}$ is the material derivative. Based on the assumption [41, 174] that an acoustic wave is linear and accompanied by small

fluctuations, the flow variables can be decomposed as:

$$p(\boldsymbol{x},t) = \overline{p} + p'(\boldsymbol{x},t), \tag{2.2a}$$

$$\rho(\boldsymbol{x},t) = \overline{\rho} + \rho'(\boldsymbol{x},t), \tag{2.2b}$$

$$\boldsymbol{u}(\boldsymbol{x},t) = \overline{\boldsymbol{u}} + \boldsymbol{u}'(\boldsymbol{x},t), \tag{2.2c}$$

where the fluctuation amplitude, $(\cdot)'$, is much smaller than the mean value, $\overline{(\cdot)}$. Substituting Eqs. 2.2a – 2.2c into Eqs. 2.1a – 2.1b, gives the linearised governing equations for an acoustic wave:

$$\frac{\overline{\mathrm{D}}\rho'}{\mathrm{D}t} + \overline{\rho}\boldsymbol{\nabla}\cdot\boldsymbol{u}' = 0, \tag{2.3a}$$

$$\frac{\overline{\mathrm{D}}\boldsymbol{u}'}{\mathrm{D}t} + \frac{1}{\overline{\rho}}\boldsymbol{\nabla}p' = 0, \tag{2.3b}$$

with $\overline{\mathrm{D}}/\mathrm{D}t = \partial/\partial t + \overline{\boldsymbol{u}}\cdot\boldsymbol{\nabla}$. Subtracting the spatial derivative (∇) of Eq. 2.3b from the time derivative ($\partial/\partial t$) of Eq. 2.3a, gives:

$$\frac{\overline{\mathrm{D}}^2\rho'}{\mathrm{D}t^2} - \boldsymbol{\nabla}^2 p' = 0. \tag{2.4}$$

For an isentropic wave, $p' = \overline{c}^2\rho'$, with $\overline{c}$ the mean speed of sound, Eq. 2.4 can be rewritten as:

$$\left(\frac{1}{\overline{c}^2}\frac{\overline{\mathrm{D}}^2}{\mathrm{D}t^2} - \boldsymbol{\nabla}^2\right)p' = 0. \tag{2.5}$$

Equation 2.5 is known as the "convected wave equation" of an isentropic acoustic wave. The associated velocity fluctuation, $\boldsymbol{u}'$, can then be solved by inserting the p' solution of Eq. 2.5 into Eq. 2.3b. In this work, all the modelled acoustic waves are assumed isentropic.

2.2 Acoustic Wave Propagation in a Constant Area Duct

In an isothermal 3-D duct with constant cross-sectional area, as shown in Fig. 2.1, the convected wave equation only permits the propagation of 1-D plane waves at low frequencies [29] (see Section 2.2.2 for more details). Based on this "1-D wave" assumption, the original convected

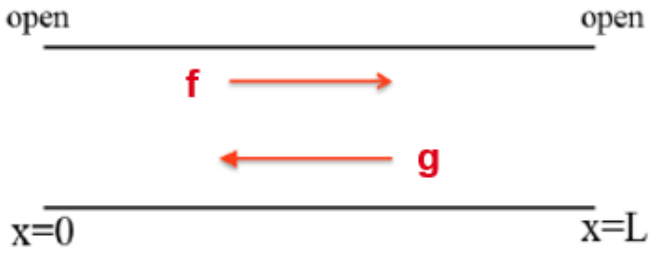


FIGURE 2.1: A 3-D constant area duct with upstream and downstream travelling plane acoustic waves.

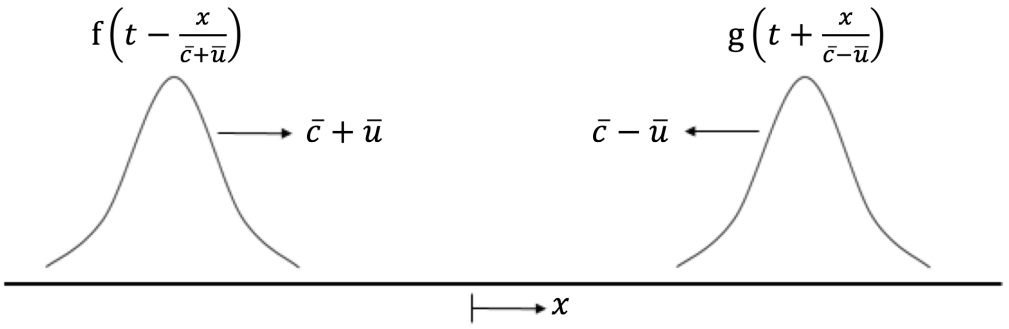


FIGURE 2.2: Motions of upstream and downstream travelling plane acoustic waves.

wave equation, Eq. 2.5, can be simplified as:

$$\left(\frac{1}{\bar{c}^2}\frac{\bar{\mathrm{D}}^2}{\mathrm{D}t^2}-\frac{\partial^2}{\partial x^2}\right)p'=0, \tag{2.6}$$

with u the axial flow velocity. These plane acoustic waves travel both downstream and upstream, with a wave amplitude denoted f and g, respectively. The pressure (p'), density (ρ') and velocity (u') fluctuations in this duct can then be modelled as:

$$p'(x,t)=\mathrm{f}\left(t-\frac{x}{\bar{c}+\bar{u}}\right)+\mathrm{g}\left(t+\frac{x}{\bar{c}-\bar{u}}\right), \tag{2.7a}$$

$$\rho'(x,t)=\frac{1}{\bar{c}^2}\left[\mathrm{f}\left(t-\frac{x}{\bar{c}+\bar{u}}\right)+\mathrm{g}\left(t+\frac{x}{\bar{c}-\bar{u}}\right)\right], \tag{2.7b}$$

$$u'(x,t)=\frac{1}{\bar{\rho}\,\bar{c}}\left[\mathrm{f}\left(t-\frac{x}{\bar{c}+\bar{u}}\right)-\mathrm{g}\left(t+\frac{x}{\bar{c}-\bar{u}}\right)\right]. \tag{2.7c}$$

The general motions of these acoustic waves are shown in Fig. 2.2, which have different propagation speeds in the downstream and upstream directions.

For harmonic waves, the plane wave solutions of Eqs. 2.7 can be further expressed in the frequency domain as:

$$\widehat{p}(x,t) = A\ e^{i(\omega_i t - k^+ x)} + Be^{i(\omega_i t + k^- x)}, \tag{2.8a}$$

$$\widehat{\rho}(x,t) = \frac{1}{\overline{c}^2}\left[Ae^{i(\omega_i t - k^+ x)} + Be^{i(\omega_i t + k^- x)}\right], \tag{2.8b}$$

$$\widehat{u}(x,t) = \frac{1}{\overline{\rho}\ \overline{c}}\left[Ae^{i(\omega_i t - k^+ x)} - Be^{i(\omega_i t + k^- x)}\right], \tag{2.8c}$$

where $\widehat{(\cdot)}$ denotes amplitude fluctuation in the frequency domain. A and B are constant amplitudes for the downstream and upstream-travelling waves, respectively. $\omega_i = 2\pi f$ is the angular frequency, $k^+ = \omega_i/(\overline{c} + \overline{u})$ and $k^- = \omega_i/(\overline{c} - \overline{u})$ are the wave numbers for the downstream and upstream-propagating waves, respectively.

2.2.1 Plane wave solutions with zero mean flow

For a constant area duct with both ends open (see Fig. 2.1), the acoustic boundary conditions are defined as:

$$\widehat{p} = 0 \quad \text{at} \quad x = 0 \quad \text{and} \quad \widehat{p} = 0 \quad \text{at} \quad x = L, \tag{2.9}$$

with L the duct length. Inserting Eq. 2.9 into Eq. 2.8a and applying a zero mean flow velocity (i.e. $\overline{u} = 0$), gives:

$$A + B = 0 \quad \text{and} \quad -2iAe^{i\omega_i t}\sin\left(\frac{\omega_i L}{\overline{c}}\right) = 0. \tag{2.10}$$

Since A is an arbitrary constant, $\sin(\omega_i L/\overline{c}) = 0$ should always be satisfied. The solution for the angular frequency, ω_i, is then obtained as:

$$\omega_{im} = \frac{m\pi\overline{c}}{L}, \tag{2.11}$$

where m can be any positive integer and known as the "mode number", which represents a 1-D wave mode solution. The wavelength, λ_m, for the m-th mode is defined as:

$$\lambda_m = \frac{2\pi\overline{c}}{\omega_{im}} = \frac{2L}{m}. \tag{2.12}$$

Assuming the duct length $L = 1$ m, wave amplitudes $A = -B = 1$ Pa, mean speed of sound $\overline{c} = 1$ m/s, mean density $\overline{\rho} = 1$ kg/m^3, and time $t = 0$ s, results in the first three wave mode solutions ($m = 1, 2$ and 3) illustrated in Fig. 2.3. All the three wave modes are plotted in the form of p' or u' axial profile. By changing the acoustic boundary conditions (e.g., using a closed duct end) or adding a non-zero mean flow velocity, these wave mode solutions can be varied.

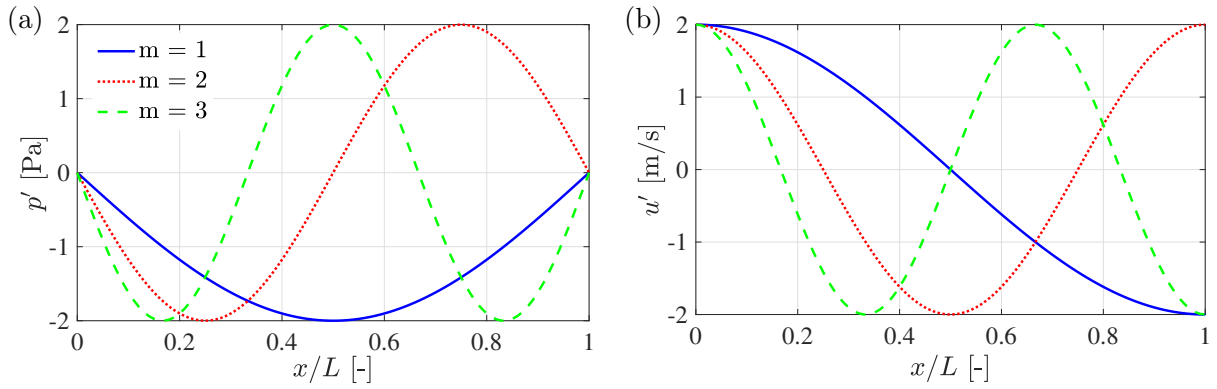


FIGURE 2.3: The first three acoustic wave modes in a constant area duct with both ends open, in the form of axial distributions of (a) pressure p' and (b) velocity u' fluctuations.

2.2.2 Frequency limits for the 1-D wave assumption

The above 1-D wave assumption is only valid below a certain frequency, denoted ω_{ic}. For instance, in a square duct with constant height and width of a (see Fig. 2.4), the acoustic waves are assumed harmonic and thus satisfy the 3-D wave equation, Eq. 2.5. The mean axial velocity, $\overline{u}$, is assumed zero. The acoustic boundary conditions are defined as [175]:

$$v' = 0 \quad \text{and} \quad \partial p'/\partial y = 0 \quad \text{at upper/lower walls,} \tag{2.13}$$

$$w' = 0 \quad \text{and} \quad \partial p'/\partial z = 0 \quad \text{at two side walls.} \tag{2.14}$$

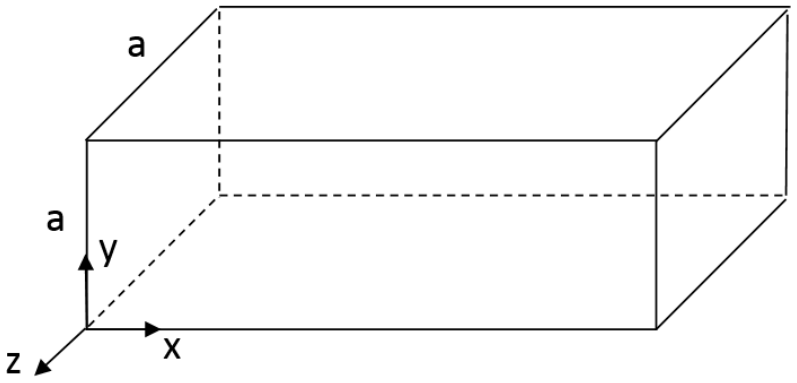


FIGURE 2.4: A 3-D square duct with constant width and height of a.

Based on these boundary conditions, the pressure fluctuation, p', in Eq. 2.5 can be solved as [29]:

$$p'(x,y,z,t) = \cos\left(\frac{l\pi y}{a}\right)\cos\left(\frac{m\pi z}{a}\right)\left[A_{lm}e^{i(\omega_i t - k_{lm}x)} + B_{lm}e^{i(\omega_i t + k_{lm}x)}\right], \tag{2.15}$$

where l and m are integer wave mode numbers in the vertical (y) and horizontal (z) directions, respectively. A_{lm} and B_{lm} are constant amplitudes of the downstream and upstream-travelling waves. The combined wave number, k_{lm}, is then given as [176]:

$$k_{lm} = \sqrt{\frac{\omega_i^2}{\bar{c}^2} - \frac{\pi^2}{a^2}(l^2 + m^2)}. \tag{2.16}$$

If any acoustic wave propagates in the vertical or horizontal direction, the wave number, k_{lm}, must be both real and positive. Based on Eq. 2.16, the angular frequency should then satisfy: $\omega_i > \pi\bar{c}/a \cdot \sqrt{l^2 + m^2}$, which has its minimal value equal to $\pi\bar{c}/a$ only if $l = 1, m = 0$ or $m = 1, l = 0$. In other words, if $\omega_i \leq \pi\bar{c}/a$, only 1-D axial acoustic waves can exist in this 3-D duct. The value of $\omega_{ic} = \pi\bar{c}/a$ is thus known as the "upper frequency limit" for the 1-D wave assumption to be valid in a square duct. For a cylindrical pipe, ω_{ic} is equal to 1.84 $\bar{c}/r$, with r the pipe's cross-sectional radius.

2.3 Flame-Acoustic Interaction in a Constant Area Combustor

Based on the above 1-D acoustic wave modelling, the interaction between an acoustic wave and a flame can now be studied. As shown in Fig. 2.5, a constant area duct has a thin flame inside, which separates the flow field into upstream and downstream zones. The axial extent of the flame region is assumed much shorter than the dominant acoustic wavelengths, known as the "acoustically compact" assumption. For example, for a premixed methane flame in an industrial combustor [24], the entire flame region's axial thickness is less than 0.1 m, while the acoustic wavelengths in the same combustor can be as long as 1 – 5 m [177]. This thin flame region can then be represented by an infinitely thin 1-D "flame sheet" (see Fig. 2.6). The flow conservation equations are then applied across this flame sheet, satisfying [18]:

1. Continuity equation:

$$\rho_1 u_1 = \rho_2 u_2, \tag{2.17a}$$

2. Momentum equation:

$$p_1 + \rho_1 u_1^2 = p_2 + \rho_2 u_2^2, \tag{2.17b}$$

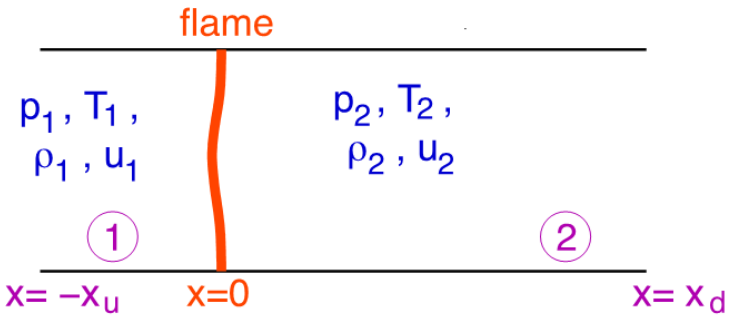


FIGURE 2.5: Constant area duct with an acoustically compact flame located at $x = 0$.

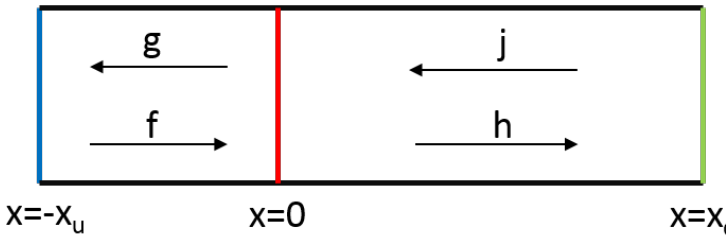


FIGURE 2.6: 1-D acoustic waves separated by a 1-D flame sheet in a constant area duct.

3. Energy equation:

$$\left(c_p T_1 + \frac{1}{2}u_1^2\right)\rho_1 u_1 \mathbb{A} - \left(c_p T_2 + \frac{1}{2}u_2^2\right)\rho_2 u_2 \mathbb{A} = \dot{Q}, \tag{2.17c}$$

with T the temperature, $\mathbb{A}$ the duct's cross-sectional area, $\dot{Q}$ the total heat release rate from the flame, and c_p the specific heat capacity at constant pressure. The subscripts "1" and "2" denote the upstream and downstream zone of the flame, respectively.

In order to model the 1-D plane acoustic waves separated by a 1-D flame sheet, as shown in Fig. 2.6, Dowling [18] derived two "jump conditions" (Eqs. 2.18) based on the above Eqs. 2.17. The ideal gas theory, $p = \rho R_g T$, is applied, with $R_g = c_p - c_v$ the specific gas constant and c_v the specific heat capacity at constant volume. Both jump conditions are independent of ρ_2 and T_2 from the flame-downstream zone:

$$(p_2 - p_1) + \rho_1 u_1 (u_2 - u_1) = 0, \tag{2.18a}$$

$$\frac{\gamma}{\gamma - 1}(p_2 u_2 - p_1 u_1) + \frac{1}{2}\rho_1 u_1 \left(u_2^2 - u_1^2\right) = \dot{Q}/\mathbb{A}, \tag{2.18b}$$

where $\gamma = c_p/c_v$ is the ratio of specific heat capacities. The 1-D wave solutions upstream to the flame (i.e. $-x_u < x < 0$) follow the forms of Eqs. 2.7, with f and g the downstream and

upstream-travelling wave strengths, respectively. At the duct inlet, the two wave strengths are linked to each other via:

$$\mathrm{f}\left(t\right) = R_1 \cdot \mathrm{g}\left(t - \tau_u\right), \tag{2.19}$$

where τ_u is the time delay between the two waves at the inlet. $R_1 = \mathrm{f}/\mathrm{g}$ is called "inlet pressure reflection coefficient", which is the ratio of the reflected wave amplitude (f) to the incident wave amplitude (g) at the inlet. The value of R_1 depends on the acoustic boundary condition. For example, for a choked inlet, $R_1 = (1 - \overline{M}_1)/(1 + \overline{M}_1)$, which is a function of the mean flame-upstream Mach number, $\overline{M}_1$, only [178].

Similarly, the 1-D wave solutions downstream of the flame ($0 < x < x_d$) follow Eqs. 2.7, with the strengths of the upstream and downstream-travelling waves denoted j and h, respectively (see Fig. 2.6). The two wave amplitudes, j and h, satisfy:

$$\mathrm{j}\left(t\right) = R_2 \cdot \mathrm{h}\left(t - \tau_d\right), \tag{2.20}$$

where $R_2 = \mathrm{j}/\mathrm{h}$ is the pressure reflection coefficient at the outlet, being the amplitude ratio of the reflected wave (j) to the incident wave (h). For an open outlet, $R_2 = -1$ [18]. τ_d is the time delay between the two waves at the outlet plane.

By inserting the 1-D wave solutions (Eqs. 2.7) and the boundary wave strength relations (Eqs. 2.19 – 2.20) into the two jump equations, Eqs. 2.18, the flame-upstream wave strength, g, and the flame-downstream wave amplitude, h, can be both linked to the flame heat release rate, $\dot{Q}(t)$, and the same wave strengths at earlier times:

$$\overline{X}\begin{bmatrix} \mathrm{g}(t) \\ \mathrm{h}(t) \end{bmatrix} = \overline{Y}\begin{bmatrix} \mathrm{g}(t-\tau_u) \\ \mathrm{h}(t-\tau_d) \end{bmatrix} + \begin{bmatrix} 0 \\ \left(\dot{Q} - \overline{\dot{Q}}\right)/\left(\mathbb{A}\overline{c}_1\right) \end{bmatrix}, \tag{2.21}$$

where $\overline{X}$ and $\overline{Y}$ are two 2×2 matrices containing the linearised versions of jump conditions, which involve mean flow properties (e.g., $\overline{u}_1$, $\overline{T}_1$, see [18] for more details). Note that Eq. 2.21 only holds at the flame sheet location, $x = 0$.

To solve the above matrix equation, Eq. 2.21, the heat release rate is firstly assumed constant, i.e. $\dot{Q} = \overline{\dot{Q}}$, reducing the above expression into its homogeneous form, Eq. 2.22, which is expressed

in the frequency domain for harmonic waves as:

$$\left(\overline{X} - \overline{Y}\begin{bmatrix} e^{-i\omega_i\tau_u} & 0 \\ 0 & e^{-i\omega_i\tau_d} \end{bmatrix}\right)\begin{bmatrix} \widehat{\mathrm{g}}(\omega_i) \\ \widehat{\mathrm{h}}(\omega_i) \end{bmatrix} = \begin{bmatrix} 0 \\ 0 \end{bmatrix}. \tag{2.22}$$

In order to ensure that Eq. 2.22 always holds for arbitrary wave amplitudes, i.e. $\widehat{\mathrm{g}}$ and $\widehat{\mathrm{h}}$, the determinant of the matrix terms within the round brackets must be constantly zero, which results in the wave mode solutions under a constant heat release rate.

For a turbulent premixed flame typical of gas turbine combustors, however, the flame's heat release rate is usually unsteady (i.e. $\dot{Q}' \neq 0$), which makes Eq. 2.22 inhomogeneous as:

$$\left(\overline{X} - \overline{Y}\begin{bmatrix} e^{-i\omega_i\tau_u} & 0 \\ 0 & e^{-i\omega_i\tau_d} \end{bmatrix}\right)\begin{bmatrix} \widehat{\mathrm{g}}(\omega_i) \\ \widehat{\mathrm{h}}(\omega_i) \end{bmatrix} = \begin{bmatrix} 0 \\ \widehat{\dot{Q}}/(\mathbb{A}\bar{c}_1) \end{bmatrix}. \tag{2.23}$$

In order to solve Eq. 2.23, an additional "flame model" is required, which links the total heat release rate fluctuation, $\dot{Q}'$, to the flame-upstream velocity perturbation, u_1', as shown in Fig. 2.7.

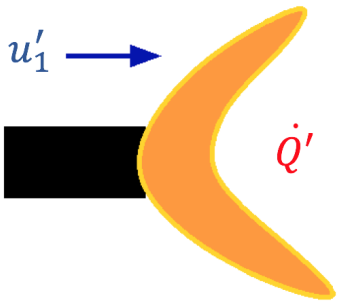


FIGURE 2.7: The flame heat release rate fluctuation, $\dot{Q}'$, responding to an upstream velocity perturbation, u_1'.

For a small velocity perturbation amplitude, e.g., $|u_1'/\overline{u}_1| \leq 10 - 15\%$, the linear flame transfer function (FTF), defined in Eq. 1.7, is usually adequate to capture the flame-to-acoustic responses. A well-known FTF is the "$n - \tau$" flame model, developed by Crocco [57], which can be written in the time domain as:

$$\frac{\dot{Q}'(t)}{\overline{\dot{Q}}} = n_f \frac{u_1'(t - \tau_f)}{\overline{u}_1}, \tag{2.24}$$

where n_f and τ_f are constant FTF gain and time delay between $\dot{Q}'$ and u_1'. Equation 2.24 can also be expressed in the frequency domain as:

$$\frac{\widehat{\dot{Q}}(\omega_i)}{\overline{\dot{Q}}} = n_f e^{-i\omega_i \tau_f} \frac{\widehat{u}_1(\omega_i)}{\overline{u}_1}, \tag{2.25}$$

where the absolute FTF phase, $\omega_i \tau_f$ ($= 2\pi f \tau_f$), linearly increases with the frequency, f.

Since all flames exhibit low-pass behaviour naturally [54], the flame responses to upstream excitations are usually stronger at lower frequencies. In order to better capture the real flame responses, a 1st-order low-pass filter is added to the original "$n - \tau$" model, Eq. 2.25, giving larger FTF gains at low frequencies but smaller gains at higher frequencies [67]:

$$\frac{\widehat{\dot{Q}}(\omega_i)}{\overline{\dot{Q}}} = \frac{\omega_i^c}{\omega_i + \omega_i^c} \cdot n_f e^{-i\omega_i \tau_f} \frac{\widehat{u}_1(\omega_i)}{\overline{u}_1}, \tag{2.26}$$

where $\omega_i^c = 2\pi f_c$ is the filter's "cut-off" angular frequency.

However, for a higher upstream perturbation level (e.g., $|u_1'/\overline{u}_1| > 15\%$), which is common for a realistic combustor, the flame's heat release response to the perturbation may become nonlinear [53], involving the saturation of FTF gain across perturbation amplitudes. In this case, the nonlinear flame describing function (FDF), defined in Eq. 1.8, is more accurate, which can be analytically modelled (e.g., [60]), experimentally measured (see Section 1.3), or numerically simulated (see Section 1.4), etc. In this thesis, the LES simulations of FDFs for realistic combustor flames are performed in Sections 4.4 and 7.4.

2.4 Thermoacoustic Solvers

The above modelled acoustic wave solutions and the flame responses are finally combined into a thermoacoustic solver to predict thermoacoustic instability. Several solvers are possible (see Section 1.2.3), and in this section the two solvers used in this thesis are introduced in detail.

2.4.1 Wave-based low order network solver: OSCILOS

The first solver used is the open-source solver OSCILOS [60, 67], developed based on the "wave-based low order network" approach. It simplifies the complex combustor geometry into a network

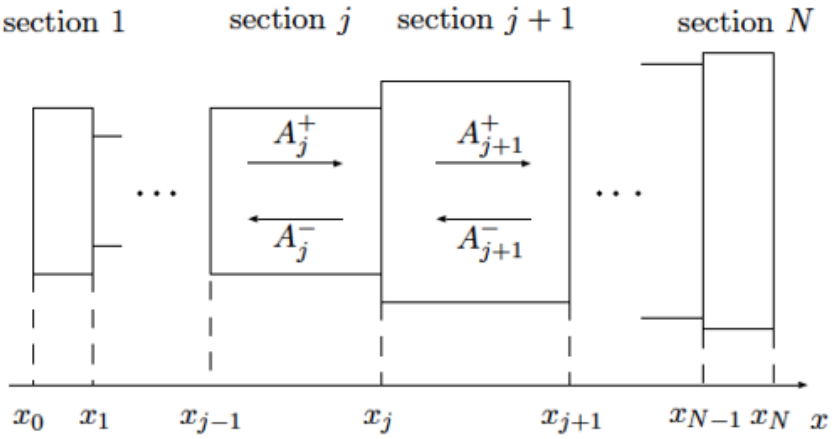


FIGURE 2.8: Network representation of a real combustor: connected constant area modules with constant acoustic wave amplitudes in each module.

of connected constant area modules (or "sections", see Fig. 2.8), with each module referring to a main component of the combustor. The acoustic waves in each module are assumed as 1-D plane waves propagating with constant amplitudes, which only vary across the module interfaces.

Take the j-th network module in Fig. 2.8 as an example: its inlet and outlet locate at $x = x_{j-1}$ and $x = x_j$, respectively, with $j = 1, 2, \ldots, N$ and N the total number of modules. Based on the 1-D acoustic wave solutions, Eqs. 2.8, the fluctuations of flow variables within the j-th module are modelled as:

$$\widehat{p}_j(x) = \widehat{A}_j^+(\omega)e^{-\omega\tau_j^+} + \widehat{A}_j^-(\omega)e^{-\omega\tau_j^-}, \tag{2.27a}$$

$$\widehat{\rho}_j(x) = \frac{\widehat{A}_j^+(\omega)e^{-\omega\tau_j^+} + \widehat{A}_j^-(\omega)e^{-\omega\tau_j^-}}{\overline{c}_j^2} - \frac{\widehat{E}_j(\omega)e^{-\omega\tau_j^s}}{\overline{c}_j^2}, \tag{2.27b}$$

$$\widehat{u}_j(x) = \frac{\widehat{A}_j^+(\omega)e^{-\omega\tau_j^+} - \widehat{A}_j^-(\omega)e^{-\omega\tau_j^-}}{\overline{\rho}_j\overline{c}_j}, \tag{2.27c}$$

with $\widehat{A}_j^+$ and $\widehat{A}_j^-$ the strengths of the downstream and upstream-travelling waves in the j-th module, respectively. Please note $\widehat{E}_j = \overline{\rho}_j\overline{c}_j^2\widehat{s}_j/c_{p,j}$ (with $\widehat{s}_j$ the specific entropy fluctuation) is the strength of the entropy wave, which is generated by the unsteady temperature fluctuations from the flame and always advects downstream. Since the temperature change directly leads to the density variation, an additional term describing the entropy wave's impact on the density is added to Eq. 2.27b. When the flame is absent in a module and has no entropy wave, the density expression, Eq. 2.27b, is reduced to Eq. 2.8b in that module.

The three time delay terms in Eqs. 2.27 are defined as $\tau_j^+ = (x - x_{j-1})/(\overline{c}_j + \overline{u}_j)$, $\tau_j^- = (x_j - x)/(\overline{c}_j - \overline{u}_j)$ and $\tau_j^s = (x - x_{j-1})/\overline{u}_j$, respectively. All the wave strengths and flow

variables remain constant in each module and only vary across the module boundaries. For those modules with a flame sheet inside, Eqs. 2.27 can be inserted into Eq. 2.23 to combine with the flame model, solving the wave modes separated by the flame sheet. By applying the above modelling procedures to all the modules, a global matrix, $\mathcal{G}_{1\to N}(\omega)$, can be established to link the waves from the 1st module ($j = 1$) to those in the last module ($j = N$):

$$\begin{bmatrix} \widehat{A}_N^+(\omega) \\ \widehat{A}_N^-(\omega) \\ \widehat{E}_N(\omega) \end{bmatrix} = \mathcal{G}_{1\to N}(\omega) \cdot \begin{bmatrix} \widehat{A}_1^+(\omega) \\ \widehat{A}_1^-(\omega) \\ \widehat{E}_1(\omega) \end{bmatrix}. \tag{2.28}$$

In order to solve Eq. 2.28, the acoustic boundary conditions at both network inlet and outlet need to be defined, usually in the form of "pressure reflection coefficients", $R = A_r/A_i$, with A_r and A_i the amplitudes of the reflected and incident acoustic waves at the same boundary.

Based on the solutions of matrix Eq. 2.28, the thermoacoustic modes of a network system can be calculated. The OSCILOS solver uses the "shooting method" [68] based on R to perform the calculations. If the incident wave strength at the network inlet is denoted $\widehat{A}_1^-(\omega)$, then the reflected wave strength at the inlet satisfies: $\widehat{A}_1^+(\omega) = R_1(\omega)\widehat{A}_1^-(\omega)\exp(-\omega\tau_1^+)$, with R_1 the reflection coefficient at inlet. By inserting $\widehat{A}_1^-$ and $\widehat{A}_1^+$ into Eq. 2.28, and guessing the growth rate (σ) and frequency (f) of the complex variable, $\omega = \sigma + i2\pi f$, the incident and reflected wave strengths at network outlet, $\widehat{A}_N^+$ and $\widehat{A}_N^-$, can be both estimated. The error between the estimated and the correct values of $\widehat{A}_N^-$ is then called the "outlet boundary error", defined as:

$$\delta_e(\omega) = \widehat{A}_N^-(\omega) - R_2(\omega)\widehat{A}_N^+(\omega)\exp(-\omega\tau_N^+), \tag{2.29}$$

where R_2 is the outlet reflection coefficient. The first term on the RHS is the estimated value of $\widehat{A}_N^-$, with the second term the correct value of $\widehat{A}_N^-$. The combination of the guessed growth rate (σ) and frequency (f) which results in a minimal value of δ_e then determines the location of a thermoacoustic mode. After all the thermoacoustic modes have been calculated, the thermoacoustic stability of the entire network system can be finally predicted. The application of this prediction approach on a realistic gas turbine combustor can be found in Section 5.1.

2.4.2 Helmholtz solver via COMSOL

The second thermoacoustic solver considered is called the "Helmholtz solver" (e.g., [179]), also known as the "H-solver". In this work, the H-solver used is provided by the Finite Element Method (FEM)-based software COMSOL Multiphysics (version 5.3) [69, 180]. Different from the above low order network solver OSCILOS, the H-solver retains the original combustor geometry as the computational domain without any simplification, but neglects the mean flow (i.e. $\overline{u} = 0$). It solves the Helmholtz equation in the frequency domain (see Eq. 2.30), and treats the volumetric heat release rate field, $\widehat{\dot{q}}(\boldsymbol{x})$, as a monopole pressure source [69, 181]:

$$\frac{\Omega^2}{\overline{c}^2(\boldsymbol{x})}\widehat{p}(\boldsymbol{x}) + \overline{\rho}(\boldsymbol{x})\nabla\cdot\left(\frac{1}{\overline{\rho}}\nabla\widehat{p}(\boldsymbol{x})\right) = -\frac{i\Omega\left(\gamma(\boldsymbol{x})-1\right)}{\overline{c}^2}\widehat{\dot{q}}(\boldsymbol{x}), \tag{2.30}$$

where $\Omega = 2\pi f + i\sigma$ is a complex frequency (different from ω). It is noted that Eq. 2.30 does not contain any mean flow effect. The flame models (e.g., FTFs or FDFs) for the heat source can be applied to a particular region in the domain which has a finite volume.

The finite-element discretisation of Eq. 2.30 together with the prescribed boundary conditions then lead to the following eigenvalue equation [51, 179]:

$$2\mathcal{A}\mathbf{P} + \Omega\mathcal{B}(\Omega)\mathbf{P} + \Omega^2\mathcal{C}\mathbf{P} = \mathcal{D}(\Omega)\mathbf{P}, \tag{2.31}$$

where $\mathbf{P}$ denotes the vector of eigenmodes, and matrices $\mathcal{A}$ and $\mathcal{C}$ both contain coefficients originating from the discretisation of Helmholtz equation. $\mathcal{B}(\Omega)$ is the matrix containing boundary conditions, and matrix $\mathcal{D}(\Omega)$ contains the source term from unsteady heat release rate. Equation 2.31 is nonlinear and can be solved using an iterative algorithm (e.g., [51, 52, 182]). For example, at the k-th iteration, Eq. 2.31 is reduced to a linear eigenvalue problem as:

$$\left[\mathcal{A} + \Omega_k^*\mathcal{B}(\Omega_k^*) - \mathcal{D}(\Omega_k^*)\right]\mathbf{P} + \Omega_k^2\mathcal{C}\mathbf{P} = 0, \tag{2.32}$$

where $\Omega_k^* = \Omega_{k-1}$ is the result from the previous $(k-1)$-th iteration. Once the iteration error defined by $\epsilon = |\Omega_k - \Omega_k^*|$ is lower than a specific value, typically 10^{-6}, the real part of Ω then yields the mode frequency, i.e. $f = \mathcal{R}(\Omega)/(2\pi)$, and the imaginary part of Ω corresponds to the mode growth rate, i.e. $\sigma = \mathcal{I}(\Omega)$, which allow the identification of all the thermoacoustic modes. A growth rate of $\sigma > 0$ refers to an unstable mode, while $\sigma < 0$ indicates a stable mode.

2.5 Entropy Wave Transport within a Combustor Flow

Following the brief introduction of entropy wave and entropy noise in Section 1.5, the mathematical description of entropy wave transport in a combustor flow field is now discussed in detail. According to Eqs. 2.27b and 2.28, the entropy wave may play an important role in determining the thermoacoustic modes of a network. The entropy noise generated from entropy wave acceleration may even have the potential to affect the stabilities of these modes (e.g., [146, 154, 160, 161]).

The transport of entropy perturbations can be studied by starting from the equations for a compressible viscous flow without any external forces. The conservation of mass and momentum results in the Navier-Stokes equations [41]:

$$\frac{\mathrm{D}\rho}{\mathrm{D}t} + \rho\frac{\partial u_i}{\partial x_i} = 0, \tag{2.33a}$$

$$\rho\frac{\mathrm{D}u_i}{\mathrm{D}t} = -\frac{\partial p}{\partial x_i} + \frac{\partial \tau_{ij}}{\partial x_j}, \tag{2.33b}$$

with τ_{ij} the viscous stress tensor. The ideal gas law of $p = \rho R_g T$ is applied. The conservation of energy then gives:

$$\rho\frac{\mathrm{D}}{\mathrm{D}t}\left(e + \frac{1}{2}u_i^2\right) = -\frac{\partial(pu_i)}{\partial x_i} + \dot{q} + \frac{\partial}{\partial x_i}\left(k_T\frac{\partial T}{\partial x_i}\right) + \frac{\partial(\tau_{ij}u_i)}{\partial x_j}, \tag{2.34}$$

with $e = c_v T$ the specific internal energy, k_T the thermal conductivity. The specific sensible enthalpy, $h = e + p/\rho$, is then combined with Eqs. 2.33b and 2.34, resulting in the enthalpy conservation equation:

$$\rho\frac{\mathrm{D}h}{\mathrm{D}t} = \frac{\mathrm{D}p}{\mathrm{D}t} + \dot{q} + \frac{\partial}{\partial x_i}\left(k_T\frac{\partial T}{\partial x_i}\right) + \tau_{ij}\frac{\partial u_i}{\partial x_j}. \tag{2.35}$$

Since h also satisfies the thermodynamic relation, $\mathrm{d}h = T\mathrm{d}s + \mathrm{d}p/\rho$, with s the specific entropy, the entropy conservation equation within a fluid flow can be derived as [154]:

$$\rho T\frac{\mathrm{D}s}{\mathrm{D}t} = \dot{q} + \frac{\partial}{\partial x_i}\left(k_T\frac{\partial T}{\partial x_i}\right) + \tau_{ij}\frac{\partial u_i}{\partial x_j}, \tag{2.36}$$

where $\frac{\partial}{\partial x_i}\left(k_T\frac{\partial T}{\partial x_i}\right)$ denotes the thermal gradients which lead to entropy diffusion, while $\tau_{ij}(\partial u_i/\partial x_j)$ is the frictional heating rate that results in the viscous production of entropy. For entropy

transport downstream of the flame region, the heat release rate, $\dot{q}$, is zero; both the thermal conductivity, k_T, and the dynamic viscosity, μ (hidden within τ_{ij}), are assumed constant for simplicity.

For small perturbations, a flow variable can be decomposed into the sum of the mean $\overline{(\cdot)}$ and fluctuating $(\cdot)'$ components. Applying this decomposition to the entropy definition, $s = c_v \ln(p/\rho^\gamma)$, gives: $s' = c_v p'/\overline{p} - c_p \rho'/\overline{\rho}$, which is then combined with the ideal gas relation, $p = \rho R_g T$, and leads to [4]:

$$\breve{s}' = \frac{s'}{c_p} = \frac{T'}{\overline{T}} - \frac{\gamma - 1}{\gamma}\frac{p'}{\overline{p}}, \tag{2.37}$$

where $\breve{s}'$ denotes the non-dimensional entropy fluctuation. The normalised temperature fluctuation, $T'/\overline{T}$, is found an order of magnitude larger than the pressure fluctuation, $p'/\overline{p}$ [4], giving $T' \approx \overline{T} s'/c_p = \overline{T}\breve{s}'$. This relation is then inserted into Eq. 2.36 and performs linearisation, resulting in the linearised governing equation for the normalised entropy perturbation, $\breve{s}'$:

$$\underbrace{\frac{\partial \breve{s}'}{\partial t} + u_i \frac{\partial \breve{s}'}{\partial x_i}}_{A_L} = \underbrace{\frac{k_T}{\rho c_p}\frac{\partial^2 \breve{s}'}{\partial x_i \partial x_i}}_{D_L} + \underbrace{\frac{1}{\rho c_p \overline{T}}\left(\tau'_{ij}\frac{\partial \overline{u}_i}{\partial x_j} + \overline{\tau}_{ij}\frac{\partial u'_i}{\partial x_j}\right)}_{P_L}. \tag{2.38}$$

where on the LHS the linearised entropy advection term is denoted A_L, and on the RHS the linearised thermal diffusion and viscous production terms are denoted D_L and P_L, respectively. It is assumed that the entropy fluctuation ($\breve{s}'$) and its associated temperature and density fluctuations all have negligible effects on the continuity (Eq. 2.33a) and momentum (Eq. 2.33b) equations, commonly known as the Boussinesq approximation. Based on this, the linearised entropy transport equation, Eq. 2.38, can be decoupled from the Navier-Stokes equations and be individually solved.

2.5.1 Entropy wave transport with an entropy source

Since this work does not focus on the detailed mechanism of entropy wave generation from the flame, as relevant studies can be found in [183, 184], etc., an artificial entropy source [161, 185] is instead "injected" at the flame to provide entropy fluctuations. The transport of these fluctuations downstream of the flame is then studied.

In order to introduce entropy fluctuations with a sufficiently high bandwidth to allow their transport behaviour across a wide range of frequencies to be studied, a time-impulsive entropy

source term, $\dot{Q}_S$, is introduced, defined by a sharp Gaussian shape function in time, which approximately mimics a time delta-function. This source is highly localised spatially, occurring only on the mean volumetric heat release rate field, $\overline{\dot{q}}(x,y,z)$, which approximately coincides with the location at which the entropy fluctuation is in practice generated by an appropriate flame. The entropy source term is then defined as:

$$\dot{Q}_S(x,y,z,t) = \frac{\overline{\dot{q}}(x,y,z)}{\iiint_{\mathcal{V}} \overline{\dot{q}}(x,y,z)\,\mathrm{d}\mathcal{V}} \cdot G_S(t), \text{ where } G_S(t) = \frac{1}{\sqrt{\pi}\Delta\tau_1} \exp\left[-\left(\frac{t}{\Delta\tau_1}\right)^2\right], \quad (2.39)$$

where $\overline{\dot{q}}/(\iiint_{\mathcal{V}} \overline{\dot{q}}\,\mathrm{d}\mathcal{V})$ is the normalised mean heat release rate field, determining the mean flame shape for entropy source injection. The temporal evolution of $\dot{Q}_S$ is defined by the Gaussian function, $G_S(t)$, with $\Delta\tau_1$ a small "dispersion time", which results in a highly time-impulsive signal. It is also found that $G_S = \dot{Q}_{\mathcal{V}} = \iiint_{\mathcal{V}} \dot{Q}_S\,\mathrm{d}\mathcal{V}$, with $\dot{Q}_{\mathcal{V}}$ the volume-integrated entropy source term.

Adding the defined entropy source, $\dot{Q}_S$, to the RHS of the above entropy transport equation, Eq. 2.38, gives:

$$\underbrace{\frac{\partial S}{\partial t} + u_i \frac{\partial S}{\partial x_i}}_{A_S} = \underbrace{\frac{k_T}{\rho c_p} \frac{\partial^2 S}{\partial x_i \partial x_i}}_{D_S} + \underbrace{\frac{1}{\rho c_p \overline{T}\mathcal{V}} \left(\tau'_{ij} \frac{\partial \overline{u}_i}{\partial x_j} + \overline{\tau}_{ij} \frac{\partial u'_i}{\partial x_j}\right)}_{P_S} + \dot{Q}_S, \quad (2.40)$$

where $S = \breve{s}'/\mathcal{V}$ denotes the concentration of the normalised entropy fluctuation, $\breve{s}'$. Following Eq. 2.38, the advection, diffusion and production of the entropy concentration, S, are defined as: $A_S = A_L/\mathcal{V}$, $D_S = D_L/\mathcal{V}$ and $P_S = P_L/\mathcal{V}$, respectively. Equation 2.40 is known as the "forced entropy transport equation".

2.5.2 Non-dimensionalisation of entropy transport equation

In order to fully capture the transport of entropy perturbations, the relative importance of each individual term (i.e. A_S, D_S, P_S) in Eq. 2.40 must all be accurately assessed, especially for the thermal diffusion (D_S) and viscous production (P_S) terms. The non-dimensional form of the linearised entropy equation, Eq. 2.38, is thus investigated. The coordinate x, time t, flow speed u, temperature T and shear stress tensor τ_{ij} are all normalised (denoted $\breve{(\cdot)}$) by the characteristic

length L, bulk velocity U, bulk temperature T_b and dynamic viscosity μ of the flow as:

$$\breve{x} = \frac{x}{L}, \quad \breve{t} = \frac{tU}{L}, \quad \breve{u} = \frac{u}{U}, \quad \breve{T} = \frac{T}{T_b}, \quad \breve{\tau}_{ij} = \frac{\tau_{ij} L}{\mu U}. \tag{2.41}$$

The non-dimensional entropy transport equation is then derived as:

$$\frac{\partial \breve{s}'}{\partial \breve{t}} + \breve{u}_i \frac{\partial \breve{s}'}{\partial \breve{x}_i} = \frac{1}{\mathrm{Re}\ \mathrm{Pr}} \frac{\partial^2 \breve{s}'}{\partial \breve{x}_i^2} + \frac{(\gamma - 1) M^2}{\mathrm{Re}\ \breve{T}} \left(\breve{\tau}'_{ij} \frac{\partial \overline{\breve{u}}_i}{\partial \breve{x}_j} + \overline{\breve{\tau}}_{ij} \frac{\partial \breve{u}'_i}{\partial \breve{x}_j} \right), \tag{2.42}$$

where $\mathrm{Re} = \rho U L / \mu$ is the bulk flow Reynolds number, $\mathrm{Pr} = c_p \mu / k_T$ the Prandtl number, and $M = U/c$ the bulk flow Mach number. For a low Mach number ($M << 1$), large Reynolds number ($\mathrm{Re} >> 10,000$) flow, typical of a gas turbine combustor, the diffusion and production terms on the RHS of Eq. 2.42 are both negligible compared to the advection term on the LHS, leading to a purely advective entropy transport equation:

$$\frac{\partial \breve{s}'}{\partial \breve{t}} + \breve{u}_i \frac{\partial \breve{s}'}{\partial \breve{x}_i} = 0. \tag{2.43}$$

Equation 2.43 indicates that any change in the entropy wave strength is primarily caused by the advective dispersion of the velocity field, with diffusion and production of entropy having only minor effects. This assumption has been applied in previous studies (e.g., [154, 186]), and will be validated in this thesis (see Section 6.1 for more details).

2.6 Segmentation of a Very Long Flame

The thermoacoustic prediction performed by the above low order network solver is based on the assumption that the flame is "acoustically compact", and can thus be treated as a thin flame sheet. However, when the flame length is sufficiently long compared to the dominant acoustic wavelengths, this assumption may become invalid. In this case, the spatial variation of the heat release response along the flame length needs to be accounted for, also subsequently for the axial variation in the generated acoustic perturbations. This largely complicates the thermoacoustic prediction process for a low order network solver (e.g., OSCILOS).

One solution for the above challenge is to axially split the long continuous flame into a discrete series of equal-sized "flame segments", as shown in Fig. 2.9. Each flame segment (e.g., $x \in [x_{j,c}, x_{j+1,c}]$) is sufficiently short in the axial direction to be considered as "acoustically compact", and

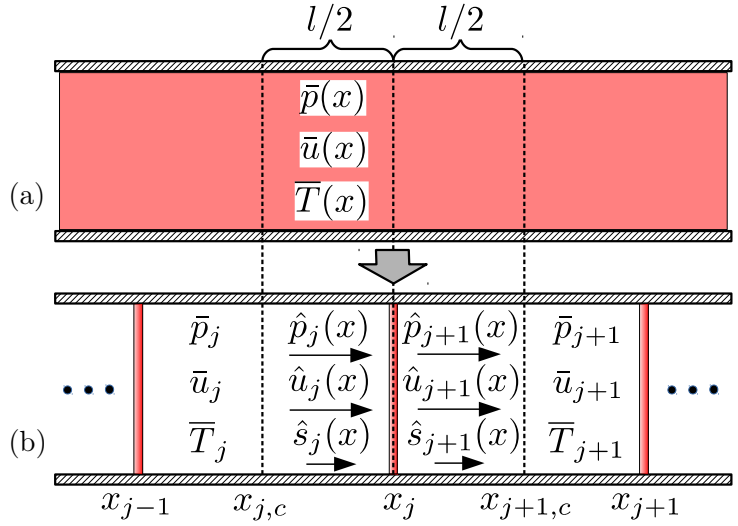


FIGURE 2.9: Sketches of (a) a very long continuous flame and (b) its segmentation as a series of discrete compact flame sheets (figures taken from [5]). The j-th segment ranges between $[x_{j,c},\, x_{j+1,c}]$, with its flame sheet located in the centre (i.e. $x = x_j$).

can thus be represented by an infinitely thin 1-D flame sheet in the network approach [5]. If the axial length of a segment is denoted l, it must satisfy both $l \ll \overline{c}/f$ and $l \ll \overline{u}/f$ in order to ensure that the axial changes in the acoustic wave fluctuation and entropy wave fluctuation are both very small within this segment [45]. The limitation on the value of l can be used as the criterion of the longest segment length or the minimum flame segment number.

This flame segmentation method then allows us to implement a series of compact local flame models for the heat release response in all the segments to an incoming acoustic excitation, and to apply a series of compact acoustic jump conditions for the subsequent effect on the acoustic perturbations (see [5] for more details). Between the neighbouring compact flame sheets, the acoustic perturbations are considered comprised of constant strength waves without any heat release. With the above treatments, the response of a continuous long flame can be modelled by a series of axially-varying discrete local flame models. For example, the heat release rate in the j-th flame segment, $\hat{\dot{Q}}_j$, can be linked to an upstream velocity perturbation, u_1, at a fixed reference location via a local FDF:

$$\mathcal{F}_j(\omega, A_u) = \frac{\hat{\dot{Q}}_j/\overline{\dot{Q}}}{\widehat{u}_1/\overline{u}_1}, \tag{2.44}$$

where $A_u = |\widehat{u}_1/\overline{u}_1|$ is the normalised perturbation amplitude, and $\overline{\dot{Q}} = \sum_{j=1}^{N_{\text{seg}}} \overline{\dot{Q}}_j$ is the total mean heat release rate from the entire flame (with N_{seg} the total segment number). Substituting the above local discrete FDFs for all the segments into the acoustic jump conditions, and

combining with the transfer matrices for the wave propagation (e.g., Eq. 2.28) and boundary conditions, the governing equation for the long flame system can be established (refer to [5] for more details). The complex frequency, ω, calculated when the determinant of the governing matrix, $\mathbf{D}$, satisfies $\det(\mathbf{D}) = 0$, yields the frequency (f) and growth rate (σ) of all the thermoacoustic modes. The thermoacoustic stability of the network is then determined by the sign of the mode growth rate, with a positive value corresponding to an unstable mode.

2.7 Summary

In this chapter, the acoustic wave motion in a constant area duct is modelled analytically, with the governing equations for these waves derived. Their interaction with an acoustically compact flame is then described using a flame model, which is combined with the modelled acoustic waves in a low order network solver or a Helmholtz solver to predict the system's thermoacoustic instability. The equation governing entropy wave transport in a combustor flow is derived, with entropy wave advection, viscous production and thermal diffusion terms all present. It is followed by the introduction of the segmentation method for a very long non-compact flame, whose response to upstream acoustic perturbation is represented by a discrete series of local flame models. The flame and acoustic modelling parts are mainly based on the existing analytical approaches, while the entropy wave transport and long flame response studies are mainly the author's original work.

In the next chapter, the numerical methodology used in this thesis is briefly explained, including the principle of incompressible LES, the sub-grid scale turbulence and combustion models used, and the simulation method for the entropy wave transport, etc.

Chapter 3

Numerical Methodology

Following the analytical acoustic wave modelling introduced in Chapter 2, the flame response model to an upstream acoustic perturbation is now required, which is numerically computed in this thesis by using the incompressible large eddy simulations (LES). In this chapter, the principle of the incompressible LES is firstly introduced, followed by the comparisons of the used sub-grid scale turbulence and combustion models, and the applied chemical reaction schemes. The numerical methods for the entropy wave transport simulation are also briefly explained. The main contents of this chapter are based on the literature and the existing numerical models.

3.1 Mathematical Formulation of Incompressible LES

The filtered conservation equations of mass, momentum, species mass fractions and enthalpy solved by the incompressible LES are recalled as [162]:

$$\begin{cases} \dfrac{\partial \bar{\rho}}{\partial t} + \dfrac{\partial \bar{\rho}\widetilde{u}_i}{\partial x_i} = 0, & \text{(3.1a)} \\ \dfrac{\partial \bar{\rho}\widetilde{u}_i}{\partial t} + \dfrac{\partial \bar{\rho}\widetilde{u}_i\widetilde{u}_j}{\partial x_j} = -\dfrac{\partial \bar{p}}{\partial x_i} + \dfrac{\partial}{\partial x_j}\left(\bar{\mu}\left[\dfrac{\partial \bar{u}_i}{\partial x_j} + \dfrac{\partial \bar{u}_j}{\partial x_i}\right]\right) - \dfrac{\partial \tau_{ij}}{\partial x_j}, & \text{(3.1b)} \\ \dfrac{\partial \bar{\rho}\widetilde{Y}_\alpha}{\partial t} + \dfrac{\partial \bar{\rho}\widetilde{u}_i\widetilde{Y}_\alpha}{\partial x_i} = \dfrac{\partial}{\partial x_i}\left(\dfrac{\bar{\mu}}{\sigma_m}\dfrac{\partial \bar{Y}_\alpha}{\partial x_i}\right) - \dfrac{\partial J_{\alpha,i}}{\partial x_i} + \bar{\rho}\widetilde{\dot{\omega}}_\alpha, & \text{(3.1c)} \\ \dfrac{\partial \bar{\rho}\widetilde{h}_e}{\partial t} + \dfrac{\partial \bar{\rho}\widetilde{u}_i\widetilde{h}_e}{\partial x_i} = \dfrac{\partial}{\partial x_i}\left(\dfrac{\bar{\mu}}{\sigma_m}\dfrac{\partial \bar{h}_e}{\partial x_i}\right) - \dfrac{\partial J_{h_e,i}}{\partial x_i}, & \text{(3.1d)} \end{cases}$$

where h_e is the enthalpy including the enthalpy of formation, which is different from the sensible enthalpy (h) mentioned in Eq. 2.35. σ_m is the Prandtl (denoted Pr) or Schmidt (denoted Sc) number as appropriate, with the latter defined as $\mathrm{Sc} = \mu/(\rho D)$ (with D the mass diffusivity) and often assumed the same for all the involved species. The Lewis number, $\mathrm{Le} = \mathrm{Sc}/\mathrm{Pr}$, is assumed unity, so that the Prandtl and Schmidt numbers are always equal. The ideal gas equation is used as the equation of state, applied together with the Fourier heat conduction and Fickian diffusion approximations. Since the pressure fluctuation, p', is much smaller than the operating mean pressure, $\overline{p}$, the incompressible LES neglects the compressibility effect of the pressure variation, i.e. $(\partial\rho/\partial p)_T = 0$, implying that the mixture density, ρ, is a function of the temperature, T, and species mass fractions, Y_α (with $\alpha = [1, \cdots, N_{sp}]$ and N_{sp} the total number of species) only, satisfying $\rho = \rho(T, Y_\alpha) = p_0 W_g/(R_u T)$, with p_0 the operating pressure constant in time and space, W_g the molar mass of the mixture and $R_u = 8.314$ J/(mol·K) the universal gas constant. The temperature and heat release rates are computed as a function of enthalpy and composition using JANAF data [187]. $\tau_{ij} = \bar{\rho}\,(\widetilde{u_i u_j} - \widetilde{u}_i\widetilde{u}_j)$ is the SGS stress tensor, and $\widetilde{\dot{\omega}}_\alpha = \widetilde{\dot{\omega}}(Y_\alpha)$ is the filtered chemical reaction rate for the α-th species. Symbol $\bar{(\cdot)}$ denotes an LES-filtered variable, defined as:

$$\bar{\phi}(\boldsymbol{x}, t) = \iiint_{\mathcal{V}} G_f(\boldsymbol{x} - \boldsymbol{x}'; \Delta(\boldsymbol{x}))\phi(\boldsymbol{x}', t)\mathrm{d}\boldsymbol{x}', \tag{3.2}$$

where $\phi(\boldsymbol{x}, t)$ is an arbitrary variable at location $\boldsymbol{x} = (x, y, z)$ and time t. G_f is the LES-filter function with a width of $\Delta = (\Delta_x\Delta_y\Delta_z)^{1/3}$, with Δ_x, Δ_y and Δ_z the local mesh cell sizes in x, y and z directions, respectively. The function of G_f is thus defined as [173]:

$$\begin{aligned} G_f(\boldsymbol{x} - \boldsymbol{x}', \Delta(\boldsymbol{x})) &= \frac{1}{\Delta^3}; \quad -\Delta/2 \le \boldsymbol{x} - \boldsymbol{x}' \le \Delta/2 \\ &= 0; \quad \text{otherwise} \end{aligned} \tag{3.3}$$

In order to avoid additional density correlation due to the large density fluctuations in a high temperature reaction zone, a "density-weighted Favre filtering" method is applied for some variables in Eqs. 3.1 as:

$$\widetilde{\phi}(\boldsymbol{x}, t) = \overline{\rho\phi}/\bar{\rho}, \tag{3.4}$$

where symbol $\widetilde{(\cdot)}$ denotes a Favre filtered variable. Equations 3.1c and 3.1d are the "scalar transport equations", with $J_{\alpha,i}$ and $J_{h_e,i}$ the SGS scalar fluxes of the α-th species's mass fraction,

Y_α, and the enthalpy, h_e, respectively [188]:

$$J_{\alpha,i} = -\frac{\mu_{\text{sgs}}}{\sigma_{\text{sgs}}}\frac{\partial \widetilde{Y}_\alpha}{\partial x_i}, \quad J_{h_e,i} = -\frac{\mu_{\text{sgs}}}{\sigma_{\text{sgs}}}\frac{\partial \widetilde{h}_e}{\partial x_i}, \tag{3.5}$$

with μ_{sgs} the turbulent eddy viscosity and σ_{sgs} the turbulent Schmidt or Prandtl number.

In order to close the above system of LES equations, i.e. Eqs. 3.1, models for the SGS stress, τ_{ij}, and the filtered reaction rate, $\widetilde{\dot{\omega}}_\alpha$, are both needed, which require the SGS turbulence and the turbulence-chemistry interaction to be taken into account, respectively. Differences in how these two variables are modelled and in the complexity of the chemical scheme used are known to lead to differences in the unforced structure of an LES-simulated premixed propane/air flame [126].

3.2 Sub-Grid Scale Turbulence Modelling

The modelling of the SGS stress tensor, τ_{ij}, requires an appropriate SGS turbulence model, which can correctly predict the cascade characters of the turbulence and energy dissipation at small length-scales. In this thesis, four SGS turbulence models have been used, which are: (*i*) the constant Smagorinsky model [8]; (*ii*) the dynamic Smagorinsky model [9]; (*iii*) the Wall-Adapting Local Eddy-viscosity (WALE) model [10]; and (*iv*) the one-equation turbulent kinetic energy model [11–13]. A detailed comparison between these models is performed in this section, and their effects on the LES flow simulations can be found in [189] for a non-reactive axisymmetric bluff body flow and in Section 4.3.1 for a swirling reacting flow.

3.2.1 Constant Smagorinsky model

The constant Smagorinsky model [8], also known as the Smagorinsky-Lilly model, models the anisotropic SGS stress tensor as:

$$\tau_{ij}^a = -2\mu_{\text{sgs}}\left(\widetilde{S}_{ij} - \frac{\delta_{ij}}{3}\widetilde{S}_{kk}\right), \tag{3.6}$$

where the superscript "a" denotes the anisotropic components. The isotropic part of the stress tensor, τ_{kk}, can be absorbed into the filtered pressure in the momentum equation, Eq. 3.1b, as: $p^* = \bar{p} + \frac{1}{3}\tau_{kk}$, with p^* the pressure after absorption. δ_{ij} is the Kronecker delta, with $\delta_{ij} = 1$ for

$i = j$ and otherwise zero. $\widetilde{S}_{ij}$ is the filtered strain tensor, defined as:

$$\widetilde{S}_{ij} = \frac{1}{2}\left(\frac{\partial \widetilde{u}_j}{\partial x_i} + \frac{\partial \widetilde{u}_i}{\partial x_j}\right), \tag{3.7}$$

with $\widetilde{S}_{kk}$ the isotropic part of $\widetilde{S}_{ij}$. The turbulent eddy viscosity, μ_{sgs}, is now modelled as:

$$\mu_{\text{sgs}} = \bar{\rho}\left(C_s\Delta\right)^2 \left|\left|\widetilde{S}_{ij}\right|\right|, \tag{3.8}$$

with C_s a model constant. The higher C_s is, the larger the damping on the resolved turbulence will be. In this work, C_s is set as 0.167 [190], suitable for the flow configurations analysed. The LES-filter width, Δ, is the cubic root of the local mesh cell sizes, same as that in Eq. 3.3. $\left|\left|\widetilde{S}_{ij}\right|\right|$ is the Frobenius form of the resolved strain rate tensor, defined as:

$$\left|\left|\widetilde{S}_{ij}\right|\right| = \sqrt{2\widetilde{S}_{ij}\widetilde{S}_{ij}}. \tag{3.9}$$

3.2.2 Dynamic Smagorinsky model

For a high Reynolds number flow in a complex geometry, the Smagorinsky model constant, C_s, defined in Eq. 3.8 needs to vary with position throughout the flow field. The value of C_s also needs to reduce to zero in a laminar flow. Germano et al. [191, 192] thus developed a dynamic model to determine the correct C_s value automatically over the entire flow domain, by assuming that C_s is a function of space and time and calculated in terms of the resolved scales. This function is based on an assumption that the information in the resolved scales can be used to model the sub-grid scale variables.

In order to achieve this, a test filter, denoted $\widehat{(\cdot)}$, is defined in the resolved scale, which is larger than the LES filter size, Δ. Flow variables in the largest sub-grid scale are now assumed to behave in the same way as those at the test filter size, $\widehat{\Delta}$, and the value of C_s is assumed not affected by any scale size. The resolved turbulent stress tensor, L_{ij}, known as the "Germano identity", is defined as:

$$L_{ij} = T_{ij} - \widehat{\tau}_{ij}, \tag{3.10}$$

where T_{ij} is the SGS stress tensor in the test filter's scale, $\widehat{\Delta}$, defined as:

$$T_{ij} = \widehat{\bar{\rho}}\left(\widehat{\widetilde{u_i}\widetilde{u_j}} - \widehat{\widetilde{u}}_i\widehat{\widetilde{u}}_j\right), \tag{3.11}$$

with the anisotropic part of T_{ij} satisfying:

$$T_{ij}^{a} = -2\widehat{\bar{\rho}}\left(C_s\widehat{\Delta}\right)^2 \widehat{\widetilde{S}}_{ij}\sqrt{2\widehat{\widetilde{S}}_{ij}\widehat{\widetilde{S}}_{ij}}, \tag{3.12}$$

where the strain tensor, $\widehat{\widetilde{S}}_{ij}$, is defined as:

$$\widehat{\widetilde{S}}_{ij} = \frac{1}{2}\left(\frac{\partial\widehat{\widetilde{u}}_j}{\partial x_i} + \frac{\partial\widehat{\widetilde{u}}_i}{\partial x_j}\right). \tag{3.13}$$

The test-filtered SGS stress tensor, $\widehat{\tau}_{ij}$, in the original filter scale, Δ, is given as:

$$\widehat{\tau}_{ij} = \widehat{\bar{\rho}}\left(\widehat{\widetilde{u_i}\widetilde{u_j}} - \widehat{\widetilde{u}_i}\widehat{\widetilde{u}_j}\right), \tag{3.14}$$

with the anisotropic part of τ_{ij} satisfying Eq. 3.6. Equation 3.10 should hold at all time instants and spatial locations, but it may become ill-conditioned as this formulation leads to an over-determined system. This problem can be solved by using the least-squares error method (see [193] for more details). The varying model coefficient, $C_s(\boldsymbol{x}, t)$, can now be modelled as [9, 103]:

$$(C_s\Delta)^2 = -\frac{\left[L_{ij}^{a} - 2\bar{\rho}C_s^{*}\widehat{\left|\left|\widetilde{S}_{ij}\right|\right|\widetilde{S}_{ij}^{a}}\right]\widehat{\widetilde{S}}_{ij}}{2\widehat{\bar{\rho}}\left|\left|\widehat{\widetilde{S}}_{ij}\right|\right|\widehat{\left|\left|\widetilde{S}_{ij}^{a}\right|\right|}\,\widehat{\widetilde{S}}_{ij}^{a}}, \tag{3.15}$$

where L_{ij}^{a} is the anisotropic part of the Germano identity, and C_s^{*} is the value of C_s computed at earlier time-steps. The modelled C_s function is independent of the filter's width (e.g., Δ or $\widehat{\Delta}$). In this work, the magnitude of C_s is clipped between 0 and 0.15 to avoid numerical instability, suggested by previous LES studies on turbulent flows (e.g., [194, 195]).

3.2.3 WALE model

The third SGS turbulence model studied is the Wall-Adapting Local Eddy-viscosity (WALE) model [10], which was originally defined to capture the near-wall behaviour for confined flows in complex geometries. The eddy viscosity, μ_{sgs}, is now modelled as:

$$\mu_{\text{sgs}} = \bar{\rho}\left(C_\omega\Delta\right)^2 \frac{\left(S_{ij}^{d}S_{ij}^{d}\right)^{3/2}}{\left(\widetilde{S}_{ij}\widetilde{S}_{ij}\right)^{5/2} + \left(S_{ij}^{d}S_{ij}^{d}\right)^{5/4}}, \tag{3.16}$$

where C_ω is a constant and set as 0.325 in this thesis. S_{ij}^d denotes the traceless symmetric part of g_{ij}^2, with $g_{ij} = \partial u_i/\partial x_j$ the velocity gradient tensor. S_{ij}^d satisfies:

$$S_{ij}^d = \frac{1}{2}\left(\widetilde{g}_{ij}^2 + \widetilde{g}_{ji}^2\right) - \frac{1}{3}\delta_{ij}\widetilde{g}_{kk}^2. \tag{3.17}$$

3.2.4 One-equation turbulent kinetic energy model

The last turbulence model used [11–13] is based on the SGS turbulent kinetic energy, k_{sgs}, defined as:

$$k_{\text{sgs}} = \frac{1}{2}\left(\widetilde{u_i^2} - \widetilde{u}_i^2\right). \tag{3.18}$$

A transport equation is then established for k_{sgs} as:

$$\frac{\partial k_{\text{sgs}}}{\partial t} + \frac{\partial(\widetilde{u}_j k_{\text{sgs}})}{\partial x_j} = \frac{\partial}{\partial x_j}\left(\frac{\mu_{\text{sgs}}}{\bar{\rho}\sigma_k}\frac{\partial k_{\text{sgs}}}{\partial x_j}\right) - \frac{\tau_{ij}}{\bar{\rho}}\frac{\partial \widetilde{u}_i}{\partial x_j} - C_\epsilon\frac{k_{\text{sgs}}^{3/2}}{\Delta}, \tag{3.19}$$

where the last term on the RHS represents the SGS dissipation rate. σ_k and C_ϵ are two constants and set as 1.0 and 1.048 [190], respectively. The SGS stress tensor, τ_{ij}, is now modelled as:

$$\tau_{ij} = -2\mu_{\text{sgs}}\widetilde{S}_{ij} + \frac{2}{3}\bar{\rho}k_{\text{sgs}}\delta_{ij}, \tag{3.20}$$

where the SGS eddy viscosity, $\mu_{\text{sgs}} = \bar{\rho}C_k k_{\text{sgs}}^{1/2}\Delta$, with constant $C_k = 0.094$ [190] in this thesis, calculated based on $C_s = 0.167$ used in the constant Smagorinsky model. It should be noted that when using this turbulence model, the initial value of k_{sgs} at time $t = 0$ should always be positive (i.e. $k_{\text{sgs}}|_{t=0} > 0$).

3.3 Sub-Grid Scale Combustion Modelling

In order to model the filtered chemical reaction rate, $\widetilde{\dot{\omega}}_\alpha$, an accurate SGS combustion model is needed, which describes the interaction between the turbulence and the chemical reactions. Two SGS combustion models are used in this thesis, which are: (*i*) the Probability Density Function (PDF)-based Eulerian stochastic field model [172, 196, 197], known as "LES-PDF"; (*ii*) the Partially Stirred Reactor (PaSR) model [198, 199], known as "LES-PaSR". Both models have been employed by many LES solvers to simulate different combustors, such as [173, 200] with the LES-PDF model and [119, 201] with the LES-PaSR model, etc.

3.3.1 PDF-based Eulerian stochastic field model

For the LES-PDF combustion model, Eqs. 3.1c and 3.1d are not solved directly, instead the scalar probability density function (PDF) is applied to model the filtered flow variables. The fine-scale PDF (denoted P_α) for an arbitrary scalar variable, $\phi_\alpha(\boldsymbol{x}, t)$, is defined as:

$$P_\alpha = \delta\left(\psi_\alpha - \phi_\alpha\right), \tag{3.21}$$

where ψ_α is the sample (composition) space of the scalar. δ is the Dirac delta function. Based on Eq. 3.21, the joint sub-grid scale PDF (denoted P_{sgs}) for the global composition, $\psi_g = [\psi_1, \psi_2, \ldots, \psi_{N_s}]$, of all the relevant scalar variables is defined as [202, 203]:

$$P_{\text{sgs}}(\psi_g; \boldsymbol{x}, t) = \prod_{\alpha=1}^{N_s} P_\alpha = \prod_{\alpha=1}^{N_s} \delta\left[\psi_\alpha - \phi_\alpha(\boldsymbol{x}, t)\right], \tag{3.22}$$

where $N_s = N_{sp} + 1$ denotes the total number of relevant scalars, i.e. N_{sp} species plus the enthalpy, h_e. Applying the density-weighted filtering on P_{sgs} gives:

$$\widetilde{P}_{\text{sgs}}(\psi_g; \boldsymbol{x}, t) = \frac{1}{\bar{\rho}} \int_{\mathcal{V}} \rho(\boldsymbol{x}') P_{\text{sgs}}(\psi_g; \boldsymbol{x}', t) G_f(\boldsymbol{x} - \boldsymbol{x}', \Delta) \mathrm{d}\boldsymbol{x}'. \tag{3.23}$$

The modelled transport equation for the Favre filtered joint scalar PDF, $\widetilde{P}_{\text{sgs}}$, is then constructed as [173, 204]:

$$\begin{aligned} &\bar{\rho}\frac{\partial \widetilde{P}_{\text{sgs}}\left(\psi_g\right)}{\partial t} + \bar{\rho}\widetilde{u}_i \frac{\partial \widetilde{P}_{\text{sgs}}\left(\psi_g\right)}{\partial x_i} + \underbrace{\sum_{\alpha=1}^{N_s} \frac{\partial}{\partial \psi_\alpha}\left[\bar{\rho}\dot{\omega}_\alpha\left(\psi_g\right)\widetilde{P}_{\text{sgs}}\left(\psi_g\right)\right]}_{\text{Closed chemical reaction term}} = \\ &\underbrace{\frac{\partial}{\partial x_i}\left[\left(\frac{\mu}{\sigma_m} + \frac{\mu_{\text{sgs}}}{\sigma_{\text{sgs}}}\right)\frac{\partial \widetilde{P}_{\text{sgs}}\left(\psi_g\right)}{\partial x_i}\right]}_{\text{SGS convection term}} - \underbrace{\frac{\bar{\rho}C_d}{2\tau_{\text{sgs}}}\sum_{\alpha=1}^{N_s}\frac{\partial}{\partial \psi_\alpha}\left[\left(\psi_\alpha - \phi_\alpha(\boldsymbol{x}, t)\right)\widetilde{P}_{\text{sgs}}\left(\psi_g\right)\right]}_{\text{LMSE closure}}, \end{aligned} \tag{3.24}$$

where σ_{sgs} and C_d are both constants and set as 1.0 and 2.0, respectively. τ_{sgs} is the SGS micro-mixing time scale, defined as:

$$\tau_{\text{sgs}} = \frac{\bar{\rho}\Delta^2}{C_d(\mu + \mu_{sgs})}. \tag{3.25}$$

The filtered chemical reaction rate, $\widetilde{\dot{\omega}}_\alpha$, now appears in the closed form, $\dot{\omega}_\alpha\left(\psi_g\right)$, on the LHS of Eq. 3.24. Any modelling beyond the specification of a chemical reaction scheme is not needed.

The two terms on the RHS of Eq. 3.24 represent the sub-grid scale convection and mixing of the joint PDF, respectively [103]. The convection term can be approximated by a gradient model analogous to the constant Smagorinsky turbulence model [8], whilst the SGS mixing term is expressed in the form of Linear Mean Square Estimation (LMSE) closure [205], where a property's rate of change is assumed proportional to the "distance" from its mean value.

Equation 3.24 is then solved using the Eulerian stochastic field method [172, 196], where the filtered joint-PDF, $\widetilde{P}_{\text{sgs}}$, is represented as an ensemble of N_f stochastic fields, each comprising N_s scalars, namely $\xi^n_\alpha(\boldsymbol{x},t) = \left[\xi^n_1,\ldots,\xi^n_{N_s}\right]$, with $1 \leq \alpha \leq N_s$ and $1 \leq n \leq N_f$ over the entire flow domain. These stochastic fields are not real flow fields, and thus have no direct physical significance; instead they represent an equivalent stochastic system that has the same one-point PDF as that given by Eq. 3.24 [206].

With these stochastic fields, the joint scalar PDF, P_{sgs}, defined in Eq. 3.22 can be reconstructed as:

$$P_{\text{sgs}}(\psi_g;\boldsymbol{x},t) = \frac{1}{N_f}\sum_{n=1}^{N_f}\prod_{\alpha=1}^{N_s}\delta\left[\psi_\alpha - \xi^n_\alpha(\boldsymbol{x},t)\right]. \tag{3.26}$$

Based on Eq. 3.26, the filtered joint-PDF transport equation, Eq. 3.24, can be rewritten using the Ito formulation [207], which advances $\xi^n_\alpha(\boldsymbol{x},t)$ from time t to $t+\mathrm{d}t$ as:

$$\bar{\rho}\mathrm{d}\xi^n_\alpha + \bar{\rho}\widetilde{u}_i\frac{\partial\xi^n_\alpha}{\partial x_i}\mathrm{d}t = \frac{\partial}{\partial x_i}\left[\left(\frac{\mu}{\sigma_m}+\frac{\mu_{\text{sgs}}}{\sigma_{\text{sgs}}}\right)\frac{\partial\xi^n_\alpha}{\partial x_i}\right]\mathrm{d}t + \sqrt{2\bar{\rho}\frac{\mu_{\text{sgs}}}{\sigma_{\text{sgs}}}}\frac{\partial\xi^n_\alpha}{\partial x_i}\mathrm{d}W^n_i - \frac{\bar{\rho}C_d}{2\tau_{\text{sgs}}}\left(\xi^n_\alpha - \widetilde{\phi}_\alpha\right)\mathrm{d}t + \bar{\rho}\dot{\omega}^n_\alpha\left(\xi^n_g\right)\mathrm{d}t, \tag{3.27}$$

where $\mathrm{d}W^n_i$ denotes an increment of a vector Wiener process, which is continuous in both time and space and also differentiable in space. The value of $\mathrm{d}W^n_i$ is different for each stochastic field, and is independent of the spatial location, $\boldsymbol{x}$. In this work, $\mathrm{d}W^n_i$ is approximated by the time-step increments, $\eta^n_i\sqrt{\mathrm{d}t}$, with η^n_i a $\{-1,1\}$ dichotomic random variable. ξ^n_g denotes the entire ensemble of stochastic fields for the global composition, ψ_g, of all the involved scalars.

The moments of an arbitrary Favre-filtered scalar, $\widetilde{\phi}_\alpha$, can thus be obtained by averaging over all the corresponding stochastic fields as:

$$\widetilde{\phi}_\alpha = \frac{1}{N_f}\sum_{n=1}^{N_f}\xi^n_\alpha. \tag{3.28}$$

In order to accurately represent a PDF at a time instant, a sufficiently large number of stochastic fields may be needed for each scalar variable. However, if only the statistical or mean flow fields

are of interest, the needed number of stochastic fields may be much smaller.

3.3.2 Partially stirred reactor model

Different from the above stochastic PDF model, the partially stirred reactor (PaSR) combustion model focuses on the reaction processes in each mesh cell. The reacting flow in a mesh cell is divided into two parts: (i) a "perfectly-stirred reactor", where all the species are assumed homogeneously mixed and reacting; (ii) the "surroundings", filling with non-reacting sub-grid scale flow structures. The burnt products from part (i) are mixed with the surrounding flow due to turbulence — this correspondingly takes place during the turbulent mixing time, τ_m. This results in the final species concentrations in the entire, partially-stirred, computational cell [68]. In any cell the reaction only occurs within domain (i).

The relative proportions of these two flow parts in each cell are controlled by the "reactive volume fraction", κ [208], as:

$$Y_\alpha = (1-\kappa)Y_\alpha^N + \kappa Y_\alpha^R, \tag{3.29}$$

where the superscripts R and N denote the reacting and non-reacting part, respectively. The filtered chemical reaction rate for the α-th species, $\widetilde{\dot{\omega}}_\alpha$, can then be scaled by κ and modelled as [68, 208]:

$$\widetilde{\dot{\omega}}_\alpha \simeq \frac{C_1^\alpha - C_0^\alpha}{\Delta t} = \kappa \cdot \dot{\omega}_\alpha \left(\bar{\rho}, \widetilde{T}, \widetilde{Y}_\beta, C_1^\alpha\right), \quad \text{with} \quad \beta = 1, 2, \ldots, N_{sp} \tag{3.30}$$

where C_1^α is the spatially averaged concentration for the α-th species that is leaving the cell, while C_0^α is the initial concentration of the same species inside the cell. Δt denotes the computational time step, and $\dot{\omega}_\alpha$ is the unfiltered "laminar" Arrhenius reaction rate of the α-th species. The modelling of $\widetilde{\dot{\omega}}_\alpha$ is now reduced to the modelling of κ, which is governed by the chemical reaction time, τ_c, and the turbulent mixing time, τ_m [68]:

$$\kappa = \frac{\tau_c}{\tau_c + \tau_m}. \tag{3.31}$$

The chemical reaction time, τ_c, is approximated [199] by ν/S_u^2, with ν the molecular kinematic viscosity and S_u the (unstretched) laminar burning velocity. In order to determine the correct value of S_u, an accurate chemical reaction scheme is required. Since the accuracy of a reaction scheme is expected to increase with the number of its reaction steps, in this thesis two chemical

TABLE 3.1: The simple 4-step chemical reaction scheme for methane [16].

Reaction step	Reaction
R1	$CH_4 + \frac{1}{2}O_2 \Longrightarrow CO + 2H_2$
R2	$H_2 + \frac{1}{2}O_2 \Longrightarrow H_2O$
R3	$CO + \frac{1}{2}O_2 \Longrightarrow CO_2$
R4	$CO + H_2O \Longleftrightarrow CO_2 + H_2$

TABLE 3.2: The systematically reduced 15-step reaction scheme for methane [17].

Reaction step	Reaction
R1	$2H + 2OH \Longleftrightarrow 2H_2 + O_2$
R2	$2H \Longleftrightarrow H_2$
R3	$H + HO_2 \Longleftrightarrow H_2 + O_2$
R4	$H + H_2O_2 \Longleftrightarrow H_2 + HO_2$
R5	$OH + CH_3 \Longleftrightarrow H_2 + CH_2O$
R6	$H + CH_4 \Longleftrightarrow H_2 + CH_3$
R7	$H + OH + CO \Longleftrightarrow H_2 + CO_2$
R8	$CH_2O \Longleftrightarrow H_2 + CO$
R9	$O_2 + C_2H_2 \Longleftrightarrow H_2 + 2CO$
R10	$OH + C_2H_4 \Longleftrightarrow H_2 + CH_3 + CO$
R11	$C_2H_6 \Longleftrightarrow H_2 + C_2H_4$
R12	$H + OH \Longleftrightarrow H_2O$
R13	$2NO \Longleftrightarrow O_2 + N_2$
R14	$H_2 + CO + NO \Longleftrightarrow H + O_2 + HCN$
R15	$3H + H_2O + NH_3 \Longleftrightarrow 4H_2 + NO$

schemes characterised by different complexity levels are chosen for methane/air reaction: (*i*) a simple 4-step scheme with 7 intermediate species [16]; (*ii*) a systematically reduced 15-step scheme with 19 intermediate species [17]. These two schemes are used with both the PDF and PaSR combustion models, and have been applied to simulate the turbulent reacting flow in an industrial gas turbine combustor (e.g., [16, 135] for the 4-step scheme and [14] with the 15-step reaction), which is the same combustor as that studied in Chapters 4 – 6. The detailed reaction steps involved in the two schemes are listed in Tables 3.1 and 3.2, respectively. The effects of these two schemes on the unforced flame LES and forced flame responses will be studied in Chapter 4 in detail.

In order to compute the value of turbulent mixing time, τ_m, a newly-developed mixing model [119, 199, 209] is applied in this thesis:

$$\tau_m = C_m \sqrt{\tau_{\text{sgs}} \cdot \tau_K}, \tag{3.32}$$

where $\tau_{\text{sgs}} = \Delta / u'_{\text{sgs}} = \Delta / \sqrt{2k_{\text{sgs}}/3}$ denotes the SGS micro-mixing time, with u'_{sgs} the SGS velocity fluctuation and k_{sgs} the SGS turbulent kinetic energy [119]. Please note that in PaSR model the definition of τ_{sgs} is different from that used by the PDF model (see Eq. 3.25). $\tau_K = \sqrt{\nu/\epsilon_{\text{sgs}}}$ is the Kolmogorov time, with ϵ_{sgs} the SGS dissipation rate. The mixing time constant, C_m, is determined by the relative strengths of turbulence and chemical reactions. The computed time scales of τ_c and τ_m are then used to calculate the reactive volume fraction, κ, in Eq. 3.31, which is finally used to model the filtered chemical reaction rate in Eq. 3.30.

In a brief summary, the two SGS combustion models used have different concepts: the LES-PDF model is built based on the probability of a species appearing at one location at a time instant, and represents it using Eulerian stochastic fields, solving the distribution of all the involved species statistically (the more stochastic fields used, the more accurate the solution would be expected) and obtaining the chemical reaction rate. On the other hand, the LES-PaSR model does not involve any stochastic process, instead it splits a continuous flow field in a mesh cell into reacting and non-reacting parts, and models the filtered chemical reaction rate based on the relative volume fractions of these two parts. It is thus interesting to compare the performances of these two combustion models on their simulation of a realistic gas turbine combustor flow, which has been completed in Chapter 4.

In this thesis, the two combustion models used are implemented into two incompressible LES solvers, respectively, which are: (*i*) the incompressible version of the in-house code, BOFFIN [171, 173, 210, 211]; (*ii*) the low Mach number ReactingFOAM-LES solver in the open-source CFD toolbox, OpenFOAM (version 2.3.0) [122]. Both LES solvers apply the incompressibility assumption as described in Section 3.1. The LES-PDF combustion model is implemented into BOFFIN, whilst the LES-PaSR model is used by OpenFOAM.

3.4 Simulation of Entropy Wave Transport

Based on the above introduced numerical methods, the transport of entropy waves within a turbulent reacting combustor flow field can also be simulated using incompressible LES. The forced entropy transport equation, Eq. 2.40, is decoupled from the Navier-Stokes equations and implemented in a superimposed manner within the LES solver. In this thesis, the ReactingFOAM-LES solver from OpenFOAM is used for entropy wave transport simulation.

As suggested in the normalised entropy transport equation, Eq. 2.42, the contributions of both thermal diffusion and viscous production terms to the entropy wave transport are likely to be negligible, leaving the entropy advection term being dominant. In order to validate this assumption, the effects of both the large-scale resolved flow features and the SGS unresolved turbulent eddies on the LES of Eq. 2.40 must be considered. For example, the entropy diffusion term, D_s, defined in Eq. 2.40 can be numerically expressed as:

$$D_s = \alpha_E \frac{\partial^2 S}{\partial x_i \partial x_i}, \quad \text{where} \quad \alpha_E = \frac{\nu}{\mathrm{Pr}} + \frac{\nu_{\mathrm{sgs}}}{\mathrm{Pr}_{\mathrm{sgs}}}, \tag{3.33}$$

where the coefficient in the original diffusion term, $k_T/(\rho C_p)$, has been replaced by the "effective thermal diffusivity", denoted α_E. The contributions from the SGS turbulent eddies, e.g., ν_{sgs} the turbulent kinematic viscosity and $\mathrm{Pr}_{\mathrm{sgs}}$ the turbulent Prandtl number, are both included.

Similarly, the entropy production term, P_s, in Eq. 2.40 can be numerically realised as:

$$P_s = \frac{1}{\rho c_p \overline{T} \mathcal{V}} \left[(\tau_{ij}^E)' \frac{\partial \overline{u}_i}{\partial x_j} + \overline{\tau_{ij}^E} \frac{\partial u_i'}{\partial x_j} \right], \quad \text{where} \quad \tau_{ij}^E = \frac{\mu + \mu_{\mathrm{sgs}}}{2} \left(\frac{\partial u_i}{\partial x_j} + \frac{\partial u_j}{\partial x_i} \right), \tag{3.34}$$

where symbol $\overline{(\cdot)}$ refers to time-averaging. The effects of both laminar (μ) and turbulent eddy viscosities (μ_{sgs}) are now considered in the simulation of production term.

3.5 Summary

In this chapter, the key concepts of the incompressible LES have been firstly introduced, followed by the description of different sub-grid scale turbulence and combustion models used to solve the filtered stress tensor and chemical reaction rate, etc. The different treatments on these filtered variables lead to different modelling assumptions, and the effect of these assumptions

on the LES of a turbulent reacting flow needs systematic evaluation, which will be discussed in Chapter 4. Finally, the numerical method for simulating the entropy wave transport is explained, ensuring both the resolved and the sub-grid scale contributions are considered in the computation of entropy diffusion and production terms. The detailed simulation process for entropy wave transport in a realistic combustor flow will be presented in Chapter 6.

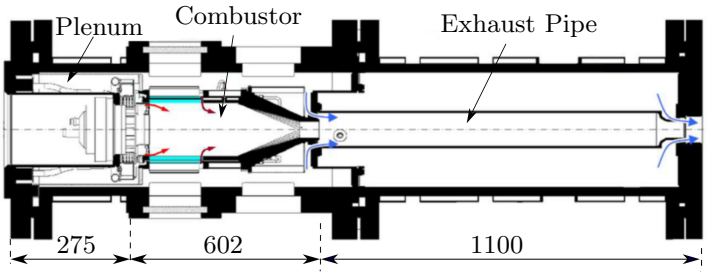
Chapter 4

SGT-100 Industrial Combustor: Flow Simulation and Flame Responses

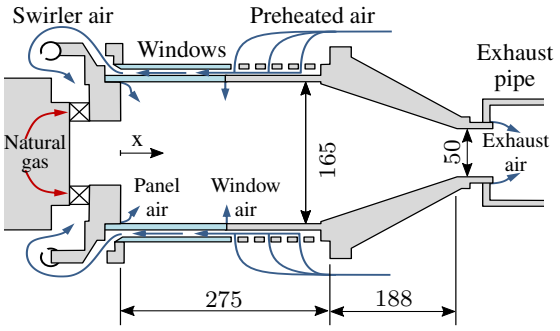
Based on the above introduction on theoretical modelling and numerical methods, a realistic industrial gas turbine combustor will be investigated in the following three chapters. In this chapter, the unforced combustor flow field and the flame behaviour are firstly simulated and compared across several cases, evaluating the effects of SGS turbulence model, combustion model, reaction chemistry, operating pressure, wall heat losses and mesh density, etc., on the unforced LES results. The forced flame heat release responses to an upstream acoustic perturbation are then computed, constructing the flame models (i.e. FTFs and FDFs) for this combustor. The influences of SGS combustion model, reaction chemistry and mean pressure on these flame response models are also analysed.

4.1 Experimental Set-up

The combustor taken from an original Siemens SGT-100 gas turbine is studied. In order to measure it, a high pressure test facility called "TURCHEMI" was built in the German Aerospace Centre (DLR), as shown in Fig. 4.1. The entire test facility (see Fig. 4.1(a)) comprises a longitudinal swirling combustor, a 1.0 m long exhaust pipe, and a spray water section (not shown) connecting to the atmosphere, plus a cylindrical air plenum installed upstream to the combustor, providing uniform preheated air inflows. The detailed structure of the combustor itself is shown in Fig. 4.1(b). It consists of a 12-slot radial swirler entry and a premixing chamber, followed by



(a) High pressure DLR facility



(b) SGT-100 gas turbine combustor

FIGURE 4.1: Schematics of (a) DLR high pressure test facility and (b) SGT-100 gas turbine combustor. All dimensions reported in mm, with the x-origin located at the combustion chamber entrance. Images adapted from [6, 7].

a dump expansion into a ∼0.5 m long main combustion chamber, in which the flow field exhibits large-scale features (e.g., swirl, separation, recirculation and vortex cores). The main combustion chamber consists of two parts: (*i*) a 275 mm long straight duct of square cross-section (height and width both 165 mm), slightly modified from the original circular cross-section in order to install quartz windows for optical measurements; (*ii*) a 188 mm long contraction duct whose circular cross-section has a linearly decreasing diameter from 165 mm to 50 mm. The chamber sizes and equivalent cross-sectional areas are the same as those in the original combustor. The exit of the contraction duct is connected to a short straight circular pipe with a length and diameter of both 50 mm. German Natural Gas (CH_4: 96.97%, C_2H_6: 1.553%, C_3H_8: 0.35%, C_4H_{10}: 0.05%, CO_2: 0.27%, N_2: 0.753%) [14] is injected at temperature ∼305 K through the swirler entry and mixed with the preheated air inflows in the premixing chamber at ∼685 K, reaching a global equivalence ratio of $\phi_e \simeq 0.60$ in the combustion chamber [24]. A series of operating pressures from 1 bar to 6 bar have been tested in the experiments. In this thesis, only two non-atmospheric pressures, $\overline{p} = 3$ bar and 6 bar, are considered, these exhibiting a bulk Reynolds number ranging between 18,400 – 120,000 and a bulk Mach number varying from 0.02

TABLE 4.1: Measurement uncertainties for some flow variables, including temperature (T) and species mass fractions in fresh mixture and burnt products [14].

Cold fresh mixture	T	O_2	N_2	CH_4	
Uncertainty [%]	6	6	5	4	
Hot burnt products	T	O_2	N_2	CO_2	H_2O
Uncertainty [%]	13	21	6	20	14

to 0.29. This high pressure rig has been studied experimentally (e.g., [6, 7, 24]) and numerically (e.g., [14, 104, 136]) to understand the behaviour of unforced turbulent swirling flames. High quality PIV and 1D Raman experimental data are available at both 3 bar and 6 bar pressures (see [14] for more details). The measurement uncertainties for some important flow variables are listed in Table 4.1. For simplicity, in the following chapters this DLR test facility is referred to as the "SGT-100 combustor", unless otherwise specified.

The thermoacoustic stability of the SGT-100 combustor was measured to be dependent on the mean operating pressure: it was stable at $\overline{p} = 3$ bar, but experienced nonlinear instability at $\overline{p} = 6$ bar [24, 201]. Figure 4.2(a) shows the time-signal of the normalised pressure fluctuation, $p'/\overline{p}$, at 6 bar, measured at a single location that is 231 mm downstream of the combustion chamber entrance (and also downstream of the entire flame). An enlarged time-scale between 20 s and 21 s allows better visualisation of this signal, which exhibits stable oscillations in $p'/\overline{p}$; this is known as the "limit cycle oscillation".

Given the high noise level in the original pressure signal, an averaging technique [212] was used to compute the frequency and amplitude of the limit cycle based on the signal's power spectrum. 40 windows of 1 s each with no overlapping were used for the time-signal in Fig. 4.2(a). The averaged spectrum, shown in Fig. 4.2(b), exhibits a main spectral peak at frequency 216 Hz with an amplitude of $|\widehat{p}| \simeq 5000$ Pa. These correspond to the measured limit cycle oscillation frequency and amplitude, respectively.

The above measured single-point pressure signal is also analysed with a wide-window averaging method (window size: 8192; overlap size: 1024). The power spectral densities (PSD) of the averaged pressure signal have resulted in seven main spectral peaks under each operating pressure, as shown in Fig. 4.3. Each spectral peak can be referred to as a "measured thermoacoustic mode". It has been observed that all the measured modes are stable at 3 bar, giving relatively lower magnitude spectral peaks over frequency (see Fig. 4.3). In contrast, the spectral peaks at

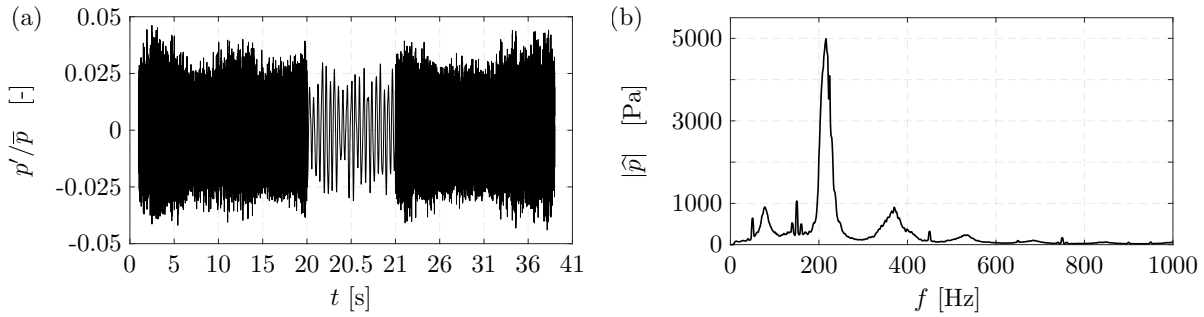


FIGURE 4.2: (a) Time-signal of the normalised pressure fluctuation, $p'/\overline{p}$, at 6 bar pressure, measured by DLR at a single location of 231 mm beyond the combustor entrance, at a sampling rate of 10 kHz; (b) Power spectrum of the pressure signal. Experimental data provided by Siemens.

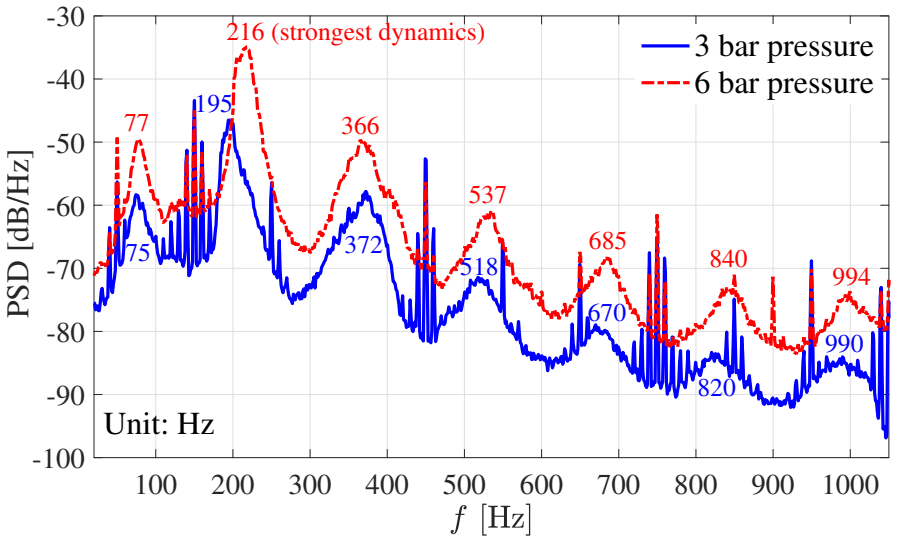
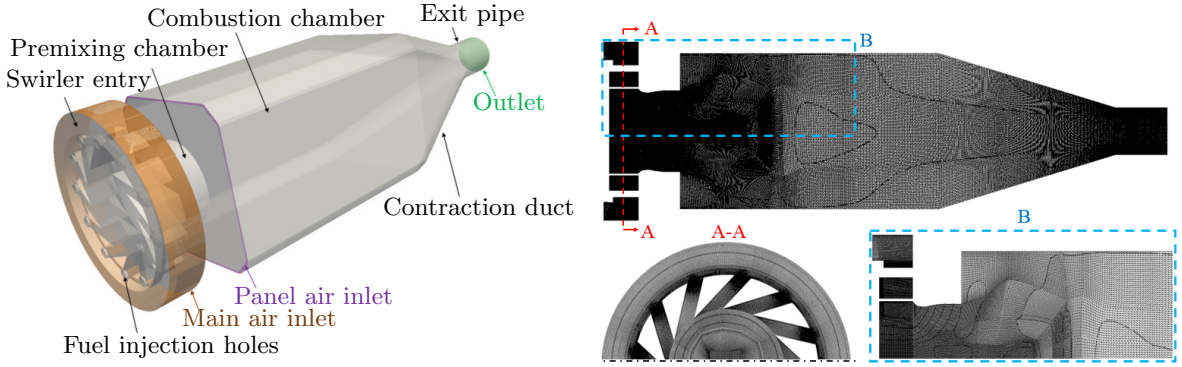


FIGURE 4.3: Power spectral densities (PSD) of the pressure time-signal, measured by DLR at 3 bar (solid line) and 6 bar (dash-dotted line) pressure at single location $x = 231$ mm. Window size: 8192; overlap size: 1024. Experimental data provided by Siemens.

6 bar pressure are globally higher, with the highest peak appearing at 216 Hz, being consistent with the averaged spectrum shown in Fig. 4.2(b).

4.2 Numerical Framework

Based on the above experimental set-up, the present LES simulates the SGT-100 combustor using a simplified fuel which combines all the hydrocarbons into methane, resulting in the following composition [14]: CH_4: 98.97%, CO_2: 0.27%, N_2: 0.753%. The LES computational domain is shown in Fig. 4.4(a); it neglects the upstream plenum and the long exhaust pipe since the



(a) Computational domain (b) 7-million-cell multi-block structured mesh

FIGURE 4.4: (a) LES computational domain and (b) mesh arrangement for the SGT-100 combustor.

TABLE 4.2: Prescribed inlet boundary conditions for the computational domain.

Main air velocity [m/s]	Panel air velocity [m/s]	Air temperature [K]	Fuel temperature [K]
4.87	5.28	685.33	319.80
Base hole fuel velocity [m/s]	**Top hole fuel velocity [m/s]**	**Low hole fuel velocity [m/s]**	
66.84	59.05	59.15	

flame is restricted to the front part of the main combustion chamber. A velocity inlet boundary condition consistent with the measured inflow rate is imposed at the swirler entry, which includes the radial main air inlet and multiple fuel injection holes. The panel air inlet refers to the front edge of the combustion chamber where a small amount of air enters the domain. The domain outlet corresponds to the combustor exit plane where a zero-gradient and a "non-reflecting" outflow condition are applied for pressure and velocity, respectively. Here the "non-reflecting" outflow condition is a specific artificial boundary condition, designed to neglect diffusion effects near the outlet and assumes that the outflow is purely advective (i.e. "non-reflective") [213]; it inhibits the occurrence of negative velocities at an outflow boundary. All the solid boundaries are defined as non-slip adiabatic walls, consistent with previous LES works on the same combustor (e.g., [14, 136, 214]). In this chapter, the effect of wall heat losses on the LES simulation is also studied, as presented in Section 4.3.4. The prescribed inlet boundary conditions used by the LES domain are listed in Table 4.2. In this LES work, the equivalence ratio used is fixed at $\phi_e = 0.6$, regardless of a small variation in ϕ_e across the operating pressures during the real experiments.

The entire computational domain is discretised into multiple blocks, with each block meshed

with structured cells, resulting in a total of ∼7.0 million cells (see Fig. 4.4(b)). This computational grid is the result of optimisation studies performed by Bulat et al. [14], which has been shown to correctly capture the characteristics of the unforced flame with fully detailed chemical schemes [136]. The sizes of the mesh cells range from Δx = 0.281 – 4.16 mm in the axial direction, Δy = 0.086 – 5.24 mm in the vertical direction, and Δz = 0.083 – 5.33 mm in the horizontal direction. Mesh refinement is applied to the swirler, premixing chamber and front part of the combustion chamber to better resolve the flame responses to upstream perturbation.

For the incompressible LES solvers, both the in-house code, BOFFIN [171], and the open-source code, OpenFOAM [122], are applied. In BOFFIN, a 2nd-order central difference scheme is used for the spatial discretisation of all the convection and diffusion terms, except for the convective terms in equations of scalar quantities, where a Total Variation Diminishing (TVD) scheme is applied. On the other hand, OpenFOAM adopts a linear Gaussian interpolation method for spatial discretisation (which is a central difference scheme), coupled with a Sweby limiter [215] to improve the numerical stability in regions with rapidly changing gradients but adding numerical diffusivity. Both solvers apply an implicit 2nd-order Crank-Nicolson scheme for the temporal discretisation. The LES-PaSR combustion model (see Section 3.3.2) is applied within OpenFOAM, with the value of the mixing time constant, C_m, fixed as 0.8 (see Eq. 3.32). Instead, the LES-PDF combustion model described in Section 3.3.1 is used by BOFFIN, which uses only one field (i.e. $N_f = 1$, see Eq. 3.26).

It is understood that for BOFFIN, using only one field in the Eulerian stochastic method for the PDF model means that the resulting PDF reduces to a δ-function (one unique realisation), which is no longer stochastic. Thus the SGS turbulence-chemistry interactions are ignored in the present BOFFIN study. The reason to use this "no-SGS-model" PDF approach in this code is due to the negligible effect of increasing the number of stochastic fields on the simulated FDFs, as shown in Fig. 4.24. Besides, Bulat [103] has compared the unforced simulations on the same combustor using one field and eight stochastic fields, and found that the resulting temperature and mixture fraction distributions are very similar, suggesting that one field may be sufficient for the present combustor.

For the BOFFIN code, the discrete from of the continuity equation is used to derive a Poisson equation for the pressure fluctuation, p'. This equation is then solved for the pressure correction field which is then used to update both the mass flux terms and the velocities [171]. For the OpenFOAM solver, the PIMPLE method [216] (i.e. merged PISO/SIMPLE algorithms)

TABLE 4.3: Incompressible LES solvers: BOFFIN vs. OpenFOAM.

LES solver	BOFFIN	OpenFOAM
Accessibility	In-house	Open-source
Combustion model	LES-PDF	LES-PaSR
Turbulence model	Dynamic Smagorinsky	
Spatial discretisation	2nd-order (TVD for convection terms, central difference scheme for the rest)	2nd-order (Gaussian linear scheme)
Time integration	2nd-order implicit Crank-Nicolson scheme	
Chemical scheme	4-step + 7 intermediate species	
	15-step + 19 intermediate species	
Computational time-step	5×10^{-7} s	
CFL number	≤ 0.3	

is employed for pressure correction, with the number of iterations used to solve the pressure equation and momentum corrector chosen to be 3. The number of loops completed over the entire system of equations in each time step is 2, which means the system is solved twice in each time step.

Finally, an appropriate computational time step is needed by both LES solvers to keep the CFL number sufficiently low to avoid any divergence of the flow variables. In this SGT-100 work, a small fixed computational time step of $\Delta t = 5 \times 10^{-7}$ s is applied for all the LES simulations, ensuring a CFL number below 0.3 and maintaining the temporal accuracy of the simulations. The above detailed comparisons between BOFFIN and OpenFOAM are summarised in Table 4.3.

4.3 Unforced LES Results and Validation

Based on the above numerical settings, the unforced LES simulation results are now presented and validated by available high-quality experimental data. The effect of the SGS turbulence model on the flow field is firstly investigated, followed by the effect evaluation of the SGS combustion model, chemical reaction scheme, wall heat losses and mesh density, etc., on the unperturbed flow field and flame behaviour. The influence of the mean operating pressure on the simulations is also discussed. To facilitate systematic comparisons, five LES cases with different modelling assumptions and operating conditions are defined, listed in Table 4.4.

TABLE 4.4: LES cases used to study the effects of different factors.

Case No.	I	II	III	IV	V
LES solver	OpenFOAM	BOFFIN	BOFFIN	BOFFIN	BOFFIN
Combustion model	LES-PaSR	LES-PDF	LES-PDF	LES-PDF	LES-PDF
Reaction chemistry	4-step	4-step	15-step	4-step	15-step
Operating pressure	3 bar	3 bar	3 bar	6 bar	6 bar

4.3.1 Effects of SGS turbulence and combustion modelling

First of all, the effect of SGS turbulence modelling on the unforced LES is studied, based on LES Case I (see Table 4.4), using OpenFOAM with LES-PaSR model and 4-step reaction at $\overline{p} = 3$ bar. All the four SGS turbulence models introduced in Section 3.2 are applied, compared based on their simulation accuracy for the turbulent swirling reacting flow in the combustor.

Figure 4.5 compares the LES-predicted axial (u) and vertical (v) flow velocity profiles along the vertical y-direction at axial location $x = 18.7$ mm (i.e. 18.7 mm downstream of the combustion chamber entrance), to the relevant PIV experimental data [14]. Both the mean (denoted $\overline{(\cdot)}$) and root-mean-square (denoted RMS) velocity components are presented. These simulated profiles are found to be symmetric with respect to the centreline, therefore only the top-half (from centreline to top inner wall) of the profiles are shown. It is observed that all the four turbulence models yield similar predictions for the mean axial velocity, $\overline{u}$ (see Fig. 4.5(a)), other than for the small mismatches near the top wall and centreline for the one-equation turbulent kinetic energy model. Larger discrepancies are observed for the mean vertical velocity, $\overline{v}$ (Fig. 4.5(c)): near the top wall, better predictions are achieved using the WALE and dynamic Smagorinsky models, with all the models over-predicting $\overline{v}$ near the centreline. For the fluctuating axial velocity, u_{rms} (Fig. 4.5(b)), its general distribution is correctly predicted by all the models, with the constant Smagorinsky and WALE models performing better near the top wall. A similar result is observed for the RMS vertical velocity, v_{rms} (Fig. 4.5(d)), where, in line with the prediction of $\overline{v}$, higher discrepancies are observed for all the models.

A general conclusion can then be drawn on the effect of SGS turbulence modelling on the LES-simulated flow field. While previous analyses on a non-reacting, non-swirling flow [189] have found that the constant Smagorinsky and WALE models are always more dissipative than the other two, the present study reveals that the effect of a turbulence model on a reacting, swirling

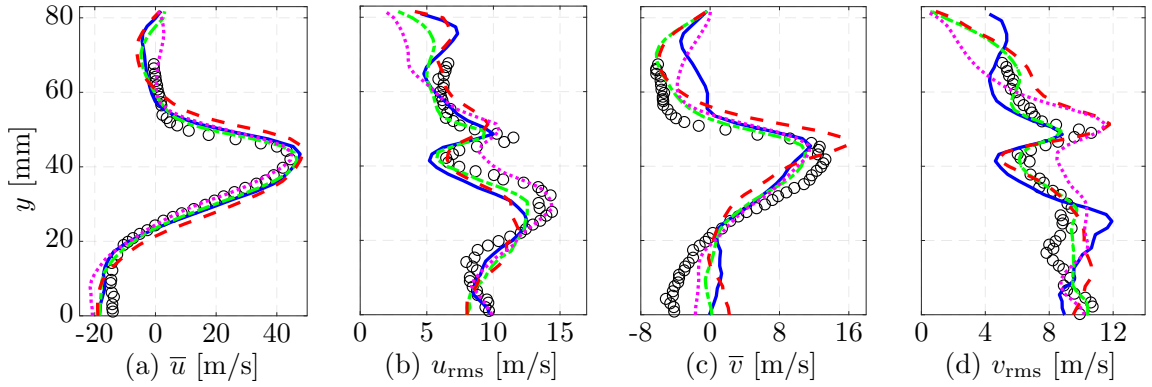


FIGURE 4.5: Vertical y-profiles of (a–b) axial, u, and (c–d) vertical, v, flow velocities at $x = 18.7$ mm, for (a, c) mean and (b, d) RMS components. Four SGS turbulence models are used: (*i*) constant Smagorinsky [8] (blue solid line); (*ii*) dynamic Smagorinsky [9] (green dash-dotted line); (*iii*) WALE [10] (red dashed line); (*iv*) one-equation turbulent kinetic energy [11–13] (magenta dotted line). The PIV experimental data [14] are marked by black circles. All simulations based on LES Case I.

flow is more complex, which varies along the vertical direction, possibly due to the flow swirl. The dynamic Smagorinsky and WALE models seem to be more accurate than the constant Smagorinsky model, but the SGS combustion model and reaction chemistry chosen to solve the reacting flow may also affect the results. In no case is the effect of the SGS turbulence model large. The remainder of this section will continue to investigate the effects of combustion model and chemistry, with all the following simulations performed using the dynamic Smagorinsky turbulence model.

Secondly, the impact of the SGS combustion model on the unforced LES is studied. The LES-PaSR and LES-PDF combustion models described in Section 3.3 are compared using LES Cases I and II, respectively, both performed with 4-step reaction at 3 bar pressure (see Table 4.4). Figure 4.6 shows the time-averaged contours of axial velocity, $\overline{u}$, temperature, $\overline{T}$, and volumetric heat release rate, $\overline{\dot{q}}$, on a 2-D symmetry plane. For each contour plot, the top-half refers to Case I and the bottom-half to Case II. The time-averaged streamlines visualised by the Line Integral Convolution (LIC) technique [217] are superimposed on the contours of mean velocity and temperature, allowing a clearer representation of the large Inner Recirculation Zone (IRZ) near the centreline and two smaller Outer Recirculation Zones (ORZ) near the top and bottom back-step corners (see Figs. 4.6(a, b)). It is observed that the mean flow fields are very similar between Cases I and II (Fig. 4.6(a)), suggesting that the SGS combustion model has very little effect on the unforced flow field.

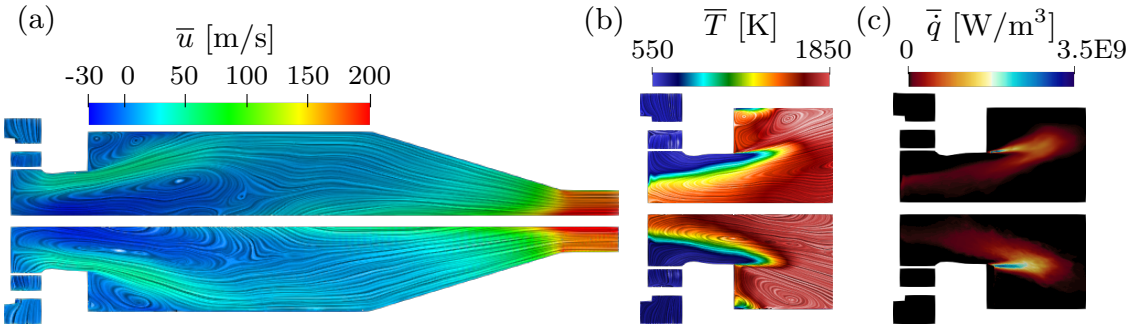


FIGURE 4.6: Time-averaged contours of (a) axial velocity, $\overline{u}$, (b) temperature, $\overline{T}$, and (c) volumetric heat release rate, $\overline{\dot{q}}$, on symmetry plane $z = 0$, computed at $\overline{p} = 3$ bar by (top-half) Case I with LES-PaSR and (bottom-half) Case II with LES-PDF models.

The detailed 3-D flow features are shown in Fig. 4.7, where a Central Vortex Core (CVC), which is typical of turbulent swirling combustor flows, is evident. The CVC extends along the centreline from the combustor exit to the mid-chamber, with the exiting low pressure zone resulting in very high exit flow velocities along the centreline, dropping off towards the two sides (see Fig. 4.6(a)). These flow features have been observed in previous experimental [24] and numerical [104, 185, 218] studies on the same combustor.

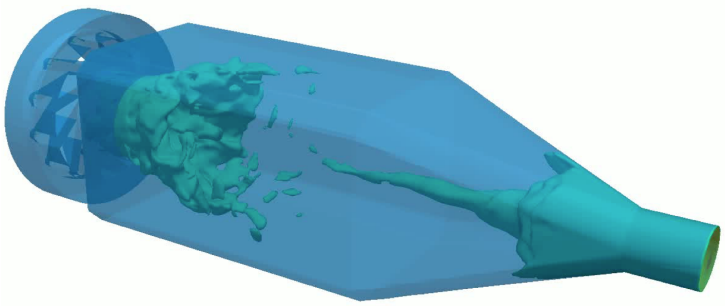


FIGURE 4.7: Central Vortex Core (CVC) along the centreline from chamber exit to mid-chamber, marked by pressure iso-surface of 310,580 Pa. Simulations based on LES Case I.

Returning to Fig. 4.6, discrepancies between Cases I and II can be observed in the contours of mean temperature and heat release rate. Figure 4.6(b) shows a longer axial extent of the low temperature zone for Case I, resulting in a lower-magnitude mean heat release rate in Fig. 4.6(c). A possible explanation is that OpenFOAM may be somewhat more diffusive than BOFFIN — because OpenFOAM uses a deeply embedded TVD-type scheme for flow velocities, which adds diffusivity. A more (numerically) diffusive solution will likely lead to a thicker combustion zone, where the corresponding spatial spread leads to a lower peak heat release rate. It is also possible that it is a result of the differences in the two combustion models utilised in the two codes.

The mean heat release rate fields shown in Fig. 4.6(c) are also compared with those measured by the experiments (e.g., [24]). It is found that the LES and measurement on the flame shape and size generally match well, although the LES-predicted flame is mainly anchored within the outer shear layer close to the premixing chamber exit, while the measured flame mainly locates inside the inner shear layer and extends further upstream into the premixing chamber. The possible reason for this flame location difference may be due to the small deviation of the LES-simulated flow field, especially the sizes of the inner and outer recirculation zones, compared to the measurement data. A very small difference in the flow field is sufficient to cause a change in the flame's anchoring point, which is sensitive to the surrounding flow features.

Another difference between LES and experiment is that the measured flame only intermittently attaches to the premixing chamber's exit plane at one or two points around the entire circumference, while the LES-simulated flame is more uniformly attaching to the same plane with a larger touching area. This may be due to the lack of complexity in the chemical reaction schemes used by the LES, which may be insufficient to capture the dynamic attaching and detaching processes of the measured flame roots. The real reason for this difference is still under investigation.

Figures 4.8–4.9 quantitatively compare the results from Cases I and II. The vertical y-profiles of velocity, temperature, mixture fraction and species mass fractions are plotted at four axial locations: $x = 18.7$, 38.7, 58.7 and 88.7 mm, with $x = 0$ mm located at the combustion chamber entrance (i.e. premixing chamber exit). For each sub-figure, the horizontal axis is split into four segments, each refers to a y-profile and has the same data range for the plotted variable (e.g., [0, 40] m/s for $\overline{u}$ in Fig. 4.8(a)). At $x = 18.7$ mm, very little simulation difference is observed between the LES-PaSR and LES-PDF models for both the mean and RMS velocity components, confirming that the SGS combustion model has little impact on the simulated flow field. Both LES cases accurately capture the experimental data. Further downstream ($x \geq 38.7$ mm), good agreement between LES and measurements is maintained for all the velocity profiles, other than for a small mismatch between the two cases near the centreline of the v_{rms} profiles (Fig. 4.9(b)). This may be due to the difference in the CVC's axial length (see Fig. 4.6(a)) predicted by the two combustion models.

For temperature (T) profiles, both combustion models correctly capture the mean and RMS profiles at the first location of $x = 18.7$ mm. Differences between LES and measurements become more pronounced further downstream, possibly due to the mismatch between the predicted and the measured axial extents of the low temperature zone (see Fig. 4.6(b)). Both combustion

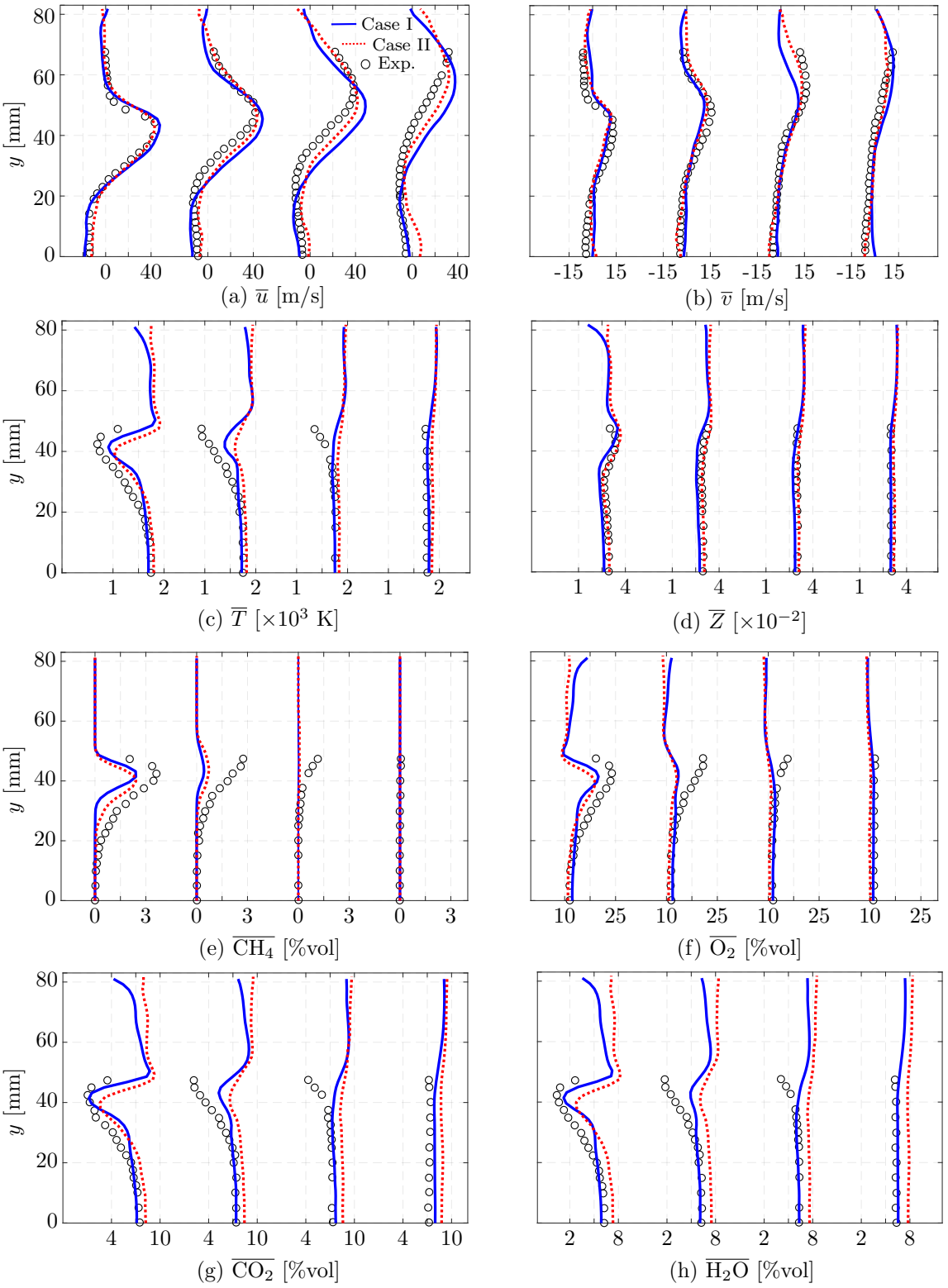


FIGURE 4.8: Vertical y-profiles of mean flow variables at 3 bar pressure for four axial locations: $x = 18.7$, 38.7, 58.7 and 88.7 mm. Blue solid line: Case I with LES-PaSR model; red dotted line: Case II with LES-PDF model; black circle: experimental data [14]. Z is mixture fraction, CH_4, O_2, CO_2 and H_2O are relevant species mass fractions.

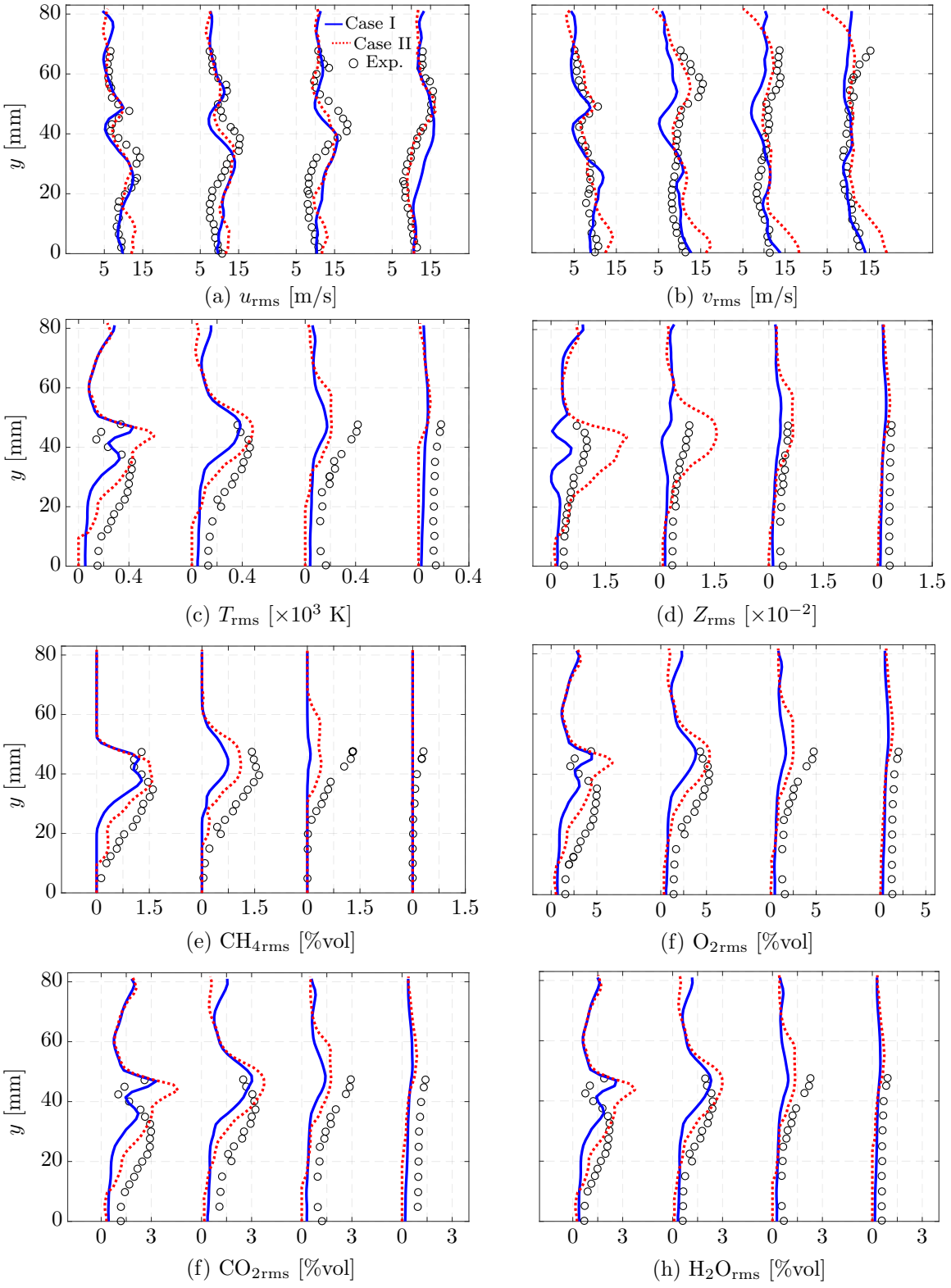


FIGURE 4.9: Vertical y-profiles of fluctuating (RMS) flow variables at 3 bar pressure, computed by Case I (solid line) and Case II (dotted line). See the caption of Fig. 4.8 for more information.

models, however, fail to accurately predict the temperature profile near the top wall, although the experimental data here are not complete. This is consistent with other studies on the same combustor (e.g., [136]). Corresponding discrepancies in the mass fractions of some important species involved in the chemical reactions (e.g., CH_4, O_2, CO_2 and H_2O) are also observed. Very good agreement is achieved for the mean mixture fraction, $\overline{Z}$, revealing a globally lean mixture uniformly distributed in the combustion zone. Although small errors exist for $Z_{\rm rms}$ between LES and experiment at some locations (e.g., x = 18.7 and 38.7 mm in Fig. 4.9(d)), bearing in mind the measurement uncertainties listed in Table 4.1, these errors are generally acceptable. The LES-PDF model (dotted line) predicts slightly higher fluctuating values for the temperature ($T_{\rm rms}$) and species mass fractions (e.g., $CH_{4\rm rms}$, $O_{2\rm rms}$, $CO_{2\rm rms}$ and $H_2O_{\rm rms}$) compared to the LES-PaSR model, being consistent with the shorter low temperature zone predicted by the same PDF model (see Fig. 4.6(b)). It is finally observed that both combustion models slightly under-predict the fluctuating temperature ($T_{\rm rms}$) and species mass fractions compared to the experimental data, especially at downstream locations (see Fig. 4.9). These phenomena are similar to those observed by Bulat [103].

4.3.2 Effect of reaction chemistry

The effect of chemical reaction scheme on the unforced LES is then investigated. To achieve this goal, the accuracy of both the 4-step [16] and 15-step [17] schemes used for methane/air reaction must be investigated at first, here by comparing their predictions of laminar burning velocity, S_u, and adiabatic flame temperature, T_a, against those computed by a fully 325-step GRI-Mech 3.0 scheme [131]. In both OpenFOAM and BOFFIN, the applied assumptions of constant Schmidt number and unity Lewis number for all the species also need validation, which can be done by comparing the LES solver predictions of S_u and T_a to those by the chemical solver, Cantera [219], in which accurate transport properties are used for each species. In this sub-section, all the calculations are performed at $\overline{p}$ = 3 bar with an ambient temperature of T_m = 650 K, the same operating conditions as for LES Cases I – III (see Table 4.4).

Figure 4.10(a) shows that with Cantera, the simplified schemes give similar S_u and T_a values to those of the detailed GRI-Mech scheme across a range of equivalence ratios. For the operating equivalence ratio of ϕ_e = 0.6, the Cantera 4-step scheme slightly over-predicts the laminar burning velocity, S_u, with the 15-step scheme matching better the detailed GRI scheme.

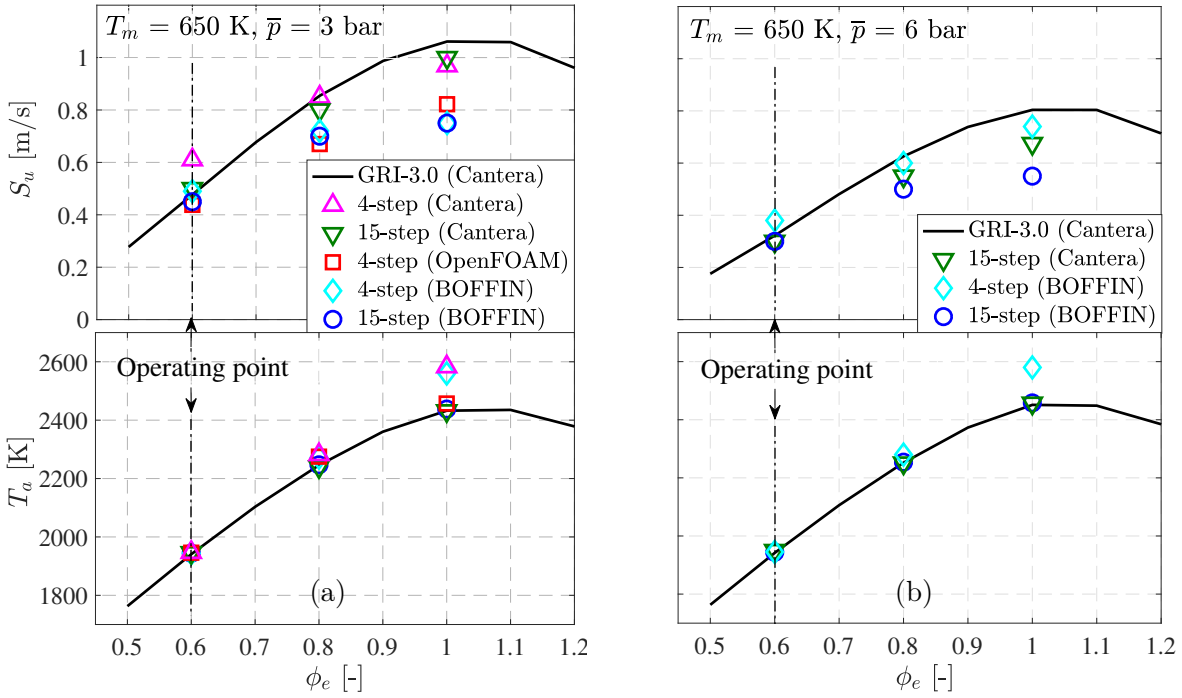


FIGURE 4.10: Laminar burning velocity (S_u) and adiabatic flame temperature (T_a) against equivalence ratio (ϕ_e) at pressure (a) $\overline{p}$ = 3 bar and (b) $\overline{p}$ = 6 bar, both with ambient temperature T_m = 650 K. Cantera with GRI-Mech 3.0 scheme (solid line); Cantera with 4-step scheme (△); Cantera with 15-step scheme (▽); OpenFOAM with 4-step scheme (□); BOFFIN with 4-step scheme (◊); BOFFIN with 15-step scheme (◯). The operating point refers to ϕ_e = 0.6.

The two tested LES solvers, however, slightly under-predict S_u for both the 4-step and 15-step schemes, especially at higher ϕ_e. These results are as anticipated given the constant Schmidt and Prandtl number assumption[1], as it is well known that this leads to an under-prediction of the burning velocity at higher equivalence ratios [162]. Nevertheless, the adiabatic flame temperature, T_a, and burning velocity, S_u, are correctly reproduced by both LES solvers at the combustor operating point of ϕ_e = 0.6; discrepancies occur around stoichiometric equivalence ratios.

Following from the above validation of both reaction schemes, the impact of reaction chemistry on the unforced LES results can be analysed. As shown in Fig. 4.11, the contour plots of mean velocity, temperature and volumetric heat release rate are compared between Case II (4-step reaction) and Case III (15-step reaction) at 3 bar pressure, both using the LES-PDF combustion model through BOFFIN. It is noted that (*i*) the impact of reaction chemistry on the mean flow field is marginal, Fig. 4.11(a); (*ii*) the 4-step scheme gives a slightly shorter

[1]Recent computations of laminar flames with BOFFIN using accurate transport properties reproduce the GRI results.

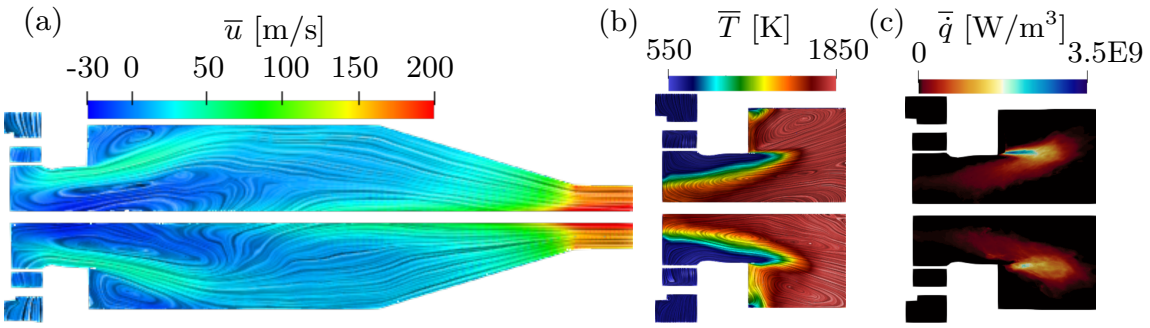


FIGURE 4.11: Time-averaged contours of (a) axial velocity, $\overline{u}$, (b) temperature, $\overline{T}$, and (c) volumetric heat release rate, $\dot{\overline{q}}$, computed at $\overline{p} = 3$ bar based on (top-half) Case II with 4-step reaction scheme and (bottom-half) Case III with 15-step reaction scheme.

axial extent of the low temperature zone, Fig. 4.11(b), and (*iii*) a higher magnitude mean heat release rate, Fig. 4.11(c). The shorter low temperature zone for the 4-step reaction may be a result of its slightly higher laminar burning velocity compared to the 15-step scheme (see BOFFIN predictions in Fig. 4.10(a)), this reducing the axial extent of the reaction zone and thus increasing the fuel burnt at the flame location, leading to a higher mean heat release rate as mentioned in (*iii*).

Figures 4.12–4.13 compare the vertical y-profiles of some flow variables, mean and RMS, between Cases II and III. The match between LES and experiments is generally good for all the variables at all locations, with errors within the limits of measurement uncertainties (Table 4.1). This confirms that both chemical schemes used are sufficiently accurate for the simulated unforced flame. It is also observed that the 4-step reaction slightly over-predicts the mean temperature, $\overline{T}$, and the mass fractions of CO_2 and H_2O, but under-predicts the mass fractions of CH_4 and O_2, compared to the 15-step scheme. These discrepancies are consistent with the differences in the unforced flame shape predicted by the two reaction schemes (see Figs. 4.11(b, c)).

4.3.3 Effect of mean operating pressure

The effect of mean operating pressure, $\overline{p}$, on the unforced LES results is also analysed. The laminar burning velocity and adiabatic flame temperature are firstly compared against the detailed GRI-Mech 3.0 scheme at 6 bar pressure (see Fig. 4.10(b)), for both the 4-step and 15-step reaction schemes. Only the BOFFIN LES solver is now included, and the results obtained using Cantera, with its accurate transport properties, are also shown.

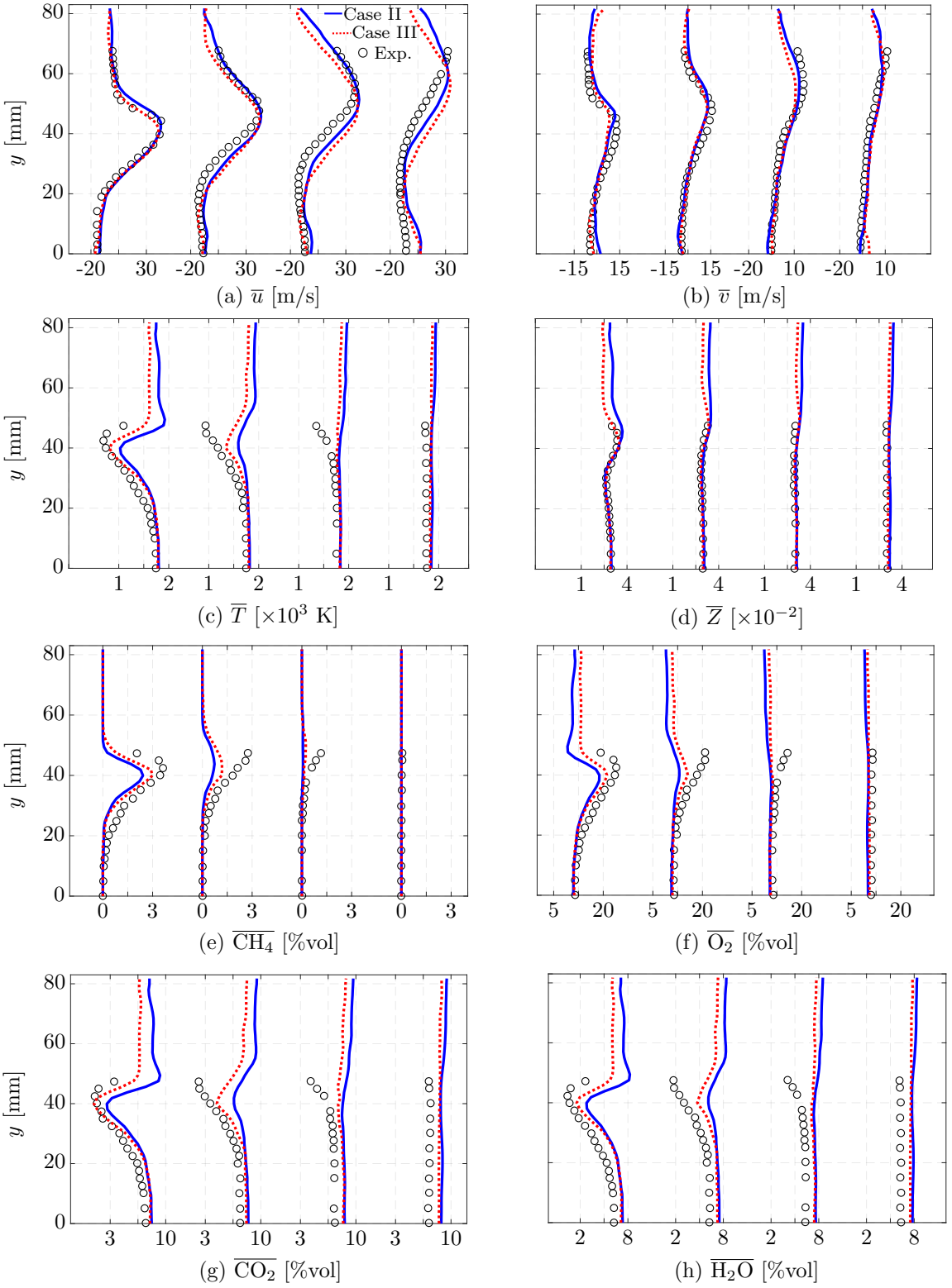


FIGURE 4.12: Vertical y-profiles of mean flow variables at 3 bar pressure for four axial locations: x = 18.7, 38.7, 58.7 and 88.7 mm. Blue solid line: Case II with 4-step reaction scheme; red dotted line: Case III with 15-step reaction scheme; black circle: experimental data [14].

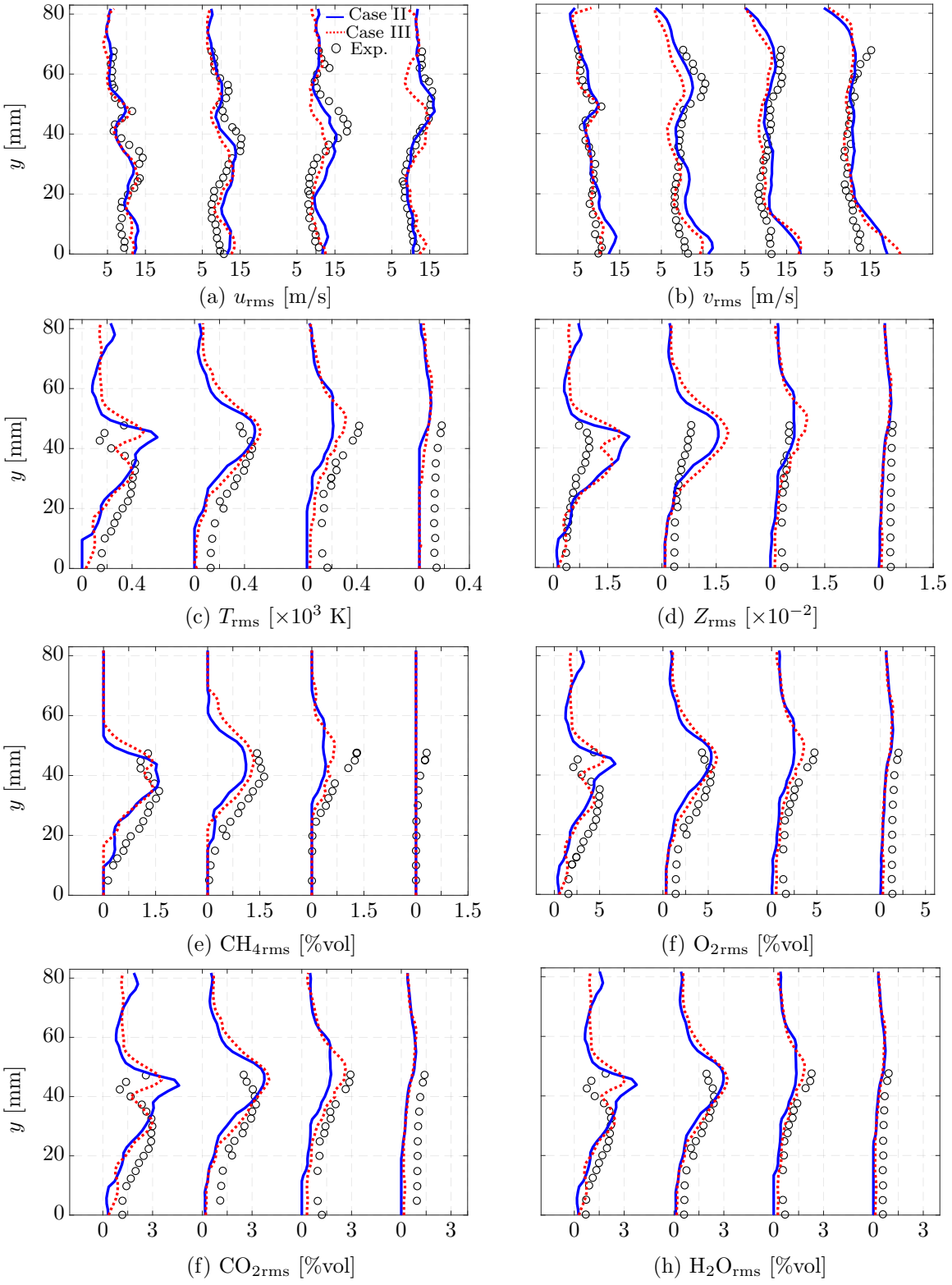


FIGURE 4.13: Vertical y-profiles of RMS flow variables at 3 bar pressure, computed by Case II (solid line) and Case III (dotted line). See the caption of Fig. 4.12 for more information.

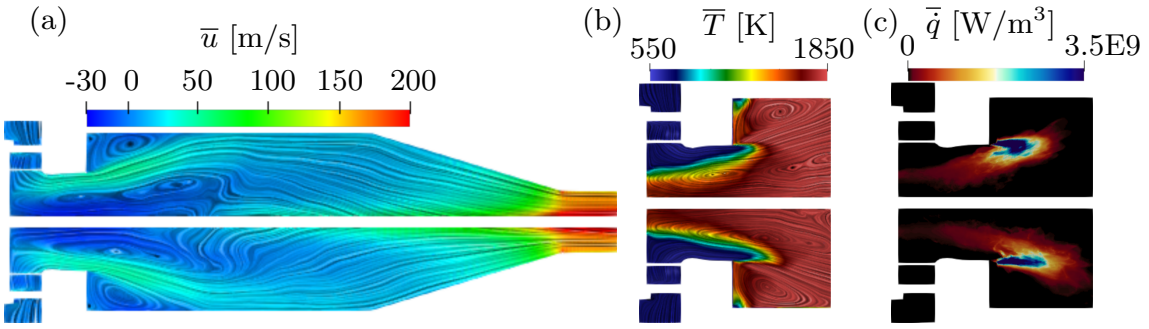


FIGURE 4.14: Time-averaged contours of (a) axial velocity, $\overline{u}$, (b) temperature, $\overline{T}$, and (c) volumetric heat release rate, $\overline{\dot{q}}$, computed at $\overline{p} = 6$ bar based on (top-half) Case IV with 4-step reaction scheme and (bottom-half) Case V with 15-step reaction scheme.

It can be seen from Fig. 4.10(b) that: (*i*) increasing the mean pressure globally decreases the laminar burning velocity, S_u, for all equivalence ratios, but does not affect the adiabatic flame temperature, T_a, consistent with findings in [162]; (*ii*) both the 4-step and 15-step reaction schemes generally predict the correct burning velocity and temperature at 6 bar over the equivalence ratio, with discrepancies between the present schemes and GRI-Mech 3.0 increasing with ϕ_e; (*iii*) the BOFFIN 4-step scheme gives a slightly higher burning velocity than the BOFFIN 15-step scheme at 6 bar, consistent with the predictions at 3 bar pressure (Fig. 4.10(a)). Although the inclusion of accurate transport properties within Cantera improves the prediction of laminar burning velocity at high ϕ_e, the accuracy of BOFFIN is sufficiently good with both reaction schemes used at the operating point of $\phi_e = 0.6$.

Following from the above validation on the used reaction schemes, the contours of mean flow variables are compared at $\overline{p} = 6$ bar in Fig. 4.14 between Case IV (with 4-step reaction) and Case V (with 15-step reaction), both for BOFFIN with LES-PDF combustion model. It is observed that both reaction schemes again give very similar mean velocity fields (Fig. 4.14(a)), similar to those simulated at 3 bar pressure. Due to the predicted faster burning velocity, the 4-step chemistry gives a shorter low temperature zone and a higher heat release rate in the central zone of the flame (Figs. 4.14(b, c)). Comparing to the 3 bar predictions (see Figs. 4.11(b, c)), the predicted axial extent of the low temperature zone is much shorter at 6 bar pressure for both reaction schemes, although the magnitude of the mean heat release rate is much higher. These differences in the unforced flame features between 3 bar and 6 bar may be caused by the increase of mixture density associated with a higher mean pressure and correspondingly a higher Reynolds number and chemical reaction rate [186].

The vertical profiles of flow variables at $\overline{p} = 6$ bar are then compared between Cases IV and V

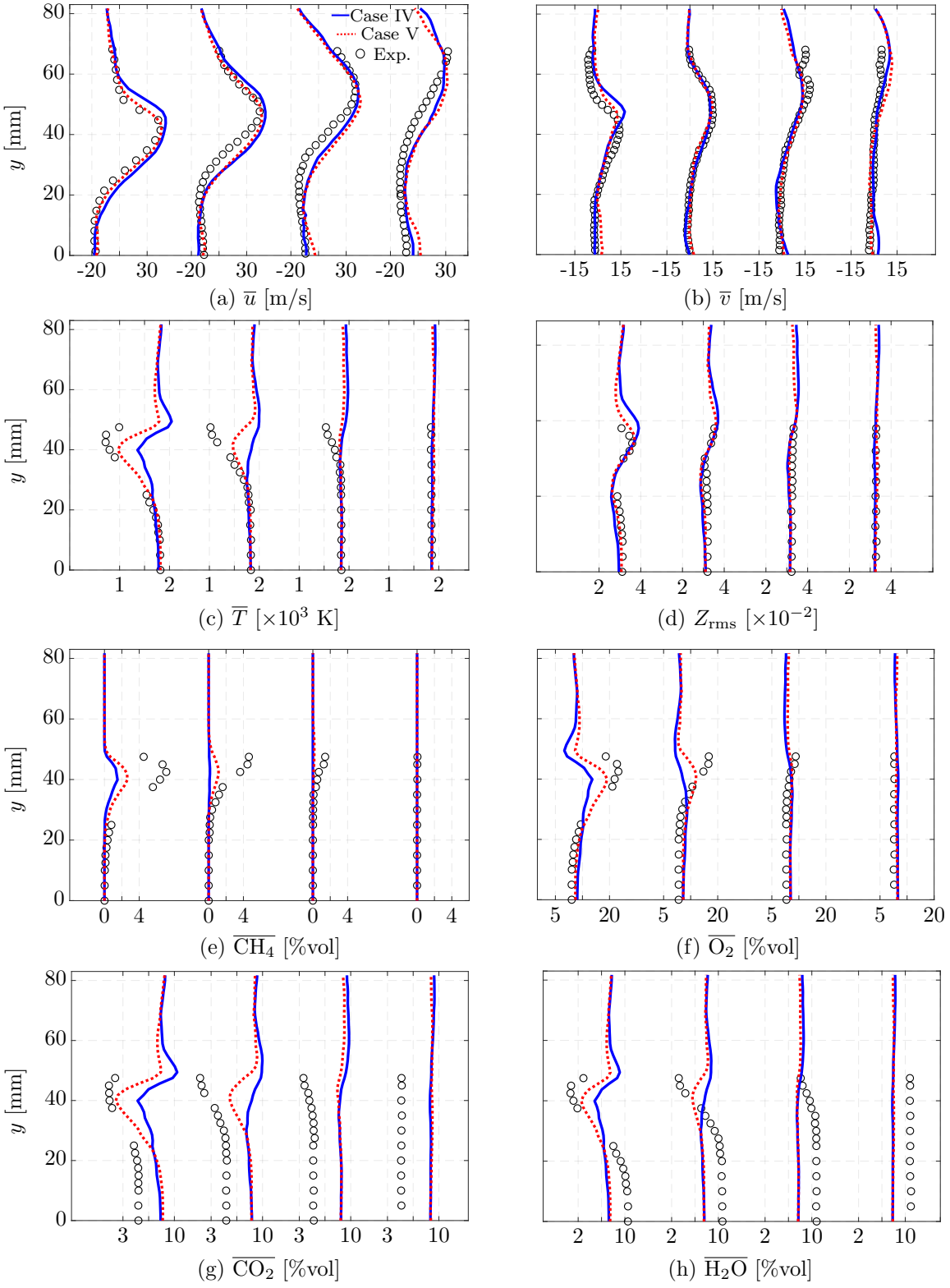


FIGURE 4.15: Vertical y-profiles of mean flow variables at 6 bar pressure for four axial locations: x = 18.7, 38.7, 58.7 and 88.7 mm. Blue solid line: Case IV with 4-step reaction scheme; red dotted line: Case V with 15-step reaction scheme; black circle: experimental data from DLR.

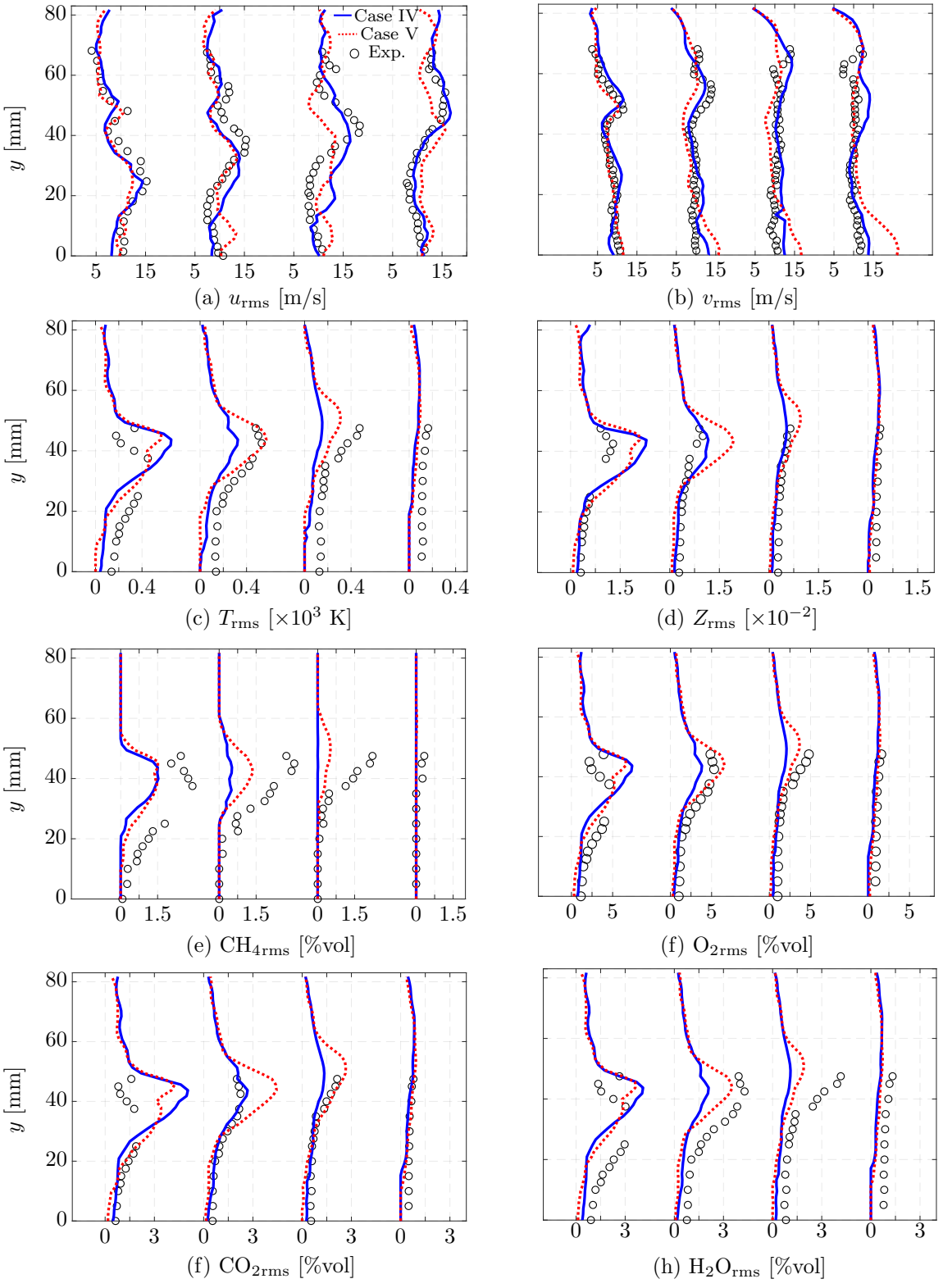


FIGURE 4.16: Vertical y-profiles of RMS flow variables at 6 bar pressure, computed by Case IV (solid line) and Case V (dotted line). See the caption of Fig. 4.15 for more information.

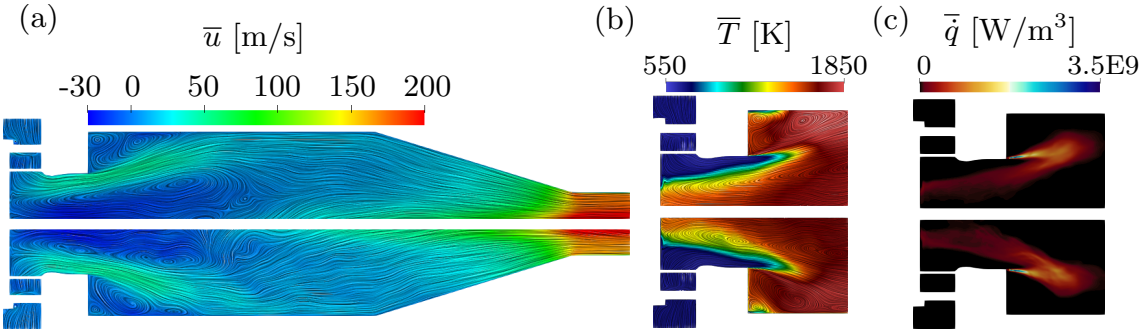


FIGURE 4.17: Time-averaged contours of (a) axial velocity, $\overline{u}$, (b) temperature, $\overline{T}$, and (c) volumetric heat release rate, $\overline{\dot{q}}$, all computed by LES Case I. Top-half: adiabatic wall condition; bottom-half: non-adiabatic wall condition with fixed wall temperatures.

in Figs. 4.15 and 4.16. A slightly larger deviation between the LES and experimental profiles is observed than those at 3 bar pressure, especially for some RMS variables (e.g., CH_{4rms} in Fig. 4.16(e)). This may be due to the fact that the analysed combustor is stable at 3 bar, but becomes unstable at 6 bar pressure with large amplitude limit cycle oscillations (see Fig. 4.2). Although the 4-step chemistry is sufficiently accurate for the flow velocity, the more detailed 15-step scheme gives slightly better predictions for the temperature (T) and mass fractions of some species, e.g., CH_4 and H_2O. This comparison highlights that a more detailed reaction scheme may yield a more accurate reproduction of the unforced flame, especially at higher operating pressures.

4.3.4 Other factors: wall heat losses and mesh density

Apart from the above-discussed modelling assumptions and operating conditions, some other factors may also affect the unforced simulation results. For example, the impact of wall heat losses on the unforced LES is now discussed, by comparing the adiabatic and non-adiabatic wall thermal conditions. The latter often applies fixed wall temperatures, which has been used in [127, 220, 221] for different combustors. Based on LES Case I, fixed wall temperatures of 682 K and 1,273 K are applied on the solid domain boundaries upstream and downstream of the combustion chamber entrance, respectively. The former is based on the preheated air inlet temperature, while the latter is equal to the measured temperature on the quartz windows [24].

Figure 4.17(a) illustrates that the mean velocity fields are not largely affected by the change of wall thermal condition. Similarly, both the mean temperature (Fig. 4.17(b)) and heat release rate (Fig. 4.17(c)) contours are not highly modified by the wall heat losses from non-adiabatic

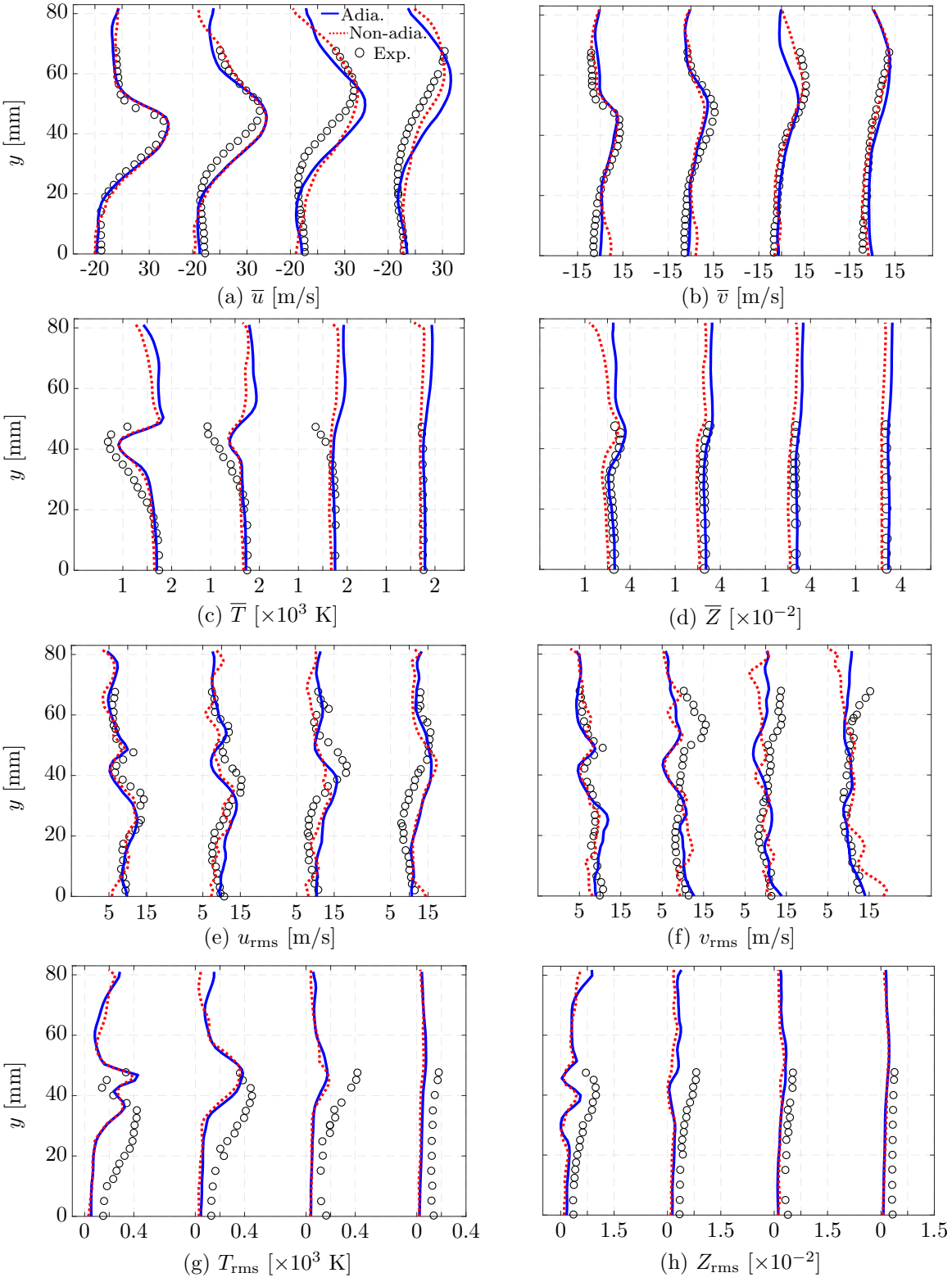


FIGURE 4.18: Vertical y-profiles of (a–d) mean and (e–h) RMS flow variables at: x =18.7, 38.7, 58.7 and 88.7 mm, all computed by Case I. Blue solid line: adiabatic wall condition; red dotted line: non-adiabatic wall condition with fixed wall temperatures; black circle: experimental data [14].

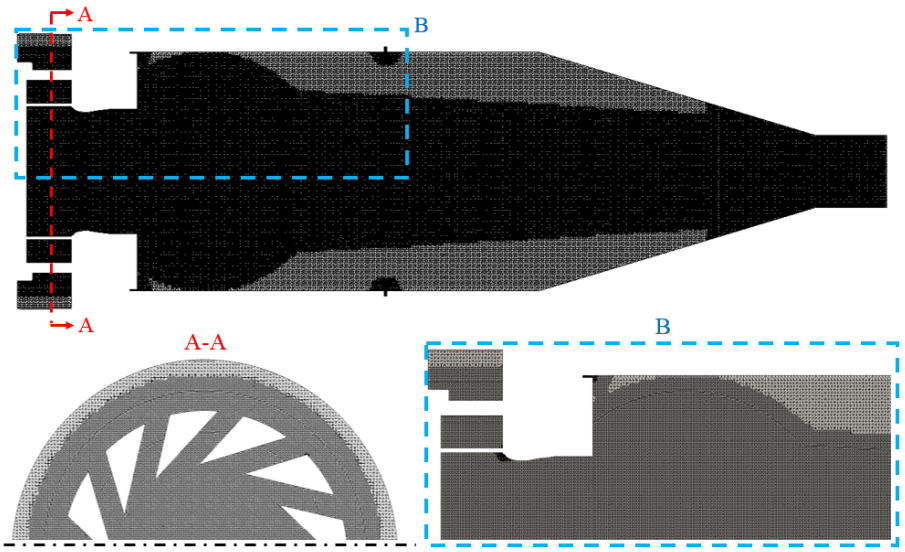


FIGURE 4.19: A refined unstructured mesh with 14.5 million cells for the LES computational domain of the SGT-100 rig, used by OpenFOAM based on LES case I.

walls. The vertical profiles of flow variables are compared in Fig. 4.18, showing that the wall heat losses only slightly decrease the temperature close to the top/bottom inner chamber walls. This indicates that the thermal boundary condition of the solid walls has very limited influence on the unforced flow and flame simulations, possibly due to (*i*) the entire flame region being far away from the top/bottom walls (e.g., Fig. 4.17(c)); (*ii*) the computational mesh near the inner chamber walls not being fine enough to capture the heat loss effect.

To further investigate the impact of mesh density on the unforced flame, a refined mesh of ∼14.5 million unstructured cells (see Fig. 4.19) has been applied by OpenFOAM to the same computational domain shown in Fig. 4.4(a). Compared to the coarse and structured mesh in Fig. 4.4(b), the refined mesh largely increases the cell density within the swirler, premixing chamber and front part of the combustion chamber, etc., and also along the chamber centreline towards the exit.

The time-averaged contours of the flow field and the flame obtained by Case I with adiabatic walls using OpenFOAM are compared in Fig. 4.20. It is discovered that (*i*) the mean flow fields are generally similar between the two mesh arrangements, except for the central recirculation zone. In the coarse mesh, this zone is a single continuous large region, while in the refined mesh the recirculation zone is broken and consists of multiple smaller vortices (see the streamlines in Fig. 4.20(a)); (*ii*) the axial extension of the low temperature zone becomes slightly shorter with the refined mesh (Fig. 4.20(b)), and (*iii*) the mean heat release rate is slightly higher at

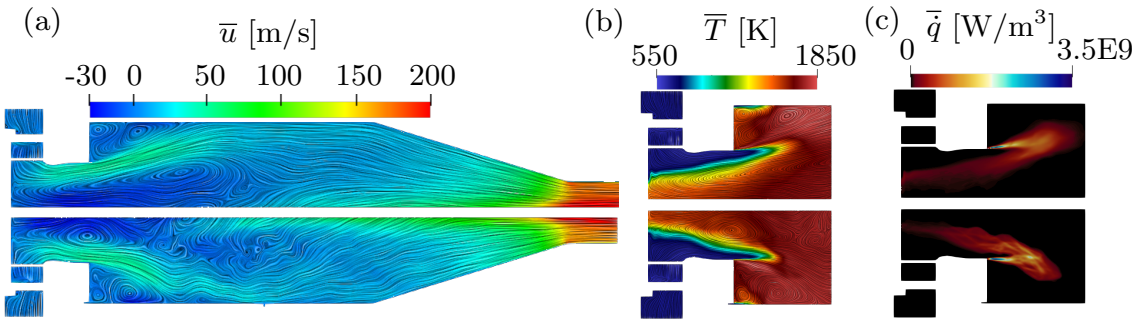


FIGURE 4.20: Time-averaged contours of (a) axial velocity, $\overline{u}$, (b) temperature, $\overline{T}$, and (c) volumetric heat release rate, $\overline{\dot{q}}$, computed by LES Case I with (top-half) 7.0-million-cell structured mesh and (bottom-half) 14.5-million-cell unstructured mesh.

some locations within the flame for a higher mesh density (Fig. 4.20(c)). Although a longer simulation time may be needed for the refined LES results to fully converge, it is expected that the flame simulated with a refined mesh is generally similar to that with a coarse mesh. The higher $\overline{\dot{q}}$ magnitudes at certain locations may be due to the increase of mesh density allowing the reaction rate within smaller flow structures to be computed directly, thus the local reaction processes in the flame can be better captured, illustrating some local regions with higher heat release rates. Nevertheless, for the present combustor an increase of the mesh density does not significantly improve the simulations of unforced flow and flame, except for providing more details of the flow features and flame structures at some locations.

Figure 4.21 compares some flow variables obtained by both coarse and refined meshes. It is noted that all the selected variables generally match well between the two meshes and agree with the experimental data. At some locations (e.g., $x = 88.7$ mm for v_{rms}, Fig. 4.21(f)), the coarse structured mesh even has a slightly better accuracy compared to the refined mesh, suggesting that a longer simulation time may be needed by the refined mesh case. Another possible reason for the difference between the two meshes may be due to the tetrahedral cell type used by the unstructured refined mesh, which has higher numerical dissipation rates than the structured hexahedral mesh. These imply that the 7-million-cell structured mesh (see Fig. 4.4(b)) is sufficiently accurate for the present SGT-100 combustor study.

4.4 Flame Describing Functions

Based on the above-validated unforced LES results, the forced flame responses to an upstream velocity perturbation are investigated in this section. The computed flame responses are then

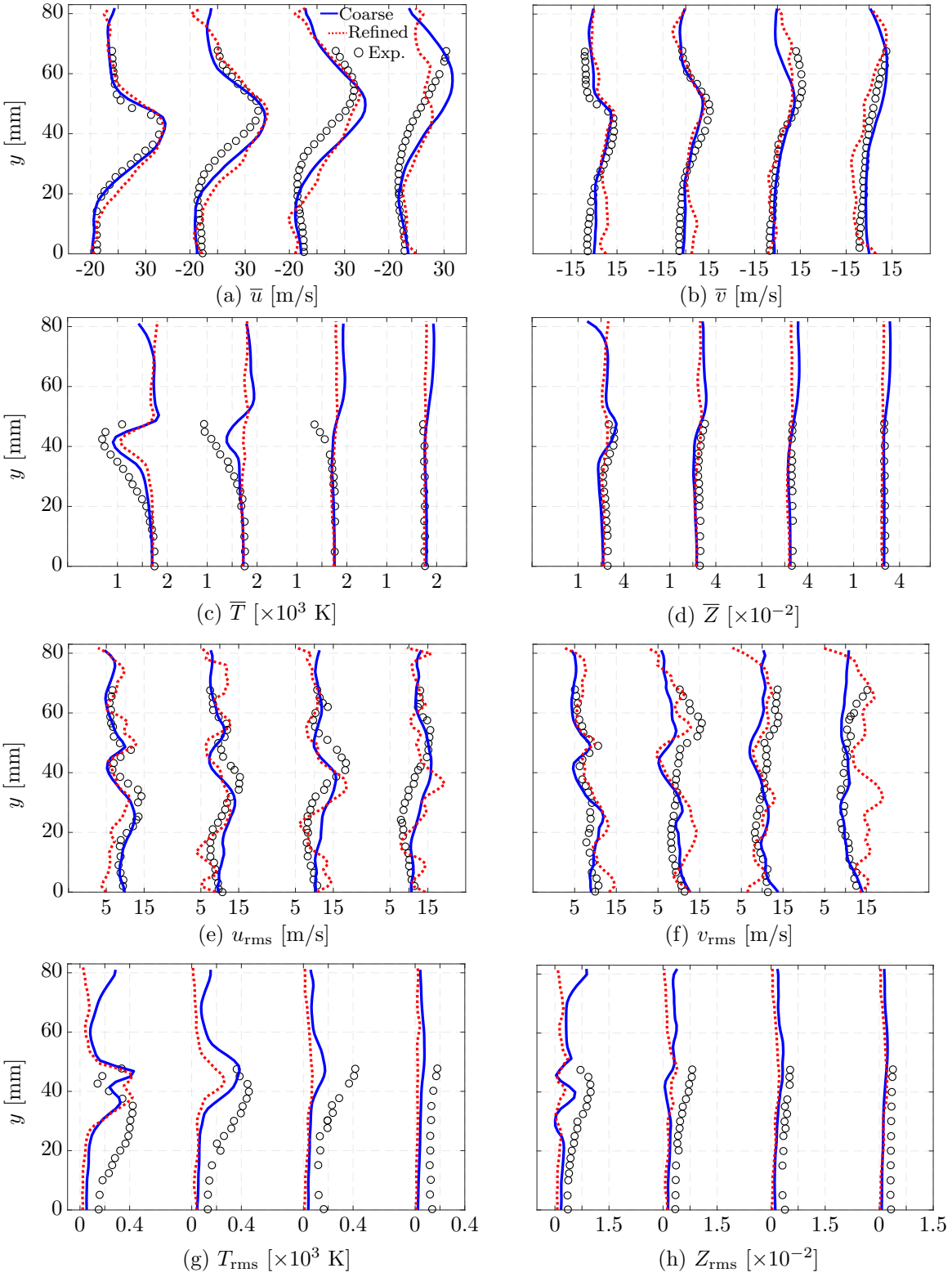


FIGURE 4.21: Vertical profiles of (a-d) mean and (e-h) RMS flow variables at: x =18.7, 38.7, 58.7 and 88.7 mm, all computed by LES Case I with adiabatic wall condition. Blue solid line: 7 million cell structured mesh; red dotted line: 14.5 million cell unstructured mesh; black circle: experimental data [14].

TABLE 4.5: Forced flame simulations based on each LES case. f_u: perturbation frequency; A_u: normalised perturbation amplitude.

Forced Simulation No.	1	2	3	4	5	6	7	8
A_u [-]				0.1				
f_u [Hz]	200	300	400	500	600	800	1000	1500
Forced Simulation No.	9	10	11	12	13	14	15	16
A_u [-]				0.2				
f_u [Hz]	200	300	400	500	600	800	1000	1500

used to construct the weakly nonlinear flame describing functions (FDFs), as defined in Eq. 1.8.

Firstly, the simulated unforced flame is submitted to an upstream velocity perturbation, u_1, located at the radial main air inlet at the swirler entry, varying harmonically as:

$$u_1 = \overline{u}_1 \cdot [1 + A_u \sin(2\pi f_u t)], \tag{4.1}$$

where f_u is the perturbation frequency and $A_u = |u_1'/\overline{u}_1|$ the normalised perturbation amplitude. The mean inflow velocity, $\overline{u}_1$, is fixed at 4.87 m/s. In this work, two perturbation amplitudes (A_u = 0.1 and 0.2) across eight forcing frequencies within the range f_u = 200 – 1500 Hz are considered, resulting in a total of 16 forced simulations for each LES case (see Table 4.5). In Section 5.1.3, the forcing amplitude for LES Case V will be further extended up to $A_u = 0.5$ for nonlinear thermoacoustic predictions. The adiabatic wall condition and the coarse structured mesh in Fig. 4.4(b) are used by all the forced simulations.

The reason to choose the above two forcing amplitudes is based on the experiments performed by Balachandran et al. [53], who measured that the flame heat release response became nonlinear under a velocity perturbation amplitude of ∼15% of the bulk inflow velocity. Therefore $A_u = 0.1$ falls in the linear flame response regime while $A_u = 0.2$ corresponds to nonlinear flame responses, which allows the comparison between the linear and nonlinear flame models. The selected forcing frequency range, f_u = 200 – 1500 Hz, covers the limit cycle oscillation frequencies typical of gas turbine combustor instabilities [222].

For each forced simulation, the volumetric heat release rate field, $\dot{q}(x, y, z)$, is computed at each time step and spatially integrated over the entire domain volume, $\mathcal{V}$. This leads to the total

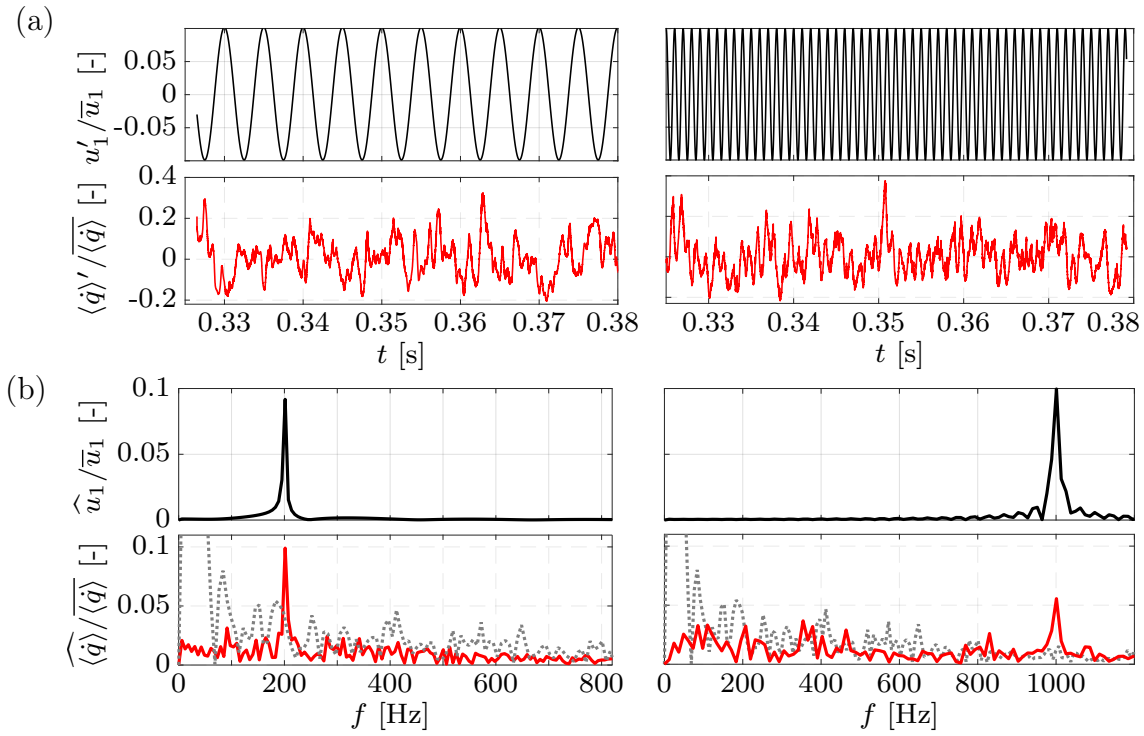


FIGURE 4.22: Two forced simulations based on Case I with forcing level $A_u = 0.1$ at forcing frequency (left) $f_u = 200$ Hz and (right) $f_u = 1000$ Hz. (a) Time-signals of (top) $u_1'/\overline{u}_1$ and (bottom) $\langle\dot{q}\rangle'/\overline{\langle\dot{q}\rangle}$; (b) FFT spectra magnitude of (top) $\widehat{u}_1/\overline{u}_1$ and (bottom) $\widehat{\langle\dot{q}\rangle}/\overline{\langle\dot{q}\rangle}$. The spectra of $\widehat{\langle\dot{q}\rangle}/\overline{\langle\dot{q}\rangle}$ for the unforced Case I are marked by grey dotted lines.

heat release rate, $\langle\dot{q}\rangle = \iiint_{\mathcal{V}} \dot{q}(x,y,z)\mathrm{d}\mathcal{V}$. The time-signal of $\langle\dot{q}\rangle$ is recorded for at least 15 – 20 forcing cycles after the initial transients vanish, and the convergence of the computation is usually achieved after 10 – 12 cycles. Since the weakly nonlinear theory [62] assumes that the main heat release response occurs at the forcing frequency, f_u, the time-variation of $\langle\dot{q}\rangle$ can be approximated by a harmonic expression (cf., Eq. 4.1):

$$\langle\dot{q}\rangle = \overline{\langle\dot{q}\rangle} \cdot [1 \ + A_{\dot{q}} \sin(2\pi f_u t + \varphi_{\dot{q}})], \tag{4.2}$$

where $A_{\dot{q}} = \left(\widehat{\langle\dot{q}\rangle}/\overline{\langle\dot{q}\rangle}\right)|_{f_u}$ is the magnitude of the fast Fourier transform (FFT) of the time-series, $\langle\dot{q}\rangle'/\overline{\langle\dot{q}\rangle}$, at forcing frequency, f_u. The term $\varphi_{\dot{q}}$ is the phase difference between the forcing velocity, u_1, and the resulting total heat release rate, $\langle\dot{q}\rangle$, and is found from the phase value at which the cross-correlation between the time-variations of u_1 and $\langle\dot{q}\rangle$ has the maximum magnitude.

Two forced simulations are illustrated in Fig. 4.22 based on LES Case I. The forcing amplitude for both simulations is $A_u = 0.1$, with one having a low forcing frequency of $f_u = 200$ Hz, and

the other has a higher forcing frequency of $f_u = 1000$ Hz. Figure 4.22(a) shows that for both forced simulations, although the imposed velocity perturbation, $u_1'/\overline{u}_1$, is an ideal harmonic signal at a single frequency, the responding signal of the total heat release rate fluctuation, $\langle\dot{q}\rangle'/\overline{\langle\dot{q}\rangle}$, is much more irregular. Its FFT spectrum contains a wide range of frequencies (see Fig. 4.22(b)-(bottom)). Nevertheless, the main spectral peak of $\widehat{\langle\dot{q}\rangle}/\overline{\langle\dot{q}\rangle}$ is found exactly at the forcing frequency, f_u, for both simulations, with the responses at all the other frequencies being much weaker. The same phenomena have been found across the other LES cases, validating the weakly nonlinear assumption used for the FDF.

It is also noted that the forced flame response magnitude (red solid line) always rises significantly above the background noise (grey dotted line) from the unforced turbulent flow at the same frequency (see Fig. 4.22(b)-(bottom)), indicating that the background noise has very little impact on the computed flame response. Besides, the forced spectral peak at $f = 200$ Hz is much higher than that at $f = 1000$ Hz, indicating a stronger flame response at a lower frequency. This is consistent with the wide observation that the flame acts as a low-pass filter, whose response to upstream excitation decays with increasing frequency [54].

After calculating the values of $A_{\dot{q}}$ and $\varphi_{\dot{q}}$, defined in Eq. 4.2, for each of the forced simulations listed in Table 4.5, the gain, G, and phase, φ, of the FDF follow from:

$$G = A_{\dot{q}}/A_u \quad \text{and} \quad \varphi = \varphi_{\dot{q}} \pm N \cdot 2\pi, \tag{4.3}$$

where N is an appropriate integer. A high-order polynomial fitting is then performed, using the "fitfrd" command in MATLAB [223], for all the G and φ data points over frequency at each forcing amplitude. These result in the complete FDFs shown in Figs. 4.23 – 4.28 for LES Cases I – V. For all of the simulated FDFs, some common trends are evident:

(*i*) The FDF gain, G, has two local maxima with a local minimum in between. The higher of the gain maxima occurs at a lower frequency which falls in the range $f \simeq 200$ – 300 Hz, with the local gain minimum near $f = 600$ Hz and the second gain maximum at $f = 800$ Hz. The presence of these local gain extrema is consistent with the experimental and numerical studies of atmospheric pressure swirling combustors (e.g., [81, 224]), which has been proved to be associated with the constructive and destructive interactions between the imposed longitudinal perturbation and the azimuthal perturbations generated by the swirling flow. In contrast to the atmospheric pressure findings (e.g., [81]), for which the magnitude of

the local gain minimum falls almost to zero, the FDF of the present pressurised combustor exhibits a less pronounced gain minimum with $G \simeq 0.5$ at $f = 600$ Hz (e.g., see Fig. 4.23).

(ii) The FDF phase, φ, approximately linearly decreases with frequency, this being consistent with recent LES studies (e.g., [81]). The likely reason is that the phase mainly relies on the time delay between the upstream perturbation and downstream flame response, which is inversely proportional to the mean flow velocity, $\overline{u}$, and is little affected by other factors such as the mean pressure or reaction chemistry, etc. Although some dynamics in φ occur near the frequency of the local gain minimum, these are much less pronounced for this high pressure rig than at atmospheric pressure [81, 224] (e.g., see Fig. 4.23).

(iii) An increase in the upstream perturbation amplitude, A_u, leads to a decrease in the FDF gain, G, especially at higher perturbation frequencies. This is known as the "saturation" of the FDF gain, caused by the levelling-off of heat release rate oscillations at higher perturbation levels, and has been observed in previous LES works (e.g., [119]). However, very little forcing amplitude dependence is evident for the FDF phase, φ (e.g., see Fig. 4.25).

The simulated FDFs for all the LES cases defined in Table 4.4 are now compared, in order to systematically evaluate the effects of SGS combustion model, reaction chemistry, operating pressure and wall heat losses, etc., on the forced flame response to an upstream perturbation.

4.4.1 Effect of SGS combustion model on FDFs

The effect of SGS combustion model on the forced flame is firstly studied. The FDFs for LES Case I with the LES-PaSR combustion model and Case II with the LES-PDF model are compared in Fig. 4.23, with only the lower forcing amplitude, $A_u = 0.1$, plotted. The trends of both the FDF gain, G, and phase, φ, generally match well, other than for small gain mismatches at lower frequencies (e.g., $f = 300 - 600$ Hz). This may be associated with the higher mean heat release rate predicted by the LES-PDF model, as shown in Fig. 4.6(c). Overall, the effect of the SGS combustion modelling on the forced flame response is relatively small.

For the LES-PDF model, the effect of increasing the stochastic field number on the FDF is studied based on Case III (with 15-step reaction at $\overline{p} = 3$ bar). As shown in Fig. 4.24, the computed FDF gain and phase values using 8 stochastic fields are very close to those obtained with only one field. This similarity applies to both perturbation levels ($A_u = 0.1$ and 0.2) across

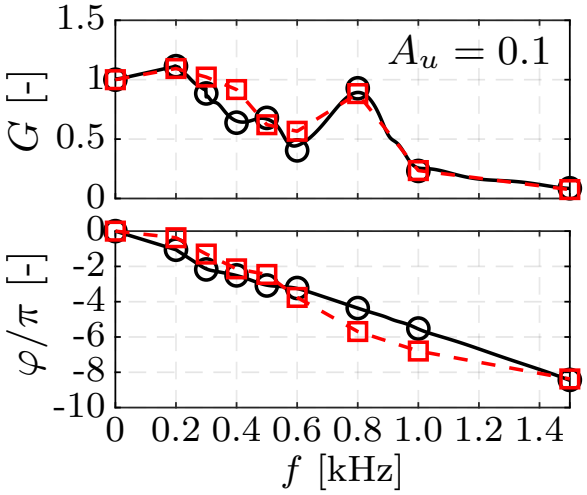


FIGURE 4.23: FDFs at forcing level $A_u = 0.1$ (i.e. FTFs), obtained at $\overline{p} = 3$ bar with 4-step chemistry for Case I with LES-PaSR model (solid line with circles) and Case II with LES-PDF model (dashed line with squares). (Top) gain G; (bottom) phase φ.

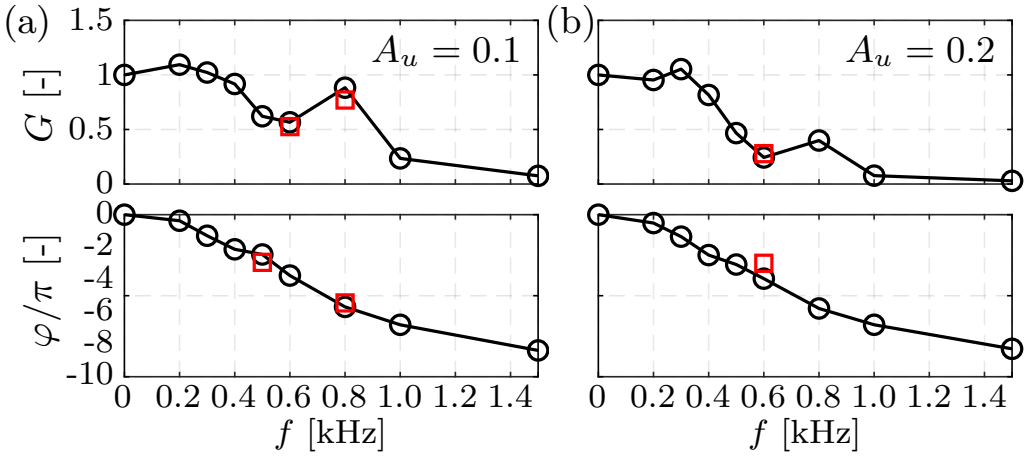


FIGURE 4.24: FDFs at $\overline{p} = 3$ bar, obtained for Case III with LES-PDF combustion model using one field (solid line with circles) or 8 stochastic fields (squares). (Top) gain G; (bottom) phase φ. Forcing amplitude: (a) $A_u = 0.1$; (b) $A_u = 0.2$.

two perturbation frequencies ($f_u = 600$ and 800 Hz). Although a more detailed analysis of the field number effect is needed at other frequencies, the presented good match between one field and 8 fields FDFs indicates that one field may be sufficient for the present combustor, which is therefore used for all the following BOFFIN simulations in this thesis.

4.4.2 Effect of reaction chemistry on FDFs

The impact of chemical reaction scheme on the flame response is then investigated. The FDFs simulated for Case II (with 4-step chemistry) and Case III (with 15-step chemistry) are compared

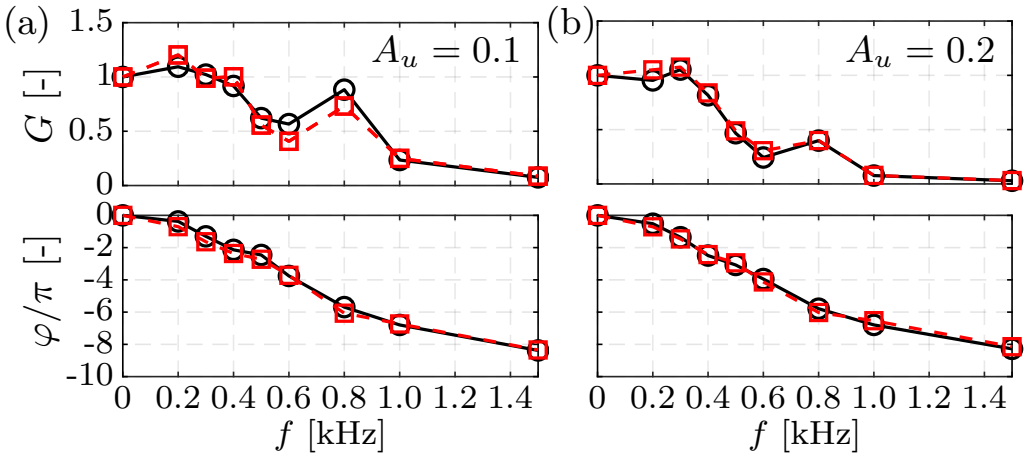


FIGURE 4.25: FDFs at $\overline{p} = 3$ bar for Case II with 4-step reaction scheme (solid line with circles) and Case III with 15-step reaction scheme (dashed line with squares), with (top) gain G and (bottom) phase φ. Forcing amplitude: (a) $A_u = 0.1$; (b) $A_u = 0.2$.

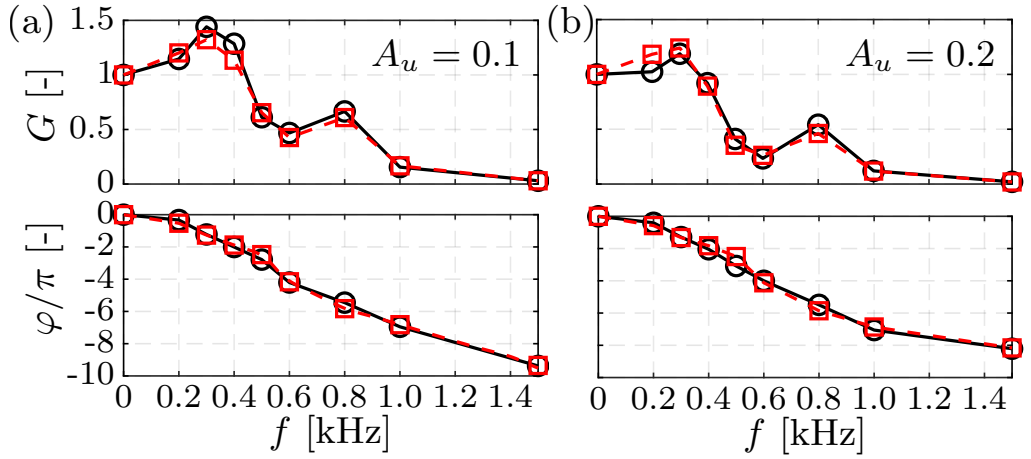


FIGURE 4.26: FDFs at $\overline{p} = 6$ bar for Case IV with 4-step reaction scheme (solid line with circles) and Case V with 15-step reaction scheme (dashed line with squares), with (top) gain G and (bottom) phase φ. Forcing amplitude: (a) $A_u = 0.1$; (b) $A_u = 0.2$.

at $\overline{p} = 3$ bar in Fig. 4.25, at both forcing amplitudes ($A_u = 0.1$ and 0.2). The magnitudes and trends of the FDF gain, G, and phase, φ, both match well, with the gain's difference below 10%. These good matches are maintained at a higher pressure of $\overline{p} = 6$ bar (see Fig. 4.26), which compares Cases IV and V. Although the predicted mean flame shapes differ with the reaction schemes used at both pressures, with the more detailed 15-step chemistry better predicting the unforced flame, this difference barely affects the forced flame responses and the resulting FDFs.

To further investigate the effect of reaction chemistry on the forced flame responses, the unsteady flame heat release rate at $\overline{p} = 3$ bar for Case II (with 4-step reaction) and Case III (with 15-step reaction) are compared in Figs. 4.27(a, b). An upstream forcing signal with frequency

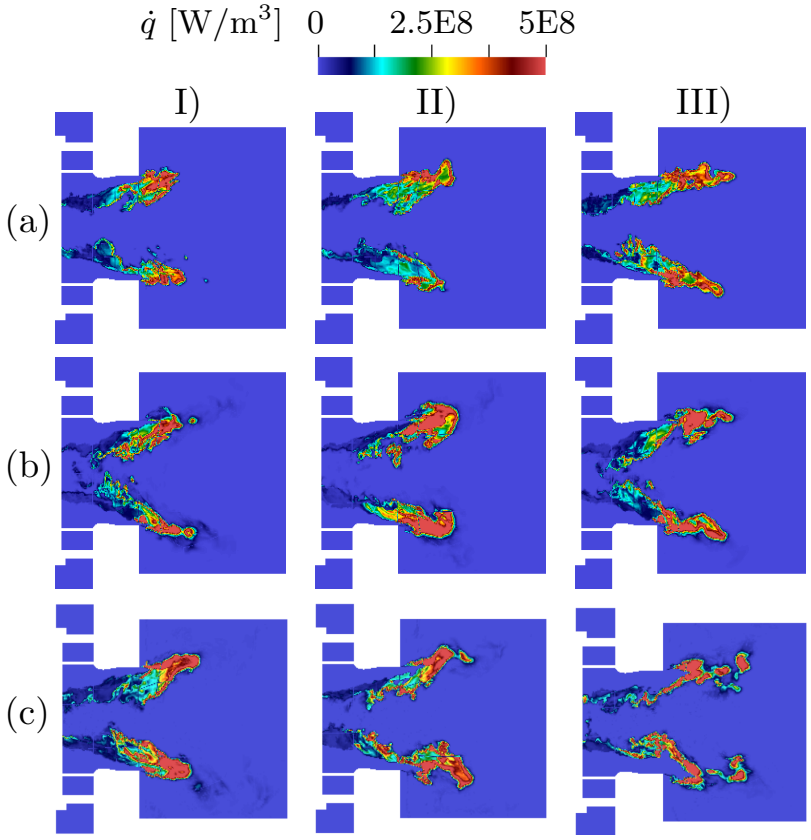


FIGURE 4.27: Contours of volumetric flame heat release rate, $\dot{q}(x, y, z)$, on a symmetry plane of $z = 0$, all forced by the same perturbation of $A_u = 0.1$, $f_u = 300$ Hz. (I) $\langle\dot{q}\rangle'/\overline{\langle\dot{q}\rangle}$ = -0.1 (minimum); (II) $\langle\dot{q}\rangle'/\overline{\langle\dot{q}\rangle} = 0$; (III) $\langle\dot{q}\rangle'/\overline{\langle\dot{q}\rangle} = 0.1$ (maximum). (a) Case II (4-step reaction, $\overline{p} = 3$ bar); (b) Case III (15-step reaction, $\overline{p} = 3$ bar); (c) Case V (15-step reaction, $\overline{p} = 6$ bar).

$f_u = 300$ Hz and amplitude $A_u = 0.1$ is imposed, leading to strong flame heat release oscillations. Three time snapshots of the volumetric heat release rate field, $\dot{q}(x, y, z)$, are then plotted within a forcing period, these being chosen to correspond to the normalised spatial integration of $\dot{q}'$, i.e. $\langle\dot{q}\rangle'/\overline{\langle\dot{q}\rangle}$, having its minimum, zero and maximum values. Although the mean heat release rate, $\overline{\langle\dot{q}\rangle}$, differs between the two reaction schemes used, the flame's oscillatory behaviour around its mean position is generally similar — the flame is always the shortest when $\langle\dot{q}\rangle'/\overline{\langle\dot{q}\rangle}$ has its minimum value of -0.1 (Fig. 4.27-I), becoming longer when $\langle\dot{q}\rangle'/\overline{\langle\dot{q}\rangle}$ equals zero (Fig. 4.27-II), and being the longest for the maximum value of $\langle\dot{q}\rangle'/\overline{\langle\dot{q}\rangle} = 0.1$ (Fig. 4.27-III).

For the present highly-turbulent flame, its heat release rate fluctuation is mainly associated with the variation in the flame surface area. The comparison between Cases II (Fig. 4.27(a)) and III (Fig. 4.27(b)) indicates that a change in the reaction scheme may modify the response of the flame's internal structure to the upstream forcing, even under the same operating pressure.

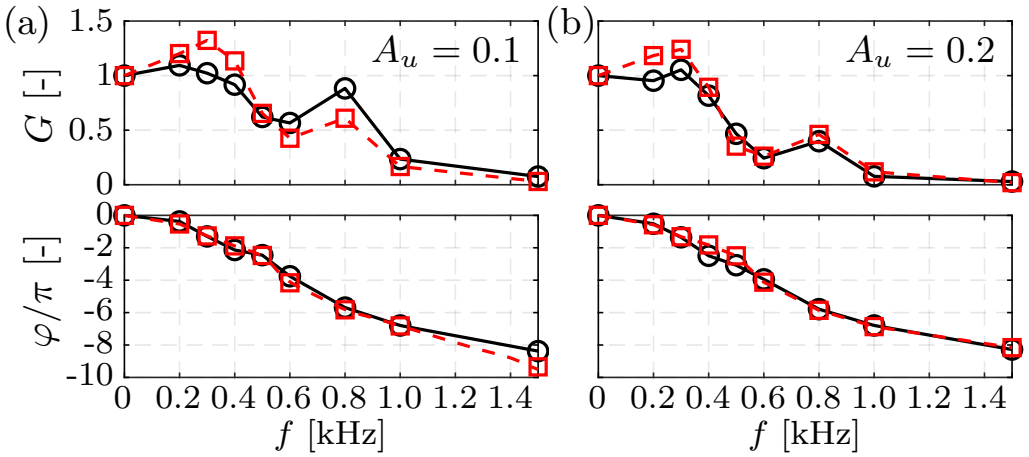


FIGURE 4.28: FDFs obtained for Case III at $\overline{p} = 3$ bar (solid line with circles) and Case V at $\overline{p} = 6$ bar (dashed line with squares), both with LES-PDF combustion model and 15-step chemistry. (Top) gain G; (bottom) phase φ. (a) $A_u = 0.1$; (b) $A_u = 0.2$.

Although the more detailed 15-step reaction scheme yields a slight increase in the axial flame length (i.e. the penetration distance of the heat release zone into the combustion chamber) throughout the cycle (see Fig. 4.27(b)), consistent with the predicted longer unforced flame in Fig. 4.11(c), the differences in the detailed flame internal structure may still result in a similar total flame surface area for the two cases, explaining the similarity in the FDF gains between the two reaction schemes (see Fig. 4.25).

4.4.3 Effect of operating pressure on FDFs

Thirdly, the effect of mean operating pressure on the simulated FDFs is analysed, by comparing Case III ($\overline{p} = 3$ bar) and Case V ($\overline{p} = 6$ bar), both using the LES-PDF combustion model and 15-step chemistry. Figure 4.28 shows that at both forcing amplitudes ($A_u = 0.1$ and 0.2), increasing the mean pressure leads to an increase in the FDF gain at lower frequencies ($f \leq$ 500 Hz). This behaviour is in agreement with a recent experiment by Sabatino et al. [96], who investigated the effect of mean pressure on the local gain maximum of fully-premixed swirling flame forced responses in a lab-scale combustor.

As shown in Fig. 4.28(a), the present flame also exhibits a strong pressure-dependence of the frequency of the maximum FDF gain: at $\overline{p} = 3$ bar the maximum $G \simeq 1.1$ and is found at frequency $f = 200$ Hz, while at $\overline{p} = 6$ bar it increases in magnitude to $G \simeq 1.3$ and shifts to frequency $f = 300$ Hz. This, however, is not in agreement with what was measured in [96]. In their experimental work, a mean pressure increase from 1 bar to 5 bar resulted in the gain's

maximum remaining at the same frequency, except at 5 bar where a very small frequency shift of ∼30 Hz was observed. A more evident disagreement between the present flame FDF, which at higher frequencies (e.g., $f = 600 - 1000$ Hz) shows a slight decrease in gain with pressure (Fig. 4.28(a)), and the methane flame FDF in [96] is observed, although a similar gain decrease with pressure at high frequencies was measured for a propane flame in the same experimental study [96]. These discrepancies may arise from the differences in the combustor geometry, flame shape, fuel type and operating pressure, etc.

Furthermore, the equivalence ratio used in experiments [96] was adjusted with the mean pressure to ensure the same mean axial flame length at all pressures, while in the present SGT-100 study a fixed equivalence ratio of $\phi_e = 0.6$ is used at both 3 bar and 6 bar pressures, giving slightly different mean axial flame lengths. These may lead to different coupling strengths between the flame response and the imposed hydrodynamic perturbation across the two operating pressures, shifting the frequency of the maximum FDF gain as shown in Fig. 4.28(a).

At the higher forcing level of $A_u = 0.2$ (see Fig. 4.28(b)), however, the dependence of the FDF gain on the mean pressure is much weaker, especially at higher frequencies. This is mainly due to the stronger saturation of the flame heat release rate oscillation at higher forcing levels and frequencies. For the FDF phase, φ, the effect of operating pressure is always negligible, which has been confirmed by experiments [96].

Further insights into the effect of mean operating pressure on the simulated FDFs are provided by the flame dynamics for Case III ($\overline{p} = 3$ bar, Fig. 4.27(b)) and Case V ($\overline{p} = 6$ bar, Fig. 4.27(c)). The predicted flame structures are now similar, probably due to the same 15-step reaction scheme used by the two cases. Their flame surface areas can thus be compared by examining their axial flame lengths. Increasing the mean pressure slightly increases the axial flame length, likely to be associated with the lower laminar burning velocity predicted at 6 bar (see Fig. 4.10(b)).

The above frequency dependence of FDF gains with mean pressure (see Fig. 4.28(a)) may now be explained: the increase in mean pressure gives a lower laminar burning velocity and thus a longer flame length and a longer flame response time. At lower forcing frequencies (e.g., $f_u =$ 300 Hz), the time-scale (i.e. period) of the perturbation signal is also large, leading to a stronger coupling between the time-scales of perturbation and flame response and thus larger FDF gains at 6 bar. In contrast, at higher forcing frequencies (e.g., $f_u = 800$ Hz), the forcing time-scale

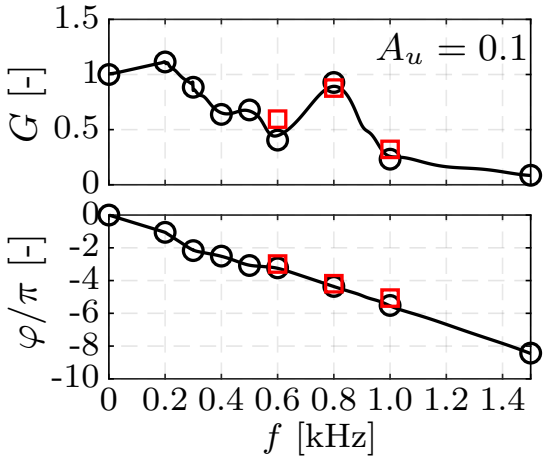


FIGURE 4.29: FDFs at $\overline{p} = 3$ bar for forcing amplitude $A_u = 0.1$, obtained for Case I with (solid line with circles) adiabatic wall condition and (squares) non-adiabatic wall condition with fixed wall temperatures. (Top) gain G; (bottom) phase φ.

becomes smaller, leading to a weaker coupling with the flame response time and thus smaller FDF gains at a higher pressure.

It has also been noted that the above difference in the flame axial lengths across the pressures does not perfectly match previous experimental data (e.g., OH PLIF) on the same combustor [24], where the flame penetration lengths are much closer between the two pressures and even slightly longer at a lower pressure. This may be because in the real experiments the equivalence ratio is slightly lower (i.e. leaner) at 3 bar pressure, giving a lower laminar burning velocity and thus a longer reaction zone. In the present LES study, however, the equivalence ratio is fixed at both pressures, allowing the pressure effect on the flame axial length to be more evident.

In order to better illustrate the variation of the forced flame responses across different operating pressures, variables such as the flame surface density, flame wrinkling strength and the "centroid" of the heat release field, etc., also need to be systematically compared. However, these studies are beyond the scope of the present thesis.

4.4.4 Effect of wall heat losses on FDFs

Finally, the effect of wall heat losses on the simulated FDFs is discussed. Following the unforced LES results based on Case I, the influence of non-adiabatic wall condition (with fixed wall temperatures) on the mean flow variables is found negligible except near the inner chamber walls, where most heat transfer occurs through the solid walls (see Figs. 4.17– 4.18).

The same analysis is performed here for the forced flame responses, through spot-check forced simulations across several forcing frequencies. As shown in Fig. 4.29, the full FDF obtained by Case I with adiabatic wall condition is compared against the gain and phase data points computed by the non-adiabatic wall condition with fixed wall temperatures. It is observed that for forcing frequencies f_u = 600, 800 and 1000 Hz at a fixed forcing amplitude of A_u = 0.1, the wall heat losses always have a very limited impact on the magnitudes of both FDF gain and phase. This is consistent with the unforced LES observation in Figs. 4.17(b, c), where the flame tips are distant from the inner chamber walls, and thus not highly affected by the thermal boundary conditions of the solid walls.

4.5 Summary

In this chapter, the flow field and flame responses in the pressurised industrial SGT-100 combustor are numerically investigated. Firstly, the unforced flow field and mean flame behaviour are simluated using two incompressible LES solvers (BOFFIN and OpenFOAM) and validated by high quality experimental data. A series of LES cases have been performed to evaluate the effects of SGS turbulence model, SGS combustion model (LES-PaSR vs. LES-PDF), chemical reaction scheme (4-step vs. 15-step), operating pressure (3 bar vs. 6 bar), wall heat losses and mesh density, etc., on the unforced LES results. Both SGS combustion models and the two reaction schemes used are validated against experiments and found accurate to capture the flow field and the flame behaviour. The dynamic Smagorinsky model is recommended for the SGS turbulence modelling.

Several key phenomena have been observed: (*i*) the mean flow field is only marginally affected by all the above-mentioned factors; (*ii*) the LES-PDF combustion model, 4-step reaction scheme and 6 bar operating pressure all lead to a shorter axial extent of the low temperature zone and an increase of the mean heat release rate level in the combustor; (*iii*) the more detailed 15-step chemistry gives a slightly better prediction of the mean flame shape, especially at a higher pressure; (*iv*) neither the wall heat losses nor the mesh refinement largely affects the mean flame shape, suggesting that a relatively coarse mesh with adiabatic wall condition is likely to be sufficient for the present simulation and should be used as the optimal choice.

Secondly, the forced heat release responses of the above turbulent swirling flame are computed based on the same series of LES cases, by submitting the flame to an upstream single-frequency

harmonic velocity perturbation with varying frequency and amplitude. The resulting flame describing functions (FDFs) have some common trends: (*i*) all the FDFs have two gain maxima and one gain minimum in between in the frequency domain; (*ii*) the FDF phase generally linearly decreases with frequency; (*iii*) the saturation of FDF gain with increasing perturbation level is evident. For the effects of different modelling assumptions and operating conditions, it is found that: (*i*) at a fixed pressure, the SGS combustion model has a very small impact on the FDF gain. Only one field is used by the LES-PDF model, which has been shown to offer sufficient accuracy; (*ii*) the impact of reaction chemistry on the FDF is marginal, although the mean flame shape and heat release rate differ between the two reaction schemes used. The faster 4-step reaction is thus adequate to capture the forced flame responses for the present combustor; (*iii*) an increase in the mean pressure results in a considerable rise of the FDF gain at low frequencies, but a decrease at higher frequencies, mainly due to the different time-scale coupling strengths between velocity perturbation and flame response across different frequencies.

To reduce the computational costs, the 4-step reaction scheme is recommended for future flame response computations due to its good accuracy and significantly faster computational speed compared to the 15-step scheme. Since the two combustion models used have very close computational speeds and accuracy, both of them can be used for future forced flame simulations.

In summary, a main contribution of this chapter is to find that even though the mean flame shape and dynamics are affected by the SGS combustion model and reaction chemistry used, the forced flame responses and the resulting FDFs are actually very little influenced by these modelling assumptions (i.e. to a lesser degree). These findings may need to be compared with relevant experiments, which is however beyond the scope of this thesis and recommended for the future work.

Chapter 5

SGT-100 Industrial Combustor: Thermoacoustic Instability

Based on the above flow field and flame response LES simulations, the FDFs computed in Chapter 4 for the SGT-100 combustor are now combined with thermoacoustic solvers in this chapter to predict the thermoacoustic instability. Two solvers have been used, which are: (*i*) the low order network wave-based solver, OSCILOS; (*ii*) the Helmholtz-equation-based "H-solver". The thermoacoustic modes computed by both solvers provide the stability maps for the analysed combustor. For those unstable modes, the resulting nonlinear limit cycle oscillations are also predicted.

It should also be stated here that some of the results presented in Chapters 4– 5 have been published in [177, 225].

5.1 Thermoacoustic Stability Predictions by OSCILOS

Firstly, the simulated FDFs are coupled with the low order network thermoacoustic solver, OSCILOS [60, 67]. This solver was introduced in detail in Section 2.4.1, and has been widely used and validated against various experimental data (e.g., [5, 68, 177]).

In order to correctly model the acoustic wave behaviour, the network approach used by OSCILOS simplifies the DLR test rig geometry (Fig. 4.1(a)) into a network of connected simple modules, as shown in Fig. 5.1. In this network geometry, the main combustor components, e.g., the

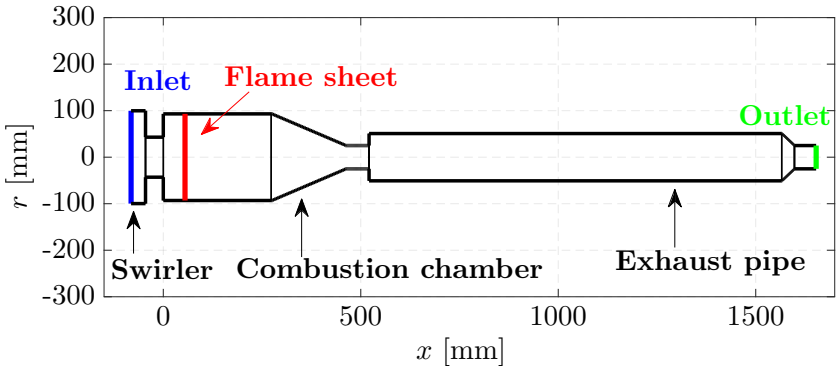


FIGURE 5.1: The simplified network geometry representing the SGT-100 combustor, with the origin $x = 0$ located at the combustion chamber entrance. r: radial coordinate.

swirler, premixing chamber, combustion chamber and exhaust pipe, etc., are all represented as straight duct modules, with their lengths and cross-sectional areas chosen to match the original geometry and the measured mass flow rates. The further downstream water spray section is neglected due to the large anticipated dissipation of acoustic energy inside it. The upstream air plenum is also neglected as it is easier for OSCILOS to prescribe a physical acoustic boundary condition at the swirler inlet. The decreasing cross-sectional area of the contraction part of the combustion chamber is modelled as a sequence of 50 constant area ducts with linearly decreasing diameters [67]. The mean flow through the entire rig is accounted for, with all the time-averaged flow variables (e.g., $\overline{p}$, $\overline{\rho}$, $\overline{u}$) assumed constant within each duct module, changing only across the module interfaces.

In the above network geometry, the acoustic wave amplitudes are assumed sufficiently small, so the flow perturbations can be treated as linear [54, 174]. At the low frequencies, it follows that only plane acoustic waves can exist — the cut-off frequency, ω_{ic}, of higher-order modes for the present network is ∼2 kHz, calculated based on the theory introduced in Section 2.2.2. The acoustic perturbations satisfy the convected wave equations in each network module, using separate strengths for the downstream and upstream propagating acoustic waves, respectively (see Eqs. 2.27). These wave strengths are tracked between modules using linearised flow conservation equations — these account for the losses due to stagnation pressure drop at area expansions [5]. The acoustic boundary conditions for the network geometry are prescribed using the pressure reflection coefficients, R. Since no experimental data is available for R, analytical models are used in this work for the reflection coefficients at both inlet and outlet of the network.

Since the heat release zone of the analysed flame (e.g., see Fig. 4.6(c)) has a much shorter axial extent (∼100 mm) compared to the dominant acoustic wavelengths (∼1 – 4 m), suggesting that

TABLE 5.1: Variables of the acoustic impedance model for the perforated plate at both operating pressures.

Variable	$\overline{\rho}$ [kg/m^3]	$\overline{c}$ [m/s]	μ [Pa·s]	t_p [m]
Value	1.56 (3 bar) 3.13 (6 bar)	518.31	1.8e-5	3e-3
Variable	d_h [m]	σ_p [-]	θ_f [-]	δ_h [m]
Value	4e-3	0.156	1.0	$0.25d_h$

the flame is "acoustically compact", the reaction zone is represented by an infinitely thin 1-D "flame sheet" in the present network (see Fig. 5.1). This flame sheet is located at $x_f = 45$ mm, an axial location chosen to correspond to the maximum mean heat release rate measured by the experiments [24]. Although the LES-simulated flame axial length is slightly different between the two operating pressures (Figs. 4.27(b, c)), the effect of a small axial variation in the 1-D flame sheet's location is found very small on the predicted thermoacoustic modes. Therefore, a fixed flame sheet location is used in this network. The jump conditions for acoustic wave strengths, Eqs. 2.18, derived from the linearised flow conservation equations, are applied across this thin flame sheet (see Section 2.3 for more details).

At the inlet of the above network geometry, the acoustic reflection coefficient, R_{in}, is determined by the damping effect of a metallic perforated plate [226], installed between the air plenum exit and the swirler entry to provide uniform air inflows. The complex acoustic impedance, Z_a, of this plate can be modelled as [227]:

$$Z_a = \left[\frac{1}{\sigma_p}\sqrt{\frac{8\mu k_p}{\overline{\rho}\,\overline{c}}}\left(1+\frac{t_p}{d_h}\right)+\theta_f\right]+i\frac{k_p}{\sigma_p}\left(t_p+\delta_h\right), \tag{5.1}$$

where $\overline{\rho}$ denotes mean fluid density, $\overline{c}$ the mean speed of sound, $k_p = 2\pi f/\overline{c}$ the wave number for this plate, t_p the perforated plate thickness, d_h the hole diameter on the plate and σ_p the porosity (i.e. the ratio of total hole area to the plate area). θ_f is the additional flow resistance [228] caused by the metallic sleeve, and δ_h the hole end correction which is equal to $0.25d_h$. The values of these parameters are listed in Table 5.1, and the inlet reflection coefficient is then given as: $R_{\text{in}} = (1 - Z_a)/(1 + Z_a)$.

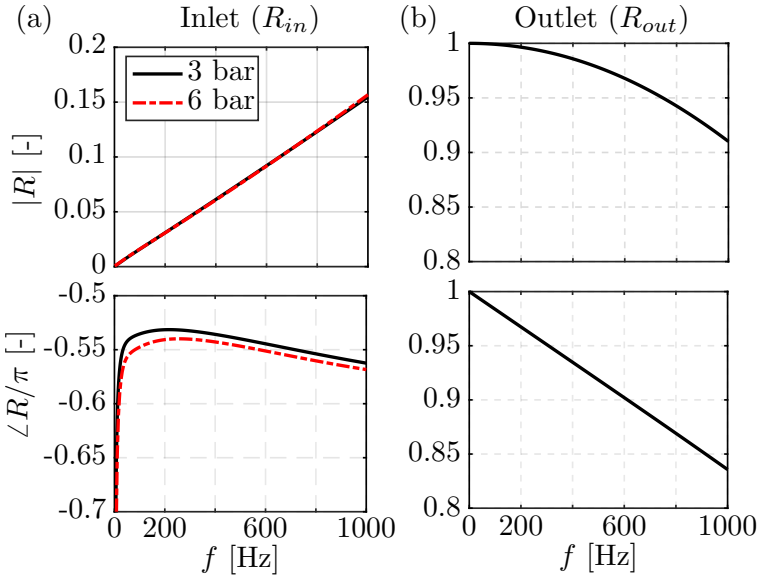


FIGURE 5.2: Pressure reflection coefficients at (a) inlet, R_{in}, and (b) outlet, R_{out}, of the network geometry, with $|R|$ the gain and $\angle R$ the phase. Solid line: $\overline{p} = 3$ bar; dash-dotted line: $\overline{p} = 6$ bar.

For the network outlet, a damped open-end boundary condition is applied based on the acoustic model for an unflanged pipe end [229, 230]. The outlet reflection coefficient, R_{out}, is defined as:

$$R_{\text{out}} = -\left(1 - \frac{\tau_r^2}{2}\omega_i^2\right) \exp\left(-i \cdot 1.22\tau_r\omega_i\right), \tag{5.2}$$

with $\omega_i = 2\pi f$ the angular frequency and $\tau_r = r_o/\overline{c}$ the time delay between the incident and the reflected acoustic waves at the outlet, with r_o the radius of the network's exit plane.

Figure 5.2 shows the gains (denoted $|R|$) and phases (denoted $\angle R$) of the above-modelled reflection coefficients, at both network inlet and outlet. Changing the mean pressure from 3 bar to 6 bar slightly affects the inlet coefficient, but not the outlet coefficient, therefore the latter is only shown for the 3 bar pressure. The low gain magnitude of the inlet coefficient, R_{in}, over frequency (Fig. 5.2(a)) is mainly due to the acoustic energy being largely damped by the perforated plate. In contrast, the acoustic waves are only marginally damped at the network outlet, leading to a large gain for R_{out} (see Fig. 5.2(b)). These reflection coefficient profiles are then combined with the network geometry to build the complete network model. For simplicity, no acoustic damping due to entropy waves or vorticity waves is considered in this work.

To complete the wave-based acoustic modelling process, the mean flow and thermal properties along the axial extent of the network geometry are also needed. The axial variations of mean temperature, $\overline{T}_c(x)$, and mean axial velocity, $\overline{u}_c(x)$, along the network centreline are plotted in

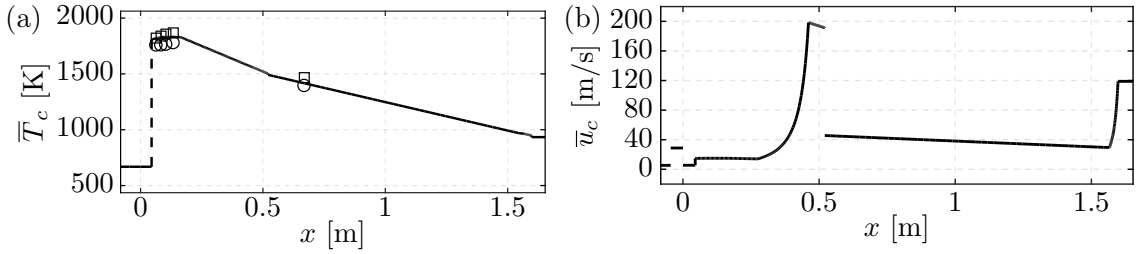


FIGURE 5.3: Axial distributions of time-averaged (a) temperature, $\overline{T}_c(x)$, and (b) axial velocity, $\overline{u}_c(x)$, along the network centreline. $\overline{T}_c(x)$ is reconstructed from experimental data at 3 bar (circles) and 6 bar (squares) pressure; $\overline{u}_c(x)$ is extracted from LES-simulated mean flow field.

Fig. 5.3. The $\overline{T}_c(x)$ profile is reconstructed from the experimental data at the two pressures, while $\overline{u}_c(x)$ is extracted from the LES-simulated mean flow field. The mean temperature increases across the flame sheet from 650 K to 1830 K, then gradually decreases downstream to 891 K. The temperature drop in the exhaust pipe is modelled by a linear function, $\overline{T}_c(x) = 1763 - 510x$ [K] (with $0.521 < x \leq 1.709$ m), which matches the measured data. For the mean velocity, $\overline{u}_c(x)$, an inflow speed of 5.346 m/s is applied at the network inlet, based on LES results and confirmed by experiments. The sudden drops of $\overline{u}_c$ at some locations (e.g., $x = 0.521$ m) are caused by the abrupt changes of cross-sectional area at module interfaces. These mean flow and thermal profiles, which remain the same for both pressures, are then combined with the network geometry in the OSCILOS solver.

5.1.1 Acoustic mode predictions with a passive flame

Based on the above established network model, the thermoacoustic stability of the present combustor can be predicted through OSCILOS. At first, a "passive flame model" is used, assuming that the heat release rate from the flame is always constant and thus has no fluctuations (i.e. $\dot{Q}' = 0$). This passive flame does not respond to any upstream acoustic perturbation.

As described in Section 2.4.1, the thermoacoustic stability of a combustion system is determined by the stabilities of its thermoacoustic modes. These modes are predicted using the "shooting method" [68] in OSCILOS, which identifies the complex frequencies, $\omega = \sigma + i2\pi f$, for which both the inlet and outlet acoustic boundary conditions are satisfied (see Section 2.4.1 for more details). With a passive flame, the predicted thermoacoustic modes are equivalent to the pure acoustic wave modes under a constant heat source, whose modal frequencies are listed in Table 5.2 between 100 – 1100 Hz for the first five modes. The OSCILOS solver predictions are compared

TABLE 5.2: Frequencies of the first 5 acoustic modes predicted by OSCILOS (denoted f_O) and H-solver (denoted f_H) with passive flame and zero mean flow assumptions.

3 bar Mode No.	1	2	3	4	5
f_O [Hz]	173	238	450	724	1018
f_H [Hz]	183	231	437	713	1008
6 bar Mode No.	**1**	**2**	**3**	**4**	**5**
f_O [Hz]	174	237	450	724	1019
f_H [Hz]	178	235	442	718	1012

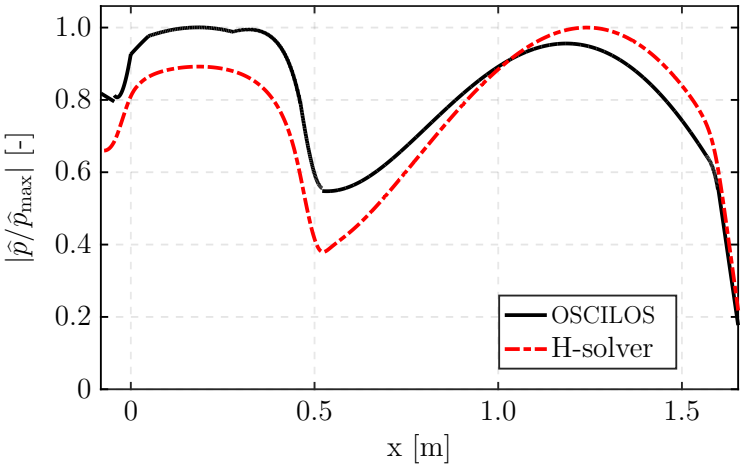


FIGURE 5.4: Shape of the 2nd acoustic mode predicted by OSCILOS (solid line) and H-solver (dash-dotted line) at $\overline{p} = 6$ bar. $\widehat{p}_{\max}$: maximum pressure fluctuation.

with those obtained by the finite element "H-solver" via software COMSOL [69, 180], which retains the original combustor geometry (see Section 2.4.2 for more details). Here both OSCILOS and H-solver neglect the mean flow field (i.e. $\overline{u} = 0$) in their predictions.

It is observed that for both operating pressures, all the predicted modal frequencies match well between OSCILOS and H-solver. Of particular interest is the second mode predicted at frequency ∼230 Hz, very close to the experimentally measured limit cycle frequency (see Fig. 4.2(b)). A comparison of its mode shape, in terms of pressure fluctuation amplitude along the axial extent of the combustor, is then performed between the two solvers at $\overline{p} = 6$ bar, as shown in Fig. 5.4. Again, a good match is retrieved, a result which validates the simplified network geometry in Fig. 5.1 and the modelling assumptions used by OSCILOS.

5.1.2 Linear thermoacoustic stability predictions

Although the above passive flame predictions correctly capture the frequencies and shapes of the acoustic wave modes, the lack of flame response model and the mean flow in the network geometry makes the prediction of actual thermoacoustic modes impossible. By assigning the fitted FDF expressions in Section 4.4 to the 1-D flame sheet located in the network and including the mean flow profile shown in Fig. 5.3(b), the thermoacoustic stability of the analysed combustor can then be predicted.

The linear stability is firstly predicted by OSCILOS under a fixed forcing amplitude perturbation (e.g., $A_u = 0.1$), at which the FDFs can be considered as linear FTFs. Here the FTFs corresponding to Case III at $\overline{p} = 3$ bar and Case V at $\overline{p} = 6$ bar at $A_u = 0.1$ are used, as shown in Fig. 4.28(a). The predicted thermoacoustic modes have now considered the flame-to-acoustic interaction, and are marked as white stars in Fig. 5.5 for frequencies up to $f = 1100$ Hz. Each mode corresponds to a minimum value of the outlet boundary condition error, $\delta_e(\omega)$, defined in Eq. 2.29. The modal frequency, f, are plotted against the mode's growth rate, σ. The mean flow field is now included in the linear predictions, in order to offer accurate acoustic damping effect.

It is discovered that all the modes at $\overline{p} = 3$ bar have negative growth rates (i.e. $\sigma < 0$, Fig. 5.5(a)), meaning that the combustor is linearly stable at this pressure. In contrast, at $\overline{p} = 6$ bar a mode at frequency $f \simeq 231$ Hz has a positive growth rate ($\sigma = 65.6$ rad/s, Fig. 5.5(b)), indicating that the combustor is linearly unstable at this frequency at 6 bar. The predicted linear stabilities at both pressures are in full agreement with the experimental measurements [24, 201] (see Fig. 4.3). The predicted stability difference between the two pressures is clearly associated with the different FTF maximum gain levels shown in Fig. 4.28(a) at $A_u = 0.1$. Similarly, the predictions using the FTFs obtained with the 4-step chemistry (i.e. based on Cases II and IV at $A_u = 0.1$) also successfully capture the correct linear stabilities at both pressures. The unstable mode at 6 bar pressure is now predicted at frequency ~232 Hz.

The underlying physics likely responsible for the above change in the linear stability with pressure is now discussed in detail. The thermoacoustic instability of a combustor can be induced by the interactions of many factors [231], e.g., the flame-to-vortex interactions, flame-to-entropy wave interactions, and the flame response to composition inhomogeneities, etc. In this work, the governing interaction is considered as the combination of (i) the acoustic wave perturbation and

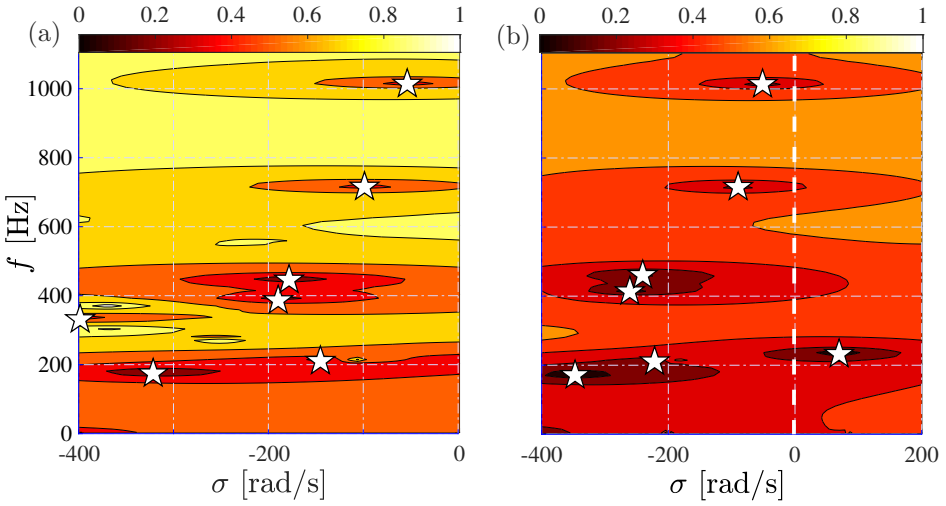


FIGURE 5.5: Linear stability maps of the SGT-100 network geometry at (a) $\overline{p} = 3$ bar and (b) $\overline{p} = 6$ bar. The predicted thermoacoustic modes are marked by white stars at the contour minima of the complex $f - \sigma$ plane for $\log_{10}|\delta_e(\omega)| / (\log_{10}|\delta_e(\omega)|)_{\max}$.

(*ii*) the unsteady flame response. For (*i*), the acoustic wave behaviour is mainly dominated by the combustor geometry, speed of sound and acoustic boundary conditions. The speed of sound in the network is unaffected by the pressure, since the mean temperature axial-profile used (see Fig. 5.3(a)) does not vary with pressure. The outlet boundary condition is pressure-independent, while the inlet reflection coefficient varies only very weakly with pressure. This implies that the acoustic wave behaviour will be almost unaffected by the mean operating pressure.

Additionally, since the mean flow field predicted by the LES (e.g., Figs. 4.11(a) and 4.14(a)) and used here is unaffected by the mean pressure, the effect of vorticity waves and its interaction with the flame do not vary with pressure. Besides, the equivalence ratio used is fixed at $\phi_e = 0.6$ across the two mean pressures, thus the level of composition inhomogeneities should remain generally the same as the pressure changes. In the present prediction, the strengths of all the entropy waves are neglected, although the unchanged mean temperature profile in the network has already guaranteed that the entropy wave effect does not change with pressure. A detailed analysis of the mean temperature contour's effect, which varies over pressure (see Figs. 4.11(b) vs. 4.14(b)) and affects the flame shape, on the stability change may be required, but it is beyond the scope of this thesis.

Therefore, the above factor (*ii*), the unsteady flame heat release response, may be treated as the main source of the stability change for the present network. Indeed, the FDF gain at low frequencies relevant to the mode whose stability changes is higher at 6 bar than at 3 bar (see

TABLE 5.3: Dominant thermoacoustic mode (frequency f, growth rate σ) and linear stability of the network at two mean pressures, predicted by an equivalent $n-\tau$ model.

$\overline{p}$ [bar]	f [Hz]	σ [rad/s]	Stability
3	148.2	70.2	Linearly unstable
6	136.2	126.1	Linearly unstable

Fig. 4.28(a)). This was felt to be linked to the reduced laminar burning velocity at increased pressure (see Fig. 4.10(b)), which increases the axial flame length (see Fig. 4.27(c)). The oscillation of the flame surface area and the resulting heat release fluctuation are then subsequently enhanced for the longer flame, increasing the propensity for thermoacoustic instability.

It is also meaningful to check if the used FTFs at $A_u = 0.1$ can be replaced by a simple $n-\tau$ model, defined in Eq. 2.25, whose gain (n_f) and time delay (τ_f) both match the numerical FTF's gain and phase levels. In this work, the gain of the $n-\tau$ model, n_f, equals $[1.09, 1.32]$, selected to match the maximum FTF gains at the two pressures (Fig. 4.28(a), $A_u = 0.1$). The time delay, $\tau_f = \varphi/(2\pi f)$, is selected as $[2.79, 3.12]$ ms, calculated based on the phases of the FTF when the maximum gains occur (Fig. 4.28(a)). By incorporating this $n-\tau$ model into OSCILOS, the linear stability of the same network can be re-predicted, as shown in Table 5.3. It is noted that the network is now linearly unstable at both pressures, with the dominant mode's frequency (∼140 Hz) much lower than that predicted by the numerical FTFs at $A_u = 0.1$. These mismatches indicate that the $n-\tau$ model may not be able to capture the correct thermoacoustic mode and linear stability, because although the parameters of the $n-\tau$ model are calculated based on the simulated FTFs, the lack of frequency-dependence of its gain (n_f) and time-delay (τ_f) largely limits its prediction accuracy. Therefore, an accurate FTF with correct frequency dependence obtained by the numerical simulation or experiment is recommended for the linear thermoacoustic predictions of a realistic combustor.

5.1.3 Nonlinear thermoacoustic stability and limit cycle predictions

Following the above linear stability predictions, the nonlinear stability analysis is then performed by OSCILOS, in order to predict the measured limit cycle oscillations shown in Fig. 4.2. Based on the unstable mode identified at 6 bar pressure (Fig. 5.5(b)), the nonlinear FDF computed by Case V at $\overline{p} = 6$ bar (Fig. 4.28(a)) is now extended to include a larger range of forcing amplitudes from $A_u = 0.1$ to 0.5 (with steps of 0.1), over two close forcing frequencies of 200 Hz

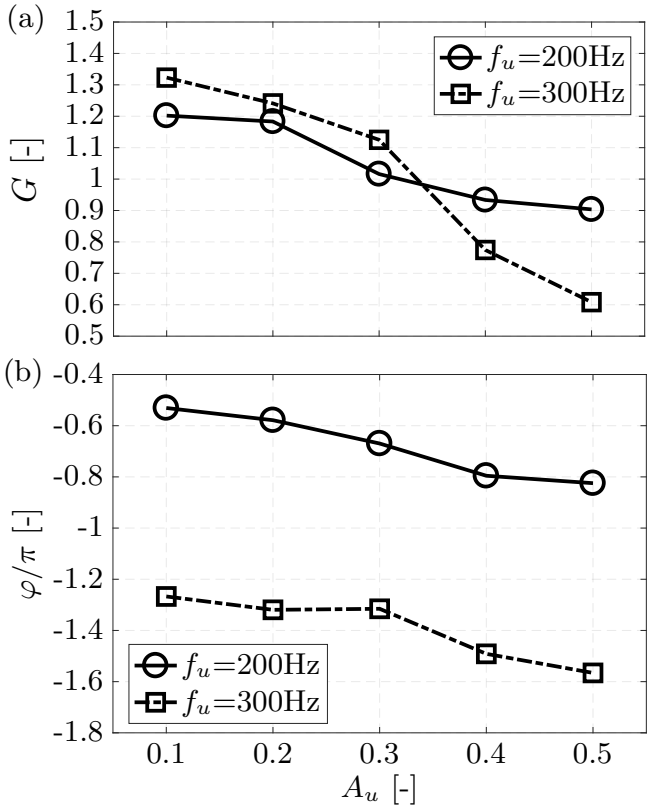


FIGURE 5.6: (a) Gain, G, and (b) phase, φ, of the FDF at forcing frequency $f_u = 200$ Hz (solid line) and $f_u = 300$ Hz (dash-dotted line) for forcing amplitudes of $A_u = 0.1 - 0.5$. All forced simulations are performed at $\overline{p} = 6$ bar based on LES Case V.

and 300 Hz, falling on either side of the frequency (∼231 Hz) of the unstable mode. The flame response against forcing level is shown in Fig. 5.6, with the predicted FDF gain continuously decreasing with forcing amplitude at both forcing frequencies, although with different falling-off trends. A stronger gain saturation is observed at $f_u = 300$ Hz, where the gain, G, drops by more than 50% as A_u increases from 0.1 to 0.5. The corresponding gain drop at $f_u = 200$ Hz is only ∼25%. This frequency dependence of the rate of the gain's falling off with forcing amplitude has been observed in previous theoretical [60], numerical [68] and experimental [53, 54] studies on various flames. Therefore, the different gain saturation trends in Fig. 5.6(a) are consistent with previous observations. In contrast, for the FDF phase, φ, it shows an almost linearly-decreasing profile over the forcing amplitude, with similar falling-off trends at both forcing frequencies (see Fig. 5.6(b)).

The above extended FDF is then incorporated into OSCILOS to predict the frequency and amplitude of the limit cycle oscillation. This nonlinear prediction relies on the assumption that the time-scale of the limit cycle oscillation amplitude's growth is much longer than that

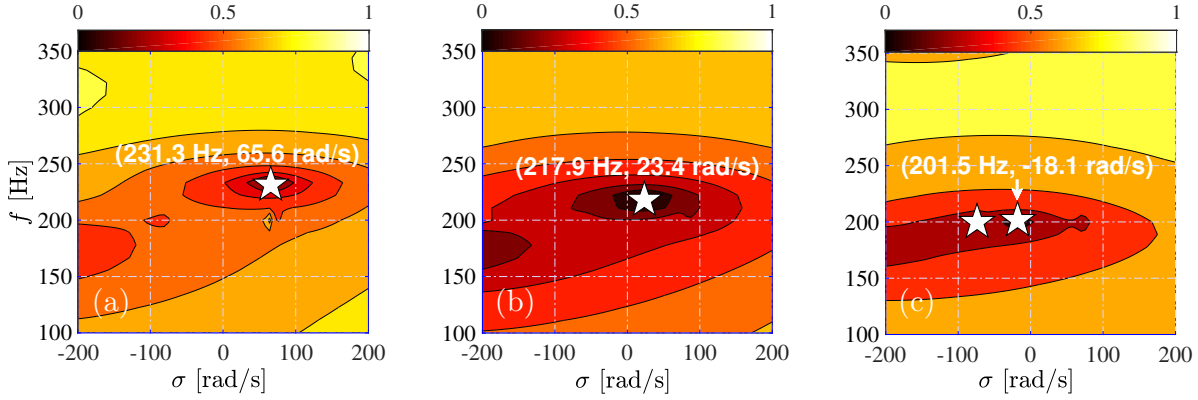


FIGURE 5.7: The variation of the linearly unstable thermoacoustic mode at $\overline{p} = 6$ bar over perturbation amplitude, A_u. (a) $A_u = 0.1$; (b) $A_u = 0.3$; (c) $A_u = 0.4$.

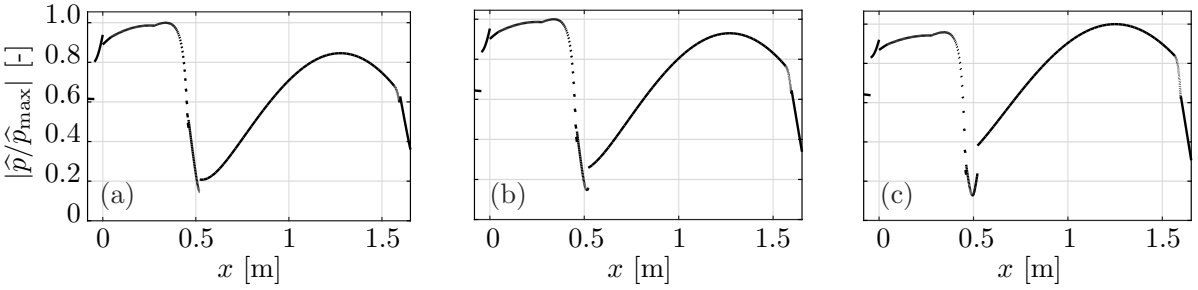


FIGURE 5.8: Shape of the linearly unstable mode in the form of normalised pressure fluctuation amplitude axial-profile, $|\widehat{p}/\widehat{p}_{\max}|$. (a) $A_u = 0.1$; (b) $A_u = 0.3$; (c) $A_u = 0.4$.

of the oscillation itself [232]. The frequency and growth rate of the linearly unstable mode (Fig. 5.5(b)) are predicted over increasing perturbation level, with the zero-growth-rate state taken to correspond to the frequency and amplitude at which the thermoacoustic oscillations no longer grow, and at which the limit cycle oscillations establish [42, 52, 54, 68, 69].

As shown in Fig. 5.7, the variation of the linearly unstable mode is plotted on the complex $f-\sigma$ plane across perturbation amplitudes, $A_u = 0.1$, 0.3 and 0.4. Starting from the unstable mode at $A_u = 0.1$ (Fig. 5.7(a)), its growth rate continuously decreases with increasing A_u, with a shift from unstable to stable state between perturbation levels of 0.3 and 0.4 (Figs. 5.7(b, c)). The corresponding shapes of this mode at these three forcing levels are plotted in Fig. 5.8, in the form of axial distribution of the normalised pressure fluctuation amplitude, $|\widehat{p}/\widehat{p}_{\max}|$, with $|\widehat{p}_{\max}|$ the maximum amplitude. Even if the global mode shape remains almost unchanged over A_u, the relative level of pressure fluctuation in the combustion chamber and exhaust pipe varies. In the most unstable condition of $A_u = 0.1$, the maximum pressure fluctuation is found within the combustion chamber ($x \leq 0.521$ m, Fig. 5.8(a)), but the difference in $|\widehat{p}|$ level between combustion chamber and exhaust pipe progressively reduces when A_u increases from 0.1 to 0.3

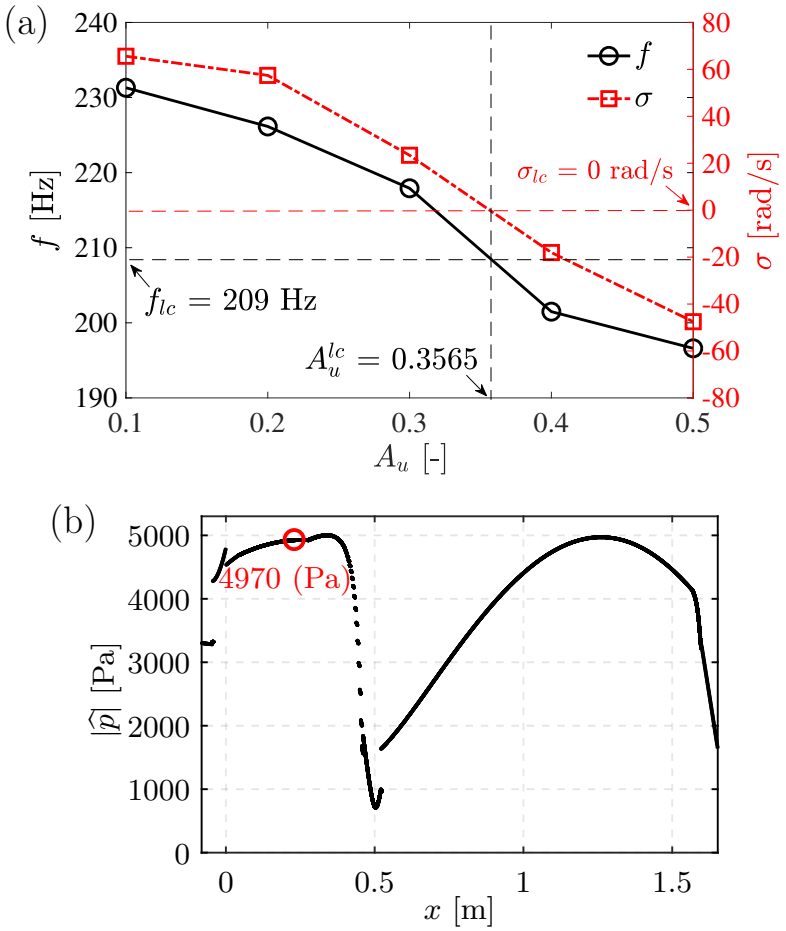


FIGURE 5.9: (a) Evolutions of frequency (f, solid line) and growth rate (σ, dash-dotted line) of the linearly unstable mode at 6 bar with forcing level, A_u. Arrows indicate the frequency, f_{lc}, and growth rate, σ_{lc}, of the limit cycle and the corresponding forcing level, A_u^{lc}. (b) Axial variation of the pressure fluctuation amplitude, $|\widehat{p}|$, when the limit cycle occurs. Red circle: value of $|\widehat{p}|$ at pressure transducer location, $x = 231$ mm.

(Fig. 5.8(b)). Then an opposite behaviour appears when A_u continues to increase — the location of $|\widehat{p}_{\max}|$ shifts to the exhaust pipe ($x > 0.521$ m, Fig. 5.8(c)) when the unstable mode is fully damped at $A_u = 0.4$. Possible reason for this shift may be the frequency change of this mode (Fig. 5.7), caused by the variations of FDF gain and phase over the perturbation amplitude.

The evolutions of frequency, f, and growth rate, σ, with perturbation amplitude for the target mode, which starts as linearly unstable at ~231 Hz, are plotted in Fig. 5.9(a). The mode's growth rate continuously decreases from a positive value for $A_u = 0.1 - 0.3$, to a negative value at $A_u = 0.4$ and 0.5, due to the decrease of FDF gain (see Fig. 5.6(a)). The limit cycle oscillations occur when the modal growth rate is equal to zero. This corresponds to an upstream perturbation amplitude, A_u^{lc}, of 0.3565, using linear interpolation. The limit cycle oscillation frequency is predicted to be $f_{lc} = 209$ Hz.

The corresponding axial distribution of the pressure fluctuation amplitude, $|\widehat{p}|$, under the limit cycle condition is shown in Fig. 5.9(b). It is firstly noted that the maximum value of $|\widehat{p}|$, i.e. $|\widehat{p}_{\max}|$, in the combustion chamber is now equal to that in the exhaust pipe, which indicates the energy balance between the two main components of the combustor at limit cycle. It has been discovered by Paschereit et al. [59] that during the transition from exponential growth into a limit cycle state, the wave mode shape transforms from a standing wave to a travelling wave, which has a phase speed of approximately the speed of sound. This may explain the same maximum wave amplitudes predicted in both components. More investigations on the variation of wave mode shape at the occurrence of limit cycle oscillation are required. At the axial location of $x = 231$ mm, where the transducer measured the pressure signal in the experiments (see Fig. 4.2), a pressure fluctuation amplitude of $|\widehat{p}| = 4970$ Pa is predicted, marked by the red circle in Fig. 5.9(b).

The above predicted limit cycle properties are then compared to the measured values, as shown in Table 5.4. It shows that both the frequency and amplitude of the predicted limit cycle perfectly match the experimental data at the pressure transducer location, with a very small error of 3.2% and 0.6%, respectively. Additionally, the predictions using the 6 bar FDFs obtained with the 4-step chemistry (i.e. based on Case IV) also correctly capture the nonlinear limit cycle properties, giving $f_{lc} = 211$ Hz, $A_u^{lc} = 0.3559$ and $|\widehat{p}| = 4940$ Pa, again all matching the measurement data. Therefore, the present OSCILOS predictions of the thermoacoustic instability and limit cycle oscillations in the SGT-100 combustor have been fully validated.

It should noted here that the flame response model plays a very important role in the computation of thermoacoustic modes, and an accurate description of the FDF gain's saturation trend is vital for the prediction of limit cycle oscillations. A small change in the FDF gain may lead to a large shift of the unstable mode location, thus a large variation of the predicted limit cycle properties. Therefore, a large number of forced simulation cases are needed to obtain an accurate FTF or FDF for the thermoacoustic instability and limit cycle predictions. In order to save the computational costs, in this work only the linear stability predictions require a complete FTF at a fixed forcing amplitude over a large frequency range. Once the linearly unstable mode is captured, a more targeted FDF across multiple forcing levels but spanning a much narrower frequency range, ideally containing the unstable mode frequency, is sufficient for the following nonlinear limit cycle predictions.

TABLE 5.4: Limit cycle oscillation frequency (f_{lc}) and amplitude ($|\widehat{p}|$) at pressure transducer location, obtained by prediction and measurement. Error = (predicted value − measured value)/measured value × 100%.

	Prediction	Measurement	Error [%]
f_{lc} [Hz]	209	216	-3.2
$\lvert\widehat{p}\rvert$ [Pa]	4970	5000	-0.6

TABLE 5.5: Sensitivities of the predicted limit cycle (f_{lc}, A_u^{lc} and $|\widehat{p}|$) to small changes in the pressure reflection coefficient magnitudes at network inlet ($|R_{\text{in}}|$) and outlet ($|R_{\text{out}}|$).

Change in $\lvert R\rvert$	f_{lc} [Hz]	A_u^{lc} [-]	$\lvert\widehat{p}\rvert$ [Pa]
Original	209	0.3565	4970
$\lvert R_{\text{in}}\rvert \times 0.9$	210	0.3557	4947
$\lvert R_{\text{in}}\rvert \times 1.1$	209	0.3574	4993
$\lvert R_{\text{out}}\rvert \times 0.9$	205	0.3825	5280
$\lvert R_{\text{out}}\rvert \times 1.1$	214	0.3358	4715

Finally, the above predicted limit cycle properties are known to be sensitive to the acoustic damping levels at network boundaries, which for the SGT-100 combustor are unknown as they were not measured. Therefore, the sensitivities of the above predictions (with 15-step chemistry FDFs) to small changes in the upstream and downstream reflection coefficient magnitudes are now investigated. As shown in Table 5.5, if R_{in} is taken to have its gain changed by 10% either way, with the outlet reflection coefficient unchanged, the limit cycle predictions change to $f_{lc} = 210$ Hz, $A_u^{lc} = 0.3557$ and $|\widehat{p}| = 4947$ Pa (for 10% decrease in $|R_{\text{in}}|$) or $f_{lc} = 209$ Hz, $A_u^{lc} = 0.3574$ and $|\widehat{p}| = 4993$ Pa (for 10% increase in $|R_{\text{in}}|$). Similarly, if R_{out} is rather to have its gain changed by 10% either way, with R_{in} unchanged, the predictions will change to $f_{lc} = 205$ Hz, $A_u^{lc} = 0.3825$ and $|\widehat{p}| = 5280$ Pa (for 10% decrease in $|R_{\text{out}}|$) or $f_{lc} = 214$ Hz, $A_u^{lc} = 0.3358$ and $|\widehat{p}| = 4715$ Pa (for 10% increase in $|R_{\text{out}}|$). Therefore, the predicted limit cycle properties have a very limited dependence on the acoustic damping levels at both network inlet and outlet.

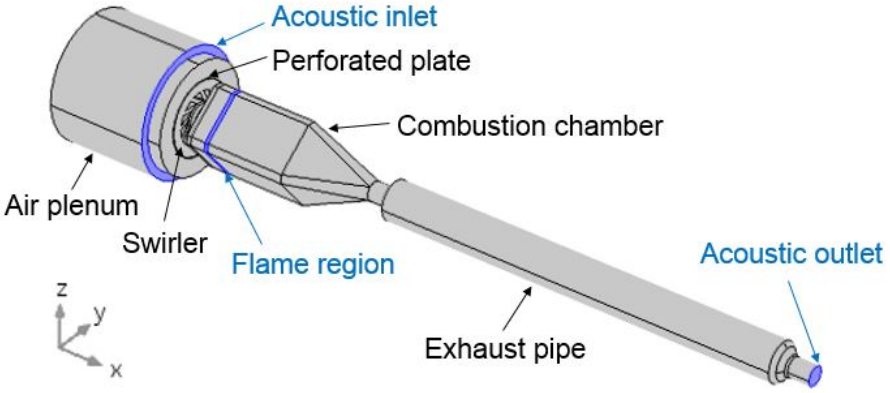


FIGURE 5.10: Computational domain used by the H-solver.

5.2 Thermoacoustic Stability Predictions by H-solver

The second solver used to predict the thermoacoustic instability is the H-solver, based on the solution of the Helmholtz equation (see Section 2.4.2 for more details). In this work, it is provided by the software COMSOL Multiphysics (version 5.3) [180]. Different from the above simplified network geometry used by OSCILOS, this H-solver retains the 3-D detailed combustor geometry.

As shown in Fig. 5.10, the computational domain used by the H-solver contains all the 3-D combustor components, including the upstream air plenum. A fully closed acoustic inlet (with no damping) is applied at the front entrance of the air plenum, with its pressure reflection coefficient $R_{\text{in}} = 1$, as it refers to a very narrow entry for the preheated air inflows. A circumferential plane is placed between the plenum exit and the swirler entry to represent the perforated plate, whose acoustic damping effect is modelled by the same impedance model in Eq. 5.1. For the domain outlet, i.e. the exit plane of the exhaust pipe, the same damped open boundary condition defined in Eq. 5.2 is used. The flame is no longer represented as an infinitely thin 1-D "flame sheet" as in the network. Instead, considering the real flame's compactness with respect to the acoustic wavelengths and the domain's axial length, a relatively thin reaction zone located within a short axial range of $x = [40, 50]$ mm is defined in this domain, where most of the heat releases are concentrated. The mean flow field is now neglected in this H-solver domain.

5.2.1 Stability analyses

The thermoacoustic stability of the above 3-D domain is now predicted by H-solver, using the procedures introduced in Section 2.4.2. The computed thermoacoustic modes are illustrated in

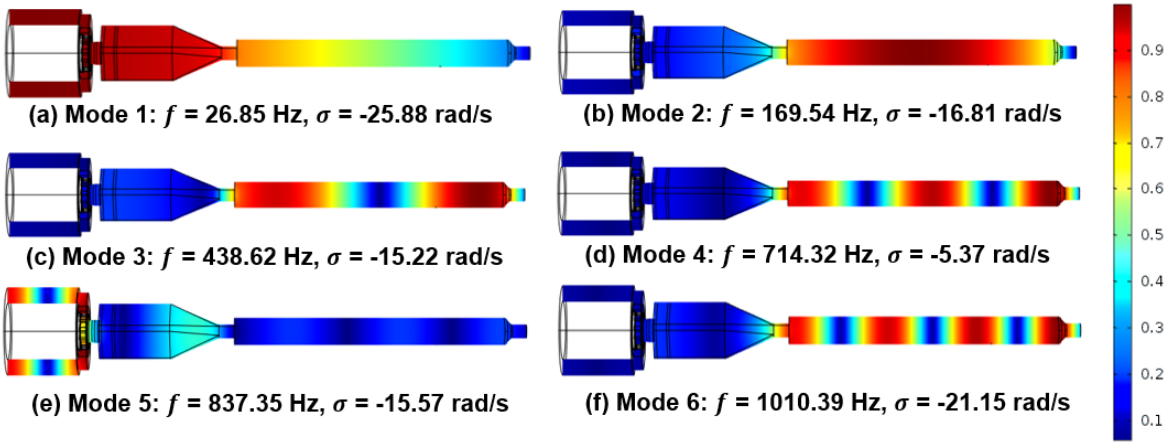


FIGURE 5.11: x-z contours of normalised pressure fluctuation amplitude, $|\widehat{p}/\widehat{p}_{\max}|$, corresponding to the thermoacoustic modes at $\overline{p} = 3$ bar, predicted by the H-solver using the FTF for LES Case III at $A_u = 0.1$.

Figs. 5.11 and 5.12 for the two operating pressures, both in the form of normalised pressure fluctuation amplitude ($|\widehat{p}/\widehat{p}_{\max}|$) contour plots.

It is observed that at $\overline{p} = 3$ bar (Fig. 5.11), a total of six thermoacoustic modes are predicted with frequencies up to ∼1 kHz, all of which have negative growth rates ($\sigma < 0$) and thus are linearly stable. The advantage of plotting these pressure contours is that the shape of each mode can be easily visualised. For example, the 2nd mode at $f \simeq 170$ Hz clearly exhibits a standing wave in the exhaust pipe (Fig. 5.11(b)). As the frequency increases, higher-order longitudinal modes with shorter wavelengths will start to occupy the same pipe (e.g., Figs. 5.11(d, f)).

At 6 bar pressure, the number of predicted modes grows to seven (see Fig. 5.12), with an unstable mode appearing at $f \simeq 239$ Hz. All the other modes remain linearly stable and are similar to those computed at 3 bar. These stability maps at both pressures are very close to those predicted by the OSCILOS solver in Fig. 5.5, also matching the experimental data (e.g., [24]). The unstable mode exhibits large amplitude waves in both the combustion chamber and the exhaust pipe (Fig. 5.12(c)), being consistent with the wave shape (i.e. the pressure fluctuation amplitude axial-profile) predicted by OSCILOS for the same mode (see Fig. 5.8).

The frequencies and growth rates of the thermoacoustic modes predicted by the H-solver are then compared in Fig. 5.13 for two forcing amplitudes ($A_u = 0.1$ and 0.2) across two operating pressures (3 bar and 6 bar). It is discovered that: (i) the increase of perturbation level (A_u) does not highly affect the frequencies of all the predicted modes, which (ii) generally match well with the experimental values, except for those measured at ∼370 Hz and ∼520 Hz, which have

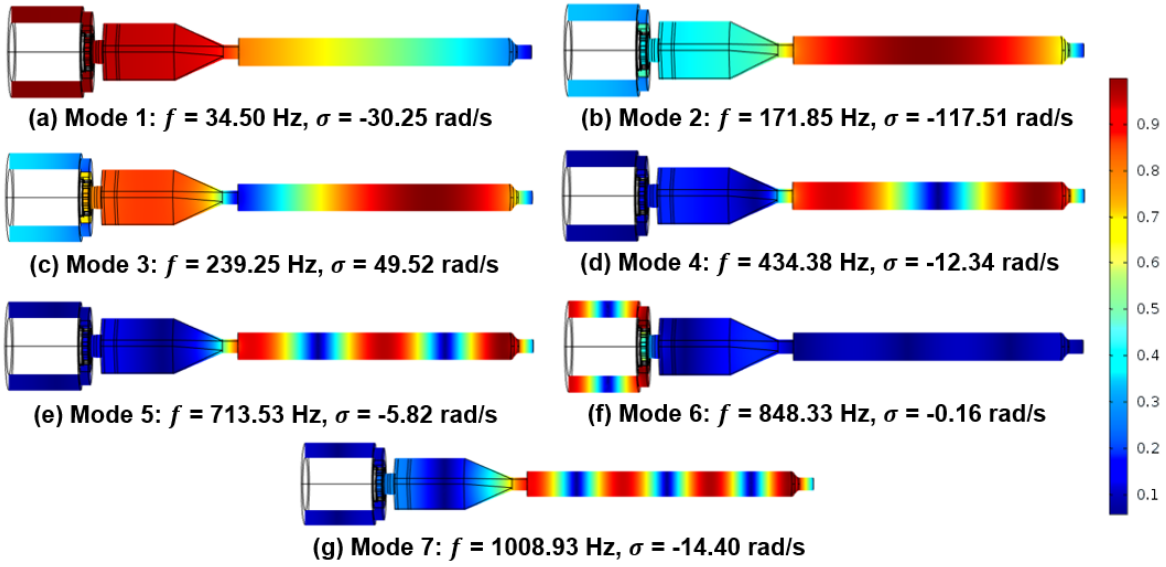


FIGURE 5.12: $x-z$ contours of normalised pressure fluctuation amplitude, $|\widehat{p}/\widehat{p}_{\max}|$, corresponding to the thermoacoustic modes at $\overline{p}$ = 6 bar, predicted by the H-solver using the FTF for LES Case V at $A_u = 0.1$.

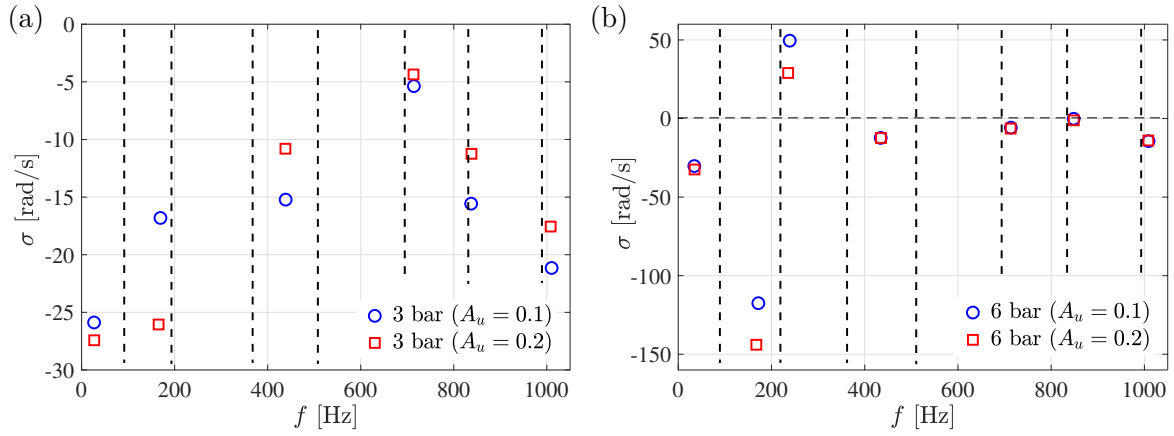


FIGURE 5.13: Thermoacoustic modes: frequencies vs. growth rates at (a) $\overline{p}$ = 3 bar and (b) $\overline{p}$ = 6 bar, predicted by H-solver at $A_u = 0.1$ (◯) and $A_u = 0.2$ (□). The measured modal frequencies are marked by vertical dashed lines.

not been captured by the H-solver. Since the unstable mode at ∼230 Hz has been correctly captured at 6 bar pressure (Fig. 5.13(b)), the small prediction errors on the other stable modes are unlikely to affect the global thermoacoustic stability.

The effect of modelling the perforated plate on the H-solver predictions is also investigated. As shown in Fig. 5.14, at $\overline{p}$ = 3 bar the stable mode at ∼180 Hz becomes unstable when the perforated plate is neglected, and at $\overline{p}$ = 6 bar the positive growth rate of the unstable mode at ∼240 Hz significantly increases in the absence of the perforated plate. It is therefore necessary to model the perforated plate in the H-solver computational domain, in order to provide the

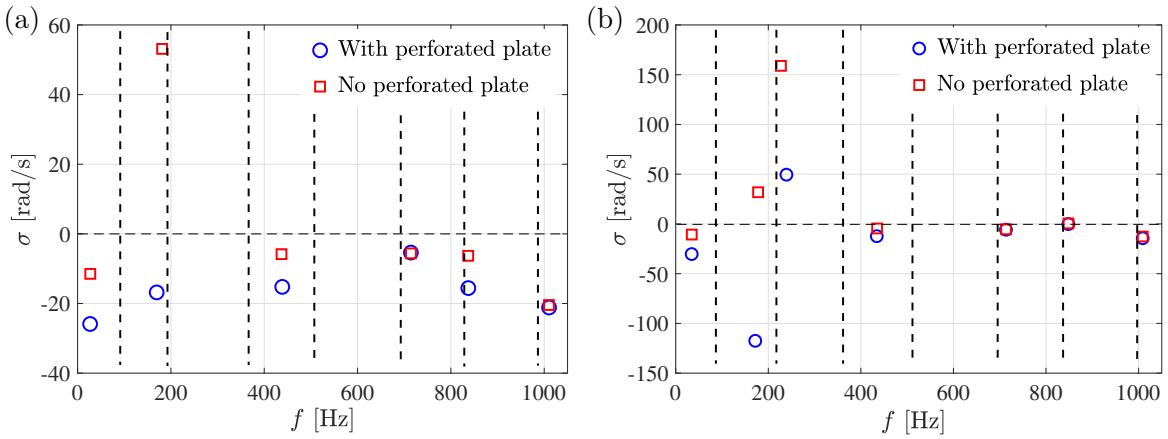


FIGURE 5.14: Thermoacoustic modes at (a) $\overline{p} = 3$ bar and (b) $\overline{p} = 6$ bar, predicted at $A_u = 0.1$ by the H-solver with (◯) or without (□) the perforated plate. The measured modal frequencies are marked by vertical dashed lines.

correct acoustic damping level for the thermoacoustic mode predictions (especially for the most dynamic modes) at both operating pressures.

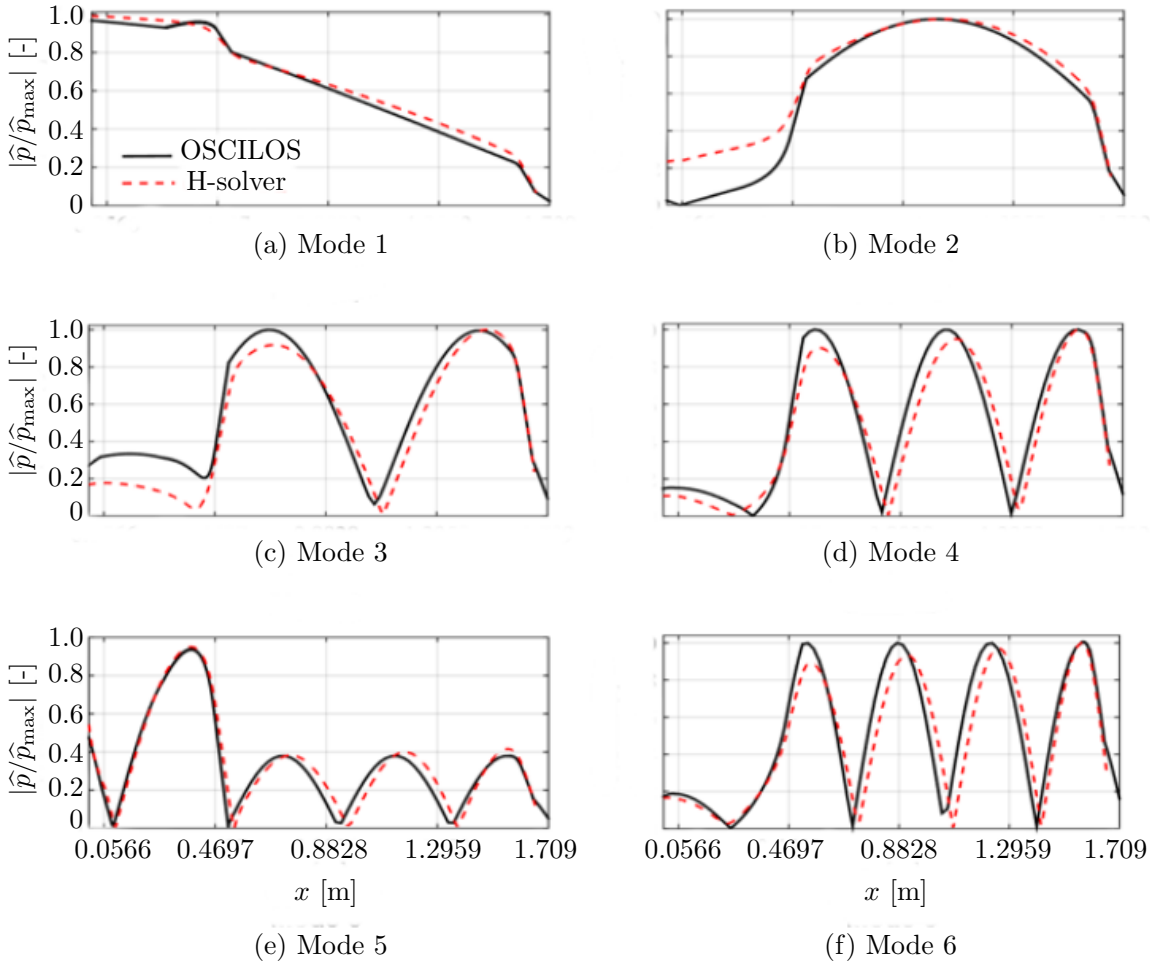
5.2.2 Comparison between OSCILOS and H-solver predictions

The thermoacoustic prediction results performed by the above two solvers are finally compared. As shown in Fig. 5.15, the shapes of all the thermoacoustic modes (in the form of axial pressure amplitude distribution, $|\widehat{p}/\widehat{p}_{\max}|$) match very well between OSCILOS and H-solver at the stable 3 bar condition. The same good match is also achieved at 6 bar pressure (not shown). This suggests that both of the thermoacoustic solvers offer very accurate mode predictions, although they use different prediction methods.

The predicted frequency and growth rate for the most dynamic mode at $\overline{p} = 6$ bar are also compared in Table 5.6. The two solvers give very similar value on the modal frequency (∼230 Hz), with the difference only around 8 Hz. On the other hand, the modal growth rate predicted by OSCILOS (∼66 rad/s) is ∼16 rad/s higher than that computed by the H-solver, which may lead to a smaller limit cycle perturbation amplitude (A_u^{lc}) if predicted by the H-solver. This difference in the growth rate may be due to (*i*) the neglect of mean flow field or (*ii*) the modelling of upstream plenum in the H-solver domain.

TABLE 5.6: Frequency and growth rate of the unstable thermoacoustic mode predicted by OSCILOS and H-solver, using the same FTF at $A_u = 0.1$ from LES Case V.

	Frequency [Hz]	Growth rate [rad/s]
OSCILOS	231.3	65.60
H-solver	239.3	49.52



(a) Mode 1 (b) Mode 2

(c) Mode 3 (d) Mode 4

(e) Mode 5 (f) Mode 6

FIGURE 5.15: Shapes of the thermoacoustic modes (in the form of $|\widehat{p}/\widehat{p}_{\max}|$ axial profile) predicted at stable 3 bar condition by OSCILOS (solid line) and H-solver (dashed line), using the same FTF at $A_u = 0.1$ from LES Case III.

5.3 Summary

In this chapter, the thermoacoustic instability of the SGT-100 combustor is successfully predicted, by combining the computed FTFs and FDFs within two thermoacoustic solvers, which are the low order network solver, OSCILOS, and the Helmholtz equation-based H-solver.

In OSCILOS, the combustor geometry is simplified as a network of connected constant area modules. The predicted thermoacoustic modes are all linearly stable at $\overline{p} = 3$ bar, while one mode at ∼231 Hz is found unstable at $\overline{p} = 6$ bar, both matching the experimental data. For the unstable mode, a nonlinear stability analysis is performed using the extended FDFs with extra forcing amplitude information near the mode frequency. By identifying the conditions for which zero-growth-rate occurs, the limit cycle oscillations with a frequency of 209 Hz, and a pressure amplitude at the measurement location of 4970 Pa, are predicted, both in very close agreement with the measurement data (216 Hz and 5000 Pa).

The same prediction procedure is then repeated for the H-solver, which retains the original 3-D combustor geometry but neglects the mean flow. The predicted thermoacoustic modes are visualised by the acoustic pressure contours, whose mode shapes match well with all the OSCILOS predicted modes. The mode properties are also accurately captured by the H-solver, providing the correct stability maps. One mode at 6 bar is also found unstable, whose frequency agrees well with the OSCILOS prediction. Its positive modal growth rate predicted by the H-solver is slightly lower than that from OSCILOS, may be due to the neglect of mean flow or the addition of upstream plenum which modifies the acoustic damping level in the H-solver domain.

To conclude, both of the thermoacoustic solvers used are sufficiently accurate, and their predictions of the thermoacoustic instability and the resulting limit cycle oscillations are validated for the SGT-100 industrial combustor.

Chapter 6

SGT-100 Industrial Combustor: Entropy Wave Transport

After predicting the forced flame responses and the thermoacoustic instability, the entropy wave transport within the SGT-100 combustor flow are finally studied in this chapter. The external entropy source is injected into the mean flame region, and the full entropy transport equation is solved within the real combustor flow field. The resulting entropy fluxes exiting the combustor are then analysed to determine the shear-dispersion level of the transported entropy wave strength. The contributions to the dispersion from the advection, viscous production and thermal diffusion of the entropy waves are all evaluated. The importance of the time-averaged and the unsteady flow features are both discussed. Finally, the effects of the wave-generated entropy noise on the thermoacoustic modes of two simple duct combustors are investigated.

The results presented in this chapter have also been published in [185, 233].

6.1 Entropy Wave Transport within Combustor Flows

6.1.1 Dispersive advection of entropy waves

The main purpose of this chapter is to simulate the entropy wave transport within the SGT-100 rig. The thermoacoustic predictions in Chapter 5 did not account for the effect of entropy noise on the thermoacoustic modes, because the entropy wave strength, which is proportional to the

generated entropy noise, is assumed much weaker than the dominant acoustic wave amplitude in this combustor. The fact that the combustion chamber exit is far from being choked (and hence exhibits limited flow acceleration, this being needed to generate significant entropy noise) and the good match between the prediction and the measurement (see Table 5.4) suggest that this assumption is valid. Nevertheless, the combustor simulations provide an ideal test bed for studying entropy wave transport within a real combustor flow field. This will be highly relevant to similar industrial combustors but which exhibit stronger exit acceleration and hence have higher potential for significant entropy noise.

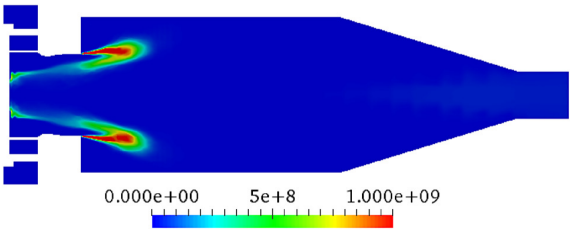
Following the forced entropy transport equation, Eq. 2.40, and the numerical expressions for the entropy diffusion and production terms, Eqs. 3.33 – 3.34, this chapter simulates the transport of entropy waves within the combustor flow using OpenFOAM solver based on the LES Case I (see Table 4.4). As shown in Fig. 6.1(a), the mean volumetric heat release rate field, $\overline{\dot{q}}(x, y, z)$, which exhibits a compact flame region, is used to build a time-impulsive entropy source term, $\dot{Q}_S$ (e.g., Fig. 6.2(a)), as defined in Eq. 2.39.

For the flow field within which the entropy perturbations are transported, the contours of mean and unsteady axial velocity fields both reveal a main flow separation and recirculation zone along the combustion chamber centreline and extending to its upstream entrance. The unsteady flow field (Fig. 6.1(c)) is very turbulent and irregular, containing large-scale unsteady flow features such as vortex shedding and CVC, etc., which are not captured by the mean flow field (Fig. 6.1(b)).

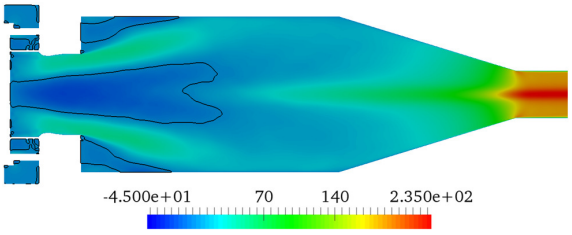
As derived in Section 2.5.1, the full equation governing the entropy wave transport in the presence of an entropy source, $\dot{Q}_S$, is repeated here as:

$$\underbrace{\frac{\partial S}{\partial t} + u_i \frac{\partial S}{\partial x_i}}_{A_S} = \underbrace{\frac{k}{\rho c_p} \frac{\partial^2 S}{\partial x_i \partial x_i}}_{D_S} + \underbrace{\frac{1}{\rho c_p \overline{T} \mathcal{V}} \left(\tau'_{ij} \frac{\partial \overline{u}_i}{\partial x_j} + \overline{\tau}_{ij} \frac{\partial u'_i}{\partial x_j} \right)}_{P_S} + \dot{Q}_S. \tag{6.1}$$

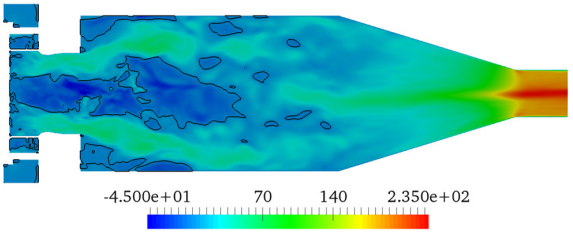
In order to study the entropy wave transport, three types of simulation cases are defined to evaluate the contributions from the entropy advection, diffusion and production terms [185, 233], respectively. These cases are: (*i*) full entropy advection, diffusion and production, denoted "$A_S + D_S + P_S$"; (*ii*) entropy advection and diffusion, denoted "$A_S + D_S$", in which only the production term is neglected; (*iii*) pure entropy advection, denoted "A_S", in which both the diffusion and production terms are ignored. All of these cases apply the same entropy source



(a) Mean heat release rate, $\overline{\dot{q}}$ (W/m^3)



(b) Mean axial velocity, $\overline{u}$ (m/s)



(c) Instantaneous axial velocity, u (m/s)

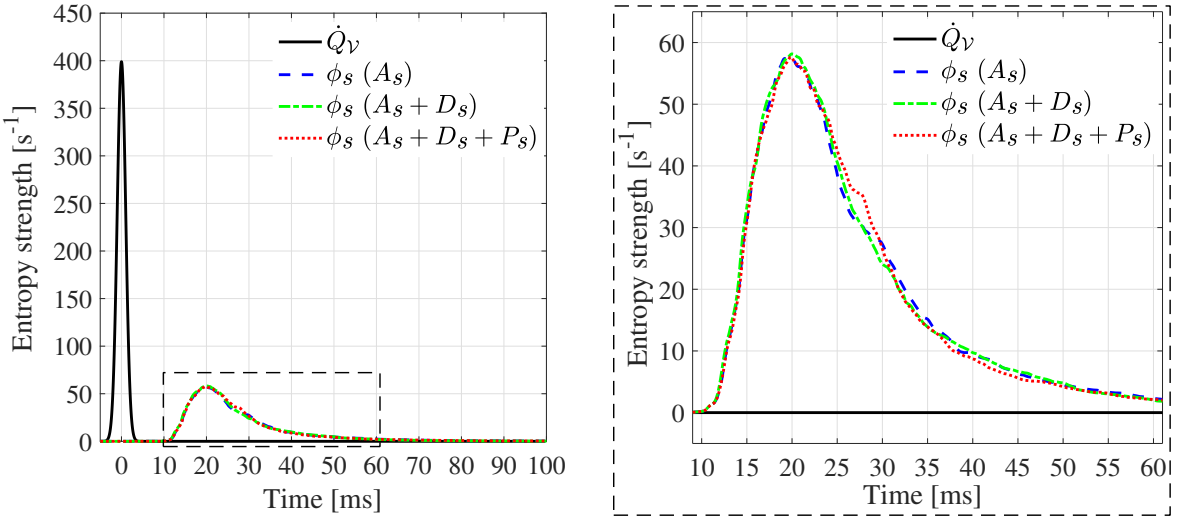
FIGURE 6.1: Contours of (a) mean volumetric heat release rate, (b) mean axial velocity and (c) instantaneous axial velocity on symmetry plane $z = 0$, all simulated by LES Case I. Black lines: iso-lines of zero axial velocity.

term, $\dot{Q}_S$, with a dispersion time of $\Delta\tau_1 = 1.414$ ms (see Eq. 2.39 for more details), and they are all simulated within the real unsteady combustor flow illustrated in Fig. 6.1(c).

In order to better quantify the strength of entropy waves after the transport process, the volumetric flux (denoted ϕ_S) of the entropy concentration, S, at the combustion chamber exit plane is defined as:

$$\phi_S = \iiint_{\mathcal{V}} (\boldsymbol{u} \cdot \boldsymbol{\nabla} S)\, \mathrm{d}\mathcal{V} = \iint_{\partial\mathcal{V}} (\boldsymbol{u} \cdot \boldsymbol{n}) S \mathrm{d}\mathbb{A}, \tag{6.2}$$

with $\partial\mathcal{V}$ the domain surface, $\mathbb{A}$ the surface area and $\boldsymbol{n}$ the surface's outflow normal unit vector. Since the normal velocity, $\boldsymbol{u} \cdot \boldsymbol{n}$, remains zero on all the adiabatic solid walls, and there is negligible entropy exiting the combustor inlet ($S \simeq 0$), ϕ_S is equal to the entropy flux exiting the combustor outlet plane. The time-variations of ϕ_S, as calculated for the above three entropy transport cases, are compared in Fig. 6.2. It is found that the three entropy exit flux profiles are almost identical (see Fig. 6.2(a)), all of which have an amplitude much lower than that of the volume-integrated entropy source, $\dot{Q}_{\mathcal{V}}$ (equal to $\iiint_{\mathcal{V}} \dot{Q}_S \, \mathrm{d}\mathcal{V}$). As shown in the zoomed-in Fig. 6.2(b), the thermal diffusion term, D_S, slightly smooths the time-distribution of ϕ_S, while the viscous production term, P_S, marginally increases the magnitude of ϕ_S within times $t = 25$ – 30 ms. Overall, both the entropy diffusion and production terms have negligible effects on the entropy wave transport process, suggesting that only the advection term, A_S, is important.



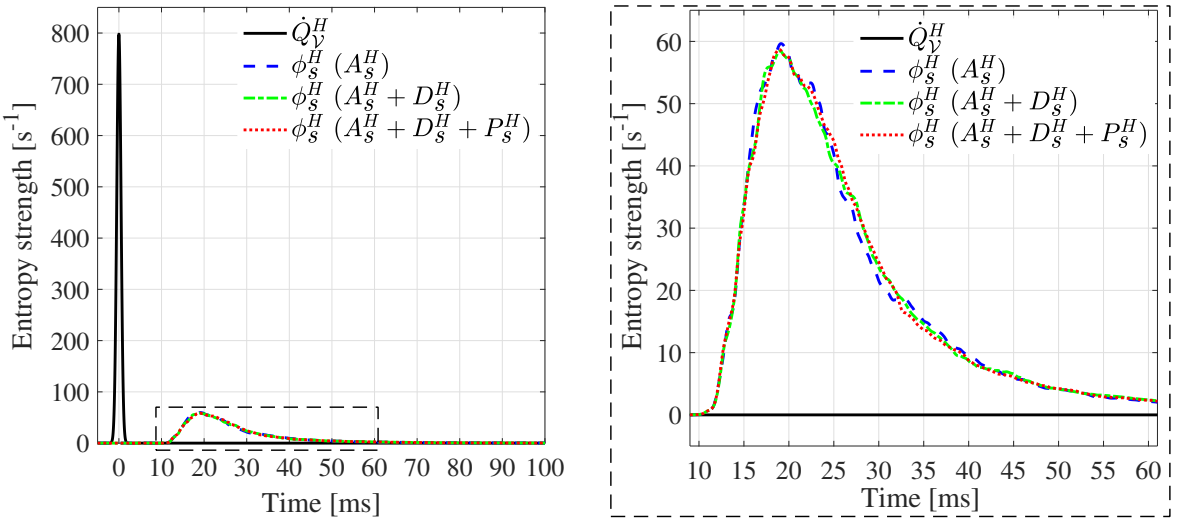
(a) Time-variations of entropy strengths (b) Zoomed-in plots of (a)

FIGURE 6.2: (a) Time-variations of volume-integrated entropy source, $\dot{Q}_{\mathcal{V}}$ (solid line), and entropy fluxes at combustion chamber exit, ϕ_S, after full transport "$A_S + D_S + P_S$" (dashed line), advection and diffusion "$A_S + D_S$" (dash-dotted line), and pure advection "A_S" (dotted line); (b) Zoomed-in plots of (a).

This finding is consistent with the "pure advection" equation, Eq. 2.43, derived from the non-dimensional analysis in Section 2.5.2.

In order to check whether the combustor exit entropy strength really represents an "impulse response" or whether it is dependent on the shape of the applied forcing in $\dot{Q}_{\mathcal{V}}$, the effect of doubling the height of $\dot{Q}_{\mathcal{V}}$ (i.e. halving the dispersion time to $\Delta\tau_1 = 0.707$ ms) is now investigated. The resulting exiting entropy fluxes (see Fig. 6.3) are almost identical to those obtained by the original entropy source in Fig. 6.2. This confirms that the exit entropy strengths indeed represent an impulse response. The effects of both entropy diffusion and production terms remain negligible, confirming that the entropy wave transport is purely dominated by advection, a nature which is not affected by the shape of the applied entropy source.

As a final note on these entropy transport terms, the relative effect of the production term, P_S, actually relies on the magnitude of the real flame-generated entropy waves, which is not included in this study. It is however expected that the amount of entropy waves generated by the flame itself is orders of magnitude higher than the turbulence-generated entropy fluctuations. Since the current study does not focus on the generation mechanism of entropy waves, but on their advection process through the flow field, the production terms are neglected in the remainder of this study (i.e. $P_S = 0$).



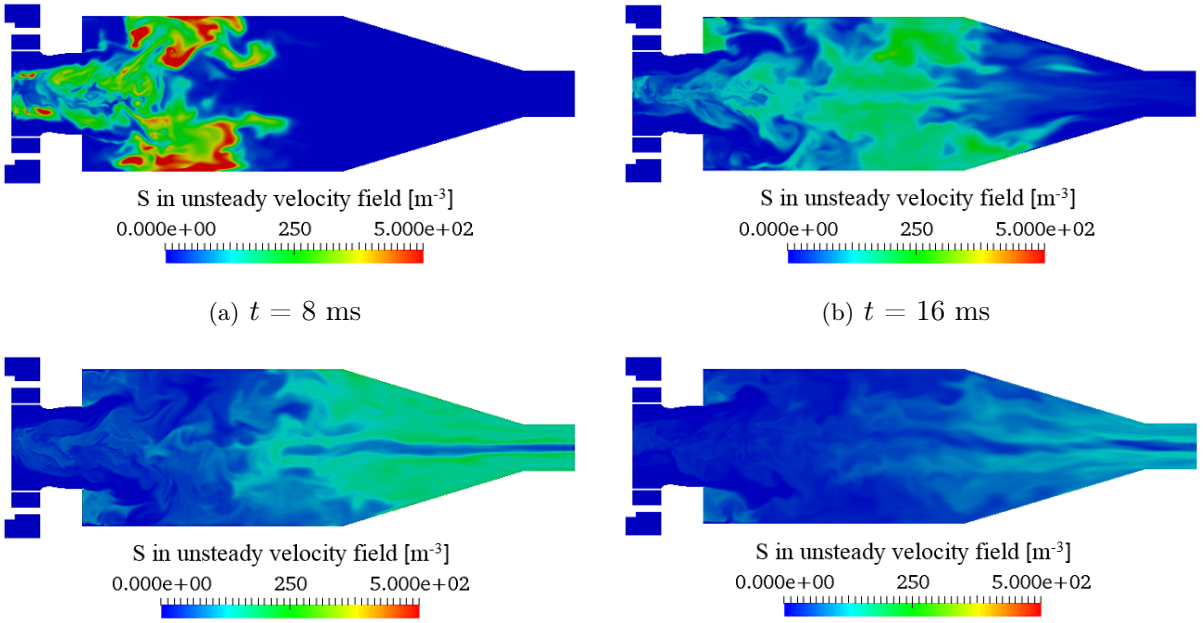
(a) Time-variations of entropy strengths (b) Zoomed-in plots of (a)

FIGURE 6.3: (a) Time-variations of volume-integrated entropy source and entropy fluxes at combustor exit. Superscript "H" denotes the source term dispersion time, $\Delta\tau_1$, is halved and the peak amplitude of the source term doubled; (b) Zoomed-in plots of (a).

The diffusion term of Eq. 6.1 may also be neglected (i.e. $D_S \simeq 0$), even within such a highly-turbulent reacting flow. This can be done because the sub-grid scale turbulence is negligible when compared to the resolved large-scale turbulent structures of the flow, as the present LES is well-resolved. This allows us to apply a simplified purely advective equation to study the entropy wave transport in the reminder of this chapter:

$$\underbrace{\frac{\partial S}{\partial t} + \boldsymbol{u} \cdot \boldsymbol{\nabla} S}_{A_S} = \dot{Q}_S. \tag{6.3}$$

The above entropy advection equation, Eq. 6.3, is accompanied by a phenomenon called "shear-dispersion" [159]. This is mainly caused by the non-uniform velocity profile of the main axial flow, which has a larger velocity near the centreline but highly reduced close to the top/bottom walls. This vertical gradient of velocity, known as shear, leads to different advection speeds of the entropy waves in the vertical direction. In order to address whether the dispersion of entropy advection is dominated by the time-averaged flow profile, or whether the unsteady flow features also play an important role, the effect of the "background" flow field is now investigated. The entropy advection equation is numerically solved firstly, then respectively superimposed on: (*i*) the real time-varying flow field (e.g., Fig. 6.1(c)), combining both time-averaged and unsteady flow features, and (*ii*) the "frozen" time-averaged flow field (Fig. 6.1(b)), in which only



(a) $t = 8$ ms (b) $t = 16$ ms

(c) $t = 24$ ms (d) $t = 32$ ms

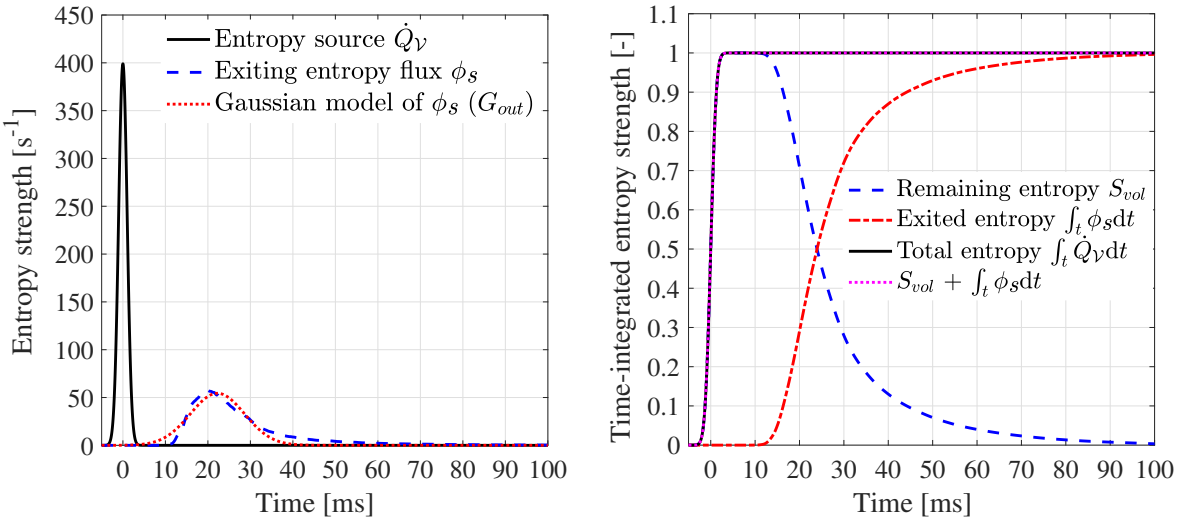
FIGURE 6.4: Contours of the entropy concentration, S, within an unsteady combustor flow field, plotted on symmetry plane $z = 0$, at four time instants after source injection.

the mean flow plays a role. In both flow fields, the same entropy source with a dispersion time of $\Delta\tau_1 = 1.414$ ms is used, located at the mean heat release rate field simulated by LES Case I (see Fig. 6.1(a)).

6.1.2 Transport within an unsteady combustor flow

The transport of entropy waves in a time-varying combustor flow is firstly investigated, by superimposing Eq. 6.3 onto the LES-simulated unsteady flow field. The resulting spatial distributions of entropy concentration, S, at four sequential time instants after the impulsive entropy injection are plotted in Fig. 6.4. The entropy advection is visibly affected by the large-scale unsteady flow features, which lead to broken entropy patterns under high turbulence level. The central flow separation and recirculation zone also has an effect, with entropy transport occurring more quickly towards the side walls, and a small amount of entropy being initially pulled upstream and trapped in the central zone.

The time-variation of exiting entropy flux, ϕ_S, is plotted in Fig. 6.5(a), which has a much lower amplitude and more spread out time-profile compared to the entropy source impulse. This is due to the dispersion of entropy wave strength arising from its advective transport. A more



(a) Time-variations of entropy strengths (b) Time-integrated entropy strengths

FIGURE 6.5: Entropy wave advection within an unsteady combustor flow: (a) time-variations of entropy source, $\dot{Q}_\mathcal{V}$ (solid line), exiting entropy flux, ϕ_S (dashed line), and Gaussian-approximation of ϕ_S (dotted line); (b) time-integrals of remaining entropy, S_{vol} (dashed line), exited entropy, $\int_t \phi_S dt$ (dash-dotted line), and injected entropy, $\int_t \dot{Q}_\mathcal{V} dt$ (solid line). Dotted line: sum of S_{vol} and $\int_t \phi_S dt$.

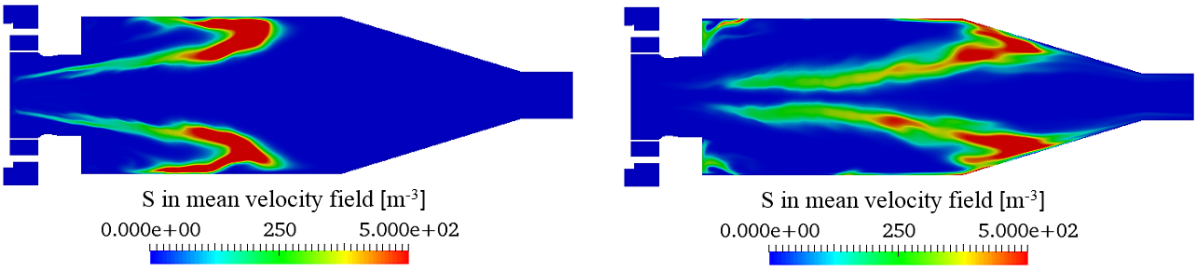
detailed analysis is performed by spatially integrating the entropy advection equation, Eq. 6.3, as:

$$\frac{\partial}{\partial t}\underbrace{\left(\iiint_\mathcal{V} S \mathrm{d}\mathcal{V}\right)}_{S_{\text{vol}}} + \underbrace{\iint_{\partial\mathcal{V}} (\boldsymbol{u}\cdot\boldsymbol{n}) S \mathrm{d}\mathbb{A}}_{\phi_S} = \underbrace{\iiint_\mathcal{V} \dot{Q}_S \, \mathrm{d}\mathcal{V}}_{\dot{Q}_\mathcal{V}}, \tag{6.4}$$

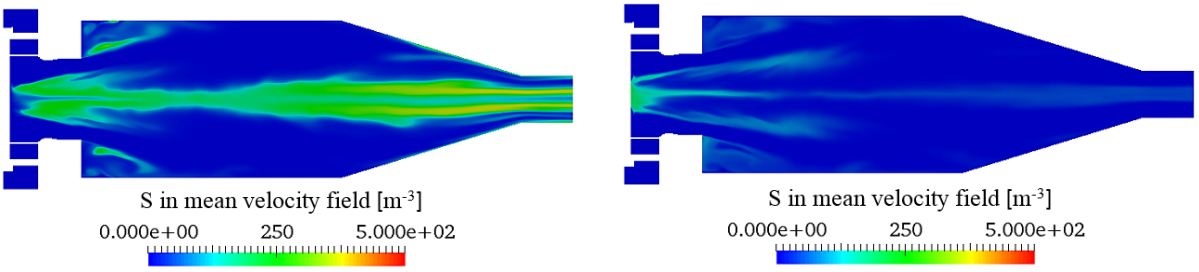
where the first term on the LHS is denoted $\partial S_{\text{vol}}/\partial t$, with $S_{\text{vol}} = \iiint_\mathcal{V} S \mathrm{d}\mathcal{V}$ the amount of entropy remaining in the combustion chamber. The second term is the exiting entropy flux, ϕ_S, defined in Eq. 6.2. According to energy conservation, the sum of $\partial S_{\text{vol}}/\partial t$ and ϕ_S is equal to the volume-integrated entropy source, $\dot{Q}_\mathcal{V}$. The time-integral of Eq. 6.4 thus satisfies:

$$S_{\text{vol}} + \int_t \phi_S \mathrm{d}t = \int_t \dot{Q}_\mathcal{V} \mathrm{d}t, \tag{6.5}$$

where the two terms on the LHS are plotted in Fig. 6.5(b). It is found that the entropy flux, ϕ_S, starts to exit the combustor at $t \simeq 10$ ms, at which point the entropy remaining in the chamber, S_{vol}, starts to drop. The exit rate of ϕ_S is fast for $t = 10 - 30$ ms, but slows down after $t = 30$ ms, resulting in a total time of ∼100 ms for all the injected entropy to leave the domain. The sum of S_{vol} and $\int_t \phi_S dt$ always equals the total amount of entropy injected, $\int_t \dot{Q}_\mathcal{V} dt$, again obeying the energy conservation law.



(a) Time $t = 10$ ms (b) Time $t = 20$ ms



(c) Time $t = 30$ ms (d) Time $t = 40$ ms

FIGURE 6.6: Contours of the entropy concentration, S, within time-averaged combustor flow field, plotted on symmetry plane $z = 0$, at four time instants after source injection.

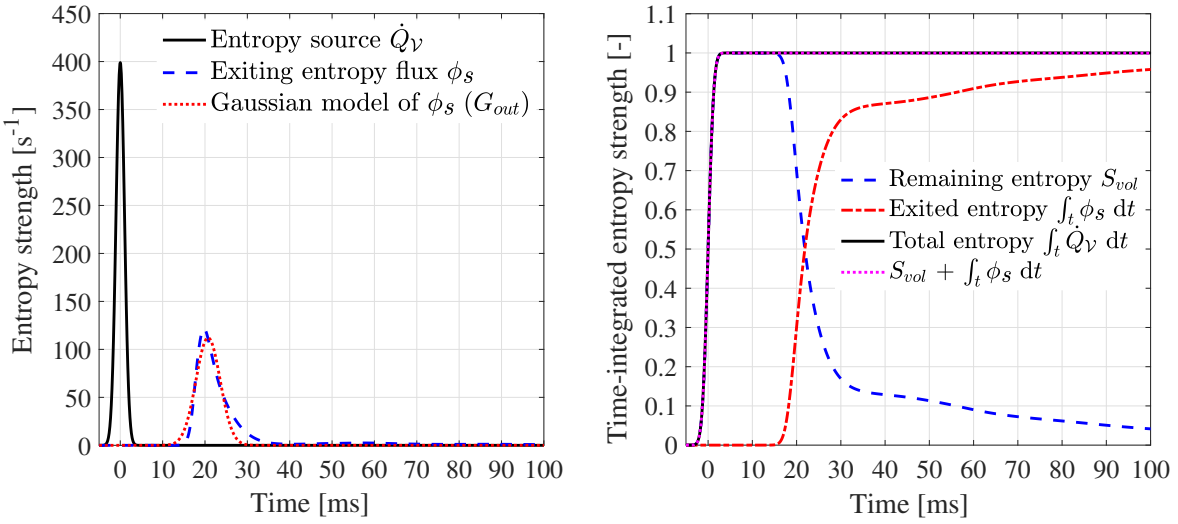
In a similar manner as for the advective dispersion in a channel flow (e.g., [154]), the time-profile of ϕ_S in a combustor flow can also be approximated by a Gaussian function, denoted G_{out}:

$$G_{\text{out}}(t) = \frac{1}{\sqrt{\pi}\Delta\tau_2} \exp\left[\frac{-(t-\tau_2)^2}{\Delta\tau_2^2}\right], \tag{6.6}$$

where τ_2 and $\Delta\tau_2$ are the mean delay time and dispersion time of G_{out}, respectively. The amplitude of G_{out} is determined by $1/(\sqrt{\pi}\Delta\tau_2)$. Using a non-linear least-squares fitting method [234], τ_2 and $\Delta\tau_2$ are calculated as 22.2 ms and 10.44 ms, respectively, for the above transport (Fig. 6.5). The increased dispersion time, $\Delta\tau_2$, compared to that of the entropy source, $\Delta\tau_1$, results in a wider Gaussian time-distribution with a lower amplitude. The Gaussian approximation, G_{out}, generally matches the profile of ϕ_S well, deviating slightly from the real shape which exhibits a longer tail, as shown in Fig. 6.5(a). This longer tail in the ϕ_S profile is mainly due to the trapping of entropy within the recirculation zone.

6.1.3 Transport within time-averaged combustor flow

Secondly, the entropy wave transport within the time-averaged "frozen" combustor flow, Fig. 6.1(b), is simulated, by fixing the velocity vector, $\boldsymbol{u}$, in Eq. 6.3 to its mean value, $\overline{\boldsymbol{u}}$, at each point in



(a) Time-variations of entropy strengths

(b) Time-integrated entropy strengths

FIGURE 6.7: Entropy wave advection within the time-averaged combustor flow field. See the caption of Fig. 6.5 for more information.

space. Four sequential time-snapshots of the entropy concentration field after the injection are plotted in Fig. 6.6. It is clear that the entropy wave advection is largely dispersed by the non-uniform mean axial velocity profile. Closer to the top and bottom side walls, the flow speeds are higher and the entropy flux reaches the exit plane earlier, while the advection near the centreline is much slower due to the flow recirculation zone. Quite a significant amount of entropy even initially travels back towards the chamber entrance (Figs. 6.6(a)–6.6(b)). As the entropy flux increasingly exits the domain, the amount of entropy remaining in the chamber decreases (Fig. 6.6(c)), with most eventually concentrated in the recirculation zone close to the combustor inlet (Fig. 6.6(d)). Although after a sufficiently long time, all of the injected entropy will leave the combustion chamber, the flow recirculation zone "traps" a small amount of entropy for a very long time.

The time-evolution of the exiting entropy flux, $\phi_\mathcal{S}$, for the mean combustor flow is shown in Fig. 6.7(a). Compared to the unsteady flow advection case (see Fig. 6.5(a)), the time-profile of $\phi_\mathcal{S}$ is much steeper, with a shorter tail at large times. This indicates that the dispersion effect of the mean flow is weaker than that of the real unsteady flow. The time-integrals of entropy strengths are shown in Fig. 6.7(b). The exiting speed of $\phi_\mathcal{S}$ is much faster at the beginning ($t = 15 - 30$ ms) than that for the unsteady flow simulation (Fig. 6.5(b)), but then significantly slows down after $t = 30$ ms, resulting in a much longer total exit time for all the entropy. This

time-delay is caused by the "dragging and trapping" effect of the flow recirculation zone, which is the dominant structure in the time-averaged flow field.

The Gaussian approximation model for ϕ_S, i.e. G_{out}, now takes values τ_2 and $\Delta\tau_2$ equal to 20.7 ms and 4.95 ms, respectively. This means the time taken for the entropy flux to firstly reach the combustor exit is almost the same for both time-varying and mean combustor flows, but the mean flow field has a much weaker dispersion effect overall.

In order to increase the applicability of the above entropy transport studies in combustor flows, the time scales for the entropy flux to exit the domain (e.g., see Figs. 6.4 and 6.6) can be normalised using a non-dimensional time, e.g., tU/L, with U the bulk velocity and L the axial length of the chamber. This allows the application of the present entropy advection analyses to other combustor flow fields.

6.2 Entropy Wave Transport within an Equivalent Pipe Flow

The above-simulated entropy wave transport in a combustor flow field (e.g., Figs. 6.4– 6.7) are now compared with that in an equivalent fully-developed pipe flow. The motivation for this comparison is to investigate whether an estimate can be obtained for the correct dispersion time, $\Delta\tau_2$, without the need for CFD simulations — the mean turbulent pipe flow profile for a given pipe length and radius are known analytically [161].

As shown in Fig. 6.8, the network geometry of the SGT-100 combustor chamber can be further simplified as an equivalent straight circular pipe. The pipe diameter, $D_p = 0186$ m, is calculated based on the height of the combustion chamber's square cross-section, $H = 0.165$ m, so that the cross-sectional area of the pipe matches the original chamber. The equivalent pipe length, $L_c = 0.349$ m, is calculated as:

$$L_c = L_0 + \frac{L_1}{2}, \tag{6.7}$$

where $L_0 = 0.225$ m, the distance from the 1-D flame sheet to the chamber's straight-contraction interface, and $L_1 = 0.248$ m, the distance from this interface to the combustor exit. The inlet of the equivalent pipe thus corresponds to the 1-D thin flame sheet, while the pipe outlet refers to the combustor exit plane (see Fig. 6.8(b)).

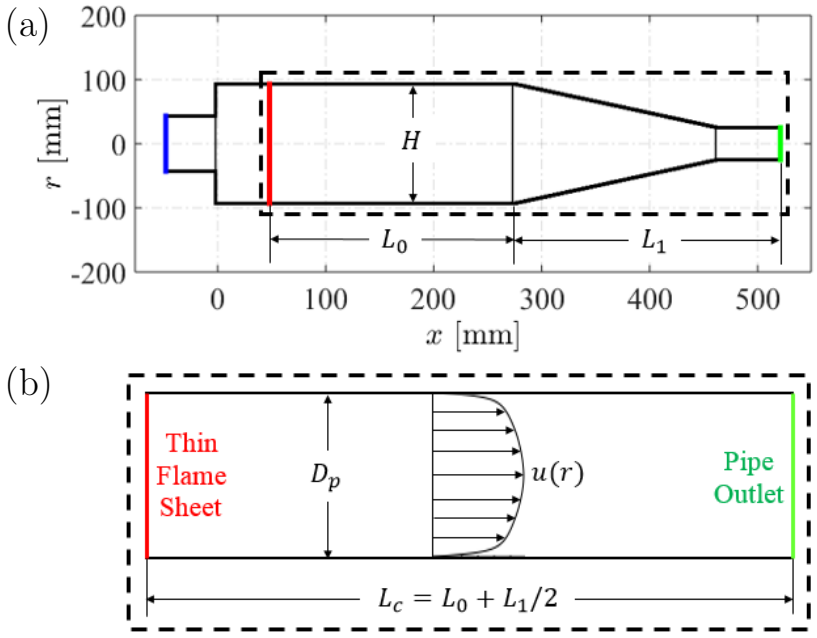


FIGURE 6.8: (a) Network representation of the SGT-100 combustor chamber, with the height of chamber straight section $H = 0.165$ m, flame-to-straight/contraction interface distance $L_0 = 0.225$ m, and interface-to-exit distance $L_1 = 0.248$ m; (b) equivalent circular pipe for (a), with diameter $D_p = 0.186$ m and length $L_c = 0.349$ m.

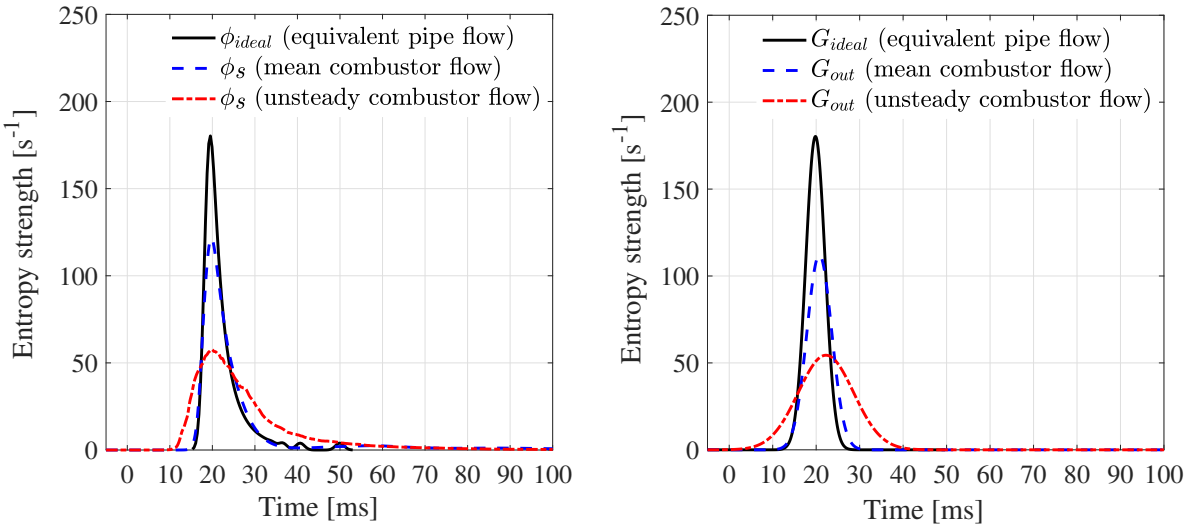
The mean bulk velocity of the 1-D pipe flow, $\overline{u}_d = 14.97$ m/s, matches the LES-simulated flow velocity just downstream of the flame region. The mean axial velocity profile in this pipe is assumed time-independent, varying only radially as [161]:

$$u(r) = u_{\max} - \frac{2.5u_{\max}}{20} \ln\left(\frac{R_p}{R_p - r}\right), \tag{6.8}$$

with r the radial distance from the pipe centreline, R_p the pipe radius equal to $D_p/2$, and $u_{\max}$ the maximum axial velocity satisfying $u_{\max} = 1.2\overline{u}_d$. The residence time profile, $\tau_{\text{res}}(r)$, for an entropy wave travelling from the flame sheet (i.e. the equivalent pipe inlet) to the combustor exit (i.e. the pipe outlet) is computed as:

$$\tau_{\text{res}}(r) = \frac{L_c}{u(r)}. \tag{6.9}$$

An ideal Dirac-function entropy source, $\dot{Q}_{\text{ideal}}$, is imposed at the pipe inlet, coinciding with the mean flame front. The time-variation of the resulting entropy flux at the pipe outlet, ϕ_{ideal}, is then equal to the probability density function (PDF) of the analytical pipe residence time, i.e. PDF(τ_{res}) [75]. As shown in Fig. 6.9(a), the maximum amplitude of ϕ_{ideal} is 180.2 s^{-1}, which is ~1.5 times higher than the maximum ϕ_s value in the mean combustor flow (119.8 s^{-1}), and



(a) Time-variations of exiting entropy fluxes (b) Gaussian approximations of entropy fluxes

FIGURE 6.9: (a) Exiting entropy fluxes for the mean (dashed line) and unsteady (dash-dotted line) combustor flows and the equivalent fully-developed pipe flow (solid line); (b) Gaussian approximations of exiting entropy fluxes in (a).

more than three times higher than the maximum ϕ_s in a time-varying combustor flow (57.7 s^{-1}). This means the unsteady combustor flow attenuates the peak amplitude of the "flame-to-outlet" entropy wave by a factor of roughly three compared to the equivalent fully-developed pipe flow.

The time-evolution of ϕ_{ideal} can also be well-estimated by a Gaussian function, G_{ideal} [161], as shown in Fig. 6.9(b). The function's mean delay time, τ_2, is calculated to be 19.8 ms, which is close to those in both unsteady (22.2 ms) and mean (20.7 ms) combustor flows. The dispersion time of G_{ideal}, i.e. $\Delta\tau_2$, is equal to 3.10 ms, which is much smaller than those for the mean (4.95 ms) and time-varying (10.44 ms) combustor flows.

The frequency responses of the entropy wave advection from flame to exit for the above three cases are finally computed by the fast Fourier transform (FFT) of the relevant signals. For the mean and unsteady combustor flow fields, the entropy source, $\dot{Q}_{\mathcal{V}}$, and the Gaussian-fitted exiting entropy fluxes, G_{out}, are used. The small dispersion time, $\Delta\tau_1$, ensures that $\dot{Q}_{\mathcal{V}}$ is close to the ideal delta impulse, $\dot{Q}_{\text{ideal}}$. The ratio of FFT(G_{out})/FFT($\dot{Q}_{\mathcal{V}}$) is then calculated over frequency. For the equivalent pipe flow, the ideally impulsive entropy input, $\dot{Q}_{\text{ideal}}$, and the subsequent Gaussian fitted output, G_{ideal}, are used, resulting in the FFT ratio of FFT(G_{ideal})/FFT($\dot{Q}_{\text{ideal}}$).

Figure 6.10(a) shows the frequency response amplitudes of entropy wave advection within above three flow fields, plotted against both normalised frequency, f^*, and frequency, f, with the

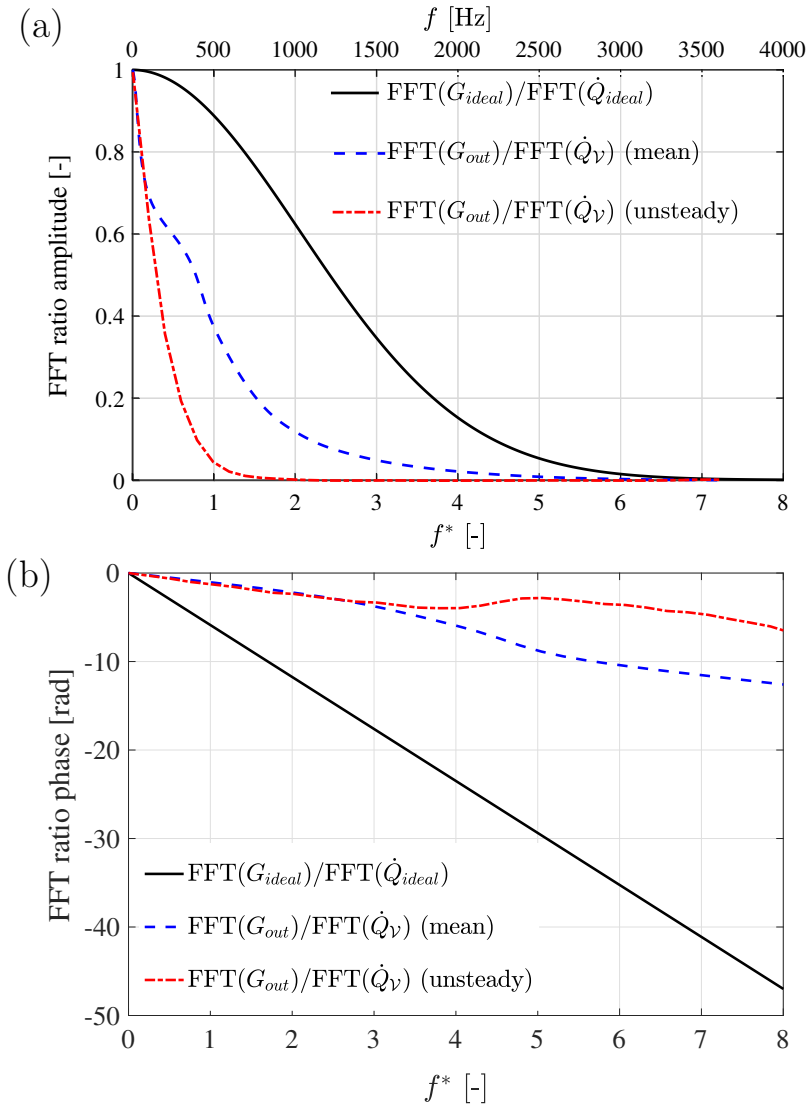


FIGURE 6.10: Frequency response (a) amplitudes and (b) phases for entropy wave advection in mean (dashed line) and unsteady (dash-dotted line) combustor flows and in an equivalent pipe flow (solid line). f^*: normalised frequency equal to $fL_c/\overline{u}_d$.

former defined as:

$$f^* = \frac{fL_c}{\overline{u}_d}, \tag{6.10}$$

where f^* is also known as the Strouhal number. For a mean bulk velocity of $\overline{u}_d = 14.97$ m/s and a characteristic length of $L_c = 0.349$ m, f^* is calculated to range between 0 and 8 (see the bottom-axis of Fig. 6.10(a)), with the corresponding range of f being [0, 335] Hz (not shown). The frequency response amplitude for the fully-developed pipe flow has the widest bandwidth, with the mean and unsteady combustor flows giving successively reduced bandwidths. The large-scale unsteady flow features (e.g., swirl) in the unsteady combustor flow thus act to reduce

the bandwidth of the frequency response, which is a significant effect that cannot be neglected.

The phases of the frequency response ratios are also plotted in Fig. 6.10(b), showing that the pipe flow advection leads to a linear phase decrease over frequency, with a large slope magnitude. In contrast, the two combustor flow fields (mean and unsteady) both offer nonlinear and much flatter phase profiles in frequency. This highlights the differences in the dispersion effects between the ideal pipe flow and the realistic combustor flows on entropy wave advection.

Note that although the present network geometry is representative of an industrial combustor, the applied mean flow speed is much lower than that under a real operating condition (e.g., [14, 24]). For these conditions, a flame-downstream Mach number of $M_d = 0.21$ is typical, referring to a mean bulk velocity of $\overline{u}_d = 179$ m/s (assuming a flame-downstream temperature of $T_d = 1800$ K and ratio of specific heats $\gamma = 1.4$). The frequency range (f) is then extended over [0, 4000] Hz for f^* in the same range of [0, 8] (see the top-axis of Fig. 6.10(a)). As can be seen, despite the presence of advective dispersion, significant entropy wave strength still reaches the combustor exit plane at low frequencies ($f \leq 500$ Hz) for all the three flow fields, and thus the entropy noise is likely to be relevant in cases where a large amount of entropy waves are generated.

6.3 Entropy Noise Effect on Duct Thermoacoustic Modes

It has been seen that a real combustor flow can result in significant dispersive attenuation on the advected entropy waves. This will significantly reduce the strength of entropy waves undergoing acceleration through the first turbine stage, and hence of the entropy noise generated.

This section now seeks to investigate the effect of entropy noise on the thermoacoustic modes of two simple duct combustors, taken to be simplified representations of industrial gas turbine combustors, in the presence of realistic dispersive attenuation. The first, denoted combustor A, considers a simplified version of the SGT-100 network geometry (Fig. 6.8(a)), retaining the same duct radius, R_p, and the flame-downstream length, L_c, as shown in Fig. 6.11(a). The duct bulk flow velocity is increased, with appropriate normalised frequency (f^*) scaling applied to the advective dispersion. The acoustic boundary condition at duct outlet is taken to be choked, so that it better represents real gas turbine operating conditions rather than laboratory tests. The inlet boundary condition is chosen to be fully closed with $R_{\text{in}} = 1$. The second combustor,

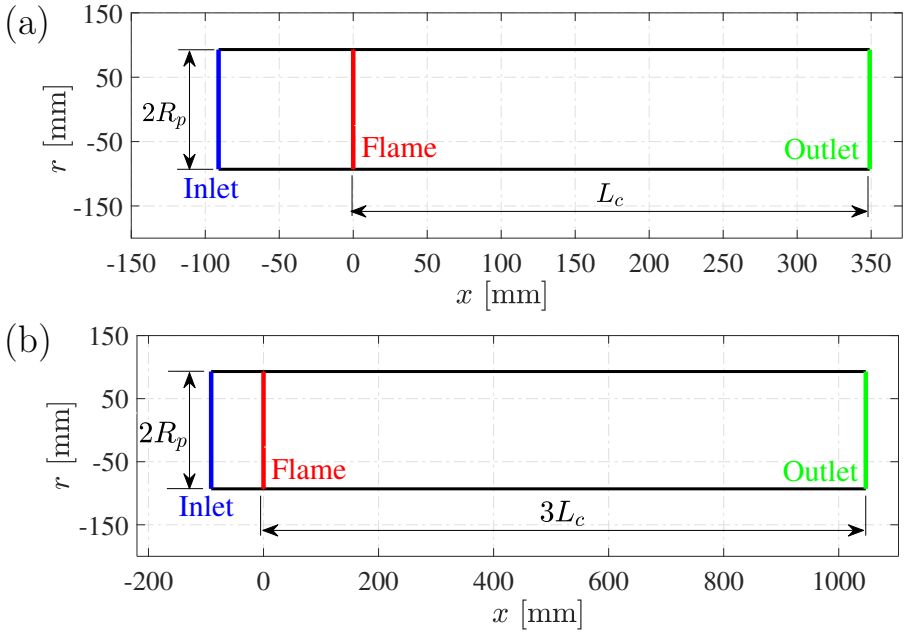


FIGURE 6.11: Two circular duct combustors with choked outlet: (a) combustor A, flame-downstream length $L_c = 0.349$ m; (b) combustor B, flame-downstream length $3L_c = 1.047$ m. Both ducts have the same pipe radius of $R_p = 0.093$ m.

TABLE 6.1: Thermal and flow properties in duct combustors A and B. Flame-upstream mean properties (subscript "1") are prescribed, and flame-downstream mean properties (subscript "2") follow from the flow conservation equations [18].

Fuel type	Equivalence ratio ϕ_e [-]	Combustion efficiency η [-]
Methane (CH_4)	0.70	0.80
Mean pressure $\overline{p}$ [bar]	**Mean temperature $\overline{T}$ [K]**	**Mean Mach number $\overline{M}$ [-]**
$\overline{p}_1$: 15 $\overline{p}_2$: 14.65	$\overline{T}_1$: 400 $\overline{T}_2$: 1643	$\overline{M}_1$: 0.1 $\overline{M}_2$: 0.22

denoted B, has the same radius, bulk velocity and boundary conditions as combustor A, but with a longer flame-downstream length of $3L_c$, as shown in Fig. 6.11(b).

As shown in Table 6.1, the mean flow properties upstream of the flame in both duct combustors are prescribed based on typical industrial conditions (e.g. [146, 161]), with the mean properties downstream calculated through the mean flow conservation equations [18].

The flame model used here in order to capture the unsteady heat release rate response, $\widehat{\dot{Q}}$, to upstream velocity perturbation, $\widehat{u}_1$, is a linear $n-\tau$ model with a 1st-order low-pass filter [18, 235], as defined in Eq. 2.26 and repeated here:

$$\frac{\widehat{\dot{Q}}(\omega_i)}{\overline{\dot{Q}}} = \frac{\omega_i^c}{\omega_i + \omega_i^c} n_f e^{-i\omega_i \tau_f} \frac{\widehat{u}_1(\omega_i)}{\overline{u}_1}. \tag{6.11}$$

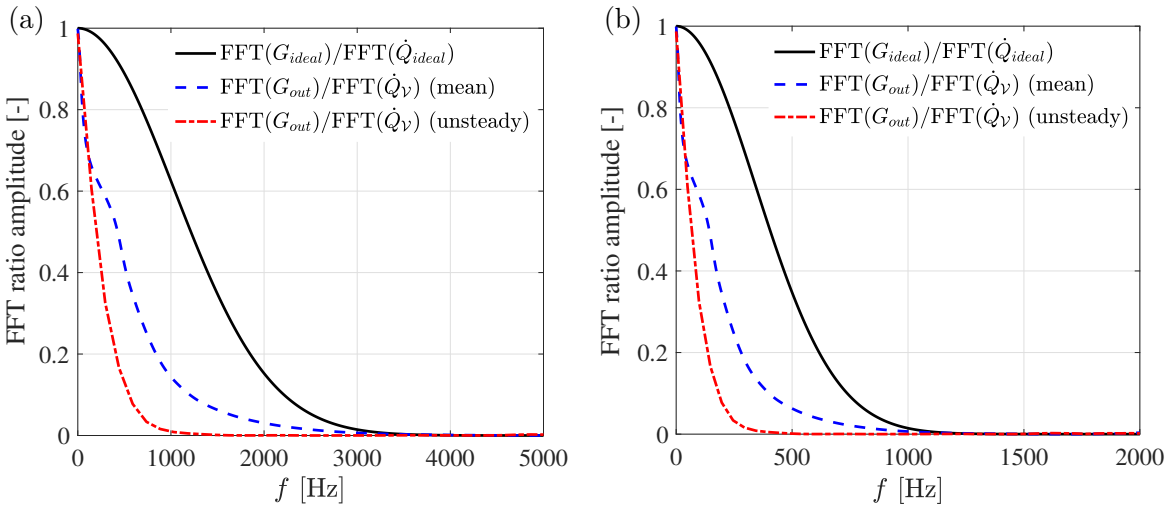
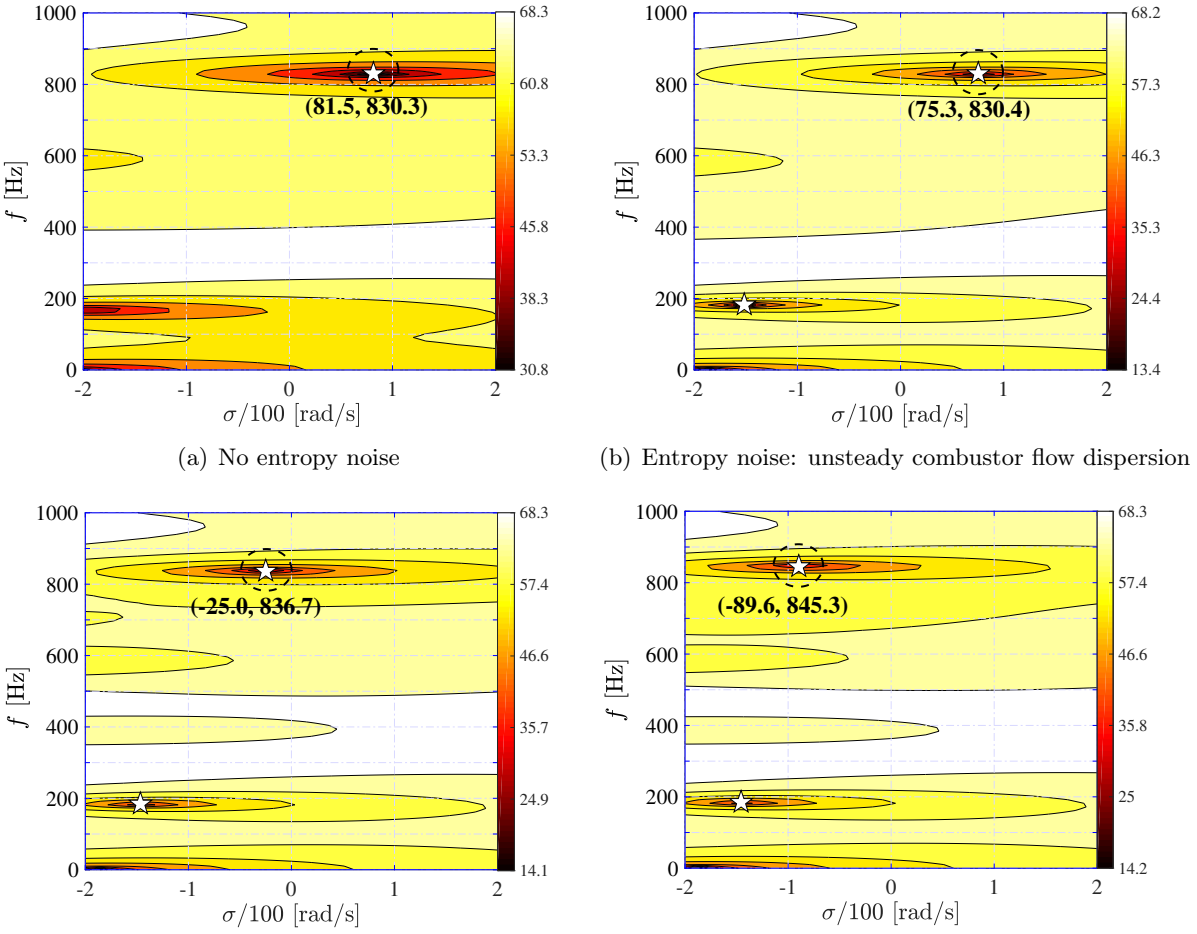


FIGURE 6.12: Amplitudes of the frequency response functions for entropy wave advection from flame to combustor exit: (a) combustor A; (b) combustor B.

The values of the model's gain (n_f), time delay (τ_f) and filter's cut-off frequency ($f_c = \omega_i^c/(2\pi)$) all depend on the combustor geometry and flame structure [231, 236]; here values of $n_f = \{1, 1\}$, $\tau_f = \{3, 1\}$ ms and $f_c = \{370, 380\}$ Hz are chosen for combustor A and B, respectively.

The final piece of information needed to calculate the thermoacoustic modes is the "dispersion time model" representing the time-spread that occurs as an entropy wave advects from the flame to the duct exit. For the short combustor A, the f^*-rescaled entropy dispersion times, $\Delta\tau_2$, are calculated to be $\{0.7279, 0.3449, 0.2161\}$ ms for dispersion by the unsteady combustor flow, mean combustor flow and fully-developed pipe flow, respectively. For the longer combustor B, the f^*-rescaled $\Delta\tau_2$ values are tripled and become $\{2.1837, 1.0347, 0.6483\}$ ms for the above three dispersion models. The normalised frequency response functions shown in Fig. 6.10(a) are then mapped onto the frequency domain via $f = f^* \cdot \overline{u}/L_c$, as shown in Fig. 6.12. The bandwidths of the resulting frequency responses for the shorter duct A are found much wider than those for the longer combustor B.

The low order network thermoacoustic solver, OSCILOS [60, 67], is then used to calculate the thermoacoustic modes for both ducts in the presence of prescribed flame models and entropy dispersion time models. For combustor A, the predicted modes both neglecting and accounting for entropy noise, the latter with three different entropy wave dispersion models, are all plotted in Fig. 6.13, with modal frequencies plotted against modal growth rates. The dominant mode has a frequency of ∼830 Hz, and its growth rate in the absence of entropy noise is positive, indicating that the mode is unstable (Fig. 6.13(a)). When the entropy noise is accounted for,



(a) No entropy noise

(b) Entropy noise: unsteady combustor flow dispersion

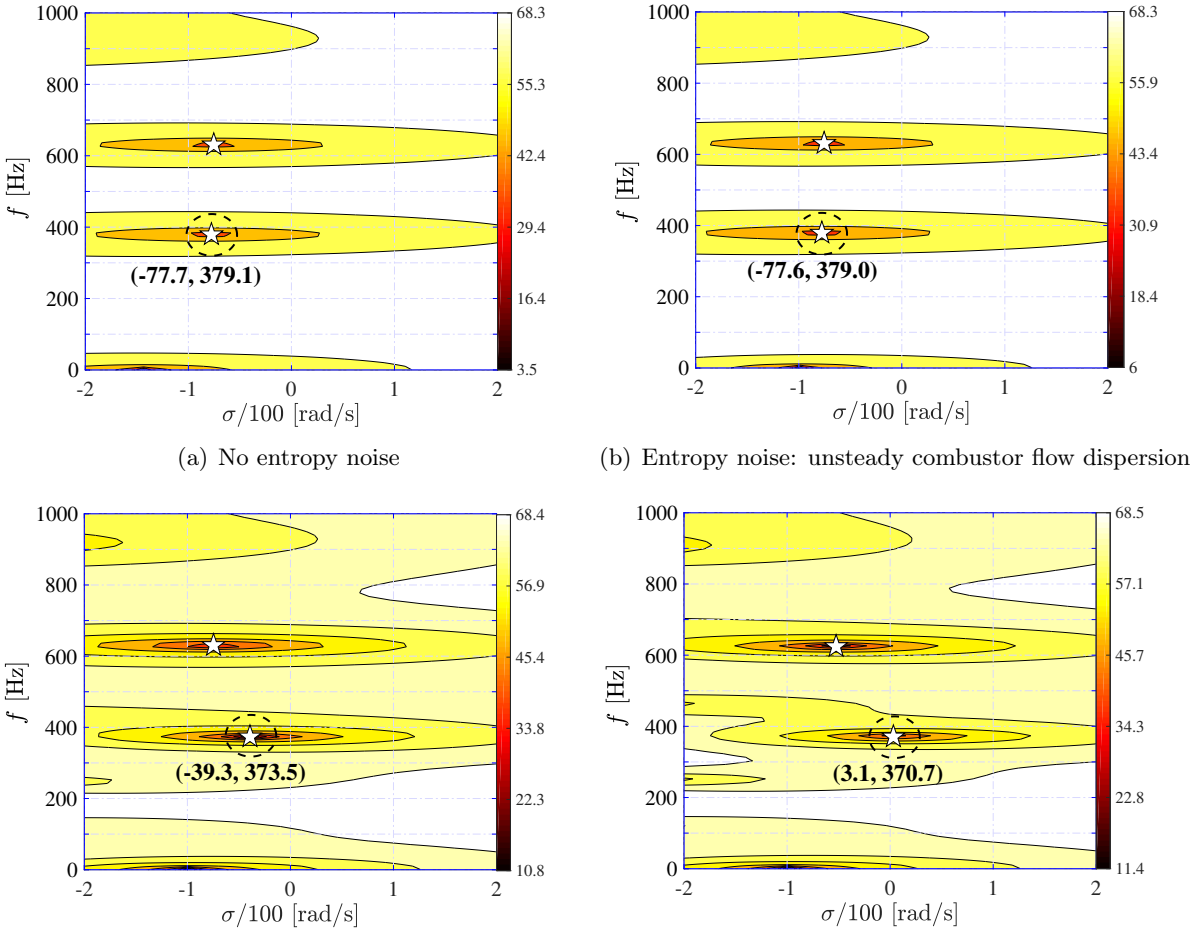
(c) Entropy noise: mean combustor flow dispersion

(d) Entropy noise: pipe flow dispersion

FIGURE 6.13: OSCILOS-predicted thermoacoustic modes for the short duct combustor A, located at minima of the f-σ plane for $\log_{10}|\delta_e(\omega)|$ and marked by white stars.

however, its modal growth rate gradually decreases so that the unstable mode is moving left and eventually stabilised — this is most pronounced for the over-simplistic pipe flow (Fig. 6.13(d)) and the "frozen" mean combustor flow (Fig. 6.13(c)) dispersion models, but also occurs for the realistic unsteady combustor flow dispersion model (Fig. 6.13(b)).

The thermoacoustic modes of the longer combustor, B, are then computed, as shown in Fig. 6.14. The frequency of the dominant mode is now ∼370 Hz. When the entropy noise is neglected, this mode has a negative growth rate and is therefore stable (Fig. 6.14(a)). Accounting for the entropy noise in the presence of the over-simplistic pipe flow dispersion model causes this mode to be destabilised (Fig. 6.14(d)). However, when the more realistic unsteady combustor flow dispersion model is used (Fig. 6.14(b)), the entropy noise fails to affect this mode at all — it remains stable with almost the same growth rate as when the entropy noise is neglected. Due to the increase in the flame-downstream length (from L_c to $3L_c$), the entropy dispersion



(a) No entropy noise

(b) Entropy noise: unsteady combustor flow dispersion

(c) Entropy noise: mean combustor flow dispersion

(d) Entropy noise: pipe flow dispersion

FIGURE 6.14: OSCILOS-predicted thermoacoustic modes for the longer duct combustor B, located at minima of the complex f-σ plane and marked by white stars.

times ($\Delta\tau_2$) are now much longer for duct B, and the bandwidth of the dispersive frequency response becomes too small to affect the mode under an unsteady combustor flow dispersion (see Fig. 6.12(b)). Finally, all the above effects of entropy noise on the dominant modes of combustors A and B are summarised in Table 6.2.

6.4 Summary

In this chapter, the transport of entropy waves within the SGT-100 combustor flows has been investigated via numerical simulation. An entropy source in the form of a time-impulsive Gaussian perturbation at the mean flame location was applied, and its transport was studied using

TABLE 6.2: Effects of entropy noise on the dominant thermoacoustic modes of two simple duct combustors (f: frequency; σ: growth rate).

Combustor A	f [Hz]	σ [rad/s]
No entropy noise	830.3	81.5
Entropy noise: unsteady combustor flow dispersion model	830.4	75.3
Entropy noise: mean combustor flow dispersion model	836.7	-25.0
Entropy noise: equivalent pipe flow dispersion model	845.3	-89.6
Combustor B	f [Hz]	σ [rad/s]
No entropy noise	379.1	-77.7
Entropy noise: unsteady combustor flow dispersion model	379.0	-77.6
Entropy noise: mean combustor flow dispersion model	373.5	-39.3
Entropy noise: equivalent pipe flow dispersion model	370.7	3.1

a passive scalar simulation superimposed on the main reacting flow LES. The transport of entropy perturbations is found dominated by the dispersive advection, with the contributions from thermal diffusion and viscous production both being negligible. It is also found that the change of entropy source shape does not affect the downstream entropy transport process, thus the detailed generation mechanism of the entropy waves from the flame is not the main focus of this work.

The advection of entropy waves within a real unsteady combustor flow is found relatively fast, controlled by both mean flow dispersion and large-scale unsteady flow features (e.g., swirl, vortices). In the time-averaged combustor flow, however, the central flow recirculation zone initially traps a large amount of entropy inside and largely delays the entire entropy advection. By comparing the entropy fluxes at the combustor exit, the large-scale unsteady flow structures are found to contribute more significantly to the advective wave dispersion, and hence to the larger entropy strength attenuation at the exit.

As compared to an equivalent fully-developed pipe flow, whose dispersion is modelled by a simple analytical expression, the dispersion level within an unsteady combustor flow is more than tripled. By scaling the normalised frequency responses to typically high bulk flow speeds, it is found that despite the advective dispersion, sufficient entropy wave strength is likely to remain at the combustor exit.

The effect of entropy noise on the thermoacoustic modes of two simple duct combustors with different axial lengths was finally studied. The entropy noise generated with the pipe flow dispersion model has the strongest strength, while the mean and unsteady combustor flow dispersion models have successively decreasing contributions to the entropy noise impact. It was then found that the effect of entropy noise on the dominant modes is much reduced when applying a realistic advective dispersion model, but that entropy noise still has the potential to influence the modes, including to cause stability changes. This finding motivates properly accounting for entropy noise via the use of accurate advective dispersion models.

Chapter 7

ORACLES Long Flame Combustor

This chapter numerically investigates the response of a very long flame to upstream perturbations in a laboratory combustor. For this combustor, thermoacoustic limit cycle oscillations were measured at an unstable condition, and the simulated flame responses and a low order network tool are therefore used to computationally predict the limit cycle oscillation behaviour. Different from the SGT-100 combustor studied in Chapters 4 – 6, this combustor does not have an upstream swirler and the flame inside has a much longer axial length, therefore the axial variation in the heat release response of this long flame to an upstream excitation must be accounted for. The thermoacoustic prediction approach then also needs to be slightly modified to account for this axially-varying flame response. The main content of this chapter has been published in [5].

7.1 Experimental Set-up

The long flame combustor studied in this chapter is called "ORACLES", standing for "One Rig for Accurate Comparisons with Large Eddy Simulations" [15, 237]. This combustor has four main sections, as schematically illustrated in Fig. 7.1(a), which from upstream to downstream are: (i) two straight settling chambers and the followed converging channels, in which the incoming fuel and air are fully mixed; (ii) a long section of two separate rectangular channels of constant cross-section, each with a height of $H = 30.4$ mm and a length of $l_{02} = 3.270$ m. This set-up is required to obtain two fully-developed turbulent channel flows. A metal plate of thickness $h_p = 10$ mm is installed along the centreline, equally splitting the two channels; (iii) a unique combustion chamber with adiabatic walls and a length of $l_3 = 2$ m, stabilising the flame region

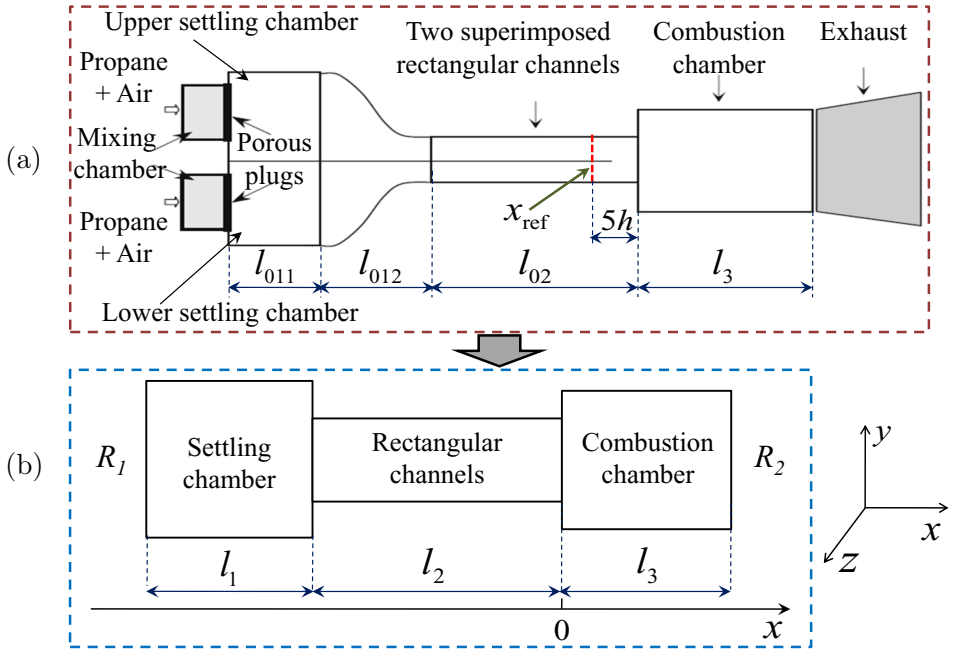


FIGURE 7.1: Schematic of (a) the ORACLES laboratory combustor and (b) its simplified network representation. Figures taken from [5].

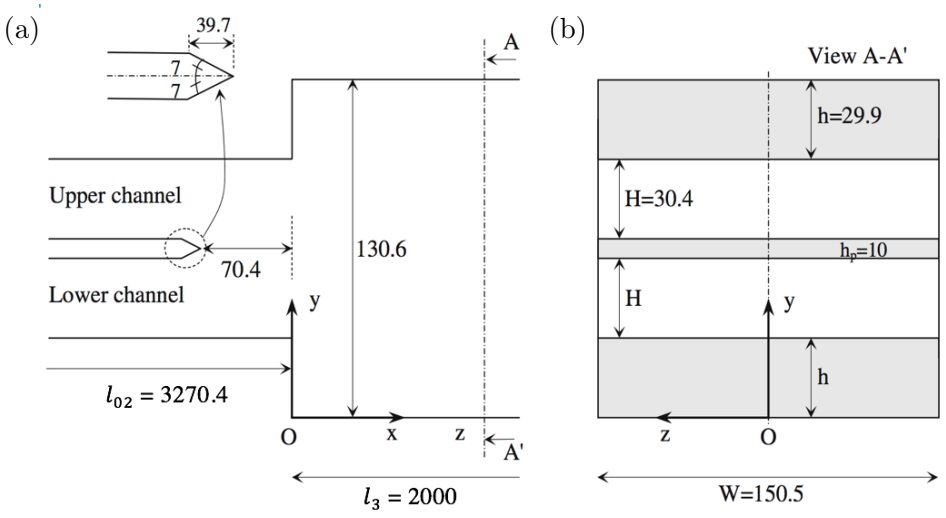


FIGURE 7.2: Geometric details of the ORACLES combustion chamber entrance, with all dimensions in mm. Figures adapted from [15].

using a symmetric sudden expansion of height $h = 29.9$ mm; (*iv*) an exhaust section. All of the four sections have the same rectangular cross-sectional width of $W = 0.1505$ m. The above geometric details near the ORACLES combustion chamber inlet are shown in Fig. 7.2.

The entire ORACLES facility is operated under atmospheric pressure (i.e. $\overline{p} \simeq 1{\times}10^5$ bar), and the fuel used is gaseous propane (C_3H_8), which is fully-premixed with air at temperature $T_0 = 276$ K at the rig inlet. The bulk velocity of the incoming mixture flow is $U = 11$ m/s,

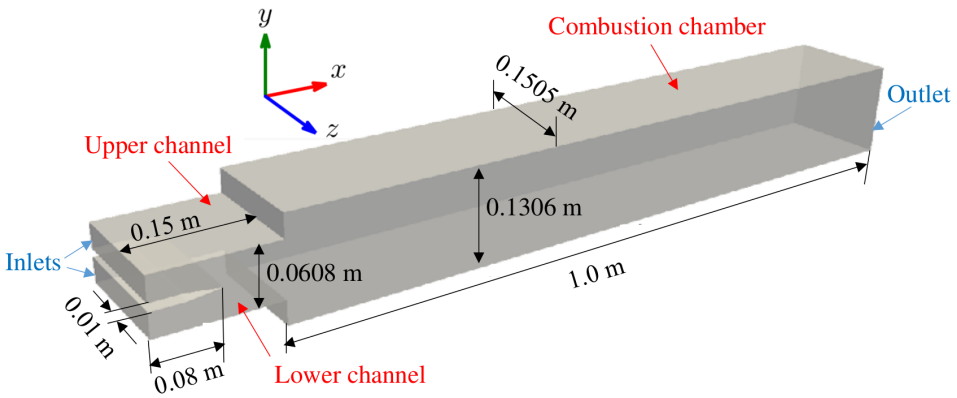
resulting in a Reynolds number of Re $\simeq$ 25,000 [15] based on T_0 and H. It was observed that a long, continuous flame attaches to the combustion chamber entrance, extending downstream for a certain axial length. In the experiments the flame length was not measured, instead it was computed to be around 1 m by LES in a previous study [115] and also in the present work. The ORACLES rig was also measured to exhibit thermoacoustic limit cycle oscillations, which has an oscillation frequency of ∼50 Hz and a corresponding upstream velocity perturbation amplitude of ∼0.29, both recorded at a reference location of $x_{\text{ref}} = -5h = -0.1495$ m (see Fig. 7.1(a)) upstream to the flame [15, 115].

7.2 Numerical Framework

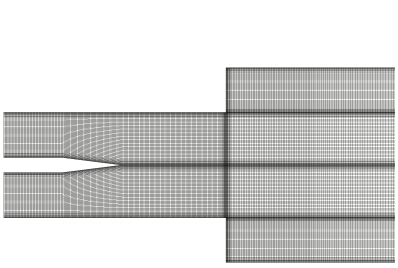
This work aims at numerically simulating the long flame responses in the ORACLES rig and using the computed flame models as the basis for the prediction of the resulting limit cycle oscillations. Previous LES studies, e.g., [238, 239], on the same combustor generally extend only over a short combustion chamber zone covering part of the long flame. These enable highly resolved prediction of the flow field in the covered region, where the experimental data are available. However, since the entire flame has a total length of ∼1 m [115], simulating such a short computational zone cannot fully capture the heat release response of the entire flame.

Therefore, in this work the LES computations are performed over a longer chamber region starting from x = -0.15 m to x = 1 m, as sketched in Fig. 7.3(a). The computational domain now extends upstream into the two separate rectangular channels, and one metre downstream into the combustion chamber, containing the reference point, x_{ref} = -0.1495 m, where the upstream velocity perturbation was measured [15], and nearly the entire heat release zone (at some instants, a very small part of the flame may leave the computational domain. However, the time-averaged heat release zone remains well within the computational domain).

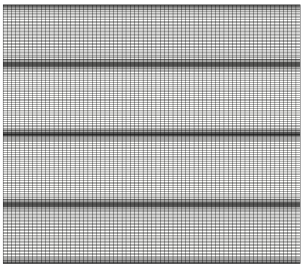
Based on previous research [238–241], the present computational domain has been meshed with structured hexahedral cells, as shown in Figs. 7.3(b, c). The total number of mesh cells is ∼5.46 million. Near the domain inlet, the mesh grid density is $180 \times 100 \times 70$ in the axial (x), vertical (y) and lateral (z) directions, respectively. Inside the combustion chamber, the mesh density is $300 \times 200 \times 70$. The first mesh point is always located 0.1 mm away from the solid boundaries. The volume of the mesh cell ranges from 8.57×10^{-11} m^3 to 1.288×10^{-5} m^3, which is sufficiently fine to capture the main flow features accurately. The maximum skewness of the mesh cell is



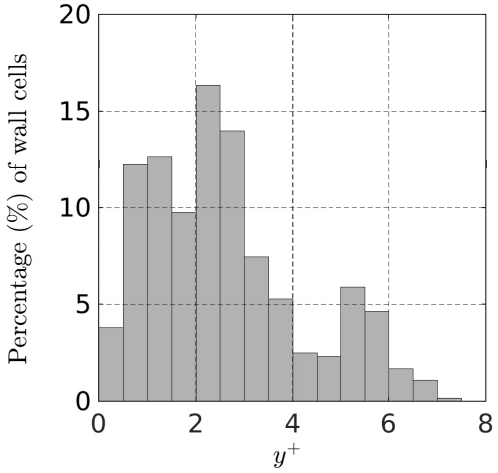
(a) 3-D computational domain



(b) $x - y$ plane at $z = 0$ m



(c) $y - z$ plane at $x = 0.5$ m



(d) Histogram of y^+

FIGURE 7.3: (a) LES computational domain, meshed with ∼5.46 million structured cells; mesh grids (b) near domain inlets and (c) within the combustion chamber. (d) Statistics of the normalised wall-normal distance, y^+, for all the cells that are closest to the solid walls.

0.157, providing a generally good mesh quality for the present LES. The closest wall-normal distance of the mesh nodes normalised by the viscous length-scale, denoted y^+, varies from 0.06 to 7.0. y^+ has the largest value near the two domain inlets, then gradually decreases along the axial direction, with local variations at some points. This is because an artificial velocity

perturbation is to be imposed at the domain inlets, therefore the velocity gradients at the walls are very high, leading to large values of y^+ at the inlets. The statistics of y^+ values are plotted in Fig. 7.3(d), where the majority (86.5%) of the near-wall cells are located within the viscous sublayer (i.e. $y^+ \leq 5$), and the averaged value of y^+ is 2.6, indicating the mesh is fine enough for the present LES.

The numerical methods used in the present work are very similar to those applied in [68]. The flame response to an upstream velocity perturbation is simulated using the incompressible LES, via the open-source CFD toolbox, OpenFOAM [122]. The state of gas equation is given as: $\rho = p_0/(R_g T)$, where the reference pressure, p_0, remains constant in time and space based on the zero-Mach number assumption implemented in the asymptotic expansion of Navier-Stokes equations [242]. The change of mixture density, ρ, is thus uniquely associated with the temperature, T. All the acoustic waves are now removed from the flow simulation, which allows a larger computational time step which is not limited by the inverse of the speed of sound. This largely accelerates the computational speed [243].

A modified ReactingFOAM-LES solver within OpenFOAM is now applied, which has been validated in previous studies (e.g., [68, 104, 244, 245]). This solver solves the Favre-filtered conservation equations of mass, momentum, species mass fractions and energy [243], by using a collocated Finite Volume Method (FVM) in which the spatial discretisation is based on the Gauss's theorem, together with a semi-implicit time-integration scheme. In the present LES study, the Preconditioned-Conjugate-Gradient (PCG) algorithm is used to solve pressure, while the Preconditioned-BiConjugate-Gradient (PBiCG) algorithm is applied for velocity, enthalpy and species mass fractions. The method used to solve the mass and momentum equations is PIMPLE [122] (merged PISO and SIMPLE algorithms), which is suitable for the present transient simulations and has been used for the SGT-100 study in Chapters 4 – 6. An implicit 2nd-order Crank-Nicolson scheme is applied for the time derivatives, with the convection terms discretised using a 2nd-order Gaussian linear scheme in space. All the heat losses involved in the simulations are captured by the energy conservation equation.

In order to close the filtered conservation equations, the one-equation SGS kinetic energy turbulence model [11–13], as introduced in Section 3.2.4, is used to model the filtered Reynolds stresses. The LES-PaSR combustion model [198], which has been described in Section 3.3.2, is applied for the turbulence-chemistry interactions; this has been validated for premixed and partially-premixed flames in various studies [68, 104, 244]. In this work, a newly developed

mixing time (τ_m) model [199, 209] has been applied in the LES-PaSR solver. Based on the SGS mixing and Kolmogorov time-scales, the mixing constant, C_m, as defined in Eq. 3.32, is now set as 3.0 to correctly capture the responses of the long flame, which is much higher than the value of 0.8 used for the compact flame in the SGT-100 rig (see Section 4.2 for more details). A global one-step propane/air reaction scheme involving 7 intermediate species [246] is applied, which was developed to model the lean premixed propane/air flames and validated by previous LES studies on thermoacoustic instability [246]. A steady fuel/air equivalence ratio of $\phi_e = 0.75$ is applied in this work, and a fixed time step of 1×10^{-5} s is used by all the computations, resulting in a maximum CFL number of $\sim$0.5.

For the boundaries of the computational domain, the zero-gradient conditions are applied for the outflow velocity and scalars at the combustion chamber exit (Fig. 7.3(a)). Except for the two inlets, the outlet and the two lateral z-planes, all the other boundaries are treated as solid adiabatic non-slip walls [238–241], as it was stated in [15, 237] that the ORACLES rig are thermally insulated with a refractory material, although it was shown in [220, 247, 248] that the heat losses (or changes in the wall temperature) may have a strong impact on the flame responses. The boundaries in the lateral z-direction (i.e. the two lateral planes) are set to be periodic [238, 240].

For the domain inlets, unsteady inflow velocities are prescribed at the two channel entrances. For the base flow without any perturbation, the used time-averaged bulk velocity at the reference location (or at the inlet plane that is very close to the reference point) is $U = 11$ m/s, which is equal to the measured value. In order to compute the FDF for the long flame, a harmonic velocity perturbation is superimposed on the mean bulk inflow with artificial turbulence fluctuations [249] at the inlet of the computational domain. This leads to an inflow axial velocity profile as:

$$u_1(y,t) = U(y)\left[1 + A_u \sin(2\pi f_u t) + w_t(t)\right], \tag{7.1}$$

where the mean velocity profile, $U(y)$, only varies along the vertical y-direction, fitted by a 7th-order polynomial to experimental data at the reference location, $x_{\text{ref}} = -5h$, on the mid $y-z$ plane. f_u is the perturbation frequency and $A_u = |u_1'/U|$ the normalised perturbation amplitude, both of which are varied independently, resulting in a series of perturbation cases in order to compute the FDF over frequency at multiple A_u levels. $w_t(t)$ is an artificial turbulence fluctuation with an amplitude of 5%, introduced based on the experimental data [15].

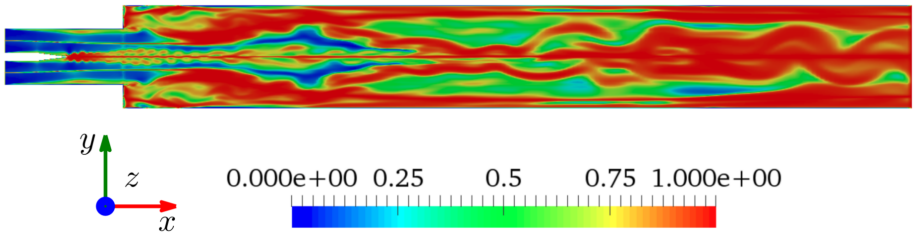


FIGURE 7.4: Contours of the sub-grid activity parameter, s_a, on $x-y$ plane at $z = 0$ m, forced by an upstream velocity perturbation of $A_u = 0.29$ and $f_u = 50$ Hz. Figure adapted from [5].

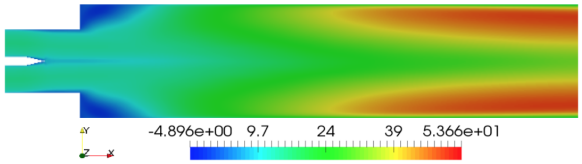
The sub-grid activity parameter [250], s_a, is also calculated as:

$$s_a = \frac{\langle \varepsilon_t \rangle}{\langle \varepsilon_t \rangle + \langle \varepsilon_\mu \rangle}, \tag{7.2}$$

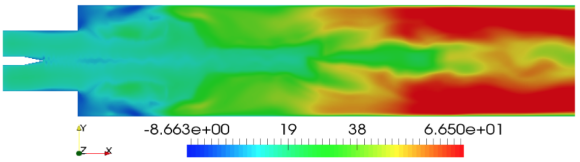
where $\langle (\cdot) \rangle = \left(\iiint_{\mathcal{V}} (\cdot) \mathrm{d}\mathcal{V} \right) / \mathcal{V}$ denotes spatial averaging over the flow domain volume, $\mathcal{V}$, and $\varepsilon_t = -\tau_{ij} \left(\partial \widetilde{u}_i / \partial x_j \right)$ and $\varepsilon_\mu = \widetilde{S}_{ij} \left(\partial \widetilde{u}_i / \partial x_j \right) / \mathrm{Re}$ are the turbulence and molecular dissipation rates, respectively, both varying with the Reynolds number, Re. Based on Eq. 7.2, the value of s_a satisfies $0 \leq s_a < 1$, with $s_a = 0$ representing DNS and $s_a = 1$ corresponding to LES with an infinitely-large Reynolds number [250]. The value of s_a thus quantifies the relative importance of the SGS models used by the present LES. The contour of s_a under an upstream perturbation of $A_u = 0.29$ and $f_u = 50$ Hz is plotted in Fig. 7.4. It is noted that the value of s_a is small within the upstream channels, but becomes larger in the downstream chamber, indicating that the mesh cells are well-refined near the domain inlets but are relatively coarser downstream, where the SGS models play a more important role in this downstream highly turbulent zone.

7.3 LES Results and Validation

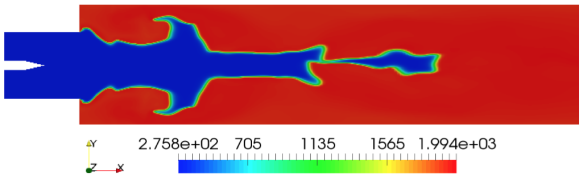
Based on the above numerical methods, the unforced LES simulations are firstly performed without any upstream perturbations. As shown in Fig. 7.5, the contours of axial flow velocity, mean temperature and mean heat release rate are plotted on the symmetry plane of $z = 0$ m. It is firstly noted that both the mean (Fig. 7.5(a)) and instantaneous (Fig. 7.5(b)) velocity fields are generally symmetric with respect to the combustion chamber's centreline, with two small outer recirculation zones near the top and bottom back-step corners. Different from the turbulent swirling flow in the SGT-100 rig (e.g., Fig. 6.1(c)), the flow field in the ORACLES rig is non-swirling and thus does not have a large upstream inner recirculation zone along the centreline.



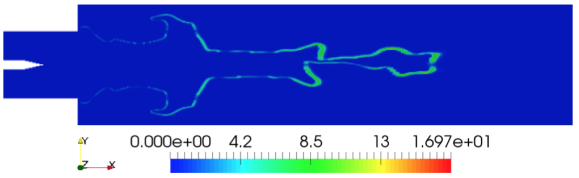
(a) Mean axial velocity (m/s)



(b) Instantaneous axial velocity (m/s)



(c) Mean temperature (K)



(d) Mean heat release rate from each cell volume (W)

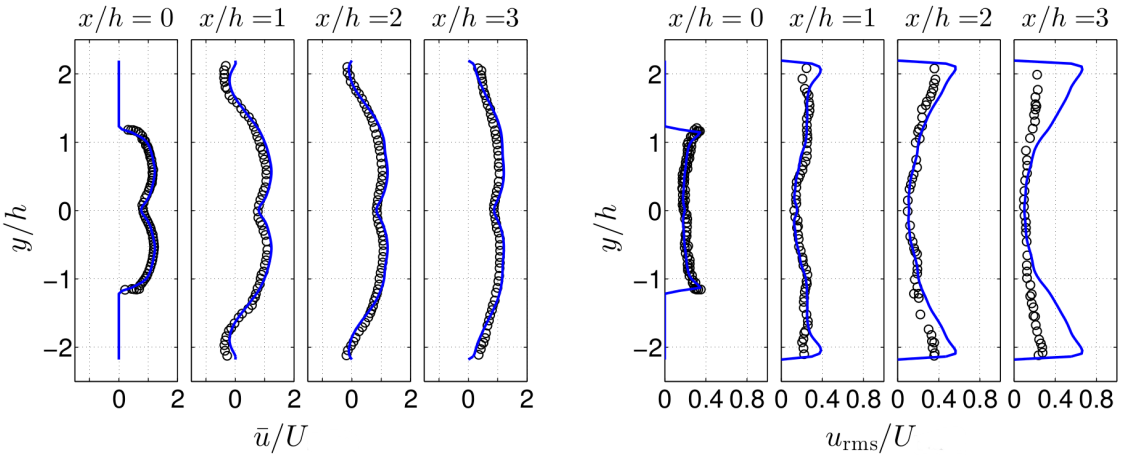
FIGURE 7.5: Contours of unforced LES-simulated (a) mean axial velocity, $\overline{u}$; (b) Instantaneous axial velocity, u; (c) mean temperature, $\overline{T}$, and (d) mean heat release rate from each cell volume, $\overline{\dot{Q}}_m$.

High flow speed regions are found downstream near the top and bottom inner walls, close to the domain exit (Figs. 7.5(a, b)). The mean temperature field (Fig. 7.5(c)) shows that a long low-temperature zone axially stretches along the centreline into the combustion chamber, with cold patterns on the two sides induced by the vortices shed from the back-steps. This results in a very long flame shown in Fig. 7.5(d), whose heat release rate field covers a large axial area.

The forced LES simulations are then performed under the measured limit cycle perturbation: $f_u = 50$ Hz, $A_u = 0.29$. As shown in Fig. 7.6 for the axial (u) and Fig. 7.7 for the vertical (v) components, the predicted vertical y-profiles of both mean and fluctuating flow velocities are compared and validated by the experimental data [15] at multiple axial locations, e.g., $x/h = 0$, 1, 2 and 3. The simulated mean flow velocities match the measurements very well (Figs. 7.6(a), 7.7(a)), with small discrepancies existing for the RMS velocities at some downstream locations and near the top and bottom inner walls (e.g., Fig. 7.6(b)). These mismatches are acceptable considering the uncertainties involved in the measurement data. The present LES results are therefore validated to be able to capture the turbulent reacting flow field, which are used as a basis for the next FDF computation.

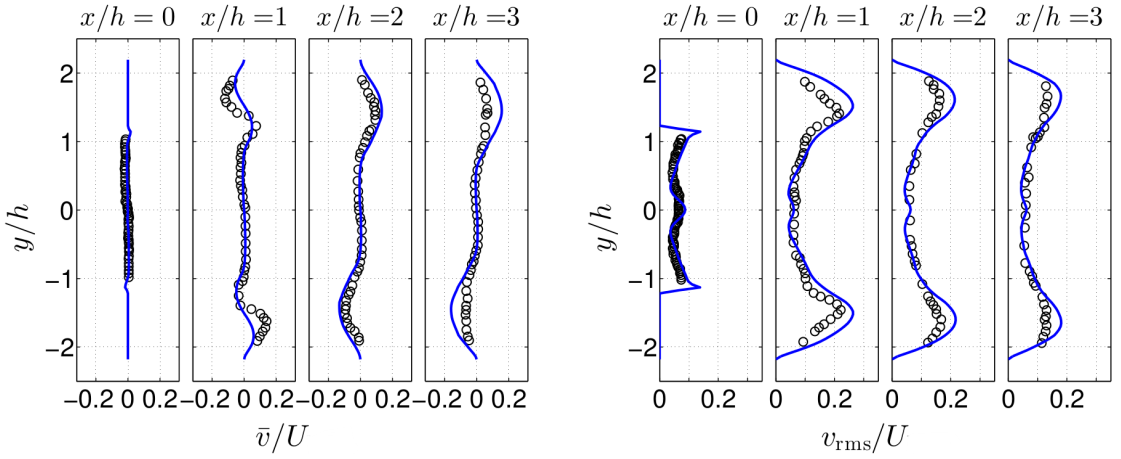
7.4 Flame Describing Functions for the Long Flame

The responses of the long ORACLES flame, forced by the upstream harmonic velocity perturbation at $x = x_{\text{ref}}$ (Eq. 7.1), are now computed. In contrast to the SGT-100 combustor, which



(a) Normalised mean axial velocity (b) Normalised RMS axial velocity

FIGURE 7.6: Vertical y-profiles of normalised (a) mean and (b) RMS axial flow velocities (u) at multiple axial locations, x/h = 0, 1, 2 and 3. Markers ∘ denote experimental data [15] and continuous lines denote forced LES results at f_u = 50 Hz, A_u = 0.29.



(a) Normalised mean vertical velocity (b) Normalised RMS vertical velocity

FIGURE 7.7: Vertical y-profiles of normalised (a) mean and (b) RMS vertical flow velocities (v). Refer to the caption of Fig. 7.6 for more information.

has an acoustically compact flame and uses a global FDF to describe the total heat release rate from the flame, the ORACLES flame is much longer and the axial variation of its unsteady response is likely to be important within a low order acoustic modelling framework. Thus a single FDF can no longer describe the entire flame's response. To deal with this, the long continuous flame needs to be axially split into multiple "flame segments", with the heat release response from each segment modelled by a "local FDF" separately [5]. This flame segmentation method is illustrated in Fig. 7.8. The original flame is now represented as a series of flame segments (e.g., $x \in [x_{j,c}, x_{j+1,c}]$ for the j-th segment), with a thin 1-D flame sheet located at each segment

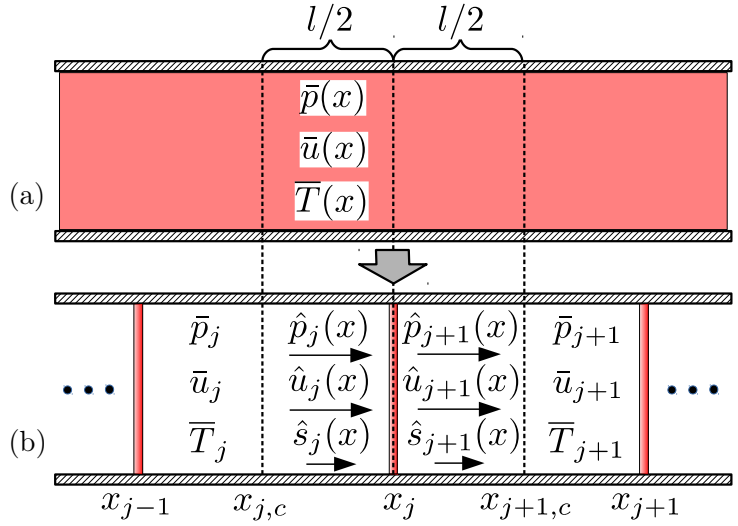


FIGURE 7.8: Sketches of (a) a long continuous flame and (b) its segmentation as a series of discrete compact flame sheets (replotted from Fig. 2.9). The j-th segment ranges between $[x_{j,c},\, x_{j+1,c}]$, with its flame sheet located in the centre (i.e. $x = x_j$).

centre (e.g., $x = x_j$ for the j-th segment). A detailed introduction of this method can be found in Section 2.6.

Practically, the combustion chamber ($x \in [0, 1]$ m) of the present ORACLES computational domain (Fig. 7.3(a)) is equally split into N_{seg} segments along the x-direction. The axial length of each segment, l, satisfies $l \ll \bar{u}/f \simeq U/f_u = 0.22$ m, with $U = 11$ m/s and $f_u = 50$ Hz. The total number of segments is initially set as $N_{\text{seg}} = 40$, resulting in a small segment length of $l = 1/N_{\text{seg}} = 0.025$ m. It will be later investigated whether this length is axially resolved enough to capture the axial variation of the heat release fluctuation, while retaining sufficient signal to noise ratios (SNR) across all the segments.

It should also be noted that the single harmonic velocity perturbation signal, u_1 (Eq. 7.1), used to force all the flame segments remains the same, which is located at a fixed reference location (i.e. $x = x_{\text{ref}}$) upstream to all the segments.

In the present LES, the heat release rate, $\dot{Q}_j$, from an arbitrary j-th segment is calculated by spatially integrating the local heat release rate field over the segment volume. It is then recorded over time for at least 20 forcing cycles after the starting transients have died away. Since the self-excited limit cycle oscillations (caused by thermoacoustic instability) were measured at $f \simeq 50$ Hz under an upstream perturbation level of $A_u \simeq 0.29$, the present forced simulation cases are performed at three perturbation frequencies: $f_u = 40$, 50 and 75 Hz, that cover the

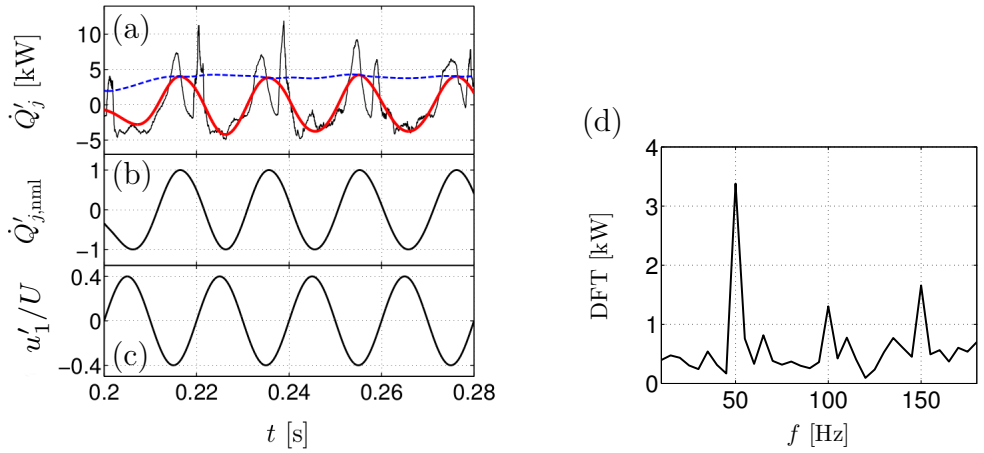


FIGURE 7.9: (a) Time evolution of heat release rate fluctuation, $\dot{Q}'_j = \dot{Q}_j - \overline{\dot{Q}}_j$ (thin solid line), in the 8th flame segment ($j = 8$, $x \in [0.175, 0.2]$ m), and its filtered signal (thick solid line) and envelope (dashed line). (b) Normalised heat release signal, $\dot{Q}_{j,\mathrm{nml}}$. (c) Normalised velocity perturbation, u'_1/U, at the reference location, x_{ref}. (d) Discrete Fourier transform (DFT) of $\dot{Q}_j$ signal in the 8th segment. The resolution is 5 Hz. $f_u = 50$ Hz, $A_u = 0.4$. Figures adapted from [5].

frequency of interest. For each forcing frequency, a total of five forcing amplitudes have been considered: $A_u = 0.1, 0.2, 0.25, 0.3$ and 0.4.

One such perturbation case is illustrated in Fig. 7.9, with the flame forced at $f_u = 50$ Hz with amplitude $A_u = 0.4$. Figure 7.9(a) shows the time-variation of the heat release rate fluctuation, $\dot{Q}'_j = \dot{Q}_j - \overline{\dot{Q}}_j$, in the 8th segment ($j = 8$, $x \in [0.175, 0.2]$ m). It is noted that the time-series of $\dot{Q}'_j$ highly deviates from a purely harmonic single-frequency signal. This is because other frequencies also present due to the flame's nonlinearity and the background noise caused by the strong turbulent flow. Nevertheless, the discrete Fourier transform (DFT) of $\dot{Q}_j$ (with $j = 8$) shown in Fig. 7.9(d) indicates that the main response frequency of $\dot{Q}_j$ perfectly matches the forcing frequency of 50 Hz, which is true for all the perturbation cases investigated. This again validates the weakly nonlinear assumption made by the FDF theory [54, 63].

In order to determine the local FDF for each of the discretised flame segments, it is necessary to extract the gain (denoted G_j) and phase values (denoted φ_j) of the heat release rate in each segment responding to the same upstream perturbation signal, u'_1/U. In this work, the DFT magnitude of $\dot{Q}_j$ at the forcing frequency, i.e. the main peak value shown in Fig. 7.9(d), is used as the local FDF gain for the j-th segment.

It is however more difficult to calculate the local FDF phase directly from the cross-correlation between $\dot{Q}'_j$ and u'_1/U, especially in the very downstream segments, where the heat release rates

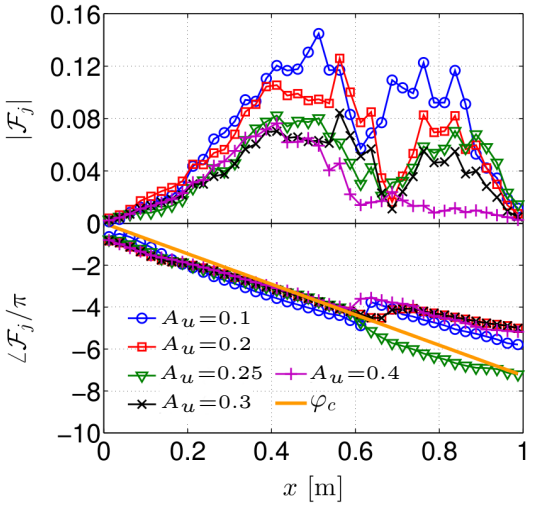
are low and the SNR is very small. A post-processing method proposed by Li et al. [251, 252] is thus applied, including steps: (*i*) the raw signal of $\dot{Q}_j$ is at first filtered using a zero-phase-shift band-pass filter to eliminate the low frequency noise due to bulk flow motion, and high frequency noise due to flame nonlinearity and small-scale turbulence. One such filter is the digital Butterworth filter with a lower cut-off frequency of 30 Hz and an upper cut-off frequency of 70 Hz, featuring an attenuation of less than 1 dB in the pass-band and at least 10 dB in the stop-band under the forcing frequency of $f_u = 50$ Hz. The filtered signal, $\dot{Q}'_{j,\mathrm{flt}}$ (thick solid line in Fig. 7.9(a)), now contains only the forcing frequency. (*ii*) A Hilbert transform is then performed on $\dot{Q}'_{j,\mathrm{flt}}$ to obtain the signal's envelope, denoted $\dot{Q}'_{j,\mathrm{evlp}}$ (dashed line in Fig. 7.9(a)). (*iii*) This envelope yields a normalised signal with constant amplitude, $\dot{Q}'_{j,\mathrm{nml}} = \dot{Q}'_{j,\mathrm{flt}}/\dot{Q}'_{j,\mathrm{evlp}}$, shown in Fig. 7.9(b). (*iv*) A cross-correlation is finally performed between $\dot{Q}'_{j,\mathrm{nml}}$ and the perturbation signal, u'_1/U (Fig. 7.9(c)), to obtain an accurate local FDF phase for the j-th flame segment at the forcing frequency.

With the gain and phase of the heat release response both computed, the local FDF for the j-th flame segment can be established in the frequency domain as:

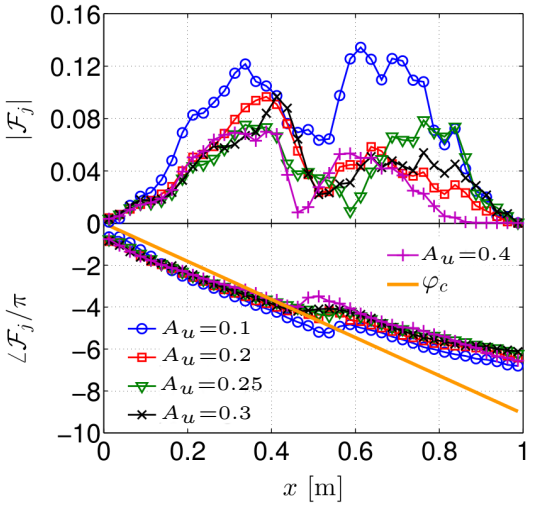
$$\mathcal{F}_j(f, A_u) = \frac{\widehat{\dot{Q}}_j/\overline{\dot{Q}}}{\widehat{u}_1/U} = G_j(f, A_u)\exp(i\varphi_j(f, A_u)), \tag{7.3}$$

where $\dot{Q}$ denotes the total heat release rate from the entire computational domain. The above signal post-processing steps are repeated across the forcing amplitudes (A_u) for each segment ($j = 1, \cdots, N_{\mathrm{seg}}$) along the flame length, yielding a series of local FDFs along x-direction.

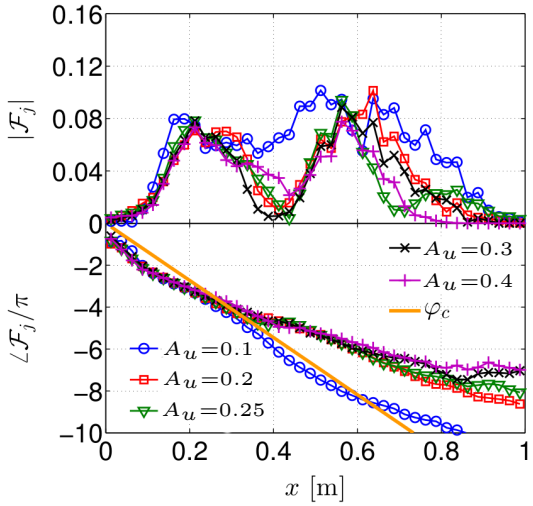
As shown in Fig. 7.10, some common trends for the obtained local FDFs are evident: (*i*) the local FDF gain, $G_j = |\mathcal{F}_j|$, generally decreases with increasing forcing level, A_u, for all the flame segments, mainly due to the nonlinear saturation of the flame surface area oscillation. The gain decreases rapidly between $A_u = 0.1$ and 0.2, but becomes slower as A_u is further increased. This is consistent with previous numerical predictions [238]. (*ii*) G_j has its maximal value at two locations, one within $x \simeq 0.2$ – 0.5 m, and the other at $x \simeq 0.5$ – 0.8 m, for all perturbation frequencies. (*iii*) The absolute FDF phase, $|\varphi_j| = |\angle\mathcal{F}_j|$, decreases with the forcing level (A_u) along the entire flame, consistent with that of a conical laminar flame [79]. (*iv*) φ_j is generally proportional to the ideal phase lag, $\varphi_c = -2\pi f x/U$, of the bulk flow convection, which linearly decreases along the flame axial length, confirmed by [253].



(a) $f_u = 40$ Hz



(b) $f_u = 50$ Hz



(c) $f_u = 75$ Hz

FIGURE 7.10: Local FDFs for the ORACLES flame, $\mathcal{F}_j$ (with $j = 1, \cdots, N_{\text{seg}}$ and $N_{\text{seg}} = 40$). Top-half: FDF gain $|\mathcal{F}_j|$ $(= G_j)$; bottom-half: FDF phase $\angle\mathcal{F}_j/\pi$ $(= \varphi_j/\pi)$. Symbols $\circ$: $A_u = 0.1$; $\square$: $A_u = 0.2$; $\triangledown$: $A_u = 0.25$; $*$: $A_u = 0.3$; $+$: $A_u = 0.4$. Solid line: phase lag due to bulk flow convection, φ_c. (a) $f_u = 40$ Hz. (b) $f_u = 50$ Hz. (c) $f_u = 75$ Hz. Figures adapted from [5].

7.5 Prediction of Thermoacoustic Limit Cycle

Based on the above simulated series of local FDFs along the flame length (Fig. 7.10), the nonlinear limit cycle oscillations induced by the thermoacoustic instability can be predicted. Since the present limit cycle was experimentally measured at around 50 Hz, the present analysis is restricted to the frequency range of $f = 25 - 100$ Hz. The FDF gain and phase values across this frequency range are then determined by performing linear interpolations on the computed FDF

data shown in Fig. 7.10, resulting in the complete axially-varying local FDFs over the frequency domain (see [5] for more details).

The low order network thermoacoustic solver, OSCILOS [60, 67], is now used for the limit cycle predictions. The network geometry for the ORACLES rig is shown in Fig. 7.1(b), which contains three rectangular constant-area modules, including the original 2-metre-long combustion chamber. As explained in Fig. 7.8, the long and continuous flame within this combustion chamber is now represented as a series of "discrete 1-D flame sheets" in the network geometry, each treated as "acoustically compact" compared to the dominant acoustic wavelengths. Each of these 1-D flame sheets is located at the centre of a flame segment (e.g., $x = x_j$ for the j-th segment), to which the computed local FDF for the same segment is assigned. Inside each flame segment (e.g., $x \in [x_{j,c}, x_{j+1,c}]$, with $x_{j,c} = x_j - l/2$ and $x_{j+1,c} = x_j + l/2$), the mean pressure, velocity and temperature are assumed constant at each side of the flame sheet (due to the small segment length), and only change across this sheet, which are controlled by the jump conditions [18] (see Section 2.3 for more details). These mean flow and thermal properties can also vary from segment to segment.

The axial profiles of mean velocity ($\overline{u}$), temperature ($\overline{T}$), speed of sound ($\overline{c}$) and the ratio of specific heats (γ), etc., used in the first half of the network combustion chamber (i.e. $x \in [0, 1]$ m) are plotted in Fig. 7.11. These are extracted from the LES results under an upstream perturbation of $f_u = 50$ Hz and $A_u = 0.29$, and averaged over the cross-section. It is noted that the mean temperature increases from 1011 K to 1854 K, and the mean velocity raises from 6 m/s to 39.4 m/s. The values of $\overline{u} = 39.4$ m/s and $\overline{T} = 1854$ K are assumed constant in the second half of the combustion chamber (i.e. $x \in [1, 2]$ m). The profiles of $\overline{c}$ and γ are computed based on the axial variation of $\overline{T}$, either dropping from 1.335 to 1.301 (for γ) or increasing from 622.5 m/s to 832.1 m/s (for $\overline{c}$) in the first half of the chamber ($x \in [0, 1]$ m).

The computed series of local FDFs (e.g., see Fig. 7.10) are then assigned to each of these discrete 1-D flame sheets in the network, and coupled with the modified acoustic wave equations [5] within the OSCILOS solver. These wave equations are derived from the acoustic jump conditions across multiple local flame sheets and the transfer matrices for acoustic wave propagations, etc.

Due to the lack of experimental data on the acoustic boundary conditions, the pressure reflection coefficients at the network inlet and outlet are assumed as $R_{\text{in}} = 1$ and $R_{\text{out}} = -1$, respectively,

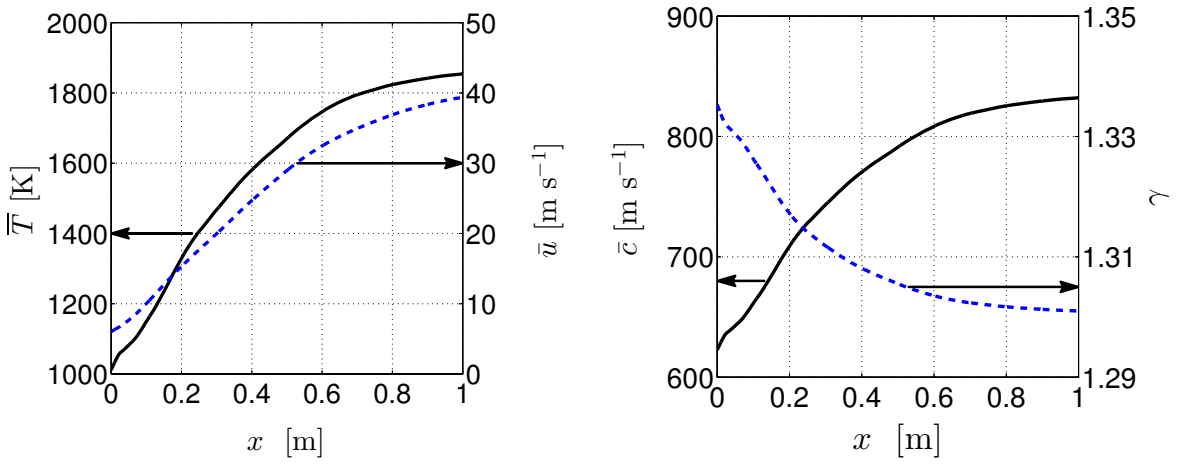


FIGURE 7.11: Axial profiles of cross-sectionally averaged mean flow and thermal properties used in the network, simulated at $f_u = 50$ Hz and $A_u = 0.29$. Figures from [5].

corresponding to a fully closed inlet and open outlet. The acoustic damping levels at the boundaries can be accounted for by decreasing the magnitudes of R_{in} and R_{out}, and the sensitivity of the predicted limit cycle properties on these damping levels will be discussed later.

The dominant thermoacoustic mode which is relevant to the limit cycle is finally predicted using the low order network approach. It is also compared to the mode computed by the reference 1-D Linearised Euler Equations (LEEs) (it is acknowledged that this part was done by Dr. Jingxuan Li in [5]). The predictions using the LEEs method apply the same acoustic boundary conditions for the network, but use the continuous mean flow and thermal properties along the axial direction (i.e. without assuming the flame segments and the associated jump conditions) to construct a continuous FDF (denoted $\mathcal{F}_c$), describing the local heat release rate response to an oncoming acoustic excitation as:

$$\mathcal{F}_c(x, \omega, A_u) = \frac{\widehat{\dot{q}}/\overline{\dot{Q}}}{\widehat{u}_1/U}, \tag{7.4}$$

where $\widehat{\dot{q}}$ denotes the local heat release rate fluctuation at an axial point. In practice, $\widehat{\dot{q}}$ is very difficult to compute based on LES or experimental data, since it is restricted to very a small area that the SNR is too small. Therefore, in this study $\mathcal{F}_c$ is reconstructed using the flame segmentation method.

When each flame segment is sufficiently short, the change in the flame response over one segment also becomes very small; the Taylor expansions for the gain and phase of the continuous FDF, $\mathcal{F}_c$, will then be dominated by terms of zeroth and first order. The gain and phase of $\mathcal{F}_c$ can thus

be approximated as linear functions of x, allowing $\mathcal{F}_c$ to be computed by linearly interpolating the discrete FDFs, $\mathcal{F}_j$, for the series of compact flame sheets. For instance, the form of $\mathcal{F}_c$ in the segment region $[x_{j,c}, x_{j+1,c}]$ (see Fig. 7.8) is defined as [5]:

$$\mathcal{F}_c = G_0 \left(1 + \beta_1 (x - x_j)\right) e^{i(\varphi_0 + \beta_2 (x - x_j))}, \tag{7.5}$$

where G_0 and φ_0 are the gain and phase of the LEEs-based FDF. β_1 and β_2 are two linear coefficients for the gain and phase, respectively. Integrating $\mathcal{F}_c$ along $[x_{j,c}, x_{j+1,c}]$ then gives:

$$\mathcal{F}_j^*(f, A_u) = \int_{x_j - \frac{l}{2}}^{x_j + \frac{l}{2}} \mathcal{F}_c \, \mathrm{d}x = \frac{G_0 e^{i\varphi_0}}{i\beta_2} \left(i2 \sin\left(\frac{\beta_2 l}{2}\right) + \beta_1 l \cos\left(\frac{\beta_2 l}{2}\right) - \frac{2\beta_1}{\beta_2} \sin\left(\frac{\beta_2 l}{2}\right) \right), \tag{7.6}$$

where l denotes the axial length of each segment. When $\beta_2 l \ll \pi$, the above equation can be simplified into:

$$\mathcal{F}_j^*(f, A_u) = l G_0 e^{i\varphi_0} = G_j(f, A_u) e^{i\varphi_j(f, A_u)}. \tag{7.7}$$

As mentioned in Section 7.4, the phase lag of the discrete local FDF, $\mathcal{F}_j$, approximately corresponds to the bulk flow convection, which has a wavelength of $U/f \simeq 0.22$ m at 50 Hz. The phase lag with the total segment number, $N_{\text{seg}} = 40$, is then $\beta_2 l \simeq 2\pi \times 0.025/0.22 = 0.23\pi \ll \pi$, satisfying the condition for Eq. 7.7 to be valid. G_0 and φ_0 are now calculated as:

$$G_0 = \frac{G_j(f, A_u)}{l} \quad \text{and} \quad \varphi_0 = \varphi_j(f, A_u).$$

The gain and phase of $\mathcal{F}_c$ at other frequencies in the range of [25, 100] Hz can then be interpolated based on the values of G_j/l and φ_j, respectively. Based on this axially-integrated continuous FDF, $\mathcal{F}_j^*$, another thermoacoustic prediction approach called the "LEEs-based method" is established, with more details described in [5].

Figure 7.12 shows the comparison between the axially integrated continuous FDF, $\mathcal{F}_j^*$, and the simulated discrete series of local FDFs, $\mathcal{F}_j$, across all the segments at $f_u = 50$ Hz, $A_u = 0.1$ with different total segment numbers (N_{seg}). The axial variations are nearly identical when $N_{\text{seg}} = 40$, indicating that this total flame segment number is a suitable choice. When coarser flame segments are used, e.g., $N_{\text{seg}} = 10$, differences between $\mathcal{F}_j^*$ and $\mathcal{F}_j$ can no longer be ignored.

The evolutions of frequency and growth rate for the predicted dominant thermoacoustic mode over the perturbation level, A_u, are then shown in Fig. 7.13. The mode's trajectories with

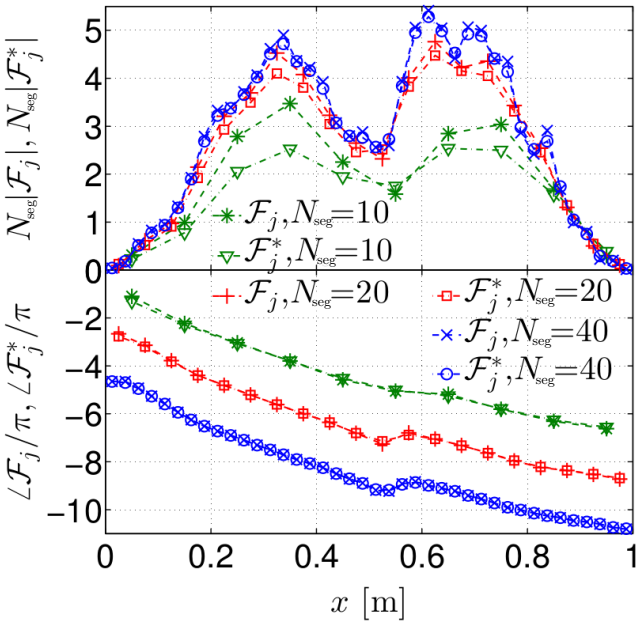


FIGURE 7.12: Discrete local FDFs, $\mathcal{F}_j$, and integrated continuous FDFs, $\mathcal{F}_j^*$, obtained with different total segment numbers, N_{seg}. Top-half: $N_{\text{seg}}\,|\mathcal{F}_j|$ and $N_{\text{seg}}\left|\mathcal{F}_j^*\right|$. Bottom-half: $\angle\mathcal{F}_j/\pi$ and $\angle\mathcal{F}_j^*/\pi$. $f_u = 50$ Hz and $A_u = 0.1$. Figure adapted from [5].

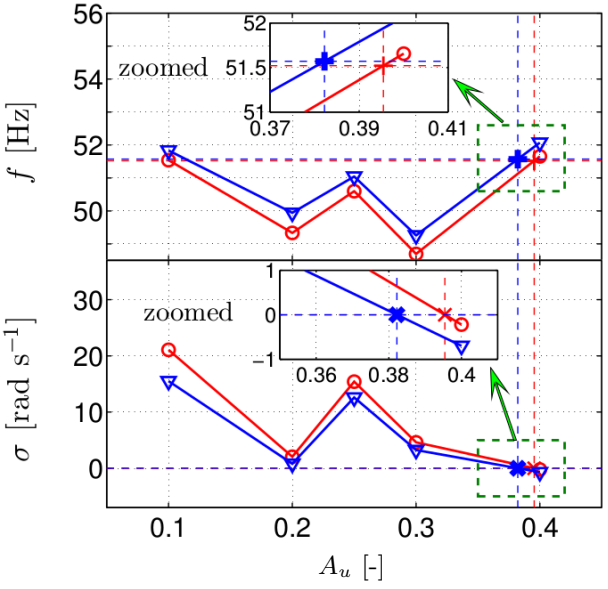


FIGURE 7.13: Evolutions of (top-half) frequency, f, and (bottom-half) growth rate, σ, of the dominant thermoacoustic mode over perturbation level, A_u, predicted by OSCILOS ($\triangledown$) and the LEEs method ($\circ$). $+$: limit cycle frequency, f_{lc}; $\times$: corresponding perturbation amplitude, A_u^{lc}. Figure taken from [5].

increasing A_u are almost identical between the low order network and the reference LEEs methods. For the lowest forcing level, $A_u = 0.1$, the modal growth rate (σ) predicted by OSCILOS is largely positive, indicating the combustor is unstable at $f = 51.8$ Hz. An increase in A_u leads to

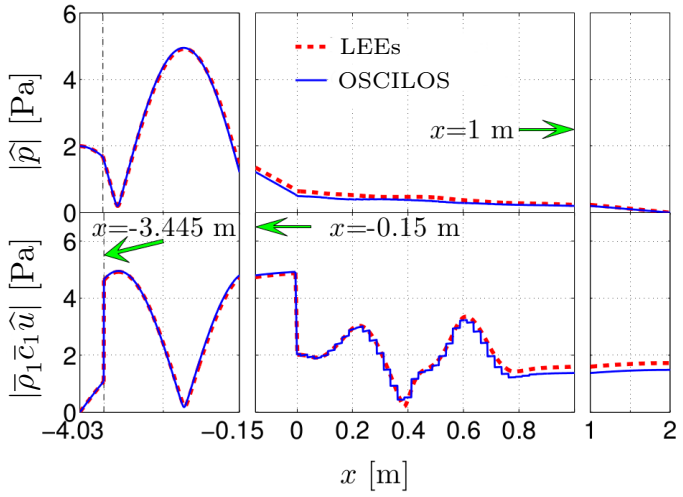


FIGURE 7.14: Shapes of the dominant thermoacoustic mode predicted by (solid line) OSCILOS and (dashed line) the LEEs method at $A_u = 0.4$, in the form of arbitrary (top-half) pressure and (bottom-half) velocity fluctuation amplitude along x-direction. $\overline{\rho}_1$ and $\overline{c}_1$ are the mean density and speed of sound in the upstream settling chamber. Figure adapted from [5].

a gradual decrease of the growth rate, and the limit cycle is established when $\sigma = 0$. This occurs when A_u is between 0.3 and 0.4. By performing linear interpolation, the zero-growth-rate state is found at perturbation level $A_u^{lc} = 0.38$, with the corresponding frequency $f_{lc} = 51.6$ Hz. These limit cycle properties are both very close to those predicted by the LEEs method, validating the low order network solver used. Compared to the experimental data [15], the predicted limit cycle frequency, f_{lc}, matches well the measured value of ∼50 Hz, while A_u^{lc} is slightly over-predicted compared to the measured level of ∼0.29. This mismatch is possibly due to the lack of acoustic damping at the modelled network boundaries.

The shapes of the dominant mode predicted by the two methods are plotted in Fig. 7.14, in the form of arbitrary pressure or velocity fluctuation profiles. The mode shapes match very well between the two solvers. Two large jumps in the velocity fluctuation are found at two locations, $x_1 = -l_2 = -3.445$ m and $x_2 = 0$ m, where the cross-sectional area abruptly changes in the network (see Fig. 7.1(b)). The low order network solver, OSCILOS, also predicts multiple small velocity jumps at the interfaces between the consecutive flame segments (see Fig. 7.14(bottom)), while the LEEs method gives smoothly changing velocity profile in the combustion chamber. The axial-variation of the velocity fluctuation is strongly affected by the FDFs applied, featuring a wave form with several cycles from the network inlet to the outlet (Fig. 7.14(bottom)). In contrast, the pressure fluctuation profile is much smoother and has no jumps in the flame region (see Fig. 7.14(top)), which is little affected by the FDFs used.

The effect of total flame segment number, N_{seg}, on the limit cycle prediction is also analysed. The initial value of $N_{\text{seg}} = 40$ is selected to ensure that the width of each segment is sufficiently small to better capture the detailed response variation, but in the meantime it also leads to relatively small SNRs in the very downstream segments, where the heat release rates are much lower (due to the occasional absence of the flame tips) and can cause errors to the computed FDF gain and phase values. By merging the consecutive segments, the total segment number can be reduced from 40 to 20, with each segment's width doubled from 0.025 m to 0.05 m. Similarly, a further merging of neighbouring segments can reduce the segment number to 10, with each as long as 0.1 m.

Figure 7.12 shows the discrete local FDFs, $\mathcal{F}_j$, simulated for total segment numbers of $N_{\text{seg}} = 40$, 20 and 10, respectively, all forced at $f_u = 50$ Hz and $A_u = 0.1$. The gains of $\mathcal{F}_j$ are divided by their corresponding segment width, l (or equivalently multiplied by the N_{seg} value), for better comparisons. It is known that when l increases or N_{seg} drops, the SNR of the heat release rate signal increases, enabling a better capture of the FDF gains and phases at the perturbation frequency. However, as shown in Fig. 7.12, the FDF gains computed with fewer segments (e.g., $N_{\text{seg}} = 10$ or 20) are always lower than those at $N_{\text{seg}} = 40$ over the entire flame (the same for higher forcing levels of $A_u = 0.2$, 0.25, 0.3 and 0.4). This is because the heat release rate signals in the merged neighbouring segments are not always in phase, and may cancel each other. Therefore, the total segment number cannot be too small or too large, and there exists an optimal number which provides a good balance between the heat release rate SNR and an accurate description of the flame response's axial variation.

The frequency (f) and growth rate (σ) of the predicted dominant mode are also compared in detail across the forcing amplitudes for five total segment numbers ($N_{\text{seg}} = 40$, 20, 10, 5 and 1), as summarised in Table 7.1. It is observed that: (i) the reduction of N_{seg} (from 40 to 10) does not highly affect the mode's frequency, but monotonically decreases its growth rate across all the forcing levels, except for $A_u = 0.2$, which has an opposite behaviour. The decrease of N_{seg} from 40 to 10 also reduces the predicted limit cycle perturbation amplitude, A_u^{lc}. (ii) When $N_{\text{seg}} \leq 5$, the predicted axial variation of the FDFs, $\mathcal{F}_j$, is completely different from that at $N_{\text{seg}} = 40$, and the combustor is now predicted linearly stable, which is incorrect. This confirms the need to use a sufficiently large total segment number to ensure the network prediction is still valid. (iii) Although the value of A_u^{lc} looks closer to the experimental data ($\sim$0.29) with few segments (e.g., $N_{\text{seg}} = 20$ or 10), it must be noted that the reflection coefficients used are ideally $R_{\text{in}} = 1$

TABLE 7.1: Frequency (f) and growth rate (σ) of the dominant thermoacoustic mode, the limit cycle frequency, f_{lc}, and the corresponding forcing level, A_u^{lc}, predicted over forcing amplitude (A_u) with different total segment numbers. Data collected from [5].

A_u		Experiment	LEEs	Low order network method with N_{seg} flame segments				
				40	20	10	5	1
0.1	f [Hz]	-	51.5	51.8	51.8	51.7	50.7	51.6
	σ [rad/s]	-	21.3	15.7	10.8	4.5	-13.7	-15.4
0.2	f [Hz]	-	49.3	49.9	50.1	50.3	49.6	48.9
	σ [rad/s]	-	2.1	0.8	1.6	2.6	0.6	-4.2
0.25	f [Hz]	-	50.6	51.0	51.2	51.5	53.7	51.1
	σ [rad/s]	-	15.4	12.6	12.4	10.5	5.1	16.7
0.3	f [Hz]	-	48.7	49.3	49.3	49.6	49.0	48.0
	σ [rad/s]	-	4.7	3.3	2.5	1.6	4.2	-3.0
0.4	f [Hz]	-	51.7	52.1	52.1	52.3	52.3	52.0
	σ [rad/s]	-	-0.2	-0.7	-2.3	-3.4	-5.1	-7.5
Limit	f_{lc} [Hz]	∼50	51.5	51.6	50.8	50.9	Linearly	Linearly
cycle	A_u^{lc} [-]	∼0.29	0.40	0.38	0.35	0.35	stable	stable

and $R_{\text{out}} = -1$, and the flow temperature remains constant within the zone $x = [1, 2]$ m, so using a smaller number of N_{seg} does not guarantee a better prediction of the limit cycle. The effects of entropy wave transport and the resulting entropy noise on the prediction results are found very small, and are therefore neglected in this work.

It has also been found that similar limit cycle properties ($f_{lc} = \sim$50 Hz and $A_u^{lc} = 0.37$) were previously predicted in [115] compared to the present calculations at $N_{\text{seg}} = 40$. In their work, however, the LES were performed at only one frequency (50 Hz), and the 1.1 m long combustion chamber used was equally segmented into only 14 slices with no criterion for the flame segment length. The computed discrete local FDFs were constructed by assuming that the gain and phase in each segment remain constant at all frequencies.

Finally, the sensitivities of the predicted limit cycle to (*i*) the acoustic boundary damping levels and (*ii*) the mean temperature ratio in the combustion chamber are both investigated. The above predictions have assumed no acoustic losses at both network inlet and outlet (i.e. $R_{\text{in}} = 1$ and $R_{\text{out}} = -1$). However, as shown in Fig. 7.1(a), the porous plugs and grids were installed near the settling chamber entrance to organise the inflow, which are highly likely to cause acoustic

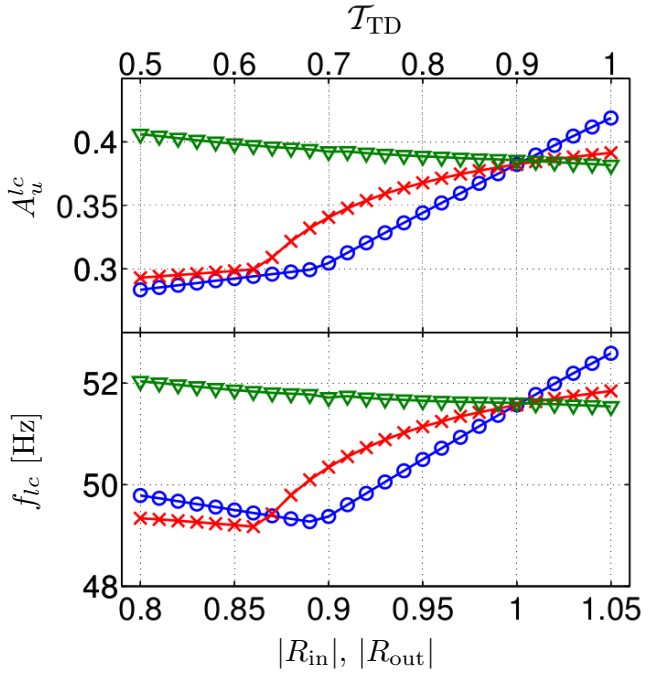


FIGURE 7.15: Markers ∘: evolutions of limit cycle (bottom-half) frequency, f_{lc}, and (top-half) corresponding forcing level, A_u^{lc}, against $|R_{\mathrm{in}}|$ (bottom axis) with $R_{\mathrm{out}} = -1$. Markers ×: evolutions of f_{lc} and A_u^{lc} over $|R_{\mathrm{out}}|$ (bottom axis) with $R_{\mathrm{in}} = 1$. Markers ▽: evolutions of f_{lc} and A_u^{lc} against the combustion chamber temperature ratio, $\mathcal{T}_{\mathrm{TD}}$ (top axis), with $R_{\mathrm{in}} = 1$ and $R_{\mathrm{out}} = -1$. Figure adapted from [5].

losses. A sensitivity analysis of the limit cycle properties to these losses is then performed by successively varying the magnitudes of R_{in} and R_{out} while keeping their phases unchanged.

As shown in Fig. 7.15, when $|R_{\mathrm{in}}|$ decreases from 1.05 to 0.8 for a fixed $R_{\mathrm{out}} = -1$ (note that the absolute reflection coefficient may exceed unity for a finite Mach number flow [145, 254]), the perturbation level for the limit cycle, A_u^{lc}, continuously decreases from 0.42 to 0.28, closer to the measured value of ∼0.29. In contrast, the variation in the limit cycle frequency, f_{lc}, is much smaller, only slightly drops by ∼3 Hz. A similar analysis is performed for the outlet reflection coefficient, $|R_{\mathrm{out}}|$, which also drops from 1.05 to 0.8 while fixing $R_{\mathrm{in}} = 1$. The predicted limit cycle perturbation level, A_u^{lc}, is found to monotonically reduce from 0.39 to 0.29, again better matching the measurement data of ∼0.29.

The second effect to be investigated is the temperature axial-variation along the combustion chamber. The above predictions have assumed that the mean temperature in the downstream half of the combustion chamber (beyond the long flame region) remains constant. However, the flame-downstream temperature may decrease axially due to heat losses [255–257]. The effect of this temperature drop can be studied by defining a linearly-decreasing axial mean temperature

profile, $\overline{T}(x)$, in the downstream half of the combustor, $x \in [1, 2]$ m (beyond the entire flame):

$$\overline{T}(x) = \overline{T}^*(\mathcal{T}_{\mathrm{TD}} - 1)(x - 1) + \overline{T}^* \ , \ x \in [1, 2] \text{ m}, \tag{7.8}$$

with $\overline{T}^* = 1854$ K the mean temperature at $x = 1$ m and $\overline{T}^*(\mathcal{T}_{\mathrm{TD}} - 1)$ the gradient of the linear profile. For example, when $\mathcal{T}_{\mathrm{TD}} = 1$, the mean temperature remains constant along x, while for $\mathcal{T}_{\mathrm{TD}} = 0.5$, the mean temperature drops from $\overline{T}^*$ at $x = 1$ m to $\overline{T}^*/2$ at $x = 2$ m, etc.

The sensitivity of the limit cycle properties to the temperature gradient, $\mathcal{T}_{\mathrm{TD}}$, is also shown in Fig. 7.15. When $\mathcal{T}_{\mathrm{TD}}$ decreases from 1.0 to 0.5, the limit cycle perturbation level, A_u^{lc}, slowly grows from 0.38 to 0.41. This is because the temperature variation acts as an acoustic energy source, which changes the total energy needed by the perturbation to trigger the limit cycle. This is consistent with previous findings in [258, 259].

In summary, based on the above sensitivity analyses, the limit cycle perturbation level, A_u^{lc}, decreases with an increase of the acoustic damping level at both combustor ends, but increases under a faster flame-downstream temperature drop. In contrast, the limit cycle frequency, f_{lc}, is only little affected by the acoustic boundary damping and the temperature gradient in the downstream chamber.

7.6 Summary

In this chapter, the forced responses of a very long flame in a lab-scale dump combustor called ORACLES is investigated. The long flame stretches in the axial direction for ∼1 m, occupying nearly half of the combustion chamber. The "acoustically compact" assumption used to represent a compact flame as a single 1-D flame sheet is no longer valid. To solve this, the continuous long flame is split into a series of equal-sized individual flame segments in the axial direction, each segment has a sufficiently short length, which can be treated as an acoustically compact flame. The series of flame segments can then be represented as a discrete series of 1-D flame sheets in the network approach.

The heat release response from each flame segment to a harmonic velocity perturbation at a fixed upstream location is then computed, resulting in a series of local FDFs for the discrete flame sheets, varying along the flame longitudinal length. The axial variations of gains and phases for these FDFs are functions of perturbation frequency, amplitude and the total segment number.

With a sufficiently large total segment number, the LES-computed discrete FDFs match well the 1-D linearised Euler equations (LEEs)-based continuous FDFs.

The ORACLES combustor was measured thermo-acoustically unstable during experiments, accompanied by nonlinear limit cycle oscillations. In order to predict this limit cycle, the low order network solver OSCILOS is used, assigning the simulated FDFs to the modelled discrete 1-D flame sheets along the flame length. With a total segment number of 40, the predicted limit cycle frequency matches well the measured value, while the corresponding upstream perturbation level is slightly over-predicted due to the lack of acoustic damping at network boundaries. By using correct acoustic damping levels at combustor inlet and outlet, and assuming a more physical temperature gradient within the downstream combustion chamber, the prediction accuracy on the limit cycle properties will be considerably improved.

Chapter 8

Conclusions and Future Work

This thesis has investigated the flame responses to acoustic perturbation and the resulting thermoacoustic instability in two gas turbine combustors, which are (*i*) the pressurised SGT-100 industrial combustor and (*ii*) the long flame ORACLES laboratory combustor. The acoustic wave behaviour has been modelled using a low order network approach or a Helmholtz solver, while the flame heat release rate response was numerically simulated and constructed as linear flame transfer functions (FTFs) or nonlinear flame describing functions (FDFs). The acoustic wave model and the flame response functions were then combined into the above solvers to predict the thermoacoustic stability of the analysed combustors, and for those unstable operations, to capture the nonlinear limit cycle oscillations. The influences of multiple numerical modelling assumptions and operating conditions on the unsteady flame response and the thermoacoustic prediction have been systematically evaluated.

8.1 Incompressible LES of Reacting Combustor Flows

The starting point for an accurate characterisation of the forced flame response is to obtain a reliable unforced flow field and flame shape in the combustor. Incompressible large eddy simulation (LES) was used for this task due to its high accuracy in capturing large scale unsteady flow features and its smaller computational cost compared to the compressible LES and DNS.

For the pressurised SGT-100 combustor, which contains a turbulent swirling methane/air flame, two incompressible LES solvers — OpenFOAM and BOFFIN, were used. The effects of sub-grid scale (SGS) turbulence model, SGS combustion model (LES-PDF vs. LES-PaSR), reaction chemistry (4-step vs. 15-step), operating pressure (3 bar vs. 6 bar), wall heat losses and mesh density, etc., on the unforced flow field and flame behaviour were analysed. It was found that:

(*i*) The large scale steady and unsteady flow features such as swirl, separation, recirculation zones and vortex cores (e.g., CVC), etc., are all evident in the flow field. However, the effects of all the above-mentioned factors on the unforced flow field are found marginal.

(*ii*) The LES-PaSR combustion model gives a more-distributed reaction zone and an axially longer flame compared to the LES-PDF model, and the use of a more-detailed 15-step reaction scheme leads to a longer flame with a lower mean heat release rate due to the lower burning velocity. In contrast, an increase of the mean pressure from 3 bar to 6 bar largely decreases the flame axial length but increases the mean heat release rate, due to the lifted chemical reaction rate at a higher pressure.

(*iii*) The accuracy of the two combustion models used are both validated by the experimental data. The dynamic Smagorinsky turbulence model offers the best accuracy, and the 15-step reaction scheme is slightly more accurate than the 4-step scheme, especially at a higher pressure. Generally, all the applied SGS combustion models and the reaction schemes used have satisfactory accuracy.

(*iv*) The effect of wall heat losses on both the flow field and the flame shape is found negligible, and the increase of mesh density does not significantly increase the simulation accuracy, except for slightly improving the local reaction processes within the flame zone.

The same incompressible LES approach was also applied to a long-flame propane/air combustor known as ORACLES, which uses the OpenFOAM LES solver and very simple reaction chemistry (e.g., one-step reaction). The non-swirling flow in the ORACLES rig is accurately captured compared to the experimental data. It is found that the non-swirling flow field stretches downstream a very long distance into the combustion chamber, consistent with the very long flame obtained. The central recirculation zone now disappears due to the lack of upstream swirler.

8.2 Forced Flame Responses and Flame Models

Building on the simulations of unforced flames, the forced flame heat release responses to upstream perturbations were investigated. A harmonic velocity perturbation was imposed upstream of the flame front, with the subsequent time-variation of the global heat release rate from the flame calculated at each time step. The computed flame response signals were then used to construct the FTFs and/or FDFs.

For the SGT-100 combustor, the flame zone is assumed acoustically compact, thus a global flame model (FTF or FDF) is sufficient. The resulting FDFs, computed using different SGS combustion models, chemical reaction schemes and operating pressures, etc., have some common trends: (*i*) the FDF gain always has two gain maxima in frequency with one gain minimum in between; (*ii*) the FDF phase generally linearly decreases over the frequency, controlled almost only by the bulk flow convection; (*iii*) an increase in the perturbation amplitude leads to a drop in the FDF gain over frequency, mainly due to the saturation of the flame surface area oscillation.

The effects of combustion model and reaction chemistry on the FDFs are both found very small, regardless of their associated differences in the unforced flame shapes. This suggests that a simpler but faster 4-step reaction scheme combined with either PDF or PaSR-based combustion model can be recommended for future flame response calculations.

In contrast, an increase in the operating pressure largely increases the FDF gain magnitudes at lower frequencies, but reduces them at higher frequencies. This may be due to the different time-scale coupling strengths between the perturbation and the flame response over the frequency. The pressure variation also shifts the frequency of the maximum FDF gain peak, likely caused by the variation of mean axial flame lengths predicted at different pressures.

For the long flame in the ORACLES rig, however, the "single flame model" assumption is no longer valid. Instead, this long flame is axially split into multiple equal-sized flame segments, with each short enough to be treated as a compact zone and represented as a discrete 1-D flame sheet. A series of local discrete FDFs are then computed by OpenFOAM LES for all the segments along the flame length, across multiple perturbation frequencies and amplitudes. A filtering approach is applied to better compute the FDF phase. Several phenomena are evident for the obtained local FDFs: (*i*) an increase of perturbation level leads to a global decrease of

the FDF gain along the entire flame; (*ii*) the absolute FDF phase generally linearly decreases with the perturbation level along the flame length; (*iii*) the FDF gain increases from zero to a maximum peak between $x = 0 - 0.3$ m, then drops to a local minimum at ∼0.5 m, followed by a rise to a second gain maximum at $x \simeq 0.6$ m, regardless of the perturbation level or frequency used. The simulated local discrete FDFs also match well the integrated continuous FDFs based on the 1-D linearised Euler equations (LEEs).

8.3 Predictions of Thermoacoustic Instability and Limit Cycle

The simulated FTFs or FDFs via LES were finally combined into the low order network solver, OSCILOS, or the Helmholtz equation-based "H-solver", to predict the thermoacoustic stability of the analysed combustors. The advantages of using these solvers include but not limited to: (*i*) the mean flow profile and the correct acoustic damping effect (e.g., at area increases) can be included in OSCILOS to better capture the thermoacoustic modes; (*ii*) the original combustor geometry can be retained in the H-solver and meshed with a much coarser grid compared to LES; (*iii*) the prediction speed is much faster with both solvers than the time-consuming compressible LES; (*iv*) both solvers are able to predict the nonlinear phenomena such as the limit cycle oscillations if the correct FDFs are provided, etc. These advantages make both solvers very attractive during the combustor design stage, offering the potential to significantly shorten the design timeframe.

For the SGT-100 combustor, the linear FTFs obtained at both 3 bar and 6 bar pressures were firstly combined with OSCILOS solver. The predicted thermoacoustic modes indicate that the combustor is linearly stable at 3 bar, but unstable at 6 bar at one frequency ∼231 Hz, both matching the experimental observations. This unstable mode was then nonlinearly analysed by extending the FDF at 6 bar, whose gain and phase both drop with perturbation amplitude. The growth rate of the unstable mode thus continuously decreases over the perturbation level, establishing the limit cycle oscillations when the growth rate drops to zero. By performing linear interpolation, the limit cycle oscillation frequency and amplitude were predicted as 209 Hz and 4970 Pa, respectively, well-matching the experimental data (216 Hz and 5000 Pa). The upstream velocity perturbation level corresponding to the limit cycle was predicted as 0.3565. The predicted limit cycle frequency and amplitude both show very limited sensitivities to small changes in the network inlet and outlet acoustic damping levels.

The above OSCILOS predictions were then compared with those obtained by the H-solver, showing that both solvers can correctly provide the linear stability maps and capture the unstable thermoacoustic mode. The frequencies of almost all the modes were also accurately predicted by both solvers, although the modal growth rates are slightly different, mainly due to the different acoustic damping models used in the two solvers.

For the ORACLES combustor, the long flame was measured unstable with limit cycle oscillations at ∼50 Hz, and the corresponding upstream perturbation level is ∼0.29. By incorporating the simulated discrete series of local FDFs along the flame length into OSCILOS, the limit cycle oscillation properties were predicted. The limit cycle frequency was predicted to be 51.6 Hz with an optimal total number of segments, well-matching the measured data. The upstream perturbation level, however, was slightly over-predicted as 0.38, but this result can be improved by assuming correct boundary acoustic damping levels and temperature gradient in the combustion combustor.

The advantages of using OSCILOS solver for the design process of gas turbine combustors include its sufficient accuracy and much less computational cost compared to fully compressible CFD simulations. Once the flame response models are simulated or measured, it is convenient to incorporate these models into OSCILOS to quickly predict the stability map of the design and identify the most dynamic thermoacoustic mode(s) which may lead to limit cycle oscillations. Then these modes can be removed or suppressed by adjusting the design plan (e.g., adding acoustic dampers in the combustion chamber). Compared to compressible LES, which are usually performed under certain unstable operating conditions, the coupled prediction approach used by OSCILOS does not require any information about these unstable conditions in advance.

8.4 Entropy Wave Transport in Combustor Flows

The entropy wave transport within the SGT-100 combustor flow fields was also simulated, using the incompressible OpenFOAM-LES solver. A time-impulsive Gaussian-shape "entropy source" was injected into the mean flame region to introduce entropy waves, which were then transported downstream within the shear-dispersive flow field. The contributions from both the thermal diffusion and viscous production terms to the entropy wave transport were firstly found negligible, suggesting that the transport process is dominated by the dispersive advection.

In a real unsteady combustor flow, the large scale unsteady flow features (e.g., swirl, vortices) significantly affect the entropy advection. The advection speeds are faster near the top and bottom chamber walls, with a small amount of entropy initially trapped by the flow recirculation zone, giving a relatively short total exit time for all the entropy to leave the combustor. The strength of the entropy flux at the combustor exit is largely attenuated compared to the entropy source, but still follows a flat Gaussian profile and remains non-negligible.

On the other hand, the entropy wave advection within a time-averaged "frozen" mean combustor flow found that the advection speed becomes much slower along the centreline, due to a large amount of entropy being trapped and delayed within the central recirculation zone. The drop of the entropy exit flux strength is also limited, thanks to the weaker shear-dispersion effect from the non-uniform mean velocity profile only. A third flow field studied was an equivalent pipe flow, whose dispersion on the entropy wave advection can be analytically described. It was discovered that the pipe flow dispersion effect is the weakest, which is only about one third of that in an unsteady combustor flow.

Based on the frequency responses of entropy flame-to-exit advection, the considerable entropy flux strength at the combustor exit has a potential to generate large amplitude entropy noise, especially with high bulk flow speeds. This may affect the thermoacoustic modes at lower frequencies (e.g., $f < 1000$ Hz). Simple duct combustors with realistic operating conditions were then studied, including the entropy noise generated from different flow dispersion models. It was found that the entropy noise can modify the dominant mode's location for all the dispersion models, and even change the mode's stability especially with the pipe flow dispersion model, whose attenuation on the entropy noise strength is the lowest. The mean and unsteady combustor flow fields give successively increasing dispersion levels and thus decreasing entropy noise effects on the dominant thermoacoustic mode.

8.5 Future Work Plans

For the future work, several further investigations which build upon the present study have been planned. Firstly, for the SGT-100 combustor, the effects of multiple factors (e.g., combustion model, chemistry, pressure) affecting the forced flame responses may be further evaluated by comparing more detailed flame structures, e.g., the flame surface density, flame wrinkling strength and the centroid of the heat release zone, etc., across a series of perturbation frequencies and

amplitudes. The effects of numerical schemes (e.g., the temporal and spatial discretisation) used in both LES solvers on the flame responses will also be investigated.

Secondly, the SGT-100 thermoacoustic predictions performed by the H-solver will be further extended to include the FDFs, which can lead to the prediction of nonlinear limit cycle oscillation in the 3-D combustor geometry.

Thirdly, a detailed effect analysis of the mean temperature contour in the SGT-100 combustor, which varies over pressure and affects the unforced flame shape, on the thermoacoustic stability change is also scheduled.

Fourthly, it is known that the effect of SGS combustion model itself on the LES results is affected by the numerical solution method and is thus complex. In order to better understand the differences between the two used combustion models on the reacting flow simulations, a non-reacting simulation case performed by both LES solvers is needed to evaluate the impact of solution method (e.g., spatial discretisation) on the isothermal flow field. This may help to isolate the effect of combustion model on the present reacting cases.

For the ORACLES combustor, it would be interesting to further investigate the sensitivities of the predicted limit cycle properties to other factors, such as the network dimensions, mean flow velocity, and different flame segmentation methods, etc. The influences of the SGS combustion model, turbulence model, and the chemical scheme used on the predictions will also be studied.

Apart from the above proposed improvements on the present studies, more types of gas turbine combustors will be considered. For example, the present combustors are both single-burner rigs only experiencing longitudinal thermoacoustic instability, while real industrial configurations often consist of multiple burners arranged in the circumferential direction, in which cases the higher-order circumferential thermoacoustic modes may become important. Future work will thus focus on an annular combustor (e.g., the NTNU configuration [92]), where the dominant thermoacoustic limit cycle was measured in the circumferential direction. The effect of the interactions between neighbouring flames on the forced flame responses and the resulting limit cycle will then be analysed in detail. Besides, the coupling mechanisms between the low-order longitudinal modes and higher-order circumferential modes and their impact on the thermoacoustic instability also need investigation.

Another planned work is to study the effect of fuel type on the flame responses and thermoacoustic limit cycle. Modern industrial combustors often implement blended fuel generated from

different sources, such as methane, hydrogen and ammonia, etc. The impact of each fuel component on the resulting flame-to-acoustic interaction thus needs detailed study. For example, a small composition of hydrogen in the methane fuel can cause significant flash-back and even extinction of the premixed flame in a gas turbine combustor [25, 26].

Finally, new acoustic modelling approaches are highly desired for a better description of the thermoacoustic interaction, and a work plan to develop an improved low order network solver (or other solvers with different theories) can be drawn. For example, the present longitudinal OSCILOS solver may be extended to model 3-D annular combustors, and to predict the spinning and standing wave modes in the circumferential direction, etc., which are typical of realistic annular combustors.

Bibliography

[1] H. Sharman. The balancing capacity issue: a ticking time-bomb under the UK's energiewende. `http://euanmearns.com/the-balancing-capacity-issue-a-ticking-time-bomb-under-the-uks-energiewende/`, 2014. Accessed 05 December 2018.

[2] C. J. Goy, S. R. James, and S. Rea. Monitoring combustion instabilities: E. On UK's experience. *Progress in Astronautics and Aeronautics*, 210:163, 2005.

[3] E. Giacomazzi, E. Giulietti, C. Stringola, S. Cassani, L. Pagliari, and S. Chiocchini. Combustion monitoring in gas turbines and enhanced stability at very lean conditions. In *ASME Turbo Expo 2014*, pages GT2014–25506, 2014.

[4] A. S. Morgans and I. Duran. Entropy noise: a review of theory, progress and challenges. *International Journal of Spray and Combustion Dynamics*, 8:285–298, 2016.

[5] J. Li, Y. Xia, A. S. Morgans, and X. Han. Numerical prediction of combustion instability limit cycle oscillations for a combustor with a long flame. *Combustion and Flame*, 185: 28–43, 2017.

[6] U. Stopper, M. Aigner, W. Meier, R. Sadanandan, M. Stöhr, and I. S. Kim. Flow field and combustion characterization of premixed gas turbine flames by planar laser techniques. *Journal of Engineering for Gas Turbines and Power*, 131(2):021504, 2009.

[7] U. Stopper, M. Aigner, H. Ax, W. Meier, R. Sadanandan, M. Stöhr, and A. Bonaldo. PIV, 2D-LIF and 1D-Raman measurements of flow field, composition and temperature in premixed gas turbine flames. *Experimental Thermal and Fluid Science*, 34(3):396–403, 2010.

[8] J. Smagorinsky. General circulation experiments with the primitive equations: I. The basic experiment. *Monthly Weather Review*, 91(3):99–164, 1963.

[9] U. Piomelli and J. Liu. Large-eddy simulation of rotating channel flows using a localized dynamic model. *Physics of Fluids*, 7(4):839–848, 1995.

[10] F. Nicoud and F. Ducros. Subgrid-scale stress modelling based on the square of the velocity gradient tensor. *Flow, Turbulence and Combustion*, 62(3):183–200, 1999.

[11] U. Schumann. Realizability of Reynolds-stress turbulence models. *Physics of Fluids*, 20 (5):721–725, 1977.

[12] J. Bardina, J. H. Ferziger, and W. C. Reynolds. Improved subgrid-scale models for large-eddy simulation. In *the 13th AIAA Fluid and Plasma Dynamics Conference*, 1980.

[13] A. Yoshizawa. A statistically derived system of equations for turbulent shear flows. *Physics of Fluids*, 28(1):59–63, 1985.

[14] G. Bulat, W. P. Jones, and A. J. Marquis. NO and CO formation in an industrial gas-turbine combustion chamber using LES with the Eulerian sub-grid PDF method. *Combustion and Flame*, 161:1804–1825, 2014.

[15] P. D. Nguyen, P. Bruel, and S. Reichstadt. An experimental database for benchmarking simulations of turbulent premixed reacting flows: lean extinction limits and velocity field measurements in a dump combustor. *Flow, Turbulence and Combustion*, 82(2):155–183, 2009.

[16] A. Abou-Taouk, B. Farcy, P. Domingo, L. Vervisch, S. Sadasivuni, and L. E. Eriksson. Optimized reduced chemistry and molecular transport for large eddy simulation of partially premixed combustion in a gas turbine. *Combustion Science and Technology*, 188:21–39, 2016.

[17] C. J. Sung, C. K. Law, and J.-Y. Chen. Augmented reduced mechanisms for NO emission in methane oxidation. *Combustion and Flame*, 125(1):906–919, 2001.

[18] A. P. Dowling. Nonlinear self-excited oscillations of a ducted flame. *Journal of Fluid Mechanics*, 346:271–290, 1997.

[19] European Environment Agency (EEA). *Nitrogen oxides (NOx) emissions*. Technical report. `https://www.eea.europa.eu/data-and-maps/indicators/eea-32-nitrogen-oxides-nox-emissions-1` Accessed: 01 August 2018.

[20] M. J. Moore. NOx emission control in gas turbines for combined cycle gas turbine plant. *Proceedings of the Institution of Mechanical Engineers, Part A: Journal of Power and Energy*, 211(1):43–52, 1997.

[21] S. Candel. Combustion dynamics and control: progress and challenges. *Proceedings of the Combustion Institute*, 29(1):1–28, 2002.

[22] J. W. S. Rayleigh. *Theory of sound*, Vol. 1 & 2, Dover Publications, New York, 1945.

[23] T. Lieuwen, Y. Neumeier, and B. T. Zinn. The role of unmixedness and chemical kinetics in driving combustion instabilities in lean premixed combustors. *Combustion Science and Technology*, 135(1-6):193–211, 1998.

[24] U. Stopper, W. Meier, R. Sadanandan, M. Stöhr, M. Aigner, and G. Bulat. Experimental study of industrial gas turbine flames including quantification of pressure influence on flow field, fuel/air premixing and flame shape. *Combustion and Flame*, 160(10):2103–2118, 2013.

[25] D. Moëll, D. Lörstad, and X. S. Bai. Numerical investigation of hydrogen enriched natural gas in the SGT-800 burner. In *ASME Turbo Expo 2015*, pages GT2015–44040, 2015.

[26] D. Moëll, D. Lörstad, and X. S. Bai. LES of hydrogen enriched methane/air combustion in the SGT-800 burner at real engine conditions. In *ASME Turbo Expo 2018*, pages GT2018–76434, 2018.

[27] A. Valera-Medina, S. Morris, J. Runyon, D. G. Pugh, R. Marsh, P. Beasley, and T. Hughes. Ammonia, methane and hydrogen for gas turbines. *Energy Procedia*, 75:118–123, 2015.

[28] A. Valera-Medina, R. Marsh, J. Runyon, D. G. Pugh, P. Beasley, T. Hughes, and P. Bowen. Ammonia–methane combustion in tangential swirl burners for gas turbine power generation. *Applied Energy*, 185:1362–1371, 2017.

[29] A. P. Dowling and J. E. Ffowcs Williams. *Sound and sources of sound.* Ellis Horwood Limited, New York, 1982.

[30] B. T. Zinn and M. E. Lores. Application of the Galerkin method in the solution of non-linear axial combustion instability problems in liquid rockets. *Combustion Science and Technology*, 4(1):269–278, 1971.

[31] F. E. C. Culick. Nonlinear behavior of acoustic waves in combustion chambers – I. *Acta Astronautica*, 3(9-10):715–734, 1976.

[32] F. E. C. Culick. Nonlinear behavior of acoustic waves in combustion chambers – II. *Acta Astronautica*, 3(9-10):735–757, 1976.

[33] A. M. Annaswamy, M. Fleifil, J. W. Rumsey, R. Prasanth, J. Hathout, and A. F. Ghoniem. Thermoacoustic instability: model-based optimal control designs and experimental validation. *Control Systems Technology, IEEE Transactions on*, 8(6):905–918, 2000.

[34] F. E. C. Culick. *Combustion instabilities in liquid-fuelled propulsion systems*. Technical report, Guggenheim Jet Propulsion Center, Caltech, https://authors.library.caltech.edu/22028/, 1988.

[35] F. E. C. Culick. *Combustion instabilities in propulsion systems.* In: *Unsteady Combustion.* pages: 173–241. Springer, 1996.

[36] F. E. C. Culick. Combustor dynamics: fundamentals, acoustics and control. *Active Control of Engine Dynamics (Conference Proceedings),* Von Karman Institute for Fluid Dynamics, Belgium, RTO-EN-20, pages 89–206, 2001.

[37] L. Benoit and F. Nicoud. Numerical assessment of thermo-acoustic instabilities in gas turbines. *International Journal for Numerical Methods in Fluids*, 47(8-9):849–855, 2005.

[38] I. Waugh, M. Geuß, and M. Juniper. Triggering, bypass transition and the effect of noise on a linearly stable thermoacoustic system. *Proceedings of the Combustion Institute*, 33 (2):2945–2952, 2011.

[39] L. Magri and M. P. Juniper. Sensitivity analysis of a time-delayed thermo-acoustic system via an adjoint-based approach. *Journal of Fluid Mechanics*, 719:183–202, 2013.

[40] K. Kashinath, S. Hemchandra, and M. P. Juniper. Nonlinear thermoacoustics of ducted premixed flames: the influence of perturbation convection speed. *Combustion and Flame*, 160(12):2856–2865, 2013.

[41] A. P. Dowling and S. R. Stow. Acoustic analysis of gas turbine combustors. *Journal of Propulsion and Power*, 19(5):751–764, 2003.

[42] S. R. Stow and A. P. Dowling. A time-domain network model for nonlinear thermoacoustic oscillations. *Journal of Engineering for Gas Turbines and Power*, 131(3):031502, 2009.

[43] W. Polifke, C. O. Paschereit, and K. Döbbeling. Constructive and destructive interference of acoustic and entropy waves in a premixed combustor with a choked exit. *International Journal of Acoustics and Vibration*, 6(3):135–146, 2001.

[44] S. Evesque and W. Polifke. Low-order acoustic modelling for annular combustors: validation and inclusion of modal coupling. In *ASME Turbo Expo 2002*, pages 321–331. Paper No. GT2002–30064, 2002.

[45] A. P. Dowling. The calculation of thermoacoustic oscillations. *Journal of Sound and Vibration*, 180(4):557–581, 1995.

[46] S. R. Stow and A. P. Dowling. Low order modelling of thermoacoustic limit cycles. In *ASME Turbo Expo 2004*, pages 775–786. Paper No. GT2004–54245, 2004.

[47] F. Nicoud, L. Benoit, C. Sensiau, and T. Poinsot. Acoustic modes in combustors with complex impedances and multidimensional active flames. *AIAA Journal*, 45(2):426–441, 2007.

[48] C. F. Silva, F. Nicoud, T. Schuller, D. Durox, and S. Candel. Combining a Helmholtz solver with the flame describing function to assess combustion instability in a premixed swirled combustor. *Combustion and Flame*, 160(9):1743–1754, 2013.

[49] F. Nicoud and L. Benoit. Global tools for thermo-acoustic instabilities in gas turbines. In *APS Division of Fluid Dynamics Meeting Abstracts*, volume 1, 2003.

[50] L. Selle, L. Benoit, T. Poinsot, F. Nicoud, and W. Krebs. Joint use of compressible large-eddy simulation and Helmholtz solvers for the analysis of rotating modes in an industrial swirled burner. *Combustion and Flame*, 145(1-2):194–205, 2006.

[51] D. Laera, K. Prieur, D. Durox, T. Schuller, S. M. Camporeale, and S. Candel. Impact of heat release distribution on the spinning modes of an annular combustor with multiple matrix burners. *Journal of Engineering for Gas Turbines and Power*, 139(5), 2017.

[52] D. Laera, T. Schuller, K. Prieur, D. Durox, S. M. Camporeale, and S. Candel. Flame describing function analysis of spinning and standing modes in an annular combustor and comparison with experiments. *Combustion and Flame*, 184:136–152, 2017.

[53] R. Balachandran, B. O. Ayoola, C. F. Kaminski, A. P. Dowling, and E. Mastorakos. Experimental investigation of the nonlinear response of turbulent premixed flames to imposed inlet velocity oscillations. *Combustion and Flame*, 143(1-2):37–55, 2005.

[54] N. Noiray, D. Durox, T. Schuller, and S. Candel. A unified framework for nonlinear combustion instability analysis based on the flame describing function. *Journal of Fluid Mechanics*, 615:139–167, 2008.

[55] G. J. Bloxsidge, A. P. Dowling, and P. J. Langhorne. Reheat buzz: an acoustically coupled combustion instability. Part 2. Theory. *Journal of Fluid Mechanics*, 193:445–473, 1988.

[56] F. E. Marble and S. Candel. An analytical study of the non-steady behavior of large combustors. In *Symposium (International) on Combustion*, volume 17, pages 761–769, 1979.

[57] L. Crocco. Aspects of combustion stability in liquid propellant rocket motors. Part I: Fundamentals. Low frequency instability with monopropellants. *Journal of the American Rocket Society*, 21(6):163–178, 1951.

[58] A. A. Peracchio and W. M. Proscia. Nonlinear heat-release/acoustic model for thermoacoustic instability in lean premixed combustors. *Journal of Engineering for Gas Turbines and Power*, 121(3):415–421, 1999.

[59] C. Paschereit, B. Schuermans, and P. Monkewitz. Non-linear combustion instabilities in annular gas-turbine combustors. In *the 44th Aerospace Sciences Meeting and Exhibit*, page 549, 2006.

[60] J. Li and A. S. Morgans. Time domain simulations of nonlinear thermoacoustic behaviour in a simple combustor using a wave-based approach. *Journal of Sound and Vibration*, 346: 345–360, 2015.

[61] B. D. Bellows, M. K. Bobba, J. M. Seitzman, and T. Lieuwen. Nonlinear flame transfer function characteristics in a swirl-stabilized combustor. *Journal of Engineering for Gas Turbines and Power*, 129(4):954–961, 2007.

[62] S. H. Strogatz. *Nonlinear dynamics and chaos: with applications to physics, biology, chemistry, and engineering.* Addison-Wesley studies in nonlinearity. Westview Press, 1994.

[63] J. Li and A. S. Morgans. Feedback control of combustion instabilities from within limit cycle oscillations using H∞ loop-shaping and the v-gap metric. *Proceedings of the Royal Society A – Mathematical Physical and Engineering Sciences*, 472(2191), 2016.

[64] S. Stow. *LOTAN: low-order thermo-acoustic network model*. Technical report, Cambridge University, Cambridge, 2005.

[65] G. Campa, S. M. Camporeale, A. Guaus, J. Favier, M. Bargiacchi, A. Bottaro, E. Cosatto, and G. Mori. A quantitative comparison between a low order model and a 3D FEM code for the study of thermoacoustic combustion instabilities. In *ASME 2011 Turbo Expo*, pages 859–869. Paper No. GT2011–45969, 2011.

[66] M. Bauerheim, M. Cazalens, and T. Poinsot. A theoretical study of mean azimuthal flow and asymmetry effects on thermo-acoustic modes in annular combustors. *Proceedings of the Combustion Institute*, 35(3):3219–3227, 2015.

[67] J. Li, D. Yang, C. Luzzato, and A. S. Morgans. *OSCILOS: the open source combustion instability low order simulator*. Technical report, Imperial College London, http://www.oscilos.com, 2014.

[68] X. Han, J. Li, and A. S. Morgans. Prediction of combustion instability limit cycle oscillations by combining flame describing function simulations with a thermoacoustic network model. *Combustion and Flame*, 162(10):3632–3647, 2015.

[69] D. Laera and S. M. Camporeale. A weakly nonlinear approach based on a distributed flame describing function to study the combustion dynamics of a full-scale lean-premixed swirled burner. *Journal of Engineering for Gas Turbines and Power*, 139(9):091501, 2017.

[70] C. O. Paschereit, E. Gutmark, and W. Weisenstein. Structure and control of thermoacoustic instabilities in a gas-turbine combustor. *Combustion Science and Technology*, 138 (1-6):213–232, 1998.

[71] C. O. Paschereit, E. Gutmark, and W. Weisenstein. Control of thermoacoustic instabilities and emissions in an industrial-type gas-turbine combustor. In *Symposium (International) on Combustion*, volume 27, pages 1817–1824, 1998.

[72] H. Torres, T. C. Lieuwen, C. Johnson, B. R. Daniel, and B. T. Zinn. Experimental investigation of combustion instabilities in a gas turbine combustor simulator. *AIAA Paper*, 99-0712:1–10, 1999.

[73] C. E. Johnson, Y. Neumeier, T. C. Lieuwen, and B. T. Zinn. Experimental determination of the stability margin of a combustor using exhaust flow and fuel injection rate modulations. *Proceedings of the Combustion Institute*, 28(1):757–763, 2000.

[74] T. C. Lieuwen. Experimental investigation of limit-cycle oscillations in an unstable gas turbine combustor. *Journal of Propulsion and Power*, 18(1):61–67, 2002.

[75] T. Sattelmayer. Influence of the combustor aerodynamics on combustion instabilities from equivalence ratio fluctuations. *Journal of Engineering for Gas Turbines and Power*, 125: 11–19, 2003.

[76] D. Noh, E. Karlis, S. Navarro-Martinez, Y. Hardalupas, A.M.K.P. Taylor, D. Fredrich, and W. P. Jones. Azimuthally-driven subharmonic thermoacoustic instabilities in a swirl-stabilised combustor. *Proceedings of the Combustion Institute*, 2018. doi: https://doi.org/10.1016/j.proci.2018.07.090.

[77] D. Fanaca, P. R. Alemela, F. Ettner, C. Hirsch, T. Sattelmayer, and B. Schuermans. Determination and comparison of the dynamic characteristics of a perfectly premixed flame in both single and annular combustion chambers. In *ASME Turbo Expo 2008*, pages 565–573. Paper No. GT2008–50781, 2008.

[78] M Stöhr, I. Boxx, C. D. Carter, and W. Meier. Experimental study of vortex-flame interaction in a gas turbine model combustor. *Combustion and Flame*, 159(8):2636–2649, 2012.

[79] D. Durox, T. Schuller, N. Noiray, and S. Candel. Experimental analysis of nonlinear flame transfer functions for different flame geometries. *Proceedings of the Combustion Institute*, 32(1):1391–1398, 2009.

[80] P. Palies, D. Durox, T. Schuller, P. Morenton, and S. Candel. Dynamics of premixed confined swirling flames. *Comptes Rendus Mécanique*, 337(6):395–405, 2009.

[81] P. Palies, D. Durox, T. Schuller, and S. Candel. The combined dynamics of swirler and turbulent premixed swirling flames. *Combustion and Flame*, 157(9):1698–1717, 2010.

[82] P. Palies, D. Durox, T. Schuller, and S. Candel. Nonlinear combustion instability analysis based on the flame describing function applied to turbulent premixed swirling flames. *Combustion and Flame*, 158:1980–1991, 2011.

[83] K. T. Kim, H. J. Lee, J. G. Lee, B. D. Quay, and D. A. Santavicca. Characterization of forced flame response of swirl-stabilized turbulent lean-premixed flames in a gas turbine combustor. *Journal of Engineering for Gas Turbines and Power*, 132(4):041502, 2010.

[84] K. T. Kim, J. G. Lee, B. D. Quay, and D. A. Santavicca. Experimental investigation of the nonlinear response of swirl-stabilized flames to equivalence ratio oscillations. *Journal of Engineering for Gas Turbines and Power*, 133(2):021502, 2011.

[85] S. Hong, R. L. Speth, S. J. Shanbhogue, and A. F. Ghoniem. Examining flow-flame interaction and the characteristic stretch rate in vortex-driven combustion dynamics using PIV and numerical simulation. *Combustion and Flame*, 160(8):1381–1397, 2013.

[86] S. Taamallah, Z. A. LaBry, S. J. Shanbhogue, and A. F. Ghoniem. Thermo-acoustic instabilities in lean premixed swirl-stabilized combustion and their link to acoustically coupled and decoupled flame macrostructures. *Proceedings of the Combustion Institute*, 35 (3):3273–3282, 2015.

[87] A.-M. Kypraiou, P. M. Allison, A. Giusti, and E. Mastorakos. Response of flames with different degrees of premixedness to acoustic oscillations. *Combustion Science and Technology*, 190(8):1426–1441, 2018.

[88] Y. Xia, D. Laera, and A. S. Morgans. Effect of flame-to-flame interaction on the flame describing function of a turbulent swirling flame in an annular combustor. In *the 25th International Congress on Sound and Vibration (ICSV25),* Hiroshima, Japan, volume 4, pages 2033–2040, 2018.

[89] N. A. Worth and J. R. Dawson. Cinematographic OH-PLIF measurements of two interacting turbulent premixed flames with and without acoustic forcing. *Combustion and Flame*, 159(3):1109–1126, 2012.

[90] J. Kopitz, A. Huber, T. Sattelmayer, and W. Polifke. Thermoacoustic stability analysis of an annular combustion chamber with acoustic low order modeling and validation against experiment. In *ASME Turbo Expo 2005*, pages 583–593. Paper No. GT2005–68797, 2005.

[91] J.-F. Bourgouin, D. Durox, J. P. Moeck, T. Schuller, and S Candel. Characterization and modeling of a spinning thermoacoustic instability in an annular combustor equipped with multiple matrix injectors. *Journal of Engineering for Gas Turbines and Power*, 137(2): 021503, 2015.

[92] N. A. Worth and J. R. Dawson. Self-excited circumferential instabilities in a model annular gas turbine combustor: global flame dynamics. *Proceedings of the Combustion Institute*, 34(2):3127–3134, 2013.

[93] J. R. Dawson and N. A. Worth. Flame dynamics and unsteady heat release rate of self-excited azimuthal modes in an annular combustor. *Combustion and Flame*, 161(10):2565–2578, 2014.

[94] D. Durox, K. Prieur, T. Schuller, and S. Candel. Different flame patterns linked with swirling injector interactions in an annular combustor. *Journal of Engineering for Gas Turbines and Power*, 138(10):101504, 2016.

[95] B. Schuermans, F. Guethe, D. Pennell, D. Guyot, and C. O. Paschereit. Thermoacoustic modeling of a gas turbine using transfer functions measured under full engine pressure. *Journal of Engineering for Gas Turbines and Power*, 132(11):111503, 2010.

[96] F. Di Sabatino, T. F. Guiberti, W. R. Boyette, W. L. Roberts, J. P. Moeck, and D. A. Lacoste. Effect of pressure on the transfer functions of premixed methane and propane swirl flames. *Combustion and Flame*, 193:272–282, 2018.

[97] C. A. Armitage, R. Balachandran, E. Mastorakos, and R. S. Cant. Investigation of the nonlinear response of turbulent premixed flames to imposed inlet velocity oscillations. *Combustion and Flame*, 146(3):419–436, 2006.

[98] G. Bulat, P. Stopford, M. Turrell, D. Frach, E. Buchanan, and M. Stöhr. Prediction of aerodynamic frequencies in a gas turbine combustor using transient CFD. In *ASME Turbo Expo 2009*, pages 585–594. Paper No. GT2009–59721, 2009.

[99] S. Ruan, T. D. Dunstan, N. Swaminathan, and R. Balachandran. Computation of forced premixed flames dynamics. *Combustion Science and Technology*, 188(7):1115–1135, 2016.

[100] A. Innocenti, A. Andreini, B. Facchini, and A. Peschiulli. Numerical analysis of the dynamic flame response of a spray flame for aero-engine applications. *International Journal of Spray and Combustion*, 9(4):310–329, 2017.

[101] H. Pitsch. Large-eddy simulation of turbulent combustion. *Annual Review of Fluid Mechanics*, 38:453–482, 2006.

[102] S. Roux, G. Lartigue, T. Poinsot, U. Meier, and C. Bérat. Studies of mean and unsteady flow in a swirled combustor using experiments, acoustic analysis, and large eddy simulations. *Combustion and Flame*, 141(1):40–54, 2005.

[103] G. Bulat. *Large eddy simulations of reacting swirling flows in an industrial burner*. PhD thesis, Imperial College London, London, UK, 2012.

[104] G. Bulat, E. Fedina, C. Fureby, W. Meier, and U. Stopper. Reacting flow in an industrial gas turbine combustor: LES and experimental analysis. *Proceedings of the Combustion Institute*, 35:3175–3183, 2015.

[105] P. Wolf, G. Staffelbach, L. Y. M. Gicquel, T. Poinsot, and V. Moureau. Massively parallel LES of azimuthal thermo-acoustic instabilities in annular gas turbines. *Comptes Rendus Mécanique*, 337:385–394, 2009.

[106] P. Wolf, R. Balakrishnan, G. Staffelbach, L. Y. M. Gicquel, and T. Poinsot. Using LES to study reacting flows and instabilities in annular combustion chambers. *Flow, Turbulence and Combustion*, 88(1-2):191–206, 2012.

[107] A. Kaufmann, F. Nicoud, and T. Poinsot. Flow forcing techniques for numerical simulation of combustion instabilities. *Combustion and Flame*, 131(4):371–385, 2002.

[108] CFD team at CERFACS. *AVBP Handbook*. CERFACS, Toulouse, France, 2009. URL `http://cerfacs.fr/~avbp/AVBP_V5.X/HANDBOOK`.

[109] I. Hernández, G. Staffelbach, T. Poinsot, J. C. R. Casado, and J. B. W. Kok. LES and acoustic analysis of thermo-acoustic instabilities in a partially premixed model combustor. *Comptes Rendus Mécanique*, 341(1):121–130, 2013.

[110] G. Staffelbach, L. Y. M. Gicquel, G. Boudier, and T. Poinsot. Large eddy simulation of self excited azimuthal modes in annular combustors. *Proceedings of the Combustion Institute*, 32(2):2909–2916, 2009.

[111] P. Palies, T. Schuller, D. Durox, L. Y. M. Gicquel, and S. Candel. Acoustically perturbed turbulent premixed swirling flames. *Physics of Fluids*, 23(3):037101, 2011.

[112] L. Tay-Wo-Chong, T. Komarek, R. Kaess, S. Foller, and W. Polifke. Identification of flame transfer functions from LES of a premixed swirl burner. In *ASME Turbo Expo 2010*, pages 623–635. Paper No. GT2010-22769, 2010.

[113] T. Lieuwen. Modeling premixed combustion-acoustic wave interactions: a review. *Journal of Propulsion and Power*, 19:765–781, 2003.

[114] S. Ducruix, T. Schuller, D. Durox, and S. Candel. Combustion dynamics and instabilities: elementary coupling and driving mechanisms. *Journal of Propulsion and Power*, 19(5): 722–734, 2003.

[115] G. Febrer, Z. Yang, and J. J. McGuirk. A hybrid approach for coupling of acoustic wave effects and incompressible LES of reacting flows. In *the 47th AIAA/ASME/SAE/ASEE Joint Propulsion Conference and Exhibit*, pages 6127–6144. Paper No. AIAA 2011-6127, 2011.

[116] H. J. Krediet, C. H. Beck, W. Krebs, S. Schimek, C. O. Paschereit, and J. B. W. Kok. Identification of the flame describing function of a premixed swirl flame from LES. *Combustion Science and Technology*, 184(7-8):888–900, 2012.

[117] H. J. Krediet, C. H. Beck, W. Krebs, and J. B. W. Kok. Saturation mechanism of the heat release response of a premixed swirl flame using LES. *Proceedings of the Combustion Institute*, 34(1):1223–1230, 2013.

[118] C. Y. Lee and S. Cant. LES of nonlinear saturation in forced turbulent premixed flames. *Flow, Turbulence and Combustion*, 99(2):461–486, 2017.

[119] X. Han and A. S. Morgans. Simulation of the flame describing function of a turbulent premixed flame using an open-source LES solver. *Combustion and Flame*, 162(5):1778–1792, 2015.

[120] F. Archambeau, N. Mehitoua, and M. Sakiz. Code Saturne: a finite volume code for the computation of turbulent incompressible flows - industrial applications. *International Journal on Finite Volumes*, 1:1–62, 2004.

[121] Y. Fournier, J. Bonelle, C. Moulinec, Z. Shang, A. G. Sunderland, and J. C. Uribe. Optimizing code Saturne computations on petascale systems. *Computers and Fluids*, 45(1): 103–108, 2011.

[122] H. G. Weller, G. Tabor, H. Jasak, and C. Fureby. A tensorial approach to computational continuum mechanics using object-oriented techniques. *Computers in Physics*, 12(6):620–631, 1998.

[123] J. Li, X. Han, Y. Xia, and A. S. Morgans. Thermoacoustic analysis of the combustor consisting long flames using low order network model approach. In *International Symposium: Thermoacoustic Instabilities in Gas Turbines and Rocket Engines: Industry Meets Academia*, Munich, Germany, May 2016.

[124] Y. Xia, J. Li, A. S. Morgans, and X. Han. Computation of local flame describing functions for thermoacoustic oscillations in a combustor with a long flame. In *the 8th European Combustion Meeting (ECM8),* Dubrovnik, Croatia, 18–21 April, 2017.

[125] X. Han, D. Laera, A. S. Morgans, C. J. Sung, X. Hui, and Y. Z. Lin. Flame macrostructures and thermoacoustic instabilities in stratified swirling flames. *Proceedings of the Combustion Institute*, 37(4):5377–5384, 2019. https://doi.org/10.1016/j.proci.2018.06.147.

[126] B. Rochette, F. Collin-Bastiani, L. Gicquel, O. Vermorel, D. Veynante, and T. Poinsot. Influence of chemical schemes, numerical method and dynamic turbulent combustion modeling on LES of premixed turbulent flames. *Combustion and Flame*, 191:417–430, 2018.

[127] M. Bauerheim, G. Staffelbach, N. A. Worth, J. R. Dawson, L. Y. M. Gicquel, and T. Poinsot. Sensitivity of LES-based harmonic flame response model for turbulent swirled flames and impact on the stability of azimuthal modes. *Proceedings of the Combustion Institute*, 35(3):3355–3363, 2015.

[128] N. Peters and B. Rogg. *Reduced kinetic mechanisms for applications in combustion systems*, volume 15. Springer Science & Business Media, 2008.

[129] C. K. Westbrook and F. L. Dryer. Simplified reaction mechanisms for the oxidation of hydrocarbon fuels in flames. *Combustion Science and Technology*, 27:31–43, 1981.

[130] K. S. Kedia, H. M. Altay, and A. F. Ghoniem. Impact of flame-wall interaction on premixed flame dynamics and transfer function characteristics. *Proceedings of the Combustion Institute*, 33(1):1113–1120, 2011.

[131] P. S. Gregory, D. M. Golden, M Frenklach, N W. Moriarty, B Eiteneer, M Goldenberg, C. T. Bowman, R. K. Hanson, S. Song, Jr. W. C. Gardiner, V. V. Lissianski, and Z. Qin. *GRI-Mech 3.0.* Technical report, UC Berkeley, http://combustion.berkeley.edu/gri-mech/, Accessed 01 December 2018.

[132] San Diego Mechanism web page. Chemical-kinetic mechanisms for combustion applications, mechanical and aerospace engineering (combustion research), University of California at San Diego (http://combustion.ucsd.edu), Accessed 01 December 2018.

[133] Philip De Goey, Victor Kornilov, Ronald Rook, and Jan Ten Thije Boonkkamp. Experimental and numerical investigation of the acoustic response of multi-slit Bunsen burners. *The Journal of the Acoustical Society of America*, 123(5):3404–3404, 2008. doi: 10.1121/1.2934109.

[134] H. Murat Altay, Kushal S. Kedia, Raymond L. Speth, and Ahmed F. Ghoniem. Two-dimensional simulations of steady perforated-plate stabilized premixed flames. *Combustion Theory and Modelling*, 14(1):125–154, 2010. doi: 10.1080/13647831003660859.

[135] A. Abou-Taouk, S. Sadasivuni, D. Lörstad, and L.-E. Eriksson. Evaluation of global mechanisms for LES analysis of SGT-100 DLE combustion system. In *ASME Turbo Expo 2013*, pages GT2013–95454, 2013.

[136] E. Fedina, C. Fureby, G. Bulat, and W. Meier. Assessment of finite rate chemistry large eddy simulation combustion models. *Flow Turbulence and Combustion*, 99 (2):385–409, 2017.

[137] A. Ehn, P. Petersson, J. J. Zhu, Z. S. Li, M. E. J. K. Aldén, E. J. K. Nilsson, J. Larfeldt, A. Larsson, T. Hurtig, N. Zettervall, et al. Investigations of microwave stimulation of a turbulent low-swirl flame. *Proceedings of Combustion Institute*, 36(3):4121–4128, 2017.

[138] S. Hermeth, G. Staffelbach, L. Gicquel, and T. Poinsot. LES evaluation of non-linear effects on the dynamic flame response in a real gas turbine combustion chamber. In *ASME Turbo Expo 2013*. Paper No. GT2013-95699, 2013.

[139] S. Hermeth, G. Staffelbach, L. Y. M. Gicquel, V. Anisimov, C. Cirigliano, and T. Poinsot. Bistable swirled flames and influence on flame transfer functions. *Combustion and Flame*, 161(1):184–196, 2014.

[140] Y. Yang, N. Noiray, A. Scarpato, O. Schulz, M. K. Düsing, and M. Bothien. Numerical analysis of the dynamic flame response in ALSTOM reheat combustion systems. In *ASME Turbo Expo 2015*. Paper No. GT2015-42622, 2015.

[141] A. Scarpato, L. Zander, R. Kulkarni, and B. Schuermans. Identification of multi-parameter flame transfer function for a reheat combustor. In *ASME Turbo Expo 2016*. Paper No. GT2016-57699, 2016.

[142] F. E. Marble and M. Candel. Acoustic disturbances from gas nonuniformities convected through a nozzle. *Journal of Sound and Vibration*, 55:225–243, 1977.

[143] W. C. Strahle. Combustion noise. *Progress in Energy and Combustion Science*, 4:157–176, 1978.

[144] J. H. Miles. Time delay analysis of turbofan engine direct and indirect combustion noise sources. *Journal of Propulsion and Power*, 25:218–227, 2009.

[145] A. S. Morgans and A. M. Annaswamy. Adaptive control of combustion instabilities for combustion systems with right-half plane zeros. *Combustion Science and Technology*, 180: 1549–1571, 2008.

[146] C. S. Goh and A. S. Morgans. The influence of entropy waves on the thermoacoustic stability of a model combustor. *Combustion Science and Technology*, 185:249–268, 2013.

[147] N. A. Cumpsty and F. E. Marble. The interaction of entropy fluctuations with turbine blade rows; a mechanism of turbojet engine noise. *Proceedings of the Royal Society of London. Series A, Mathematical and Physical Sciences*, 357:323–344, 1977.

[148] S. R. Stow, A. P. Dowling, and T. P. Hynes. Reflection of circumferential modes in a choked nozzle. *Journal of Fluid Mechanics*, 467:215–239, 2002.

[149] C. S. Goh and A. S. Morgans. Phase prediction of the response of choked nozzles to entropy and acoustic disturbances. *Journal of Sound and Vibration*, 330:5184–5198, 2011.

[150] I. Duran and S. Moreau. Solution of the quasi one-dimensional linearized Euler equations using flow invariants and the magnus expansion. *Journal of Fluid Mechanics*, 723:190–231, 2013.

[151] I. Duran and A. S. Morgans. On the reflection and transmission of circumferential waves through nozzles. *Journal of Fluid Mechanics*, 773:137–153, 2015.

[152] M. Huet, F. Vuillot, N. Bertier, M. Mazur, N. Kings, W. Tao, P. Scouflaire, F. Richecoeur, S. Ducruix, C. Lapeyre, and T. Poinsot. Recent improvements in combustion noise investigation: from the combustion chamber to nozzle flow. *Journal of Aerospace Lab*, 11:10, 2016.

[153] B. Franzelli, E. Riber, L. Y. Gicquel, and T. Poinsot. Large eddy simulation of combustion instabilities in a lean partially premixed swirled flame. *Combustion and Flame*, 159:621–637, 2012.

[154] A. S. Morgans, C. S. Goh, and J. A. Dahan. The dissipation and shear dispersion of entropy waves in combustor thermoacoustics. *Journal of Fluid Mechanics*, 733:R2, 2013.

[155] A. Giusti, N. A. Worth, E. Mastorakos, and A. P. Dowling. Experimental and numerical investigation into the propagation of entropy waves. *AIAA Journal*, 55:446–458, 2017.

[156] Y. Mahmoudi, A. Giusti, E. Mastorakos, and A. P. Dowling. Low-order modeling of combustion noise in an aero-engine: the effect of entropy dispersion. *Journal of Engineering for Gas Turbines and Power*, 140(1):011502, 2018.

[157] A. Triantafyllidis, E. Mastorakos, and R. L. G. M. Eggels. Large eddy simulations of forced ignition of a non-premixed bluff-body methane flame with conditional moment closure. *Combustion and Flame*, 156:2328–2345, 2009.

[158] S. F. Ahmed, R. Balachandran, T. Marchione, and E. Mastorakos. Spark ignition of turbulent nonpremixed bluff-body flames. *Combustion and Flame*, 151:366–385, 2007.

[159] G. I. Taylor. Dispersion of soluble matter in solvent flowing slowly through a tube. *Proceedings of the Royal Society of London. Series A. Mathematical and Physical Sciences*, 219(1137):186–203, 1953.

[160] A. S. Morgans and C. S. Goh. The effect of entropy wave dissipation and dispersion on thermoacoustic instability in a model combustor. In *the 17th AIAA/CEAS Aeroacoustics Conference (32nd AIAA Aeroacoustics Conference)*, page 2914, 2011.

[161] A. S. Morgans and J. Li. The effect of entropy noise on combustion instability on the presence of advective shear dispersion. In *the 22nd International Congress on Sound and Vibration (ICSV22), Florence, Italy*, 2015.

[162] T. Poinsot and D. Veynante. *Theoretical and numerical combustion (2nd ed.)*. RT Edwards, Inc., Philadelphia, PA, USA. p.34, 2005.

[163] M. Zellhuber, J. Schwing, B. Schuermans, T. Sattelmayer, and W. Polifke. Experimental and numerical investigation of thermo-acoustic sources related to high-frequency instabilities. *International Journal of Spray and Combustion Dynamics*, 6(1):1–34, 2014.

[164] T. Hummel, C. Temmler, B. Schuermans, and T. Sattelmayer. Reduced-order modeling of aeroacoustic systems for stability analyses of thermoacoustically noncompact gas turbine combustors. *Journal of Engineering for Gas Turbines and Power*, 138(5):051502, 2016.

[165] A. Urbano, L. Selle, G. Staffelbach, B. Cuenot, T. Schmitt, S. Ducruix, and S. Candel. Exploration of combustion instability triggering using large eddy simulation of a multiple injector liquid rocket engine. *Combustion and Flame*, 169:129–140, 2016.

[166] A. Giauque, L. Selle, L. Gicquel, T. Poinsot, H. Buechner, P. Kaufmann, and W. Krebs. System identification of a large-scale swirled partially premixed combustor using LES and measurements. *Journal of Turbulence*, 6(21):1–20, 2005.

[167] G. Campa, S. M. Camporeale, E. Cosatto, and G. Mori. Thermoacoustic analysis of combustion instability through a distributed flame response function. In *ASME Turbo Expo 2012*, pages GT2012–68243, Copenhagen, Denmark, 2012.

[168] G. Febrer. *A hybrid approach for inclusion of acoustic wave effects in incompressible LES of reacting flows*. PhD thesis, Loughborough University, 2012.

[169] R. E. Leandro and W. Polifke. Low-order modelling of distributed heat release. In *the 19th International Congress on Sound and Vibration (ICSV19)*, Vilnius, Lithuania, 2012.

[170] H. G. Weller, G. Tabor, H. Jasak, and C. Fureby. A tensorial approach to computational continuum mechanics using object-oriented techniques. *Computers in Physics*, 12(6):620–631, 1998.

[171] W. P. Jones, F. di Mare, and A. J. Marquis. *LES-BOFFIN: user's guide*. Technical report, Imperial College London, London, UK, 2012.

[172] W. P. Jones and S. Navarro-Martinez. Large eddy simulation of autoignition with a subgrid probability density function method. *Combustion and Flame*, 150(3):170–187, 2007.

[173] W. P. Jones, A. J. Marquis, and V. N. Prasad. LES of a turbulent premixed swirl burner using the Eulerian stochastic field method. *Combustion and Flame*, 159(10):3079–3095, 2012.

[174] S. R. Stow and A. P. Dowling. Modelling of circumferential modal coupling due to Helmholtz resonators. In *ASME Turbo Expo 2003, collocated with the 2003 International Joint Power Generation Conference*, pages 129–137. Paper No. GT2003–38168, 2003.

[175] Y. Xia. Predicting combustion instability in an industrial gas turbine combustor. Master's thesis, Imperial College London, U.K., 2015.

[176] A. S. Morgans. The phenomenon of sound. Lecture notes, Imperial College London, 2015.

[177] Y. Xia, D. Laera, A. S. Morgans, W. P. Jones, and J. W. Rogerson. Thermoacoustic limit cycle predictions of a pressurised longitudinal industrial gas turbine combustor. In *ASME Turbo Expo 2018*, pages GT2018–75146, 2018.

[178] P. J. Langhorne. Reheat buzz: an acoustically coupled combustion instability. Part 1. Experiment. *Journal of Fluid Mechanics*, 193:417–443, 1988.

[179] C. F. Silva, F. Nicoud, T. Schuller, D. Durox, and S. Candel. Combining a Helmholtz solver with the flame describing function to assess combustion instability in a premixed swirled combustor. *Combustion and Flame*, 160(9):1743–1754, 2013.

[180] COMSOL Multiphysics® v. 5.3. www.comsol.com. COMSOL AB, Stockholm, Sweden, 2017.

[181] S. M. Camporeale, B. Fortunato, and G. Campa. A finite element method for three-dimensional analysis of thermo-acoustic combustion instability. *Journal of Engineering for Gas Turbines and Power*, 133(1):011506, 2011.

[182] R. B. Lehoucq, D. C. Sorensen, and C. Yang. *ARPACK users' guide: solution of large-scale eigenvalue problems with implicitly restarted Arnoldi methods*. Society for Industrial and Applied Mathematics (SIAM), Philadelphia, PA, USA, 1998.

[183] L. S. Chen, T. Steinbacher, C. Silva, and W. Polifke. On generation of entropy waves by a premixed flame. In *ASME Turbo Expo 2016*, pages GT2016–57026, 2016.

[184] L. S. Chen, S. Bomberg, and W. Polifke. Propagation and generation of acoustic and entropy waves across a moving flame front. *Combustion and Flame*, 166:170–180, 2016.

[185] Y. Xia, I. Duran, A. S. Morgans, and X. Han. Dispersion of entropy perturbations transporting through an industrial gas turbine combustor. *Flow, Turbulence and Combustion*, 100(2):481–502, 2018.

[186] N. Peters. *Turbulent combustion*. Cambridge University Press, 2000.

[187] National Institute of Standards and Technology (NIST). *NIST-JANAF thermochemical tables (4th ed.)*. NIST Standard Reference Database 13, NIST, U. S. Department of Commerce, 1998. doi: 10.18434/T42S31.

[188] H. Schmidt and U. Schumann. Coherent structure of the convective boundary layer derived from large-eddy simulations. *Journal of Fluid Mechanics*, 200:511–562, 1989.

[189] C. Y. Lee and S. Cant. Assessment of LES subgrid-scale models and investigation of hydrodynamic behaviour for an axisymmetrical bluff body flow. *Flow, Turbulence and Combustion*, 98(1):155–176, 2017.

[190] S. B. Pope. *Turbulent flows*. Cambridge University Press, 2000.

[191] M. Germano, U. Piomelli, P. Moin, and W. H. Cabot. A dynamic subgrid-scale eddy viscosity model. *Physics of Fluids A: Fluid Dynamics*, 3(7):1760–1765, 1991.

[192] M. Germano. Turbulence: the filtering approach. *Journal of Fluid Mechanics*, 238:325–336, 1992.

[193] D. K. Lilly. A proposed modification of the Germano subgrid-scale closure method. *Physics of Fluids A: Fluid Dynamics*, 4(3):633–635, 1992.

[194] F. Di Mare. *Large eddy simulation of reacting and non-reacting turbulent flows*. PhD thesis, Imperial College London (University of London), 2002.

[195] V. H. Prasad. *Large eddy simulation of partially premixed turbulent combustion*. PhD thesis, Department of Mechanical Engineering, Imperial College London, 2011.

[196] W. P. Jones and V. N. Prasad. Large eddy simulation of the Sandia flame series (D, E and F) using the Eulerian stochastic field method. *Combustion and Flame*, 157:1621–1636, 2010.

[197] W. P. Jones, S. Lyra, and S. Navarro-Martinez. Large eddy simulation of a swirl stabilized spray flame. *Proceedings of the Combustion Institute*, 33(2):2153–2160, 2011.

[198] J.-Y. Chen. Stochastic modeling of partially stirred reactors. *Combustion Science and Technology*, 122(1-6), 1997.

[199] V. Sabelnikov and C. Fureby. LES combustion modeling for high Re flames using a multi-phase analogy. *Combustion and Flame*, 160:83–96, 2013.

[200] W. P. Jones, A. J. Marquis, and D. Noh. LES of a methanol spray flame with a stochastic sub-grid model. *Proceedings of the Combustion Institute*, 35(2):1685–1691, 2015.

[201] Y. Xia, A. S. Morgans, W. P. Jones, J. W. Rogerson, G. Bulat, and X. Han. Predicting thermoacoustic instability in an industrial gas turbine combustor: combining a low order network model with flame LES. In *ASME Turbo Expo 2017*, pages GT2017–63247, 2017.

[202] S. B. Pope. PDF methods for turbulent reactive flows. *Progress in Energy and Combustion Science*, 11(2):119–192, 1985.

[203] D. C. Haworth. Progress in probability density function methods for turbulent reacting flows. *Progress in Energy and Combustion Science*, 36(2):168–259, 2010.

[204] F. Gao and E. E. O'Brien. A large-eddy simulation scheme for turbulent reacting flows. *Physics of Fluids A: Fluid Dynamics*, 5(6):1282–1284, 1993.

[205] C. Dopazo. Relaxation of initial probability density functions in the turbulent convection of scalar fields. *Physics of Fluids*, 22(1):20–30, 1979.

[206] C. W. Gardiner. *Handbook of stochastic methods*, volume 3. Springer Berlin, 1985.

[207] L. Valiño. A field Monte Carlo formulation for calculating the probability density function of a single scalar in a turbulent flow. *Flow, Turbulence and Combustion*, 60(2):157–172, 1998.

[208] J. Chomiak and A. Karlsson. Flame liftoff in diesel sprays. In *Symposium (International) on Combustion*, volume 26, pages 2557–2564, 1996.

[209] C. Fureby, K. Nordin-Bates, K. Petterson, A. Bresson, and V. Sabelnikov. A computational study of supersonic combustion in strut injector and hypermixer flow fields. *Proceedings of the Combustion Institute*, 35:2127–2135, 2015.

[210] W. P. Jones and S. Navarro-Martinez. Study of hydrogen auto-ignition in a turbulent air co-flow using a large eddy simulation approach. *Computers and Fluids*, 37(7):802–808, 2008.

[211] W. P. Jones and S. Navarro-Martinez. Numerical study of n-heptane auto-ignition using LES-PDF methods. *Flow, Turbulence and Combustion*, 83(3):407–423, 2009.

[212] H. Schmid. *How to use the FFT and Matlab's pwelch function for signal and noise simulations and measurements.* Institute of Microelectronics, University of Applied Sciences Northwestern Switzerland (FHNW), 2012.

[213] E. Boström. *Investigation of outflow boundary conditions for convection-dominated incompressible fluid flows in a spectral element framework.* Master's thesis, SCI School of Engineering Sciences, KTH Royal Institute of Technology, Stockholm, Sweden, 2015. https://www.diva-portal.org/smash/get/diva2:804993/FULLTEXT01.pdf.

[214] T. Jaravel, E. Riber, B. Cuenot, and G. Bulat. Large eddy simulation of an industrial gas turbine combustor using reduced chemistry with accurate pollutant prediction. *Proceedings of the Combustion Institute*, 36(3):3817–3825, 2017.

[215] P. K. Sweby. High resolution schemes using flux limiters for hyperbolic conservation laws. *SIAM Journal on Numerical Analysis*, 21(5):995–1011, 1984.

[216] T. Holzmann. *Mathematics, numerics, derivations and OpenFOAM®.* Holzmann CFD (www.holzmann-cfd.de), 2016. doi: 10.13140/RG.2.2.27193.36960.

[217] B. Cabral and L. C. Leedom. Imaging vector fields using line integral convolution. In *the 20th Annual Conference on Computer Graphics and Interactive Techniques*, pages 263–270. ACM, 1993.

[218] G. Bulat, W. P. Jones, and S. Navarro-Martinez. Large eddy simulations of isothermal confined swirling flow in an industrial gas-turbine. *International Journal of Heat and Fluid Flow*, 51:50–64, 2015.

[219] D. G. Goodwin, H. K. Moffat, and R. L. Speth. Cantera (version 2.1.2): an object-oriented software toolkit for chemical kinetics, thermodynamics, and transport processes. `http://www.cantera.org`, 2014.

[220] L. Tay-Wo-Chong and W. Polifke. Large eddy simulation-based study of the influence of thermal boundary condition and combustor confinement on premix flame transfer functions. *Journal of Engineering for Gas Turbines and Power*, 135(2):021502, 2013.

[221] Y. Xia, D. Laera, and A. S. Morgans. Effect of wall heat transfer on the flame response to acoustic perturbation in a turbulent swirling combustor. In *the 25th International Congress on Sound and Vibration (ICSV25),* Hiroshima, Japan, volume 4, pages 2025–2032, 2018.

[222] T. C. Lieuwen and V. Yang, editors. *Combustion instabilities in gas turbine engines: operational experience, fundamental mechanisms and modeling*, Progress in astronautics and aeronautics, 2005. American Institute of Aeronautics and Astronautics. ISBN 9781563476693.

[223] MATLAB and statistics toolbox release 2017b. The MathWorks, Inc. Natick, MA, USA, 2017.

[224] D. Laera and A. S. Morgans. Large eddy simulations for the flame describing function of a premixed turbulent swirling flame. In *the 24th International Congress on Sound and Vibration (ICSV24),* London, U.K., 23–27 July, 2017.

[225] Y. Xia, D. Laera, W. P. Jones, and A. S. Morgans. Numerical prediction of the flame describing function and thermoacoustic limit cycle for a pressurized gas turbine combustor. *Combustion Science and Technology*, 2019. https://doi.org/10.1080/00102202.2019.1583221.

[226] E. Gullaud and F. Nicoud. Effect of perforated plates on the acoustics of annular combustors. *AIAA Journal*, 50(12):2629–2642, 2012.

[227] A. B. Bauer. Impedance theory and measurements on porous acoustic liners. *Journal of Aircraft*, 14(8):720–728, 1977.

[228] R. Kirby. Transmission loss predictions for dissipative silencers of arbitrary cross section in the presence of mean flow. *The Journal of the Acoustical Society of America*, 114(1): 200–209, 2003.

[229] H. Levine and J. Schwinger. On the radiation of sound from an unflanged circular pipe. *Physical Review*, 73(4):383, 1948.

[230] M. C. A. M. Peters, A. Hirschberg, A. J. Reijnen, and A. P. J. Wijnands. Damping and reflection coefficient measurements for an open pipe at low Mach and low Helmholtz numbers. *Journal of Fluid Mechanics*, 256:499–534, 1993.

[231] S. Candel. Combustion dynamics and control: progress and challenges. *Proceedings of the Combustion Institute*, 29(1):1–28, 2002.

[232] D. Laera, G. Campa, and S. M. Camporeale. A finite element method for a weakly nonlinear dynamic analysis and bifurcation tracking of thermo-acoustic instability in longitudinal and annular combustors. *Applied Energy*, 187:216–227, 2017.

[233] Y. Xia, I. Duran, A. S. Morgans, and X. Han. Dispersion of entropy waves advecting through combustor chambers. In *the 23rd International Congress on Sound and Vibration (ICSV23),* Athens, Greece, 10–14 July, 2016.

[234] B. A. Boukamp. A nonlinear least squares fit procedure for analysis of immittance data of electrochemical systems. *Solid State Ionics*, 20:31–44, 1986.

[235] M. Fleifil, A. M. Annaswamy, Z. A. Ghoneim, and A. F. Ghoniem. Response of a laminar premixed flame to flow oscillations: a kinematic model and thermoacoustic instability results. *Combustion and Flame*, 106(4):487–510, 1996.

[236] A. P. Dowling and A. S. Morgans. Feedback control of combustion oscillations. *Annual Review of Fluid Mechanics*, 37(1):151–182, 2005.

[237] M. Besson, P. Bruel, J. L. Champion, and B. Deshaies. Experimental analysis of combusting flows developing over a plane-symmetric expansion. *Journal of Thermophysics and Heat Transfer*, 14:59–67, 2000.

[238] C. Duwig and C. Fureby. Large eddy simulation of unsteady lean stratified premixed combustion. *Combustion and Flame*, 151(1–2):85–103, 2007.

[239] T. Ma, Y. Gao, A. M. Kempf, and N. Chakraborty. Validation and implementation of algebraic LES modelling of scalar dissipation rate for reaction rate closure in turbulent premixed combustion. *Combustion and Flame*, 161(12):3134–3153, 2014.

[240] C. Fureby. A fractal flame-wrinkling large eddy simulation model for premixed turbulent combustion. *Proceedings of the Combustion Institute*, 30(1):593–601, 2005.

[241] P. Domingo, L. Vervisch, S. Payet, and R. Hauguel. DNS of a premixed turbulent V flame and LES of a ducted flame using a FSD-PDF subgrid scale closure with FPI-tabulated chemistry. *Combustion and Flame*, 143(4):566–586, 2005.

[242] A. Majda and J. Sethian. The derivation and numerical solution of the equations for zero Mach number combustion. *Combustion Science and Technology*, 42(3-4):185–205, 1985.

[243] L. Y. M. Gicquel, G. Staffelbach, and T. Poinsot. Large eddy simulations of gaseous flames in gas turbine combustion chambers. *Progress in Energy and Combustion Science*, 38(6): 782–817, 2012.

[244] C. Fureby. A comparative study of flamelet and finite rate chemistry LES for a swirl stabilized flame. *Journal of Engineering for Gas Turbines and Power*, 134:041503, 2012.

[245] Y. Afarin and S. Tabejamaat. The effect of fuel inlet turbulence intensity on H_2/CH_4 flame structure of MILD combustion using the LES method. *Combustion Theory and Modelling*, 17(3):383–410, 2013.

[246] B. G. Franzelli. *Impact of the chemical description on direct numerical simulations and large eddy simulations of turbulent combustion in industrial aero-engines*. PhD thesis, Institut National Polytechnique de Toulouse, France, 2011.

[247] F. Duchaine, F. Boudy, D. Durox, and T. Poinsot. Sensitivity analysis of transfer functions of laminar flames. *Combustion and Flame*, 158(12):2384–2394, 2011.

[248] D. Mejia, L. Selle, R. Bazile, and T. Poinsot. Wall-temperature effects on flame response to acoustic oscillations. *Proceedings of the Combustion Institute*, 35(3):3201–3208, 2015.

[249] N. Kornev, E. Shchukin, E. Taranov, H. Kröger, J. Turnow, and E. Hassel. Development and implementation of inflow generator for LES and DNS applications in OpenFOAM. In *the 3rd Open Source CFD International Conference*, Barcelona, Spain, 2009.

[250] B. J. Geurts and J. Fröhlich. A framework for predicting accuracy limitations in large-eddy simulation. *Physics of Fluids*, 14(6):L41–L44, 2002.

[251] J. Li, F. Richecoeur, and T. Schuller. Determination of heat release rate disturbances in open flames based on fluctuations in the travel time of ultrasonic waves. *Combustion Science and Technology*, 184:533–555, 2012.

[252] J. Li, F. Richecoeur, and T. Schuller. Reconstruction of heat release rate disturbances based on transmission of ultrasounds: experiments and modeling for perturbed flames. *Combustion and Flame*, 160:1779–1788, 2013.

[253] T. Schuller, D. Durox, and S. Candel. A unified model for the prediction of laminar flame transfer functions: comparisons between conical and V-flame dynamics. *Combustion and Flame*, 134(1-2):21–34, 2003.

[254] E. Motheau, L. Selle, and F. Nicoud. Accounting for convective effects in zero-Mach-number thermoacoustic models. *Journal of Sound and Vibration*, 333(1):246–262, 2014.

[255] P. Weigand, W. Meier, X. R. Duan, W. Stricker, and M. Aigner. Investigations of swirl flames in a gas turbine model combustor: I. Flow field, structures, temperature, and species distributions. *Combustion and Flame*, 144(1–2):205–224, 2006.

[256] P. Schmitt, T. Poinsot, B. Schuermans, and K. P. Geigle. Large-eddy simulation and experimental study of heat transfer, nitric oxide emissions and combustion instability in a swirled turbulent high-pressure burner. *Journal of Fluid Mechanics*, 570:17–46, 2007.

[257] K. T. Kim, J. G. Lee, B. D. Quay, and D. A. Santavicca. Spatially distributed flame transfer functions for predicting combustion dynamics in lean premixed gas turbine combustors. *Combustion and Flame*, 157(9):1718–1730, 2010.

[258] J. Li and A. S. Morgans. The one-dimensional acoustic field in a duct with arbitrary mean axial temperature gradient and mean flow. *Journal of Sound and Vibration*, 400:248–269, 2017.

[259] N. Karimi, M. J. Brear, and W. H. Moase. Acoustic and disturbance energy analysis of a flow with heat communication. *Journal of Fluid Mechanics*, 597:67–89, 2008.